Defense Threat Reduction Agency
8725 John J. Kingman Road, MS 6201
Fort Belvoir, VA 22060-6201

DTRA-TR-03-33

TECHNICAL REPORT

A Regional Seismic Experiment in India to Increase Knowledge of Velocity Structure

Approved for public release; distribution is unlimited.

May 2006

DTRA01-00-C-0028

DARE Tracking
73782

James F. Lewkowicz, et al.

Prepared by:
Weston Geophysical Corporation
57 Bedford Street
Suite 102
Lexington, MA 02420

DESTRUCTION NOTICE

FOR CLASSIFIED documents, follow the procedures in DoD 5550.22-M, National Industrial Security Program Operating Manual, Chapter 5, Section 7 (NISPOM) or DoD 5200.1-R, Information Security Program Regulation, Chapter 1X.

FOR UNCLASSIFIED limited documents, destroyed by any method that will prevent disclosure of contents or reconstruction of the document.

Retention of this document by DoD contractors is authorized in accordance with DoD 5220.22M, Industrial Security manual.

PLEASE NOTIFY THE DEFENSE THREAT REDUCTION AGENCY, ATTN: IMMI, 8725 JOHN J. KINGMAN ROAD, MS-6201, FT. BELVOIR, VA 22060-6201. IF YOUR ADDRESS IS INCORRECT, IF YOU WISH IT DELETED FROM THE DISTRIBUTION LIST, OR IF THE ADDRESSEE IS NO LONGER EMPLOYED BY YOUR ORGANIZATION.

DISTRIBUTION LIST UPDATE

This mailer is provided to enable DTRA to maintain current distribution lists for reports. (We would appreciate you providing the requested information.)

- ☐ Add the individual listed to your distribution list.
- ☐ Delete the cited organization/individual.
- ☐ Change of address.

Note:
Please return the mailing label from the document so that any additions, changes, corrections or deletions can be made easily. For distribution cancellation or more information call DTRA/BDLMI (703) 767-4725.

NAME: _____

ORGANIZATION: _____

OLD ADDRESS	NEW ADDRESS
_____	_____
_____	_____
_____	_____

TELEPHONE NUMBER: ( ) _____

DTRA PUBLICATION NUMBER/TITLE	CHANGES/DELETIONS/ADDITONS, etc. *(Attach Sheet if more Space is Required)*
_____	_____
_____	_____
_____	_____

DTRA or other GOVERNMENT CONTRACT NUMBER: _____

CERTIFICATION of NEED-TO-KNOW BY GOVERNMENT SPONSOR (if other than DTRA):

SPONSORING ORGANIZATION: _____

CONTRACTING OFFICER or REPRESENTATIVE: _____

SIGNATURE: _____

DEFENSE THREAT REDUCTION AGENCY
ATTN: BDLMI
8725 John J Kingman Road, MS 6201
Fort Belvoir, VA 22060-6201

DEFENSE THREAT REDUCTION AGENCY
ATTN: BDLMI
8725 John J Kingman Road, MS 6201
Fort Belvoir, VA 22060-6201

REPORT DOCUMENTATION PAGE

Form Approved
OMB No. 0704-0188

1. REPORT DATE *(DD-MM-YYY)*	2. REPORT TYPE	3. DATES COVERED *(From - To)*
May 2006	Technical Report	

4. TITLE AND SUBTITL
A Regional Seismic Experiment in India to Increase Knowledge Of Velocity Structure (U)

5a. CONTRACT NUMBER
DTRA 01-00-C-0028

5b. GRANT NUMBER

5c. PROGRAM ELEMENT NUMBER
J21D

6. AUTHOR(S)
James F. Lewkowicz, Keith Priestley, Vinod Gaur, Jessie L. Bonner, Sara G. Russell, Delaine Ritter, Alessia Maggi, and Supryio Mitra

5d. PROJECT NUMBER
BI

5e. TASK NUMBER
SA

5f. WORK UNIT NUMBER
DH 07754

7. PERFORMING ORGANIZATION NAME(S) AND ADDRESS(ES)
Weston Geophysical Corporation
57 Bedford St., Suite 102
Lexington, MA 02420

8. PERFORMING ORGANIZATION REPORT NUMBER

9. SPONSORING / MONITORING AGENCY NAME(S) AND ADDRESS(ES)
Defense Threat Reduction Agency
8725 John J. Kingman Rd., MS 6201
Fort Belvoir, VA 22060-6201

10. SPONSOR/MONITOR'S ACRONYM(S)
DTRA

11. SPONSOR/MONITOR'S REPORT NOS.
TR-03-33

12. DISTRIBUTION / AVAILABILITY STATEMENT
Approved for public release; distribution is unlimited.

13. SUPPLEMENTARY NOTES
This work was sponsored by the Defense Threat Reduction Agency under the RDT&E RMC Code B J21D K480 BI SA 07754 24904D.

14. ABSTRACT

Weston Geophysical Corporation, Cambridge University and India Institute of Astrophysics formed a consortium in 2000 to deploy a network of high-quality broadband seismometers distributed across India. This network began operation in April 200l, and is now fully operational providing important data for studies focusing on the characterization of the velocity structure and propagation of seismic waves throughout Southern Asia. Each station consists of a Guralp CMG-3TD digital output seismometer plus a Storage and Acquisition Model (SAM) data logger. The sensors possess a broadband velocity response between 0.008 and 50 Hz, continuously record at 100 samples/second, and are time-stamped using a GPS receiver. The data are archived on nine or 18 GB disks, which are changed at intervals of approximately six months.

This report consists of two parts. The main text provides an introduction to the goals of the project and a review and summary of the highlights of the various research objectives that were accomplished. The research results are discussed in detail within the papers and presentations contained in Appendix A.

15. SUBJECT TERMS

16. SECURITY CLASSIFICATION OF:			17. LIMITATION OF ABSTRACT	18. NUMBER OF PAGES	19a. NAME OF RESPONSIBLE PERSON
a. REPORT	b. ABSTRACT	c. THIS PAGE			19b. TELEPHONE NUMBER *(include area code)*
Unclassified	Unclassified	Unclassified	SAR	171	

CONVERSION TABLE

Conversion Factors for U.S. Customary to metric (SI) units of measurement.

MULTIPLY →	BY →	TO GET
TO GET ←	BY ←	DIVIDE

angstrom	1.000 000 x E -10	meters (m)
atmosphere (normal)	1.013 25 x E +2	kilo pascal (kPa)
bar	1.000 000 x E +2	kilo pascal (kPa)
barn	1.000 000 x E -28	meter^2 (m^2)
British thermal unit (thermochemical)	1.054 350 x E +3	joule (J)
calorie (thermochemical)	4.184 000	joule (J)
cal (thermochemical/cm^2)	4.184 000 x E -2	mega joule/m^2 (MJ/m^2)
curie	3.700 000 x E +1	*giga bacquerel (GBq)
degree (angle)	1.745 329 x E -2	radian (rad)
degree Fahrenheit	$t_k = (t°f + 459.67)/1.8$	degree kelvin (K)
electron volt	1.602 19 x E -19	joule (J)
erg	1.000 000 x E -7	joule (J)
erg/second	1.000 000 x E -7	watt (W)
foot	3.048 000 x E -1	meter (m)
foot-pound-force	1.355 818	joule (J)
gallon (U.S. liquid)	3.785 412 x E -3	meter^3 (m^3)
inch	2.540 000 x E -2	meter (m)
jerk	1.000 000 x E +9	joule (J)
joule/kilogram (J/kg) radiation dose absorbed	1.000 000	Gray (Gy)
kilotons	4.183	terajoules
kip (1000 lbf)	4.448 222 x E +3	newton (N)
kip/inch^2 (ksi)	6.894 757 x E +3	kilo pascal (kPa)
ktap	1.000 000 x E +2	newton-second/m^2 ($N-s/m^2$)
micron	1.000 000 x E -6	meter (m)
mil	2.540 000 x E -5	meter (m)
mile (international)	1.609 344 x E +3	meter (m)
ounce	2.834 952 x E -2	kilogram (kg)
pound-force (lbs avoirdupois)	4.448 222	newton (N)
pound-force inch	1.129 848 x E -1	newton-meter (N-m)
pound-force/inch	1.751 268 x E +2	newton/meter (N/m)
pound-force/foot^2	4.788 026 x E -2	kilo pascal (kPa)
pound-force/inch^2 (psi)	6.894 757	kilo pascal (kPa)
pound-mass (lbm avoirdupois)	4.535 924 x E -1	kilogram (kg)
pound-mass-foot^2 (moment of inertia)	4.214 011 x E -2	kilogram-meter^2 ($kg-m^2$)
pound-mass/foot^3	1.601 846 x E +1	kilogram-meter^3 (kg/m^3)
rad (radiation dose absorbed)	1.000 000 x E -2	**Gray (Gy)
roentgen	2.579 760 x E -4	coulomb/kilogram (C/kg)
shake	1.000 000 x E -8	second (s)
slug	1.459 390 x E +1	kilogram (kg)
torr (mm Hg, 0^0 C)	1.333 22 x E -1	kilo pascal (kPa)

*The bacquerel (Bq) is the SI unit of radioactivity; 1 Bq = 1 event/s.
**The Gray (GY) is the SI unit of absorbed radiation.

TABLE OF CONTENTS

SUMMARY

Weston Geophysical Corporation (WGC), Cambridge University (CAM), and the India Institute of Astrophysics (IIA) formed a consortium in 2000 to deploy a network of high-quality broadband seismometers distributed across India. This network began operation in April 2001 and is now fully operational providing important data for studies focusing on the characterization of the velocity structure and propagation of seismic waves throughout Southern Asia. Each station consists of a Guralp CMG-3TD digital output seismometer plus a Storage and Acquisition Module (SAM) data logger. The sensors possess a broadband velocity response between 0.008 and 50 Hz, continuously record at 100 samples/second, and are time-stamped using a GPS receiver. The data are archived on 9 or 18 GB disks, which are changed at intervals of approximately six months. We experienced various difficulties with the instrument design and the operating environment during the first 18 months of deployment. These problems spurred modifications to the instrument by Guralp, Ltd. and a change in some of our operating practices. To simplify maintenance of the network we have designed and constructed an interface for the stations allowing dialup modem or internet access to the CMG-3TD + SAM, which will provide monitoring and rapid troubleshooting capabilities for the network. A significant database has already provided the basis for several noteworthy results which have been reported in numerous presentations and published papers which are included in this report in an Appendix.

This report consists of two parts. The main text provides an introduction to the goals of the project and a review and summary of the highlights of the various research objectives that were accomplished. The research results are discussed in detail within the papers and presentations contained in Appendix A.

INTRODUCTION

Recent nuclear tests detonated by India and Pakistan motivated the need for an improved understanding of the velocity structure and seismic wave propagation

characteristics of the south Asia region. The objective of this research project was to deploy seismographs in India in order to acquire seismic data needed to improve the fundamental understanding of seismic wave propagation in this region, e.g., attenuation, phase blockage and phase focusing/defocusing, and to improve the resolution of regional velocity models, such as WINPAK3D [Johnson and Vincent, 2003] An understanding of the regional attenuation structure of India is critical to evaluating phase propagation for determination of source magnitude, moment and yield estimates.

Weston Geophysical Corporation Geophysical Corporation (WGC), Cambridge University (CAM), and the India Institute of Astrophysics (IIA) formed a consortium in 2000 to deploy a network of eight high-quality broadband seismometers distributed across India (Figure 1, left).

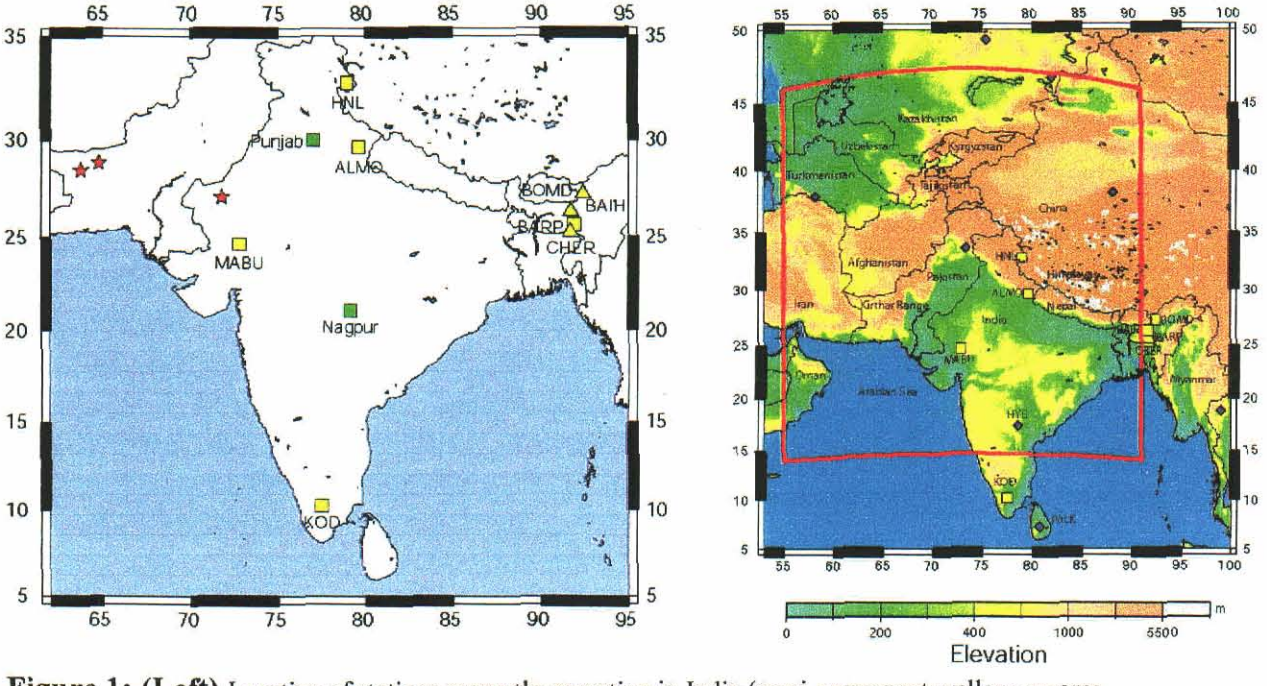

Figure 1: (Left) Location of stations currently operating in India (semi-permanent: yellow squares, mobile: yellow triangles). The Indian and Pakistan nuclear tests are shown as red stars. **(Right)** Map illustrating study region. The red box denotes the geographical extent of Weston Geophysical's WINPAK3D tomographical velocity model. The location of seismic stations in southern Asia is also shown. The yellow squares represent the WGC/CAM/IIA network installed and operated under the previous contract beginning in April 2001. Blue diamonds show locations of stations belonging to the FDSN network

This network began operation in April 2001 and is now fully operational providing important data for studies focusing on the characterization of the structure and propagation of seismic waves throughout Southern Asia. Each station consists of a

Guralp CMG-3TD digital output seismometer plus a Storage and Acquisition Module (SAM) data logger. The sensors possess a broadband velocity response between 0.008 and 50 Hz, continuously record at 100 samples/second, and are time-stamped using a GPS receiver. We experienced various difficulties with the instrument design and the operating environment during the first 18 months of deployment which, spurred modifications to the instrument by Guralp, Ltd. and a change in some of our operating practices. To simplify maintenance of the network we have designed and constructed an interface for the stations allowing dial-up modem or internet access to the CMG-3TD + SAM, which will provide monitoring and rapid troubleshooting capabilities for the network.

The significant database that has been acquired to date is the basis for the published papers that are highlighted in Table 1. The reader is referred to Appendix A

Table 1.

1. Mitra, S, S. A. Russell, K. Priestley, V. K. Gaur, S. S. Rai (2002), Measurements of frequency dependent Lg attenuation in India, *Eos Trans. AGU, **83**, Fall Meet. Suppl., Abstract, 2002.*
2. Maggi, A., Teleseismic and regional waveform modeling of the 26 Jan 2001 Bhuj earthquake sequence, PhD thesis chapter, Cambridge University, 2002.
3. Rai, S. S., K. Priestley, K. Suryaprakasam, D. Srinagesh, V. K. Gaur and Z. Du, Crustal shear velocity of south Indian shield, *J. Geophys. Res.*, 108, No. B2, 2088-2100, 2003
4. Gupta, S., S. S. Rai, K. S. Prakasam, D. Srinagesh, B. K. Bansal, R. K. Chadha, K. Priestley and V. K. Gaur, The nature of the crust in southern India: Implications for Precambrian crustal evolution, *Geophys. Res. Lett*, Vol. 30, No. 1, 2003.
5. Maggi, A., J. Jackson, K. Priestley and C. Baker, A re-assessement of focal depth distributions in southern Iran, the Tien Shan and Northern India: do earthquakes really occur in the continental mantle?, *Geophys. J. Intl.*, 143, 629-661, 2000.
6. Mitra, S., K. Priestley, V. K. Gaur, Crustal structure beneath the foreland spur in Northeastern India, *Eos Trans. AGU, **83**(47), Fall Meet. Suppl., Abstract, 2002.*
7. Rai, A., K. Priestley, and V.K. Gaur, Seismic Characteristics of the Southern Indian Granulite Terrane Around Kodaikanal, *Eos Trans. AGU, **83***(47), Fall Meet. Suppl., 2002
8. Gupta, S., S.S. Rai, K.S. Prakasam, D. Srinagesh, R.K. Chadha, K. Priestley, and V.K. Gaur, First evidence for anomalous thick crust beneath mid-archean western Dharwar craton, *Current Sci.*, May, 2003.
9. Priestley, K., and E. Debayle, Seismic evidence for a moderately thick lithosphere beneath the Siberian Platform, *Geophys. Res. Lett.*, Vol. 30, No. 3, 1118, 2003.

which, contains copies of these publications that present detailed research results. The main body of this report will be devoted to a summary description of the project and scientific results. We begin with an overview of the geological and geophysical setting of India.

THE GEOLOGY AND GEOPHYSICS OF INDIA

Southern Asia (Figure 1, right) has a complex tectonic history resulting in extreme variations of lithospheric structure. Mountain ranges extend from the Kirthar Range in southern Pakistan across the Sulaiman Range, the Himalayas in NE Pakistan, India, Tibet, Nepal, and China, and the Indo-Burmese range in NE India and Myanmar. These ranges represent a diffuse zone of deformation that is the result of continent-continent collision between India and Eurasia. A string of continental blocks, micro-continents, and island arcs have been incorporated into the plate boundaries, further complicating this deformation zone.

Most of the Indian subcontinent is a mosaic of different Archean and Proterozoic cratons which, together with intervening mobile belts, form the Indian shield. Southern India consists of the Dharwar, Singhbhnm, and Aravalli Archean cratons separated by the Delhi, Satpura, and Eastern Ghat mobile belts. The exposed parts of the cratons are composed of granulite-greenstone terranes whereas the mobile belts consist of moderate- to high-grade metamorphic rocks. Most of the Indian shield north of the Dharwar craton and east of the Aravalli craton is an early Proterozoic magmatic terrane of granite gneisses. These are exposed as far north as the southern margin of the Himalayan foreland basin and are thought to extend to the north beneath the Himalayan foreland basin and the high Himalaya, and possibly as far north as southern Tibet. Based on their correlation of early-to-middle Proterozoic intercratonic sedimentary rocks, *Radhakrishna and Nagvi* [1986] believe that the entire shield has been a coherent landmass since the late Archean or early Proterozoic.

The National Geophysical Research Institute of India has had a Deep Seismic Sounding (DSS) program for determination of crustal structure since the mid-1970's. Most studies in this program have utilized waveform correlation techniques introduced by Russian seismologists at the initiation of the Indian DSS program. The early results of

the DSS program are summarized in *Kaila and Krishna* [1992]. Data for a number of the older profiles have recently been re-examined employing ray tracing analysis [Krishna *et al.*, 1989], and this technique has been utilized in interpreting recently recorded seismic profile data [e.g., Louden, 1997; Prasad *et al.*, 1998; Krishna and Ramesh, 2000]. However, the details of crustal structure variations of the subcontinent are still poorly known.

Early surface wave studies [Bhattacharya, 1974] suggest that the Indian shield has a thin lithosphere, whereas body wave studies indicate the presence of a thick, cool lithospheric root beneath at least part of the Indian shield [Srinagesh and Rai, 1996; Gupta *et al.*, 1991; Gupta *et al.*, 2002]. For the past ~50 million years, the Indian subcontinent has been penetrating deeper and deeper into Eurasia. This collision has uplifted the Himalaya Mountains and the Tibetan Plateau, the highest mountain range and plateau on Earth. The effects of the collision, which are evident 2500 km to the north in Mongolia, attest to the great strength of the Indian lithosphere, but whether the strength lies in an unusually thick, strong upper mantle lithosphere [Sonder and England, 1986] or in an extremely strong crust [Maggi *et al.*, 2000] is currently a subject of debate [Jackson, 2002].

SEISMOGRAPH NETWORK DEPLOYMENT AND MAINTENANCE

We began installation of the WGC/IIA/CAM network in April 2001 and now have seismographs operating at eight sites. Each station consists of a Guralp CMG-3TD digital output seismometer plus a Storage and Acquisition Module (SAM) data logger.

- CMG-3T Digital Output Seismometer
  - —120 seconds to 50 Hz sensor frequency response
  - —3000 V/m/sec sensor sensitivity
  - —3 Channel 24-bit ADC
  - —16-bit environmental channels
  - —LTA/STA triggering
  - —GPS antenna
  - —RS-232 data output
- SAM Storage and Acquisition Module
  - —Continuous Data Acquisition
  - —Operates over 10 to 26 Volts input
  - —Outputs to radio, telephone, or digital telemetry
  - —9GB disks

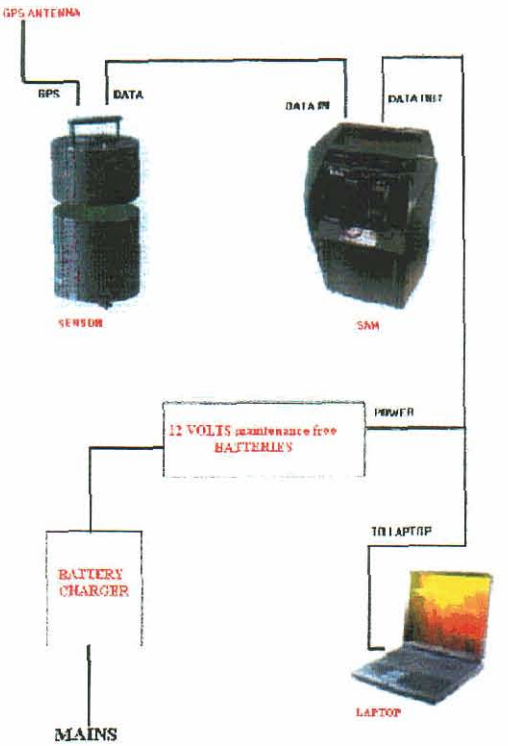

The sensors possess a broadband velocity response between 0.008 and 50 Hz, continuously record at 100 samples/second, and are time-stamped using a GPS receiver. The data are archived on 9 or 18 Gb disks which are changed at intervals of approximately six months. The data are first accessed at IIA in Bangalore, then either hand-carried or transferred by ftp to CAM from where they are sent to WGC for eventual delivery. The installation and maintenance of the stations is primarily the responsibility of Vinod Gaur, Keith Priestley, and graduate students at CAM. Figure 1 shows the distribution of the network while Figure 2 describes the operational dates of the stations. As noted earlier, numerous difficulties with the instrument design and the operating environment were experienced during the first 18 months of deployment, and these problems spurred modifications to the instrument by Guralp, Ltd. and a change in some of our operating practices. To simplify maintenance of the network we have designed

and constructed an interface for the stations allowing dialup modem or internet access to the CMG-3TD + SAM which will provide monitoring and rapid troubleshooting capabilities for the network. The network is now fully operational and we have collected a significant database that has already provided several noteworthy results. Details of the station sites and qualitative description of the data are provided in Part II of this report.

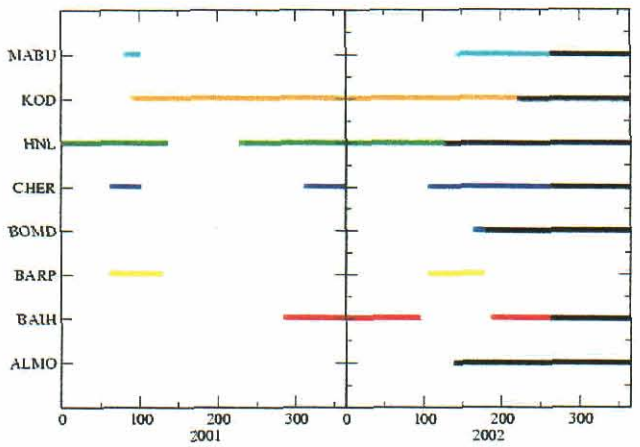

Figure 2: Chart summarizing operational dates for receivers in the WGC/CAM/IIA broadband seismic network in India. The change to black shows dates for which the stations are operating but the data has yet to be retrieved from the filed sites in Inida.

CRUSTAL STRUCTURE FROM RECEIVER FUNCTION ANALYSIS

The teleseismic *P*-wave coda contains *S*-waves generated by *P* to *S* conversions at significant velocity contrasts in the crust and upper mantle below the seismograph site. Receiver functions are radial and transverse waveforms created by deconvolving the vertical component from the radial and transverse components of the seismogram to isolate the receiver site effects from the other information contained in a teleseismic *P*-wave. We have devoted considerable effort during the past two years into determining crustal structure in India using receiver function analysis. Below, we highlight results from studies focusing on southern and northeastern Indian structure.

Rai et al. [2003] analyze receiver functions and short-period Rayleigh wave phase velocity (discussed below) along an N-S profile from NND to BGL (stations shown in Figure 5) to determine the seismic characteristics of this part of the Dharwar Craton. At

all sites, the receiver functions are extremely simple, indicating that the crust beneath each site is also simple with no significant intra-crustal discontinuities. Joint inversion of the receiver function and surface wave phase velocity data (Figure 3) shows the seismic characteristics of this part of the Dharwar crust to be remarkably uniform throughout and that it varies within fairly narrow bounds: crustal thickness (35 ± 2 km), average shear wave speed (3.79 ± 0.09 km/s), and Vp/Vs ratio (1.746 ± 0.014). There is no evidence for a high velocity basal layer in the receiver function crustal images of the central Dharwar craton, suggesting that there is no seismically-distinct layer of mafic cumulates overlying the Moho and implying that the base of the Dharwar crust has remained fairly refractory since its cratonization.

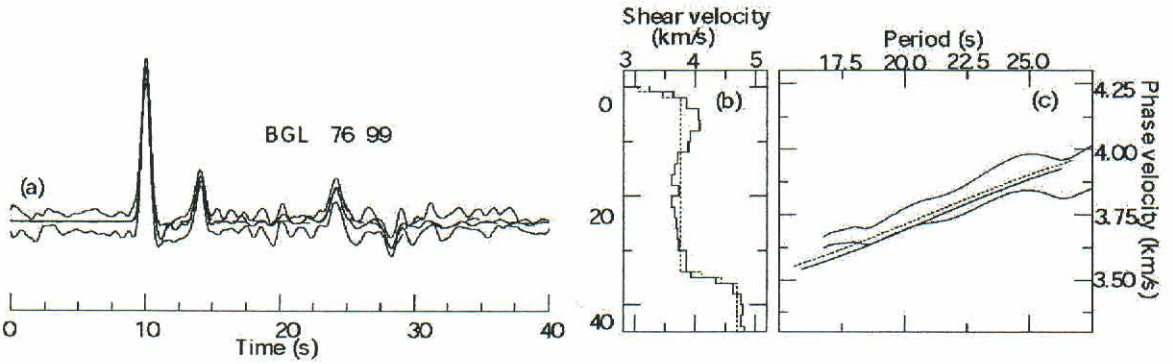

Figure 3: Results for joint inversion of receiver function and surface wave velocity data at station BGL. **(A)** Match of the 1-sigma bounds of the observed (light solid lines) and synthetic (heavy solid line) receiver function from velocity models shown in **(B).** **(C)** Fit of the theoretical Rayleigh wave phase velocity curves (heavy solid line) to the 1-sigma bounds of the observed phase velocity (light lines).

Rai et al. [2002] use receiver functions from KOD and PALK (Figure 1) to examine the velocity and anisotropy structure of the Neoproterozoic south Indian granulite terrane and compare these with the velocity and anisotropy structure beneath BGL on the Dharwar craton. Receiver function analysis shows that the crust beneath KOD is 44 km thick and consists of a 27 km thick, Vs 3.6 km/s upper layer and a 17 km thick Vs 3.95 km/s lower layer, significantly thicker than beneath the southern part of the Dhawar craton. The average Vp/Vs ratio of the South Indian granulite crust is 1.753 (Poisson's ratio of 0.26) whereas the average Vp/Vs ratio of the Dharwar craton crust is 1.74 (Poisson's ratio of 0.25). A clear arrival time difference in Moho converted phase *Ps* recorded on radial and tangential components suggests that the crust of both the south Indian granulite terrain and the Dharwar craton are anisotropic. Analysis of splitting of

P_s indicates that for the granulitic crust the fast-azimuth is oriented approximately EW with a time-delay of 0.25 s between the fast and slow components of the shear-wave (Figure 4). Beneath the southern part of the Dharwar craton the fast-azimuth is oriented approximately NS with a time-delay of about 0.2 s.

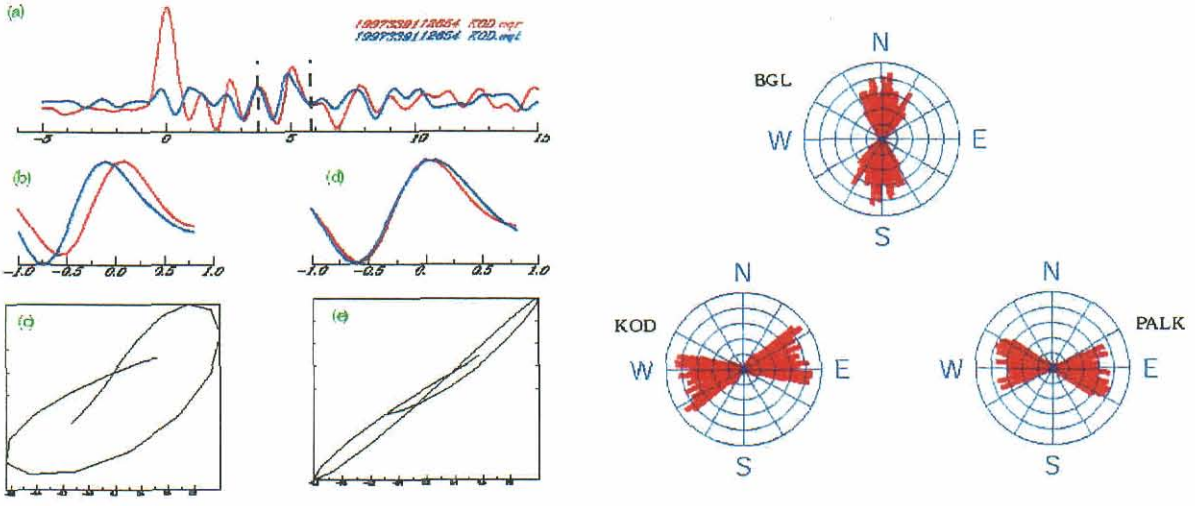

Figure 4: (Left) (a) An example of splitting observed in Moho converted Ps phase of the radial and transverse component receiver function at KOD. The analysis window is marked by the two vertical dotted lines. (b,c) The splitting waveforms and the particle motion plot. (d,e) The waveforms and particle motion plot after correcting for anisotropy. **(Right)** The rose diagrams for stations BGL, KOD, and PALK, indicating the orientation of the axis of symmetry and the split time.

Gupta et al. [2002, 2003ab] used the receiver function stacking procedure of *Zhu and Kanamori* [2000] to estimate crustal thickness and Poisson's ratio from receiver function analysis at 32 sites on the Archaean and Proterozoic terrains of South India (Figure 5). The crustal thickness in the late Archaean (2.5 Ga) Eastern Dharwar Craton varies from 34-39 km. Similar crustal thickness is observed beneath the Deccan Volcanic Province and the Cuddapah basin. The most unexpected result is the anomalous present-day crustal thickness of 42-51 km beneath the mid-Archaean (3.4-3.0 Ga) segment of the Western Dharwar Craton. The Poisson's ratio ranges between 0.24-0.28 beneath the Precambrian terrains, indicating the presence of intermediate rock type in the lower crust.

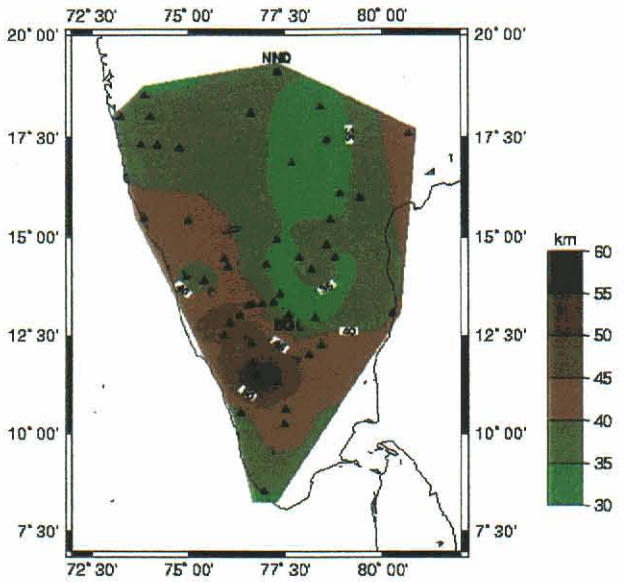

Figure 5: Crustal thickness contour map for southern India derived from the receiver function analysis with the stations contributing denoted as black triangles

Receiver function analysis of data from seven broadband seismographs in NE India shows the extreme variability of the crustal thickness in the region (Figure 6) [Gaur *et al.*, 2002]. Beneath the Bangladesh plain the crust is nearly 50 km thick but shallows to ~35 km depth beneath the Shillong Plateau, thickens to ~42 km depth beneath the Brahmaputra Valley to the north of the Shillong Plateau and to ~50 km beneath the lesser Himalayas to the north of the Brahmaputra Valley. Archean rocks of the Indian shield outcrop on the Shillong Plateau and the nature of the Shillong Plateau crust is similar to the crust of the Indian shield to the south. The thicker crust observed in both the Brahmaputra Valley and the Bangladesh plain compared to the Shillong Plateau appears to be the result of the thick sediment accumulation deposited by the Brahmaputra and Ganges rivers on a crystalline crust similar to that of the Indian shield to the south.

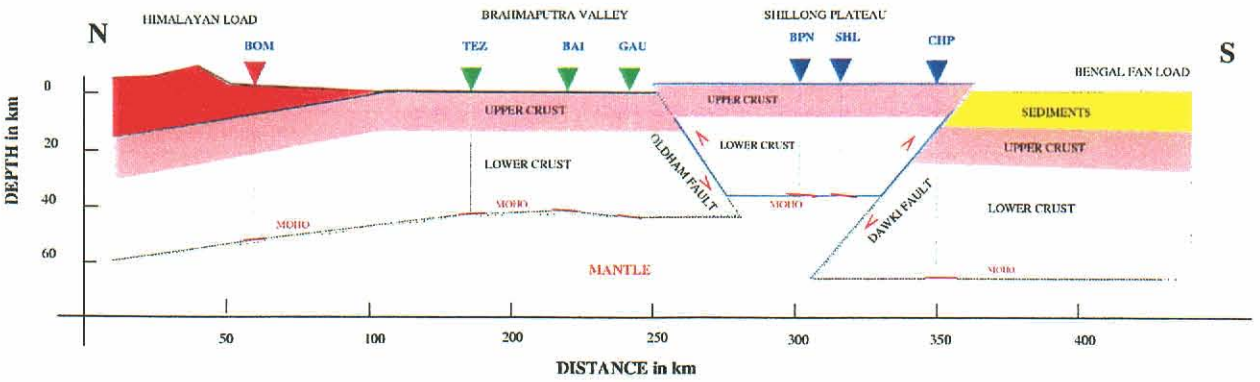

Figure 6: Schematic N-S profile from the Himalayas to the Bengal basin. The stations are marked with inverted triangles and the depth to the Mohho at the 7 sites being used as a guide to interpolate the northward dip and rising of the Shillong plateau. The basis of the schematic diagram is adopted from Bilham and England [2001].

LITHOSPHERIC STRUCTURE FROM SURFACE WAVE DISPERSION

We have used the surface and body waves from these data to help refine the crustal and upper mantle velocity structure in southern Asia. Surface wave phase and group velocities for fundamental mode Rayleigh waves have been measured for a number of paths across the south Indian shield. The analysis of short period surface wave dispersion gives an average crustal model for the south Indian shield that is used as a starting model in the receiver function inversions discussed above, and provides additional constraints in the joint receiver function/surface wave inversion. Long period surface wave dispersion curves constrain the deeper structure of the lithosphere, which is important when locating events with far-regional and near-teleseismic arrivals.

We measure two-station fundamental mode Rayleigh wave phase velocity (Figure 7) using the transfer function method of *Gomberg et al.* [1988] from eleven events nearly aligned along the same great circle path as station pairs along a profile extending from NND to BGL (Figure 5). We invert the Rayleigh wave phase velocity data using the stochastic least-squares routine of *Herrmann* [1994] and the final inversion model and the fit of the dispersion curve for this model to the observed dispersion (Figure 7) show that the average crustal structure beneath the profile consists of two layers: an upper 12 km thick layer with V_s 3.65 km/s, and a lower 23 km thick layer with V_s 3.81 km/s, overlying an upper mantle with Sn velocity 4.61 km/s.

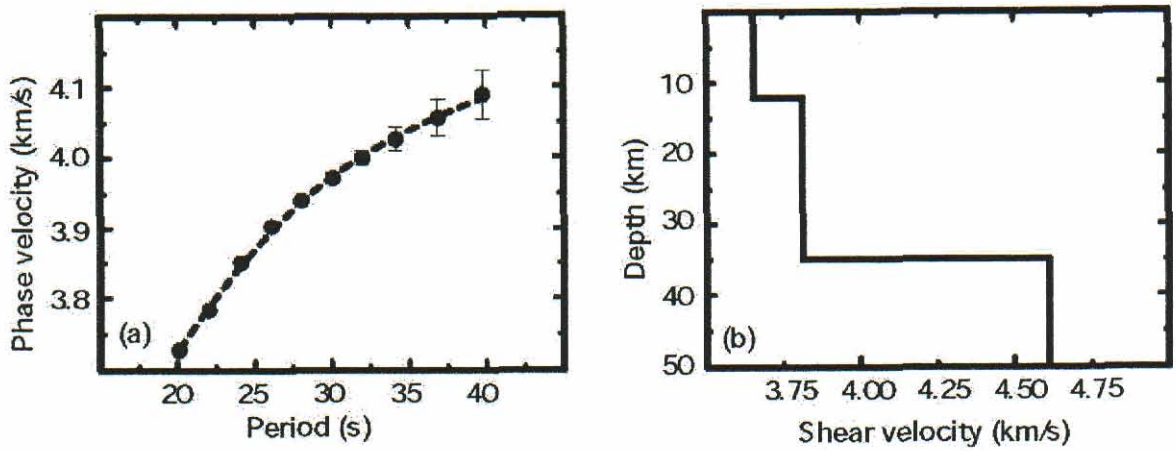

Figure 7: (Left) Average fundamental mode Rayleigh wave phase velocities (solid circles) and fit of theoretical phase velocity curve computed from crustal model on left (black line) measured along the NS transect. **(Right)** Two layer crustal model from inversion of the Rayleigh wave dispersion data.

We have also determined short-period Rayleigh wave group velocity for a large number of paths crossing India. Of particular interest are results for the Bhuj-MABU path. MABU (Figure 1) was deployed 300 km northwest of the Bhuj main shock location on March 18, 2001 and immediately began recording aftershocks, including an M_s 4.9 on March 19, 2001 (blue stars, Figure 8). During the initial three weeks of operation MABU recorded over 700 Bhuj aftershocks. We utilized this new dataset to update and expand Weston Geophysical's India and Pakistan 3-D velocity model, denoted by WINPAK3D [Reiter *et al.*, 2001; Johnson and Vincent, 2002]. The WINPAK3D model was used as the starting model to invert Rayleigh wave group velocity curves determined from the MABU data providing constraints on the shear wave velocity structure. The results (Figure 8) show the crustal thickness in this region is approximately 40 km and reveal differences between the inverted model and WINPAK3D in the upper and middle crust. We are continuing to examine events in this region for further constraints upon the northwestern Indian subset of WINPAK3D.

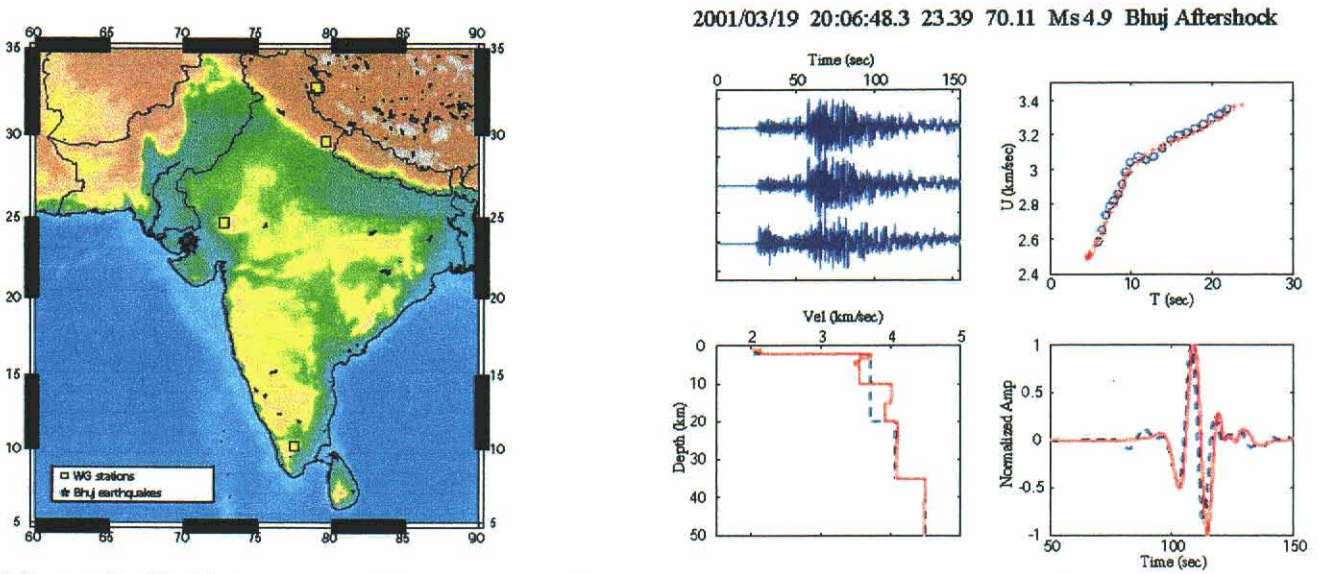

Figure 8: (Left) Map showing Bhuj earthquakes (blue stars) and the stations that were used in the surface wave inversion shown in the right panel (purple triangles and yellow box). **(Right)** (*upper left*) Three-component seismograms at MABU for a Bhuj earthquake. **(*upper right*)** Observed and modeled dispersion curves for the Rayleigh waves from this aftershock. (*lower left*) Initial (WINPAK3D) and final model from the inversion of the Rayleigh wave dispersion. *(lower right*) Comparison of observed and modeled surface waves using the final model from the inversions.

Figure 9 shows the fundamental mode Rayleigh wave dispersion measurement from seven two-station pairs using the combination of the stations NND/HYB in the north and GBA/KOD in the south. Inter-station path lengths for the two-station pairs vary from 600 to 800 km. The coherency plots shows that the dispersion is well constrained to ~180 sec period. Previous measurements of fundamental mode Rayleigh wave phase velocity have extended only to ~50 sec period [Bhattacharya, 1972; Hwang and Mitchell, 1987]. The increased period range of our dispersion measurement is important in constraining the deep structure of the south Indian shield. Inversion of the Indian phase velocity curve indicates the presence of a high velocity upper mantle lid with S-wave velocities ranging from ~4.62 km/s at 40-60 km depth to ~4.72 km/s at 80-120 km depth and a low velocity of 4.5 km/s below ~150 km depth.

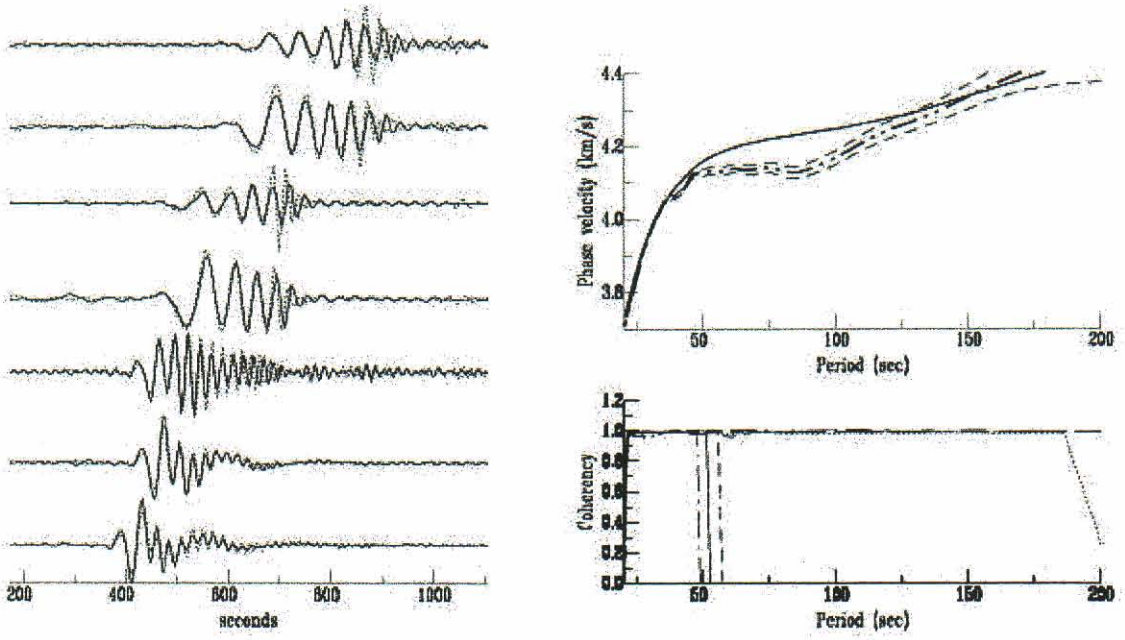

Figure 9: Long period phase velocity dispersion observations for the south Indian shield. **(LEFT)** 7 seismogram pairs with the observed seismogram at the distant station shown as the solid line and the dotted line is the match of the near seismogram after being filtered by the transfer function given by the phase velocity curve. *(upper right)* Observed phase velocity obtained for the NND/HYB – GBA/KOD path. The +/- std. deviation bounds on the measured phase velocity are shown by dashed lines. Also shown for comparison is the dispersion curve for the CANSD model (solid line) of Brune and Dorman [1963]. *(lower right)* Coherence of match indicating that the phase velocity is well constrained to about 200 sec. period.

REGIONAL WAVEFORM MODELING

We have modeled the seismograms from regional earthquakes recorded on our stations and other digital stations in India [Maggi *et al.*, 2002]. We use an adaptive forward modeling approach which efficiently samples the entire space of Earth parameters we wish to model and converges rapidly to the minimum-misfit solution. This approach is based on the neighborhood algorithm of *Sambridge* [1999]. The number of Earth parameters modeled and the range within which they are allowed to vary depends strongly upon the sensitivity of the data. We allow any subset of Earth parameters to be defined for each layer, and calculate the undefined parameters using standard relationships.

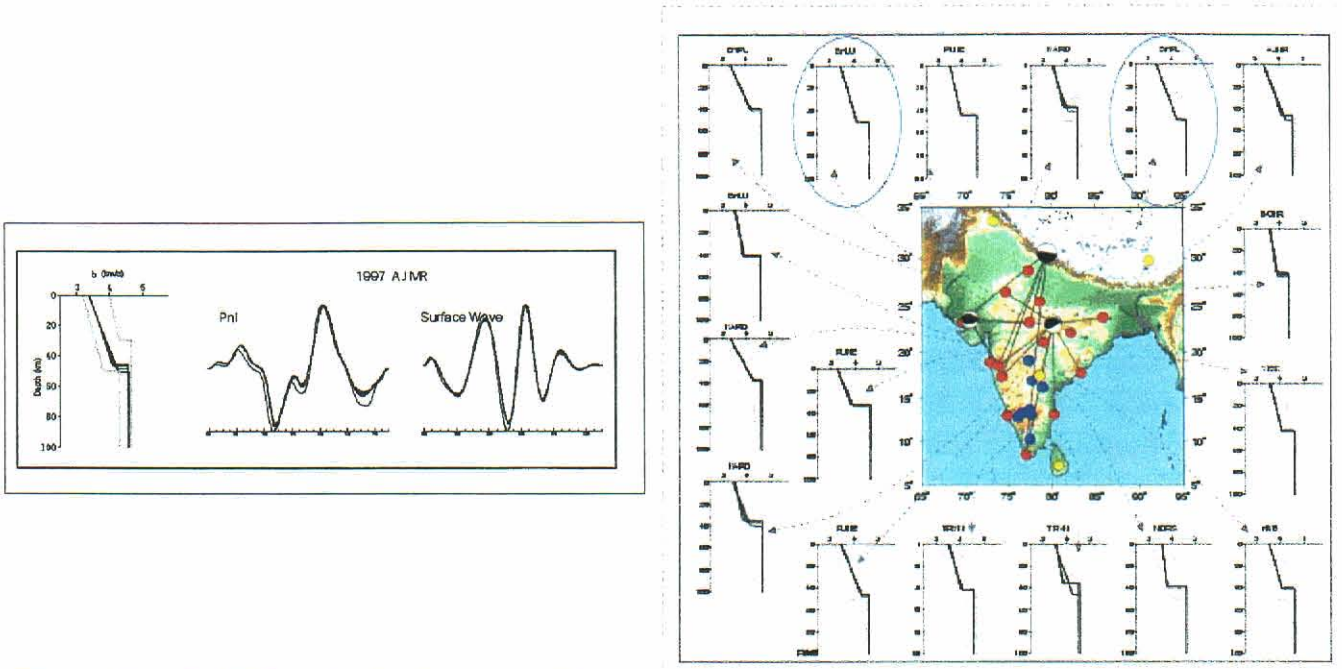

Figure 10: (Left) Example showing process of simultaneously fitting both the vertical component Pnl and surface waves. **(Right)** 1-D Earth models obtained from adaptive grid-searching.

Figure 10 shows an example of the application of this technique to data from India and also the 1-D Earth models we obtain. For each path we simultaneously fit vertical component *Pnl* and surface waveforms (Figure 10, left). For this application we searched for models with a gradient crust over a uniform mantle for all paths, and parameterized both V_s and Moho depth. Most paths are well modeled by a gradient crust over a half-space upper mantle. The integrated crustal thickness over the path varies from close to 50 km for northern India to 35-40 km for central and southern India. The two circled models (Figure 10, right) may have too large a crustal thickness compared to the other Earth models. A large portion of these two paths lie within the sediment-filled foreland-deep of the Himalayas. It is likely that a crustal gradient is no longer a good approximation to the 1-D structure for these paths and that a two-layer crust is required.

MECHANISMS OF BHUJ AFTERSHOCKS

In addition to the January 26, 2001 Bhuj earthquake (Mw = 7.6) main shock, we recorded numerous Bhuj aftershocks. We have used an adaptation of the neighborhood algorithm to determine source parameters for the aftershocks from the regional seismic

data (Figure 11, left) [Gaur *et al.*, 2001]. We first inverted teleseismic *P*- and *SH*-waveforms to determine source parameters for the main shock and the large aftershock which occurred on January 28. We then used the source mechanism of the January 28 aftershock to calibrate the propagation paths to the stations having regional recordings of this event. Using the path calibrations, we then used the neighborhood algorithm in an adaptive grid search to invert the regional waveforms to extract source parameters of the smaller Bhuj aftershocks (Figure 11, right). This study illustrates the potential of the dataset for deriving event mechanisms for India.

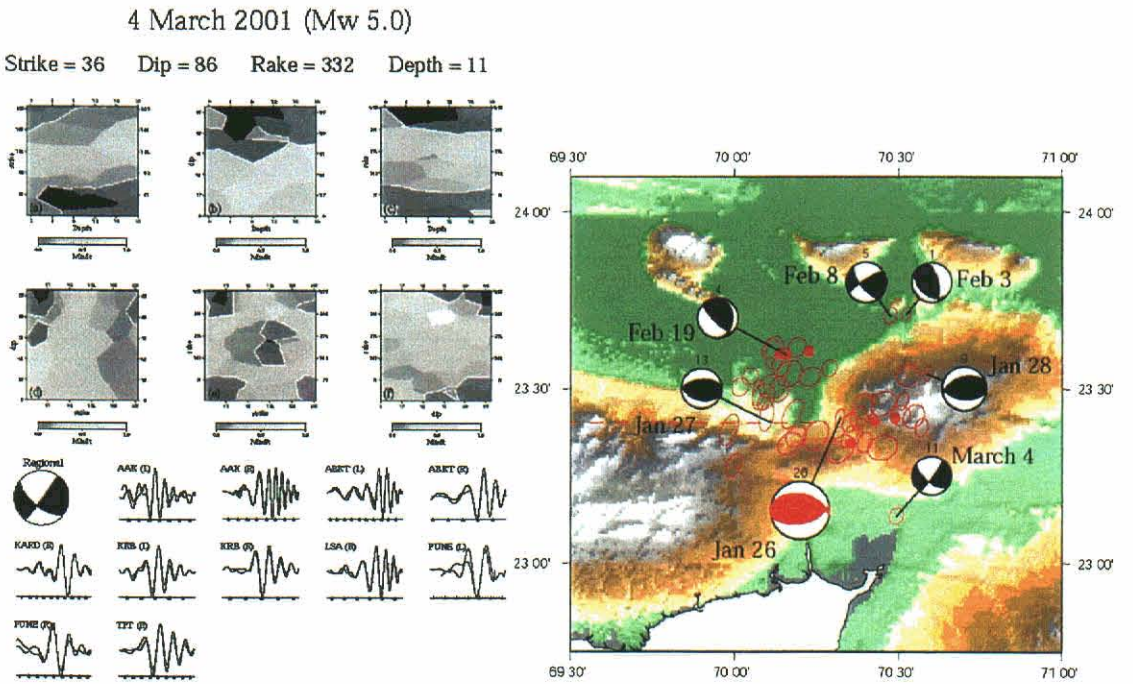

Figure 11: (Left) Schematic showing neighborhood algorithm to determine source parameters. **(Right)** Figure illustrating source parameters derived for the Bhuj main and aftershocks from teleseismic and regional waveform modeling.

L_g ATTENUATION

An understanding of the regional attenuation structure of India is critical to evaluating phase propagation for determination of source magnitude, moment and yield estimates. We have explored the attenuation characteristics of India and Pakistan crust through the analysis of the frequency dependence of *Lg* spectral decay with epicentral distance. We measure *Lg* amplitudes at varying frequencies to compute *Q*, the quality factor, and its frequency dependence in order to place constraints on the regional

attenuation structure. Figure 12 illustrates the ray paths from the three moderate size earthquakes utilized to date in this study. We assume that the attenuation structure takes the frequency dependence form of $Q(f) = Q_o f^n$ where Q_o is the quality factor at 1 Hz and f is frequency. We find that an $n = 0.67 \pm 0.03$ and a $Q_o = 655 \pm 10$ best describes the average attenuation structure for central and southern India (Figure 12) [Mitra *et al.*, 2002]. This result is consistent with Singh *et al.* [1999], who analyzed one of the same events in their study, and to previous studies examining other shield regions like eastern North America [Shin and Herrmann, 1987; Gupta and McLaughlin, 1987].

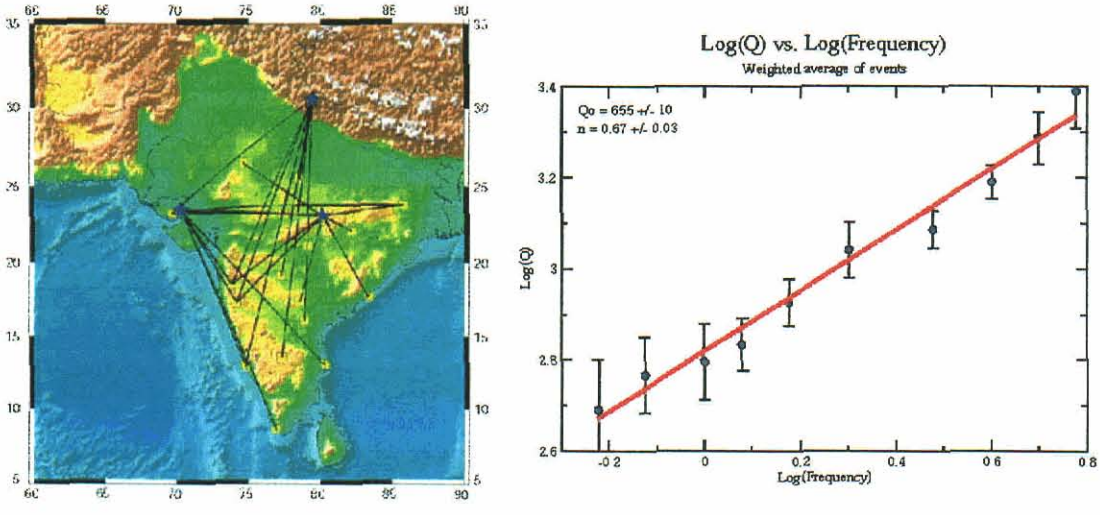

Figure 12: (Left) Map showing paths from earthquakes (blue stars) to stations (yellow boxes) analyzed to determine the average Indian shield *Lg* attenuation structure. **(Right)** Linear regression of $\mathrm{Log}_{10}(Q)$ vs. $\mathrm{Log}_{10}(\textit{frequency})$ yields a $Q_o = 655$ +/- 10 and $n = 0.67$ +/- 0.03.

CONCLUSIONS AND RECOMMENDATIONS

The goal of this project was to establish a network of temporary seismograph stations in India in order to provide a high quality database of events that is needed to improve understanding of the regional velocity structure. This goal was achieved. In addition, strong collaborative relationships with key Indian seismologists have been formed, which has been a critical and essential component of this research project.

It is noted that various difficulties with the instrument design and the operating environment were encountered during the first 18 months of deployment which prevented the project from moving as quickly as had been planned. But, these problems spurred modifications to the instrument by Guralp, Ltd. and a change in some of the field operating practices. For example, to simplify maintenance of the network we have designed and constructed an interface for the stations allowing dialup modem or internet access to the CMG-3TD + SAM which will provide monitoring and rapid troubleshooting capabilities for the network.

The network is now fully operational and we have collected a significant database that has already provided several noteworthy results as contained in the collection of research papers in Appendix A. Based on these research results, continuation of the seismograph deployment is recommended, to include the occupation of new sites, in order to expand the geographical extent of the database.

REFERENCES

Alewine, R., Theoretical and observed distance corrections for Rayleigh-wave magnitude, *Bull. Seism. Soc. Am.*, **62**, 1611-1619, 1972.

Alvarez, W., Geological evidence for the geographical patterns of mantle return-flow and the driving mechanism of plate-tectonics, *J. Geophys. Res.*, **87**, 6697-6710, 1982.

Basham, P.W., A new magnitude formula for short-period continental Rayleigh waves, *Geophys. J. R. Ast. Soc.*, **23**, 255, 1971.

Baumgardt, D., Investigation of teleseismic *Lg* blockage and scattering using regional arrays, *Bull. Seism. Soc. Am.*, **80**, 2261-2281, 1990.

Bhattacharya, S. N., Observations and inversion of surface wave group velocities across central India, *Bull. Seism. Soc. Am.*, **71**, 1489-1501, 1974.

Bilham, R., and P. England, Plateau pop-up during the 1897 Assam earthquake, *Nature*, **410**, 806-809, 2001.

Bolt, B., and M. Herraiz, Simplified estimation of seismic moment from seismograms, *Bull. Seism. Soc. Am.*, **73**, 735-748, 1983.

Bonner, J., D.G. Harkrider, E. Herrin, S.A. Russell, I. Tibuleac, and R. Shumway, Evaluation of short-period, near-regional M_s scales for the Nevada Test Site, *Bull. Seis. Soc. Am.*, accepted, 2003.

Brune, J. and L. Dorman, Seismic waves and Earth structure in the Canadian shield, *Bull. Seism. Soc. Am.*, **53**, 167-210, 1963.

Darbyshire, F., R. White, and K. Priestley, Structure of the crust and uppermost mantle of Iceland from a combined seismic and gravity study, *Earth and Planet. Sci. Lett.*, **181**, 409-428, 2000.

Denny, M.D., S. R. Taylor, and E.S. Vergino, Investigation of m_b and M_s formulas for the western United States and their impact on the Ms/mb discriminant, *Bull. Seism. Soc. Am.*, 77, 987-995, 1987.

DeMets, C., R. Gordon, D. F. Argus, and S. Stein, Effects of recent revisions to the geomagnetic reversal time scale on estimates of current plate motions, *Geophys. Res. Letts.*, **21**, 2191-2194, 1994.

Gaur, V.K., A. Maggi, K. Priestley, S.S. Rai, and S. Davaluri, Source Parameters of the Bhuj Mainshock and Larger Aftershocks from Modeling of Broadband Teleseismic and Regional Waveform data, *Eos Trans. AGU, 82*(47), Fall Meet. Suppl., 2001.

Gomberg J., K. Priestley, T.G. Masters, and J. Brune, The structure of the crust and upper mantle of northern Mexico, *Geo. J. Royal Astron. Soc.*, **94**, 1-20, 1988.

Gupta, I.N., and K.L. McLaughlin, Attenuation of ground motions in the eastern United States, *Bull. Seism. Soc. Am.*, **77**, 366-383, 1987.

Gupta, M.L., A. Sundar, and S.R. Sharma, Heat flow and heat generation in the Archaean Dharwar cratons and implications for the southern Indian Shield geotherm and lithospheric thickness, *Tectophys.*, **194**, 107-122, 1991.

Gupta, S., S.S. Rai, K.S. Prakasam, D. Srinagesh, R.K. Chadha, K. Priestley, and V.K. Gaur, First evidence for anomalous thick crust beneath mid-archean western Dharwar craton, *Current Sci.*, May, 2003.

Gupta, S., S.S. Rai, K.S. Prakasam, D. Srinagesh, B.K. Bansal, R.K. Chadha, K. Priestley, and V.K. Gaur, The nature of the crust in southern India: Implications for Precambrian crustal evolution, *Geophys. Res. Lett.*, Vol. 30, No. 1, 2003.

Gutenberg, B., Amplitudes of surface waves and the magnitudes of shallow earthquakes, *Bull. Seism. Soc. Am.*, **35**, 3, 1945.

Hartse, H., S. R. Taylor, W. S. Phillips, and G. Randall, A preliminary study of regional seismic discrimination in Central Asia with emphasis on Western China, *Bull. Seism. Soc. Am.*, **87**, 551-568, 1997.

Herrmann, R. B., Computer Programs in Seismology Version 3.15, St. Louis University, 2002.

Hwang, H., and B. Mitchell, Shear velocities, Q (sub beta) , and the frequency dependence of Q (sub beta) in stable and tectonically active regions from surface wave observations, *Geo. J. Royal Astr. Soc.*, **90**, 575-613, 1987.

Jackson, J., Strength of the continental lithosphere; time to abandon the jelly sandwich?, *GSA Today*, **12**, 4-10, 2002.

Johnson, M., and C. Vincent, 3-D velocity model of India/Pakistan region for improved event location, *Bull. Seism. Soc. Am.*, **92**, 2893-2910, 2003.

Kaila, K. L., and V.G. Krishna, Deep seismic-sounding studies in India and major upper discoveries, *Current Science*, **62**, 117-154, 1992.

Krishna, V.G., K. Kaila, and P.R. Reddy, Synthetic seismogram modeling of crustal seismic record sections from the Koyna DSS profiles in the western India, *Geo. Mono.*, **51**, 143-157, 1989.

Krishna, V.G., and D.S. Ramesh, Propagation of crustal waveguide trapped *Pg* and seismic velocity structure in the south Indian shield, *Bull. Seism. Soc. Am.*, **90**, 1281-1294, 2000.

Leidig, M., and G. Zandt, Modeling of highly anisotropic crust and application to the Altiplano-Puna Volcanic Complex of the Central Andes, *J. Geophys. Res.*, in publication, 2003.

Louden, K. E., Variations in crustal structure related to intraplate deformation – evidence from seismic-refraction and gravity profiles in the central Indian basin, *Geophys. J. Int.*, **120**, 375-392, 1997.

Maggi, A., J. Jackson, K. Priestley, and C. Baker, A re-assessment of focal depth distributions in southern Iran, the Tien Shan and northern India; do earthquakes really occur in the continental mantle?, *Geophys. J. Intl.*, **143**, 629-661, 2000.

Maggi, A., K. Priestley, V.K. Gaur, and S.S. Rai, Seismic Structure of India from Regional Waveform Matching, *Eos Trans. AGU, **83***(47), Fall Meet. Suppl., 2002.

Marshall, P. D., and P.W. Basham, Discrimination between earthquakes and underground explosions employing an improved M_s scale, *Geophys. J. R. astr. Soc.*, **28**, 431, 1972.

Mayeda, K. M., mb(LgCoda): a stable single station estimator of magnitude, *Bull. Seism. Soc. Am.*, **83,** 851-861, 1993.

Mitchell, B. J., Y. Pan, J. Xie, and L. Cong, *Lg* coda Q variation across Eurasia and its relation to crustal evolution, *J. Geophys. Res.*, **102**, 22767-22779, 1997.

Mitra, S., S.A. Russell, K. Priestley, V. Gaur, and S.S. Rai, Measurements of Frequency Dependent Lg Attenuation in India, *Eos Trans. AGU,* **83**, Fall Meet. Suppl., Abstract, 2002.

Mohan, G., and S. S. Rai, Imaging of seismic scatterers beneath the Gauribidanur (GBA) array, *Phys. Earth Planet. Inter.*, **71,** 36-45, 1992.

Mooney, W. D., P. R. Reddy, V. V. Rao, and D. M. Mall, Crustal structure of India: New insights from deep seismic profiling, *Abstract Digest for the 22nd Annual DoD/DOE Seismic Research Symposium*, 10, 2000.

Nuttli, O., Seismic wave attenuation and magnitude relations for eastern North America, *J. Geophys. Res.*, **78**, 876-885, 1973.

Patton, H.J., Unified Mo:mb(Lg) scaling relationships, *Seism. Res. Lett.*, **70**, 120, 1999.

Patton, H.J., and W.R. Walter, Regional moment; magnitude relations for earthquakes and explosions, *Geophys. Res. Lett.*, **20**, 277-280, 1993.

Phillips, W. S., Empirical path corrections for regional phase amplitudes, *Bull. Seism. Soc. Am.*, **89**, 384-393, 1999.

Phillips, W. S., H. E. Hartse, S. R. Taylor, and G. E. Randall, 1 Hz Lg Q tomography in Central Asia, *Geophys. Res. Lett.*, **27**, 3425-3428, 2000.

Prasad, B. R., H. C. Tewari, V. V. Rao, M .M. Dixit, and P. R. Reddy, Structure and tectonics of the Proterozoic Aravalli-Delhi fold belt in northwestern India from deep seismic reflection studies, *Tectonophysics*, **288**, 31-40, 1998.

Priestley, K., and H.J. Patton, Calibration of $m_b(Lg)$ scales and transportability of the Mo:mb discriminant to new tectonic regions, *Bull. Seism. Soc. Am.*, **87**, 1083-1099, 1997.

Priestley, K., and E. Debayle, Seismic evidence for a moderately thick lithosphere beneath the Siberian Platform, *Geophys. Res. Lett.*, Vol. 30, No. 3, 1118, 2003.

Press, F., and M. Ewing, Two slow surface waves across North America, *Bull. Seism. Soc. Am.*, **42**, 219-228, 1952.

Radhakrishna, and Nagvi, Precambrian continental crust of India and its evolution, *J. Geol.*, **94**, 616, 1986.

Rai, S. S., K. Priestley, K. Suryaprakasa, D. Srinagesh, V. Gaur, and Z. Du, Crustal shear velocity structure of the south Indian shield, *J. Geophys. Res.*, **108**, No. B2, 2088-2100, 2003.

Rai, A., K. Priestley, and V.K. Gaur, Seismic Characteristics of the Southern Indian Granulite Terrane Around Kodaikanal, *Eos Trans. AGU, 83*(47), Fall Meet. Suppl., 2002.

Ramesh, D.S. Ramesh, D. Srinagesh, S.S. Rai, K.S. Prakasam, and V.K. Gaur, High-velocity anomaly under the Deccan volcanic province, *Phys. Earth Planet. Int.*, 77, 285-296, 1993.

Randall, G. E., C. J. Ammon, and T. J. Owens, Moment tensor estimation using regional seismograms from portable array deployments, *Geophys. Res. Letts.*, **22**, 1665-1668, 1995.

Reese, C. C., R. R. Rapine, and J. F. Ni, Lateral variation of Pn and Lg attenuation at the CDSN station LSA, *Bull. Seism. Soc. Am.*, **87**, 325-330, 1998.

Reiter, D. T., W. Rodi, M. Johnson, C. Vincent, and A. Rosca, A new regional velocity model of the India-Pakistan region, *Proceedings of the 23rd Seismic Research Review: Worldwide Monitoring of Nuclear Explosions – October 2-5, 2001*, 305-314, 2001.

Rezapour, M., and R.G. Pearce, Bias in surface-wave magnitude M_s due to inadequate distance correction, *Bull. Seism. Soc. Am.*, **88**, 43-61, 1998.

Rodgers, A., W. Walter, R. Mellors, A. Al-Amri, and Y.-S. Zhang, Lithospheric structure of the Arabian Shield and Platform from complete regional waveform modeling and surface wave group velocities, *Geophys. J. Intl.*, **138**, 871-878, 1999.

Ruzaikin, A. I., I. L. Neresov, V. I. Khalturin, and P. Molnar, Propagation of *Lg* and lateral variations in crustal structure in Asia, *J. Geophys. Res.*, **82**, 307-316, 1977.

Sambridge, M., Geophysical inversion with a neighborhood algorithm –I: searching a parameter space, *Geophys. J. Int.*, **138**, 479-494, 1999.

Shin, T.C., and R.B. Herrmann, Lg attenuation and source studies using 1982 Miramichi data, Bull. *Seism. Soc. Am.*, 77, 384-397, 1987.

Singh, S. K., M. Ordaz, R. S. Dattatrayam, and K. K. Gupta, A spectral analysis of the 21 May 1997 Jabalpur, India earthquake (M_w=5.8) and estimation of ground motion from future earthquakes in the Indian shield region, *Bull. Seism. Soc. Am.*, **89**, 1620-1630, 1999.

Sonder, L., and P. England, Vertical averages of rheology of the continental lithosphere; relation to thin sheet parameters, *Earth Planet. Sci. Lett.*, 77, 81-90, 1986.

Srinagesh, D., and S.S. Rai, Teleseismic tomographic evidence for contrasting crust and upper mantles in South Indian Archaean terrains, *Phys. Earth Planet. Int.*, **97**, 27-41, 1996.

Stevens, J.L., and K.L. McLaughlin, Improved methods for regionalized surface wave analysis, *Seism. Res. Lett.*, **68**, 296, 1997.

Taylor, S. R., and H. E. Hartse, A procedure for the estimation of source and propagation amplitude corrections for regional seismic discriminants, *J. Geophys. Res.*, **103**, 2781-2789, 1998.

Taylor, S. R., Analysis of high-frequency *Pg/Lg* ratios from NTS explosions and western United States earthquakes, *Bull. Seism. Soc. Am.*, **86**, 1042-1053, 1996.

Tibuleac, I.M. and E.T. Herrin, An automatic method for determination of *Lg* arrival times using wavelet methods, *Seism. Res. Lett*, **70**, 577–595, 1999.

Vergino, E.S. and R.W. Mensing, Yield estimation using regional m_b(*Pn*), *Lawrence Livermore National Laboratory Report UCID-101600*, 1989.

Walter, W. R., K. M. Mayeda, and H. J. Patton, Phase and spectral ratio discrimination between NTS earthquakes and explosions. Part I. Empirical observations, *Bull. Seism. Soc. Am.*, **85**, 1050-1067, 1995.

Woods, B., S. Kedar, and D.V. Helmberger, M_L:Mo as a regional seismic discriminant, *Bull. Seism. Soc. Am.*, **83**, 1167-1183, 1993.

Woods, B. and D.G. Harkrider, Determining surface-wave magnitudes from regional Nevada Test Site data, *Geophys. J. Int.* **120**, 474, 1995.

Zhou, L., W. P. Chen, and S. Ozalaybey, Seismic properties of the central Indian shield, *Bull. Seism. Soc. Am.*, **90**, 1295-1304, 2000.

Zhu, L., and H. Kanamori, Moho depth variations in southern California from teleseismic receiver function, *J. Geophys. Res.*, **105**, 2969-2980, 2000.

APPENDIX A

PUBLISHED ARTICLES/PRESENTATIONS

1. Mitra, S, S. A. Russell, K. Priestley, V. K. Gaur, S. S. Rai (2002), Measurements of frequency dependent Lg attenuation in India, *Eos Trans. AGU, **83**, Fall Meet. Suppl., Abstract, 2002.*
2. Maggi, A., Teleseismic and regional waveform modeling of the 26 Jan 2001 Bhuj earthquake sequence, PhD thesis chapter, Cambridge University, 2002.
3. Rai, S. S., K. Priestley, K. Suryaprakasam, D. Srinagesh, V. K. Gaur and Z. Du, Crustal shear velocity of south Indian shield, *J. Geophys. Res.*, 108, No. B2, 2088-2100, 2003
4. Gupta, S., S. S. Rai, K. S. Prakasam, D. Srinagesh, B. K. Bansal, R. K. Chadha, K. Priestley and V. K. Gaur, The nature of the crust in southern India: Implications for Precambrian crustal evolution, *Geophys. Res. Lett*, Vol. 30, No. 1, 2003.
5. Maggi, A., J. Jackson, K. Priestley and C. Baker, A re-assessement of focal depth distributions in southern Iran, the Tien Shan and Northern India: do earthquakes really occur in the continental mantle?, *Geophys. J. Intl.*, 143, 629-661, 2000.
6. Mitra, S., K. Priestley, V. K. Gaur, Crustal structure beneath the foreland spur in Northeastern India, *Eos Trans. AGU, **83**(47), Fall Meet. Suppl., Abstract, 2002.*
7. Rai, A., K. Priestley, and V.K. Gaur, Seismic Characteristics of the Southern Indian Granulite Terrane Around Kodaikanal, *Eos Trans. AGU, **83***(47), Fall Meet. Suppl., 2002
8. Gupta, S., S.S. Rai, K.S. Prakasam, D. Srinagesh, R.K. Chadha, K. Priestley, and V.K. Gaur, First evidence for anomalous thick crust beneath mid-archean western Dharwar craton, *Current Sci.*, May, 2003.
9. Priestley, K., and E. Debayle, Seismic evidence for a moderately thick lithosphere beneath the Siberian Platform, *Geophys. Res. Lett.*, Vol. 30, No. 3, 1118, 2003.

Measurements of frequency dependent Lg attenuation in India

S. Mitra, University of Cambridge,UK
S.A. Russell, Weston Geophysical Corporation, Lexington, MA, USA
K. Priestley, University of Cambridge,UK
Vinod K.Gaur, Indian Institute of Astrophysics,India
S.S. Rai, National Geophysical Research Institute, India

The Indian Institute of Astrophysics, the National Geophysical Research Institute, and Cambridge University have now operated broadband seismographs on the Indian Shield since 1997. We use seismograms from local and regional earthquakes recorded on these seismographs, FSDN seismographs, and seismographs operated by the Indian Meteorological Department to measure the spatial decay of spectral amplitudes of the higher-mode seismic surface wave train Lg for numerous paths which provide a good average sampling of the shield and northern India. After correction for instrument response and geometrical spreading, we analyze the frequency dependency of Q by measuring the decay of Lg amplitude with epicentral distance over discrete frequency bands in the range $0.6 \leq f \leq 6.0$ Hz. The average Lg Q for the Indian Peninsular shield region can be expressed as $Q(f) = 655f^{0.67}$. This result is comparable to the apparent Q values found by Singh *et al.*, 1999 for the Indian shield and similar to the Lg attenuation observed in eastern North America. We observe anomalous Lg amplitudes and frequency behavior that implies the presence of regional spatial variability in the crustal attenuation structure.

Introduction

In this study we measure the spatial decay of spectral amplitudes of the higher-mode seismic surface wave train Lg for the Indian Peninsula. The shield area can be sub-divided into 3 main Archean cratons-Dharwar, Singhbhum, and Aravali (Fig 1). There is an essential coherence of the entire shield since Late Archean or early Proterozoic. Geophysical studies have confirmed that most of the Indian peninsula has normal crustal thickness(35-40km), with very small velocity variations in the crust(Kharechko, 1981). The crustal characteristics of the Indian shield are broadly typical of other shield areas in the world.

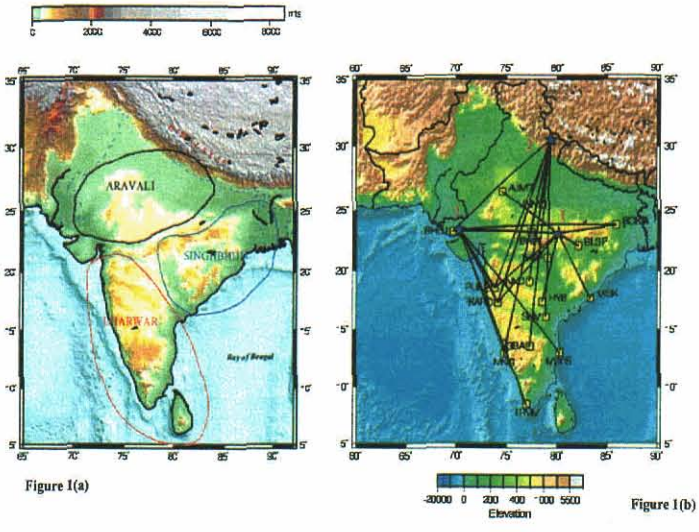

Figure 1: (a) Figure showing the 3 major Archean cratons of the Indian sub-continent, Aravali, Singhbhum and Dharwar. (b) Shows the location of the earthquakes(1-1997,2-1999,3-2001), seismic stations, and the travel path between them.

The earthquake data set for this study consists of regional, digital seismograms of 3 earthquakes, one in the Himalayas and other two in the Indian sub-continent. The data were recorded at several stations operated by NGRI, Cambridge University, Indian Institute of Astrophysics and the Indian Meteorological Department in the sub-continent(Fig 1b). We selected events which were recorded by at least 3 of the stations and covered a large range of epicentral distances. The travel paths provided a good sampling of the Indian sub-continental crust.

ANALYSIS

We determine shear wave attenuation structure of southern and central Indian shield region through spectral amplitude measurements of Lg. Lg in vertical component is extracted using a velocity window 3.6-2.8 km/s

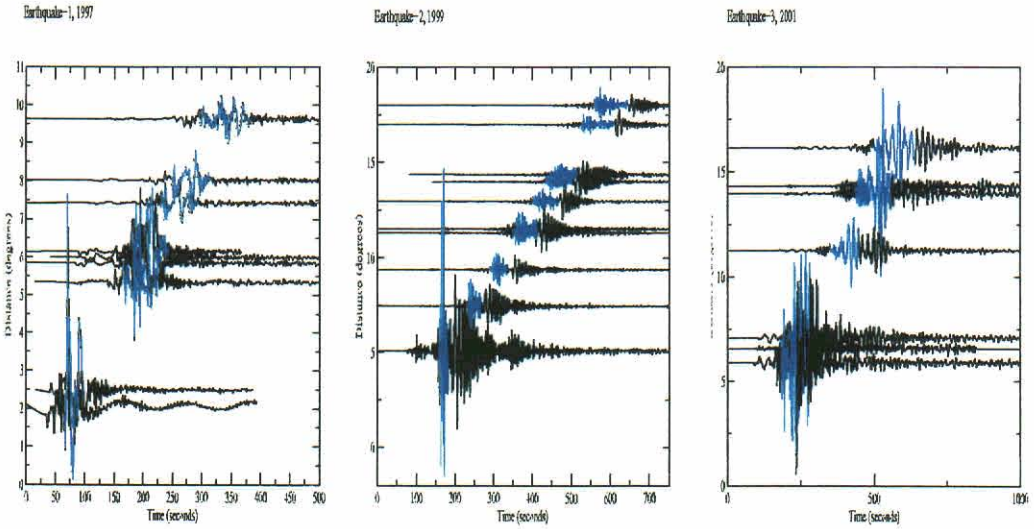

Figure 2: Record section plots of the 3 earthquakes used for the analysis. the velocity window between 3.6-2.8 km/s is coloured blue on the seismograms.

Spectral amplitudes of Lg are measured on the vertical component in frequency range 0.6-6 Hz. Amplitude as a function of frequency (f) and epicentral distance (R) of Lg can be expressed as:

$$A(R,f) = \frac{S(f)}{G(R)} * e^{\frac{-\pi f R}{vQ}} \tag{1}$$

where $S(f)$ is the source term, $G(R)$ the geometrical spreading, $\sqrt{R}$, v the average velocity, 3.5 km/s, and Q = attenuation quality factor. We take log_{10} of the amplitude equation yielding:

$$log_{10}A + 0.5log_{10}R = log_{10}S - \frac{log_{10}e\pi f}{vQ}R \tag{2}$$

For each earthquake, we plot $log_{10}A + 0.5log_{10}R$ versus R and perform a linear regression to find Q at each frequency. We assume frequency dependent Q of the form:

$$Q(f) = Q_o f^n \tag{3}$$

or

$$log_{10}Q = log_{10}Q_o + nlog_{10}f \tag{4}$$

where Q_o is Q at $f = 1$ Hz. Linear regression of $log_{10}Q$ versus f yields values for Q_o and n.

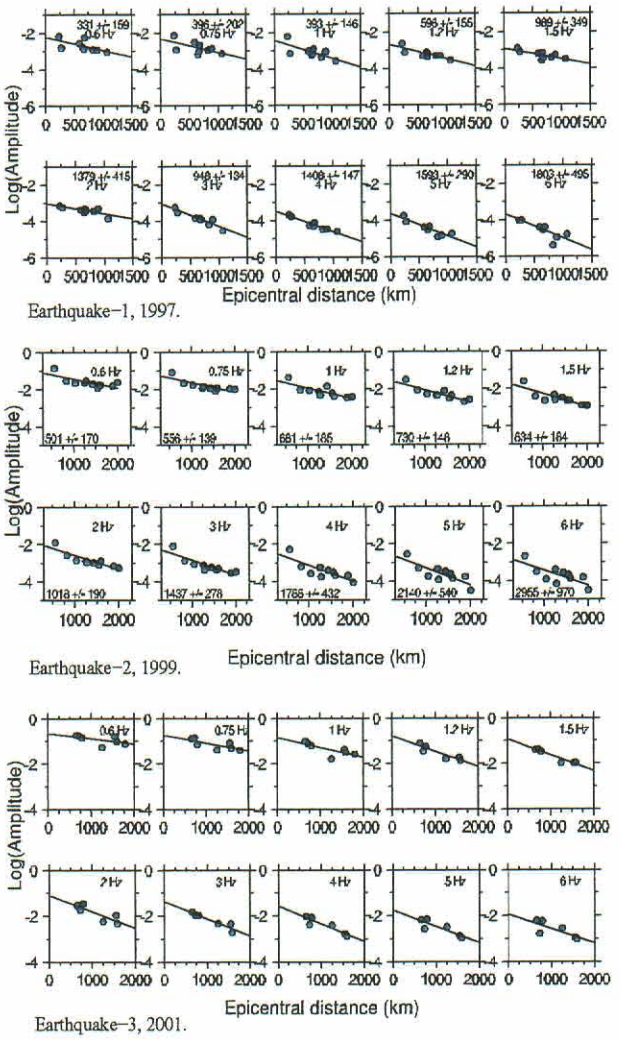

Figure 3: Log Amplitude vs Log Distance for the three earthquakes. Earthquake numbers below the plots correspond to numbers in fig 1b.

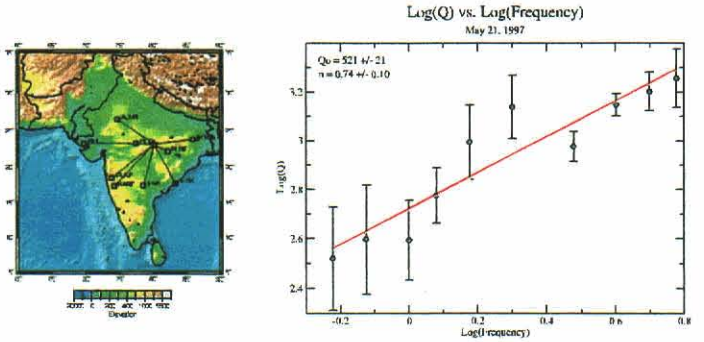

Figure 4: Left- travel paths for the 1997 Jabalpur earthquake. Right- Plot of Log Q vs Log f.

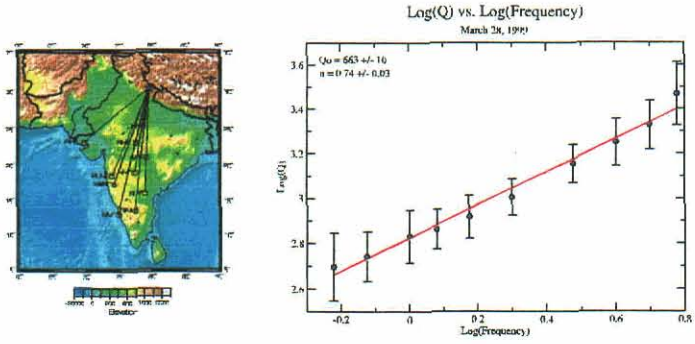

Figure 5: Left- travel paths for the 1999 Uttar Kashi earthquake. Right- Plot of Log Q vs Log f.

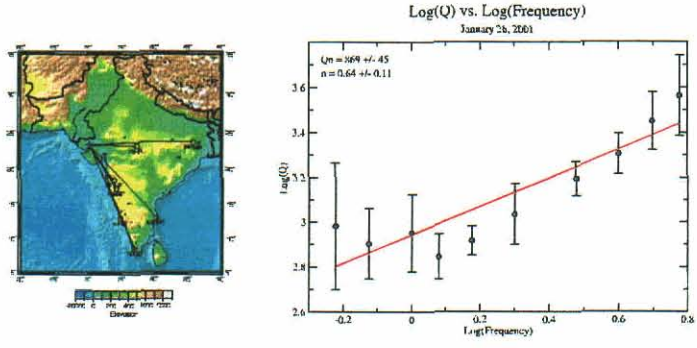

Figure 6: Left- travel paths for the 2001 Bhuj earthquake. Right- Plot of Log Q vs Log f.

Discussion and Conclusion

We measure Lg spectral attenuation for paths from 3 large Indian earthquakes sampling the shield structure of India. For the overall Indian shield region, we find an average value of $Q_o = 655 \pm 10$ and $n = 0.67 \pm 0.03$.

This value is consistent with previous results obtained by Singh et al. (1999) ($Q_o = 508$, $n = 0.48$) for the same region and is similar to the Lg attenuation results observed in eastern North America. We find variability in attenuation values for the individual earthquakes, however we are unable to constrain spatial variations without additional measurements to more precisely determine regional Q_o and n. Future work will focus on analyzing more earthquakes recorded at the IMD and NGRI/IIA/CAM broadband networks. We also plan to utilize additional measurement techniques to more fully utilize our dataset.

References

- Chavez D.E., and Priestley K.F., 1986,Measurement of frequency dependent Lg attenuation in the great basin; *Geophys. Res. Lett.* Vol-13, (6), 551-554
- Kharechko G.E., 1981, Velocity irregularities in the upper crust beneath the Indian shield.; *Geophys. J.* 3(4), 574-579.
- Singh et al., 1999, A spectral analysis of the 21 May 1997, Jabalpur, India, earthquake (Mw=5.8) and estimation of ground motion from future earthquakes in the Indian Shield region; *Bull. Seis. Soc. Am.*, 89(6) 1620-1630.
- Naqvi S.M. and Rogers J.J.W., The Precambrian Geology of India; *Oxford University Press Inc, USA.*

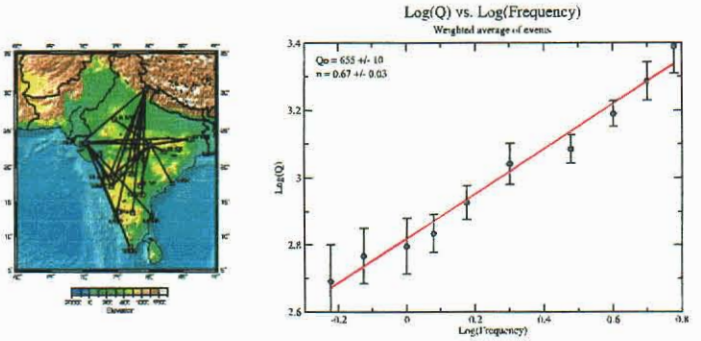

Figure 7: Left- travel paths for all the three events. Right- Plot of weighted Average Log Q vs Log f.

Teleseismic and regional waveform modelling of the 26 January 2001 Bhuj earthquake sequence

Alessia Maggi, Keith Priestley

Abstract

1 Introduction

The *Mw* 7.6 earthquake that shook the town of Bhuj in Gujarat, India on the morning of the 26 January 2001 was one of the deadliest in India's recorded history, killing approximately 20,000 people. This earthquake occurred in the Kachcch Peninsula (Figure 1), which has a long history of strong earthquakes (Bapat et al., 1983). The region is bordered to the north and south by ancient rift systems, created during the separation of the Indian subcontinent from the super-continent of Pangea (Biswas, 1987). Structures within these rift systems and on the Kachcch mainland are subjected to compressional stress and reverse faulting resulting from India's collision with Asia (Rajendran and Rajendran, 2001; Talwani and Gangopadhyay, 2001).

The 1819 Allah Bund earthquake, which occurred on a fault bounding the northern side of the Great Rann, was the first large earthquake in this region for which we have some focal mechanism information. Bilham (1998) reconstructed from original triangulation and levelling data that this earthquake occurred on a north-northeast dipping fault and produced approximately 11 m of reverse slip. There have been other damaging earthquakes in this region, of which the best located was a NE-SW trending thrust event that occurred close to Anjar in 1956 (Chung and Gao, 1995).

In this paper we discuss the Bhuj mainshock/aftershock sequence. We retrieve focal mechanisms and depths for the mainshock and the larger aftershocks, using both teleseismic and regional waveforms, and discuss these in the context of the regional tectonic structure.

2 Earthquake locations

Other than a band of tensional cracks along the range front of the Kachchh Mainland fault to the north east of the town of Bhuj, and a strike-slip rupture near the town of Manfara, on the western edge of the Wagad uplift, no surface expression of faulting connected with the Bhuj earthquake or its aftershock sequence has been found (Wesnousky et al., 2001). Field studies were severely hampered by the extensive liquefaction which followed the Bhuj mainshock. Interferometric Synthetic Aperture Radar (InSAR) techniques, which can provide excellent fault locations even in remote areas, could not be used for this event, because no coherent co-seismic interferograms could be made (Bürgmann et al., 2001). Accurate epicentral locations and mechanisms are therefore essential in identifying the structures involved in the faulting.

A local network of 8 portable seismic stations was deployed for two weeks following the earthquake (12–28 February) by the Center for Earthquake Research and Information

(CERI, Memphis). Engdahl and Bergman (2001) used six of the events located by this network with an accuracy of 1–2 km as reference events for a cluster analysis relocation of 51 earthquakes, including the Bhuj mainshock. The reference events are shown in Figure 2a as filled circles, while the epicentres of the other events located by Engdahl and Bergman (2001) are shown as ellipses indicating the formal errors of the relocation. The aftershock activity covered the eastern end of the Kachcch Mainland fault, the western side of the Wagad uplift, and the eastern portion of the Banni Plain. There were also some moderate size (M_w 5.0–5.2) outliers: two on the northern edge of the Wagad uplift and one off its southern edge.

Figure 2b shows the depth distribution of the aftershocks located by the CERI deployment (Raphael et al., 2001). We have not shown the hypocentres determined by Engdahl and Bergman (2001), because many of the events had their depths fixed to be the same as the mainshock (18 km). An average E-W striking 'fault plane' drawn through the aftershocks (thick red line in Figure 2b) has a dip of ~50° and emerges at the surface at 23.64 N. This fault plane is consistent with the topography of the northern Wagad peninsula. The corresponding traces for the Kachchh Mainland fault are shown in both pictures as dashed red lines.

2.1 Relocation of the mainshock nucleation point

An earthquake as large as the Bhuj mainshock (M_w 7.5) causes slip over a very large area of fault (~1500 km^2). This slip may be unevenly distributed, and the nucleation point determined from body wave arrivals may not coincide with the centroid of the moment release determined from long-period waveforms. Teleseismic broad-band seismograms for this event have consistently emergent first arrivals that occur between 2.5 and 3 seconds before the start of the main P-wave pulse (Figure 3a). This observation was also recorded

by the United States Geological Survey's monthly Earthquake Data Report (EDR) bulletin for January 2001. This separation between first arrivals and the start of the main P-wave arrivals suggests that the Bhuj mainshock was preceeded by a foreshock, and therefore that the location of the mainshock derived from these first arrivals (e.g. Engdahl and Bergman 2001) is actually the location of the foreshock.

The observed difference in first arrival time between two events that are separated horizontally can be calculated from geometrical arguments, and varies sinusoidally with station azimuth: the amplitude of the variation depends on the horizontal separation of the two epicentres, its phase depends on their relative azimuth, and the offset of the variation depends on the relative timing of the two events. We use measurements of the time difference between the first arrival and the start of the main P wave pulse to relocate the main event relative to the foreshock. Figure 3b is a plot of this time difference versus station azimuth. The time separation data for the Bhuj event (Figure 3b) are more consistent with a sinusoidal variation with station azimuth (offset 3 ± 0.1 s, amplitude 0.45 ± 0.1s, phase $80\pm15°$, χ^2=0.3) than with a straight line (offset 3 ± 0.2 s, χ^2=0.7). The data, therefore, suggest that there was a foreshock to the Bhuj earthquake, and that the mainshock nucleated 5–8 km further west-southwest than the location given by Engdahl and Bergman (2001).

This relocation of the Bhuj mainshock nucleation point is still very inaccurate, because the error in picking the arrivals from the seismograms is large ($\sim$0.5 s). We have used the Engdahl and Bergman (2001) epicentre for the Bhuj mainshock in the following analysis, and will discuss the event location and its implication for determining the structures actively involved in the faulting later (Section 6).

3 Teleseismic waveform modelling

Teleseismic modelling of long period body waves is a common way of determining the focal mechanism and depth of large earthquakes with good accuracy. Teleseismic body waves travel almost vertically down through the complex velocity structure of crust, without much perturbation or deviation, and therefore retain a lot of information about the earthquake source. High frequency body waves are influenced by the details of the source region crustal velocity structure, therefore good information on the structure is required to extract source information from broad-band seismograms. Longer period body waves average over most of the details of the crustal structure, so we can extract information about the earthquake source with less detailed knowledge of the velocity structure in the epicentral region. We use the MT5 version of the McCaffrey and Abers (1988) algorithm to invert long period P and SH waveform data for strike, dip, rake, centroid depth, seismic moment and source time function, as described in Maggi et al. (2000b)

Only the Bhuj mainshock and its largest aftershock (28 January 2001) produced sufficient teleseismic data to apply the waveform inversion procedure. Another aftershock, 19 Feb 2001, was also well recorded at a few teleseismic stations, and we have used these data to confirm my regional solution for the event.

3.1 26 January, 2001 (M_w 7.5) Bhuj mainshock

In the long-period teleseismic waveforms for the Bhuj mainshock, the foreshock discussed above is no longer visible. The waveforms are easily fit by a single double couple source, as shown in Figure 4. The minimum-misfit solution is an approximately East–West trending thrust (strike 281°, dip 42°, rake 107°), with a centroid depth of ~20km. The centroid depth is constrained by the width of the larger pulses in both the P and SH waveforms,

while the strike of the fault plane is mostly constrained by the polarity and amplitude of the *SH* first arrivals. My solution is consistent with the Harvard CMT solution (strike 298°, dip 39°, slip 136°) determined from very long period body waves, and in strike, dip and depth (if not location) with the aftershocks from Figure 2b.

Broad-band studies of fault–slip distribution (Yagi and Kikuchi, 2001; Antolik and Dreger, 2001) found that most of the slip occurred at depths of 18–25 km, with almost no slip occurring at the surface, consistent with no observations of surface breaks (Wesnousky et al., 2001). Figure 5 shows the Yagi and Kikuchi (2001) solution for the southward dipping plane. The rupture nucleated in the bottom half of the fault plane, and propagated westwards about 40 km and upwards about 20 km. The seismic fault–slip distribution studies, the centroid depth (20 km), and the aftershock distribution are all consistent with the Bhuj earthquake having broken through the entire seismogenic layer, which was found by Maggi et al. (2000a) to be ~40–50 km thick in the Indian Shield.

3.2 28 January, 2001 (M_w 5.7) aftershock

This event was the largest aftershock of the Bhuj earthquake, and occurred at the northern edge of the Wagad Uplift. The teleseismic waveforms for this earthquake are similar to those for the mainshock, except for the absence of a precursor, and the narrower width of the first pulse, which is controlled by both the depth and duration of the event. We therefore expect the focal mechanism of this aftershock to be similar to that of the mainshock. Figure 6 shows my *P* and *SH* waveform inversion solution for this event: an E-W trending thrust fault (strike 81°, dip 50°, rake 87°) with a centroid depth of ~9 km and a 4 second duration. The strike of the solution is again controlled by the *SH* waves, but is less well constrained than that of the mainshock, because the seismograms are noisier.

4 Regional waveform modelling: method

The remaining large aftershocks (M_w 5.0–5.2, Table 1) did not produce enough good quality teleseismic body wave records for body waveform modelling of their source parameters. We instead constrained their source parameters using regional recordings of multi-mode surface waves.

Regional multi-mode surface waves contain information about the seismic structure along the propagation path as well as about the earthquake source. It is only possible to extract the focal parameters of an earthquake from these regional recordings if the contribution from the propagation path is known. We have used a master event calibration method, outlined in Figure 7, to extract the focal parameters of the larger remaining aftershocks of the Bhuj earthquake. The method involves calibrating the surface wave propagation characteristics of all the paths to regional stations using recordings of a 'master' event with known focal parameters, and then using these calibrated propagation characteristics to extract focal parameter information from the surface wave recordings of smaller events from the same epicentral region as the 'master' event. We have calibrated the regional propagation paths using the 28 January aftershock rather than the 26 January mainshock because the recordings of the mainshock at many of the closer regional stations were clipped, and therefore these paths could not be calibrated.

4.1 Regional path calibration

The method outlined above poses no restriction on how the regional propagation paths are calibrated. We have used the NEWTON5surface waveform fitting algorithm discussed of Nolet (1990) and Van der Lee and Nolet (1997), which applies perturbations to depth–parameterised 1-D starting models in order to fit multi-mode surface waves in increasingly

wide frequency bands. We have created starting models for each path by integrating through the CRUST2 (Bassin et al., 2000) database, and have parameterised both shear wave velocity (β) and Moho depth. We have calibrated Rayleigh and Love waves separately.

It is important to note that the best-fit Earth model obtained by waveform inversion is not necessarily a unique description of the average 1-D velocity structure along the source–receiver path: any model with the same phase and group velocity dispersion characteristics will produce the same synthetic seismogram and thus match the data in the same way. This non-uniqueness is not a problem for regional path calibration, as we are only interested in the propagation characteristics along the path, and not in the details of the 1-D models themselves.

Table 2 lists the broad-band stations within regional distances of Bhuj which have good recordings of the 28 January aftershock. Only 3 of these stations are part of the Global Seismograph Network (GSN); the others are run by Indian Metereological Department (IMD), jointly by the Indian National Geophysical Research Institute and the University of Cambridge (NGRI-CU), and by the Iranian International Institute of Earthquake Engineering and Seismology (IIEES). The locations of the stations and an example of path calibration are shown in Figure 8.

4.2 Adaptive grid searching

Having calibrated the propagation characteristics of paths to regional stations, we have then extracted focal mechanism information from surface wave recordings of the aftershocks at these stations. We have used an adaptive forward modelling approach, which efficiently samples the entire space of focal parameters (strike, dip, rake, depth) and closes in on the minimum-misfit solution. This approach is similar to the neighbourhood algorithm of

Sambridge (1999), and is summarised in Figure 9.

We take a random sample of points in parameter space, calculate forward synthetic seismograms by modal summation for all stations that recorded the event (using the calibrated structure for each path), and compare them to the observed records to give a single misfit value per point in parameter space. We then subdivide the entire parameter space into subspaces around each sample point, such that each point within a subspace is closer to the sample point at its centre than any other sample point (subdivision into Voronoi cells). 'Closeness' is defined by a Euclidean distance metric which is normalised by the a-priori variances of the single parameters. We rank the sample points according to misfit, and take new random samples within the Voronoi cells around the best few sample points (typically the best 10%). By iterating this procedure, it is possible to quickly and efficiently converge to the minimum-misfit region of parameter space, mapping out deep local minima, but not getting trapped in them.

We measure the misfit, e, between an observed record and its synthetic seismogram by cross-correlation (Wallace, 1986):

$$e = 1 - \frac{s \otimes d}{(s \otimes s)^{1/2}(d \otimes d)^{1/2}}, \tag{1}$$

where s is the synthetic seismogram, d is the observed seismogram and $\otimes$ indicates 'the maximum value of the correlation function'. Comparing seismograms in this manner allows me to cope with errors in the epicentral locations of the events. Errors in epicentral location cause the synthetic seismograms to be shifted in time with respect to the observed seismograms. These time shifts translate directly into the lag of the cross-correlation function, but do not affect its amplitude or the misfit e.

5 Regional waveform modelling: results

We have used the method outlined in the previous section to extract focal parameter information for six of the larger aftershocks of the Bhuj earthquake. The resulting focal mechanisms and depths are listed in Table 1 and are shown in Figure 2. The detailed waveform modelling results for these earthquakes are shown in Figures 11–16. As a test of the master event calibration method, the first earthquake we analysed in this manner was the large aftershock of the 28 January 2001, used to calibrate the regional paths.

5.1 28 January, 2001 (Mw 5.7)

The regional solution for the 28 January aftershock (Figure 10) agrees very well with the previous teleseismic solution (Figure 6) in both focal mechanism and depth. Panels (a)–(f) in Figure 10 show the sensitivity of the solution to single parameters, and the trade-offs between the various parameters. Both depth and dip have wide minima, meaning they are less well constrained: the minimum-misfit region spans depths from 5 to 12 km, and dips from 25 to 60 degrees. There is an indication of trade-off between strike and rake (Figure 10e), although the minimum is narrow in both these parameters. The fits to the 10 Rayleigh and 7 Love waves observed for this event at regional stations are excellent.

5.2 27 January, 2001 (Mw 5.2)

Although this event was only well recorded at six regional stations, the minimum-misfit solution shows good fits to both Love and Rayleigh waveforms (Figure 11) at stations AAK, ABKT, LSA, and (though at lower frequency) TPT. The fits at stations GBA and PUNE are less convincing. Although the minimum-misfit region is very small, the 10%

acceptability contour encompasses a wide range of depths (0–15 km) and dips (20–70). The minimum-misfit focal mechanism, an E-W trending thrust, is similar to both the mainshock and the January 28 aftershock.

5.3 3 February, 2001 (Mw 5.1)

The mechanism of the February 3rd (M_w5.1) event is the least well constrained of the aftershock sequence (Figure 12), despite excellent fits to the 8 observed seismograms. Depths between 0 and 10 km, dips between 10 and 60 degrees, strikes between 80 and 160 degrees and rakes between 40 and 140 degrees all produce misfits within 1% of the minimum misfit (black regions in panels (a)–(f)). The minimum-misfit solution indicates either south-west slip on a high angle eastward dipping fault, or eastward slip on a low angle south-west dipping fault.

5.4 8 February, 2001 (Mw 5.2)

The minimum-misfit mechanism for this strike-slip event is very well constrained by excellent fits to both Rayleigh and Love waves at 7 stations (Figure 13). Dip is still the least well constrained of the focal plane parameters, and there is some indication of trade-off between strike and rake. The earthquake depth is very poorly determined: the minimum in Figure 13a-c spans all depths from 0 to 20 km.

5.5 19 February, 2001 (Mw 5.2)

The minimum-misfit solution for this event (Figure 14) is similar to that for the 3 February, but with the dips of the fault planes exchanged. This fault plane solution, however, is much

better constrained by the data, as can be seen in panels (d)–(f) of Figure 14. Depth is also better constrained, but can still vary from 2 to 10 km. Fits to all 12 of the recorded seismograms are good, although the synthetic seismograms cannot fit the long period start of the Love wave at ABKT or the tail of the Rayleigh wave at ASH very well.

The 19 February aftershock was large enough to have a Harvard CMT solution: an approximately E-W trending thrust mechanism also at a depth of 4 km. This mechanism is significantly different from the one we have recovered using regional surface waves (a NW-SE trending thrust) . Figure 15 shows comparisons between the Harvard CMT solution and the minimum-misfit surface wave solution. Using the Harvard solution to create surface wave synthetic seismograms (Figure 15a) produces worse fits at all stations, except for the Love wave at ABKT. This event was also large enough to produce a some teleseismic body waves which could be used for basic P and SH waveform modelling. Figure 15b shows comparative fits to 4 P and 2 SH teleseismic waveforms for the minimum-misfit P and SH body-wave solution and the Harvard CMT solution. Both solutions fit the seismograms reasonably well, with the minimum-misfit solution fitting significantly better only at LBTB. The body wave P and SH solution is essentially the same as the minimum-misfit surface wave solution for this event (Figure 14).

5.6 4 March, 2001 (Mw 5.0)

This was the smallest event (Mw 5.0) for which we could extract a source mechanism from regional surface waveforms. The minimum-misfit focal mechanism indicates strike-slip motion, and is similar to that for the 8 February event (Figure 13). All three focal plane parameters (strike, dip and rake) are very well constrained by the data, while the depth could vary between 2 and 15 km. The fits are good at most stations, although the Love waves at AAK and PUNE are noisy.

5.7 Summary of surface wave results

The surface wave grid-search analysis of the larger aftershocks of the Bhuj earthquake has found that the depths of the events are poorly constrained by the surface wave data. After depth, fault dip is the least well constrained parameter, while fault strike and slip (rake) direction can be very well constrained by the surface wave data.

Only two of the larger aftershocks of the Bhuj earthquake sequence (January 27 and January 28) had mechanisms (E-W trending thrusts) similar to that of the mainshock (see Figure 17). The January 27 (Mw 5.1) event occurred just north of the Kachcch Mainland fault, at the edge of the Banni Plain, and took up N-S compression along an E-W trending trust fault. The January 28 (Mw 5.7) event occurred on the north Wagad peninsula, probably on an E-W structure parallel to the northern boundary of the peninsula itself. We will discuss the location and possible fault planes of this aftershock later, in Section 6.

Two of the aftershocks (February 8th, March 4th) have well constrained strike-slip mechanisms (Figure 13, 16) with N-S P-axes that can take up N-S shortening. The epicentres of these events, respectively to the north and south of the Wagad uplift (Figure 17), place them in the salt plains and tidal regions of the Rann. There is no obvious surface expression of the faults which ruptured in these small events (M_w 5.2 and 5.0 respectively). We do, however, have confirmation of another strike-slip event with a NW-SE right-lateral nodal plane in the aftershock sequence: Wesnousky et al. (2001) reported that although they found no primary surface faulting reflecting large reverse motion, they did observe one tectonic rupture showing strike-slip motion, along the western boundary of the Wagad uplift, close the town of Manfara. This surface rupture zone strikes north-west for about 8 km, and shows primarily right-lateral motion with up to 32 centimetres of slip. Given the location of the fault, between the Kachcch mainland and the Wagad uplift, Wesnousky

et al. (2001) speculated that this strike-slip rupture occurred on a pre-existing fault, related to a structural discontinuity or tear between the two uplifted blocks.

The February 3rd and February 19th aftershocks are both thrust events with some strike-slip component. The mechanism of the February 3rd (M_w5.1) event is the least well constrained of the aftershock sequence (Figure 12). It indicates either near-vertical slip on a high angle eastward dipping fault, or westward slip on a low angle south-west dipping fault. The mechanism of the February 19th (M_w5.2) event is similar to that of the 3rd February, though the fault planes are reversed (the shallow plane dips east while the steep plane dips south west), and it is constrained by both surface wave and body wave data (Figures 14 and 15). The epicentres of these two events are both, like those of the strike-slip events, within the flat-lying tidal range of the Rann of Kachcch, and there is no obvious surface expression of the faults on which they occurred.

6 Discussion

The Kachchh region, an ancient rift system created during the separation of the Indian subcontinent from the super-continent of Pangea (Biswas, 1987), has a long history of strong earthquakes (Bapat et al., 1983). Structures within these rift systems, both on and off the Kachchh Mainland itself, are subjected to compressional stress from the collision between India and Asia, and are reactivated to take up the compression by reverse faulting (Rajendran and Rajendran, 2001; Talwani and Gangopadhyay, 2001). Some of these reverse faults are immediately visible from the topography as elongated structures with a sharp boundary on one side (indicating the transition to the foot wall), and more gradual slopes on the other side (the hanging wall). The most striking examples are the Island Belt Fault and the Kachchh Mainland Fault (Figure 1), which are both south-dipping thrust

structures (the gentle topography is on the southern side).

The 26 January, 2001 Bhuj earthquake (Mw 7.5) occurred at a depth of ~20 km, and probably ruptured through the whole thickness of the crust. Fault-slip mapping studies based on body wave analysis (Antolik and Dreger, 2001; Yagi and Kikuchi, 2001) find that the rupture propagated westwards for approximately 40 km, with locally up to 8 m of slip on the fault, dying away to nothing at the surface (Figure 5). In fact, no primary surface rupture was found in the area (Wesnousky et al., 2001), and there are few clues as to which of the faults in the region was responsible for the event.

If the Engdahl and Bergman (2001) relative relocations are correct, the epicentre of the earthquake lies north of the Kachcch Mainland Fault, at the junction between the Kachchh Mainland and the Wagad peninsula. Seismology alone cannot distinguish which of the two possible planes of the E-W trending focal mechanism (north or south dipping) was the actual fault plane. The trend of the aftershocks (Figure 17) suggests a south-dipping plane is most likely. The earthquake epicentre is too far north (even taking into account the relocation of the mainshock nucleation point relative to the foreshock described in Section 2.1) of the south-dipping Kachchh Mainland fault for this fault to have been responsible for the event. Similarly, the south-dipping Island Belt fault is too far North of the mainshock epicentre and of the aftershock distribution to have been involved.

An 'average' fault (solid red line) drawn through the preliminary aftershock locations emerges at the surface on the northern boundary of the Wagad peninsula (Figure 17). Dense vegetation makes it difficult to distinguish features on satellite images of the Wagad pensinsula (Figure 18a), but by comparing the images to cross-sections through the topography it is possible to identify possible bounding faults (Figure 18b). The northern boundary fault (J28) dips to the south, while the southern boundary fault (WF) dips to the north, making the Wagad peninsula an analogue of the Shillong Plateau pop-up structure

(Bilham and England, 2001). The northern Wagad fault is a likely candidate for rupture in the January 28 Mw 5.7 aftershock, which occurred ~10 km south of the surface trace at a well-constrained body wave depth of ~9 km.

7 Conclusions

If we are to believe the body wave fault-mapping studies, and the Bhuj mainshock ruptured westwards, then the north Wagad fault could not have been responsible for the earthquake. The Bhuj earthquake might have ruptured a completely buried and un-mapped fault within the Great Rann, continuing westwards from the north side of the Wagad peninsula. Alternatively, it might have ruptured a fault somewhat distant from the nucleation point obtained from first arrivals. There is some evidence that large earthquakes tend to nucleate at the ends of long structures, and that the main moment release occurs some distance away (Yielding et al., 1981; Berberian et al., 1999). Radar interferometry, a very powerful technique for identifying structures involved in earthquake faulting (Wright et al., 1999; Berberian et al., 2001), cannot be used for this earthquake because no cohererent co-sesimic interferograms can be made with the data available (Bürgmann et al., 2001). It is possible, therefore, that we might never discover which fault was responsible for the 26 January, 2001 earthquake.

References

M. Antolik and D.S. Dreger. Source rupture process of the 26 January, 2001 Bhuj, India, earthquake (M 7.6). *EOS Trans. AGU*, 82(47), 2001. Fall Meet. Suppl.

A. Bapat, R.C. Kulkarni, and S.K. Gutha. Catalog of earthquakes in India and neighborhood from historical period up to 1979. Technical report, India. Soc. Earthq. Tech., 1983.

C. Bassin, G. Laske, and G. Masters. The current limits of resolution for surface wave tomography in North America. *EOS Trans. AGU*, 81:897, 2000.

M. Berberian, J.A. Jackson, E. Fielding, B.E. Parsons, K. Priestley, M. Qorashi, M. Talebian, R. Walker, T.J. Wright, and C. Baker. The 14 March, 1998 Fandoqa earthquake (m_w 6.6) in Kerman province, southeast iran: re–reupture of the 1981 Sirch earthquake fault, triggering of slip on adjacent thrusts, and the active tectonics of the Gowk fault zone. *Geophys. J. Int.*, 146:371–398, 2001.

M. Berberian, J.A. Jackson, M. Qorashi, M.M. Khatib, K. Priestley, T. Talebian, and M. Ghafuri-Ashtiani. The 1997 May 10 Zirkuh (Qa'enat) earthquake ($m_w = 7.2$): faulting along the Sistan suture zone of eastern Iran. *Geophys. J. Int.*, 136:671–694, 1999.

R. Bilham. Slip parameters for the Rann of Kachchh, India, 16 June 1819, earthquake, quantified from contemporary accounts. In I.S. Stewart and C. Vita-Finzi, editors, *Coastal Tectonics*, volume 146, pages 295–319. Geological Society, London, Special Publications, 1998.

R. Bilham and P. England. Plateau pop-up in the 1897 Assam earthquake. *Nature*, 410: 806–809, 2001.

S.K. Biswas. Regional tectonic framework, structure and evolution of the western marginal basins of India. *Tectonophysics*, 135:307–327, 1987.

R. Bürgmann, D.A. Schmidt, and E. Fielding. InSAR constraints on the January 26, 2001 Bhuj earthquake. *EOS Trans. AGU*, 82(47), 2001. Fall Meet. Suppl.

W.-Y. Chung and H. Gao. Source parameters of the Anjar earthquake of July 21, 1956, India, and its seismotectonic implications for the Kutch rift basin. *Tectonophysics*, 242: 281–292, 1995.

E.R. Engdahl and E.A. Bergman. Validation and generation of reference events by cluster analysis. In *Proceedings of the 23rd Seismic Research Review: Worldwide monitoring of nuclear explosions*, volume 1, pages 205–214. NASA, DTRA, 2001.

A. Maggi, J.A. Jackson, D. McKenzie, and K. Priestley. Earthquake focal depths, effective elastic thickness, and the strength of the continental lithosphere. *Geology*, 28:495–498, 2000a.

A. Maggi, J.A. Jackson, K. Priestley, and C. Baker. A re–assessment of focal depth distribution in southern Iran, the Tien Shan and northern India: Do earthquakes really occur in the continental mantle? *Geophys. J. Int.*, 143:629–661, 2000b.

R. McCaffrey and J. Abers. SYN3: A program for inversion of teleseismic body wave form on microcomputers. Technical Report AFGL-TR-0099, Air Force Geophysical Laboratory, Hanscomb Air Force Base, Massachussets, 1988.

G. Nolet. Partitioned waveform inversion ant two-dimensional structure under the Network of Autonomously Recording Seismographs. *J. Geophys. Res.*, 95:8499–8512, 1990.

C.P. Rajendran and K. Rajendran. Characteristics of deformation and past seismicity

associated with the 1819 Kutch earthquake, Northwest India. *B. Seismol. Soc. Am.*, 91 (3):407–426, 2001.

A.J. Raphael, P. Bodin, S. Horton, and J. Gomberg. Preliminary double-difference relocations of Bhuj aftershocks. *EOS Trans. AGU*, 82(47), 2001. Fall Meet. Suppl.

M. Sambridge. Geophysical inversion with a neighbourhood algorithm – I: searching a parameter space. *Geophys. J. Int.*, 138:479–494, 1999.

P. Talwani and A. Gangopadhyay. Tectonic framework of the Kachchh earthquake of 26 January 2001. *Seismol. Res. Lett.*, 72(3):336–345, 2001.

S. Van der Lee and G. Nolet. Upper mantle S velocity structure of North America. *J. Geophys. Res.*, 102:22,815–22,838, 1997.

T.C. Wallace. Inversion of long period regional body waves for crustal structure. *Geophy. Res. Lett.*, 13(8):749–752, 1986.

S.G. Wesnousky, L. Seeber, T.K. Rockwell, V. Thakur, R. Briggs, S. Kumar, and D. Ragona. Eight days in Bhuj: field report bearing on surface rupture and genesis of the 26 January 2001 earthquake in India. *Seismol. Res. Lett.*, 72(5):514–523, 2001.

T.J Wright, B.E. Parsons, J.A. Jackson, M. Haynes, E.J. Fielding, P.C. England, and P.J. Clarke. Source parameters of the 1 October 1995 Dinar (Turkey) earthquake from SAR interferometry and seismic bodywave modelling. *Earth Planet. Sc. Lett.*, 172:23–37, 1999.

Y. Yagi and M. Kikuchi. Results of rupture process for January 26, 2001 western India earthquake (m_s 7.9). WWW: `http://wwweic.eri.u-tokyo.ac.jp/yuji/southindia/index.html`, March 2001.

J.A. Yielding, G. amd Jackson, G.C.P. King, H. Sinvhal, C. Vita-Finzi, and R.M. Wood. Relations between surface deformation, fault geometry, seismicity, and rupture characteristics during the El Asnam (Algeria) earthquake of 10 October 1980. *Earth Planet. Sc. Lett.*, 56:287–304, 1981.

Table 1 Locations and focal mechanisms of the Bhuj mainshock and larger aftershocks. Epicenters from Engdahl and Bergman (2001) except aftershock on 27-01-2001($\star$ - location from Indian Metereological Department). Depths and mechanisms from regional waveform inversion except the mainshock ($\dagger$ - teleseismic waveform inversion).

Table 2 Locations of seismic stations within regional distances of the Bhuj earthquake. Stations not from the Global Seismograph Network (GSN) are run by the Indian Metererological Department (IMD), jointly by the National Geophysical Research Institude and the University of Cambridge (NGRI-CU), or by the Iranian International Institute of Earthquake Engineering and Seismology (IIEES). Stations for which Rayleigh and/or Love wave propgation could be calibrated have an 'R' and/or an 'L' in the last column.

Figure 1 Geographical location of the Kachchh region and topography from the Shuttle Radar Topography Mission (NASA/JPL/NIMA). Superimposed on the topography image are the locations of the major faults and the towns mentioned in this paper (B: Bhuj, A: Anjar, M: Manfara). The black rectangle shows the location of the Landsat image in Figure 18.

Figure 2 (a) Focal mechanisms for the Bhuj mainshock (red) and larger aftershocks (black) as determined in this study and listed in Table 1. Depths are shown above the focal mechanisms. Other aftershocks relocated by Engdahl are shown as elipses, and the master events for the relocations, originally located by the CERI deployment, are shown as filled circles. Also shown are the locations of cross-sections A and B (blue dashed lines), shown in Figures 18, and the surface traces (red solid and dashed lines) of the trends shown in (b). (b) Depth distribution of the aftershocks located by Raphael et al. (2001), with the location of the mainshock indicated by a white star. The aftershock picture was reproduced from `http://www.ceri.memphis.edu/~withers/Gujarat/`,

and contains the projection of ~250 aftershocks onto a N-S trending vertical plane. Superimposed on the image are possible fault trends (solid and dahsed red lines); the surface traces are shown in (a).

Figure 3 (a) Selected broad-band seismograms of the Bhuj mainshock at teleseismic distances, showing the separation between the foreshock (1) and the main P wave arrival (2). Station names and azimuths are shown to the right of the seismograms. (b) The observed time difference as a function of station azimuth, and the best fitting sinusoidal curve through the data.

Figure 4 Minimum misfit solution for the Bhuj mainshock, 26 January 2001. The upper sphere shows the P wave radiation pattern and the lower sphere that for SH. Both are lower hemisphere projections. The station code by each waveform is accompanied by a letter corresponding to its position in the focal sphere. The positions are ordered clockwise by azimuth. The solid lines are the observed waveforms, the dashed lines are the synthetic waveforms. The inversion window is marked by solid bars at either end of the waveform. P and T axes within the sphere are represented by solid and open circles respectively. The source time function is shown below the P focal sphere, with the waveform time scale below it.

Figure 5 Fault–slip distribution for the Bhuj mainshock from Yagi and Kikuchi (2001), south dipping plane. The focal mechanism and moment release function (MRF) are shown in blue above the slip distribution. The direction of slip changes with position and is indicated by black arrows, while the amount of slip is indicated by the colour. The nucleation point is shown as a red circle on the slip distribution image. Fits to body wave seismograms are shown on the right.

Figure 6 Minimum misfit solution for M_w5.7 aftershock, 28 January 2001. All symbols have the same meaning as in Figure 4.

Figure 7 The master event calibration method. (1) Use teleseismic body wave records to determine the focal parameters of a master event; (2) use regional surface wave records for the master event to calibrate the propagation characteristics of regional paths; (3) extract the focal parameters of smaller events close to the master event from their regional surface wave records.

Figure 8 (a) Location of broad-band stations within regional distances of Bhuj (Table 2). GSN stations are shown as squares, IMD stations as triangles, NGRI-CU stations as circles and IIEES stations as stars. The IMD station at Bhuj is also plotted for reference. (b) Love wave calibration of the path to BHPL, showing the initial and final fit of synthetic (dotted lines) seismograms and spectra to the data (solid lines). The right hand panel contains the starting (solid) and final (dotted) Earth models.

Figure 9 The neighbourhood algorithm. (a) Flowchart of the adaptive grid-searching method. (b) Example of an inital distribution of parameters within a parameter space. (c) Example of a final distribution of parameters within a parameter space. (b) and (c) are reproduced from Sambridge (1999).

Figure 10 Regional waveform solution for the 28 January aftershock. The focal parameters for the minimum-misfit solution are shown under the event date. Panels (a)–(f) show slices through the misfit volume taken through the minimum, with two different parameters fixed at the minimum-misfit values. Regions with misfits of less than 1% are shown in black, and regions with misfits of less than 10% are surrounded by a white contour. The regional and teleseismic mechanisms are shown below the panels, and are followed by the fits of synthetic (dotted) to observed (solid) seismograms for all the available data. The letters (L) and (R) after the station names indicate the seismograms are Love and Rayleigh waves respectively. All parameters are very well constrained, and the resulting focal mechanism is almost identical to the teleseismic

solution.

Figure 11 Regional waveform solution for the 27 January aftershock. All parameters are well constrained, despite the low number of waveforms available (7), but the dip and depth have broad 10% contours. The minimum-misfit focal mechanism is almost identical to the mainshock.

Figure 12 Regional waveform solution for the 3 February aftershock. The minimum-misfit solution, a thrust striking NW-SE, is not well constrained by the data. Despite the fits being good at all 6 stations, slices through the misfit volume show that the minimum is very shallow, with both dip and strike practically unconstrained.

Figure 13 Regional waveform solution for the 8 February aftershock. The minimum-misfit solution is a strike-slip mechanism, with very well constrained focal planes. The earthquake depth is not well constrained.

Figure 14 Regional waveform solution for the 19 February aftershock. The minimum-misfit solution, a NW-SE striking thrust, is similar to that for the 3 February (Figure 12), but with the dips of the fault planes exchanged. For this event, however, the focal mechanism is well constrained (see panels (d)–(f)).

Figure 15 Comparison with the Harvard CMT solution for the 19 February aftershock. (a) Fits to the regional data: the seismograms are less well matched at all stations, except for ABKT, where the long period precursor to the Love waves is better matched by the CMT solution. (b) Fits to the teleseismic data. The first line shows the minimum-misfit teleseismic solution, obtained using 8 P and 5 SH waveforms. The second line is the fit of the Harvard CMT mechanism to the same data. Strike, dip, rake, depth (km) and seismic moment (Nm) are shown above the P and SH focal mechanisms in each line.

Figure 16 Regional waveform solution for the 4 March aftershock. The minimum-misfit solution, a strike-slip mechanism, is similar to that for the 8 February event (Figure 13), and is very well constrained by the data.

Figure 17 Summary of the Bhuj earthquake sequence. This figure is identical to Figure 2, and is repeated here for ease of reference.

Figure 18 The Wagad peninsula. (a) LANDSAT 7 image of the Wagad uplift. Dense vegetation makes interpretation difficult, but two large structures are visible: the previously mapped Wagad fault (WF) (Talwani and Gangopadhyay, 2001), and a northen structure (J28) which may have ruptured during the January 28 aftershock. (b) N-S topographic cross-section through the Wagad peninsula (location is shown by line A in Figure 17). Elevations are vertically exaggerated, and approximate positions of the bounding faults are shown as thick grey lines. (c) N-S topographic cross-section through the Kachcch mainland (B in Figure 17), with the positions of the Kachchh Mainland fault (KMF) and the Katrol Hills fault (KHF) shown for comparison.

Date	Time	Lat. N	Lon. E	M_w	Depth	Focal Mechanism
26-01-2001	03:16:40	23.415	70.322	7.5	20	281/42/107 †
27-01-2001 *	04:36:06	23.404	70.107	5.2	13	104/39/105
28-01-2001	01:02:12	23.541	70.587	5.7	9	096/48/107
03-02-2001	03:04:35	23.712	70.525	5.1	1	127/33/056
08-02-2001	16:54:42	23.705	70.475	5.2	5	141/65/167
19-02-2001	08:24:21	23.596	70.158	5.2	4	004/28/136
04:03:2001	07:54:22	23.134	70.493	5.0	11	036/86/332

Table 1:

Station	Latitude	Longitude	Elev (m)	Network	Calibrated
AAK	42.6390	74.4940	1645	GSN	L R
ABKT	37.9304	58.1189	678	GSN	L R
ASH	34.5490	50.0240	2217	IIEES	L R
BHPL	23.2410	77.4245	520	IMD	L
GBA	13.5640	77.3570	681	NGRI-CU	L
KARD	17.3075	74.1833	582	IMD	R
KAV	35.9021	50.9145	1795	IIEES	R
KRB	29.9797	56.7523	0	IIEES	L R
LSA	29.7000	91.1500	3789	GSN	L R
PUNE	18.5295	73.8492	560	IMD	L R
TPT	13.2740	76.5360	785	NGRI-CU	R

Table 2:

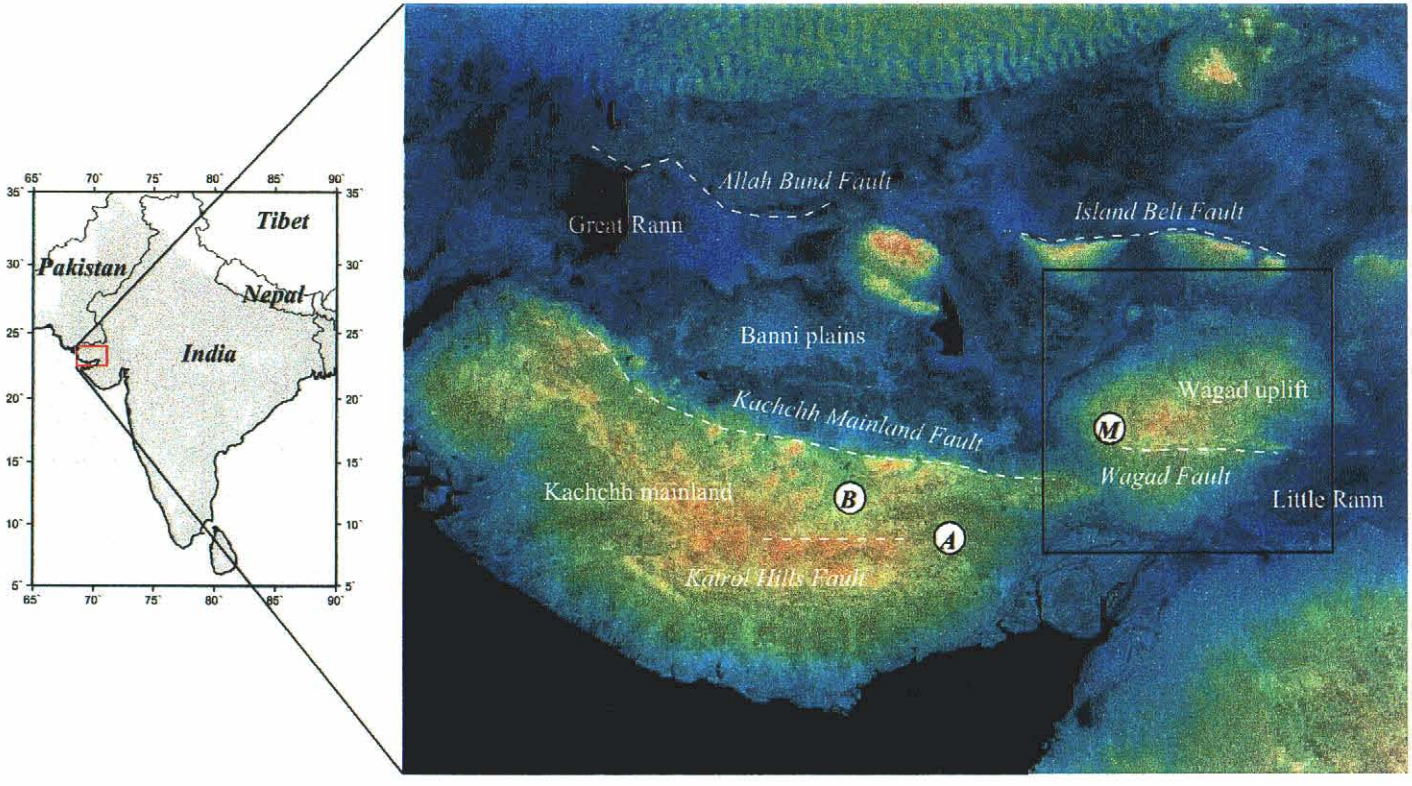
Tibet
Pakistan
Nepal
India
Allah Bund Fault
Great Rann
Island Belt Fault
Banni plains
Kachchh Mainland Fault
Wagad uplift
M
Wagad Fault
Little Rann
Kachchh mainland
B
A
Katrol Hills Fault

Figure 1:

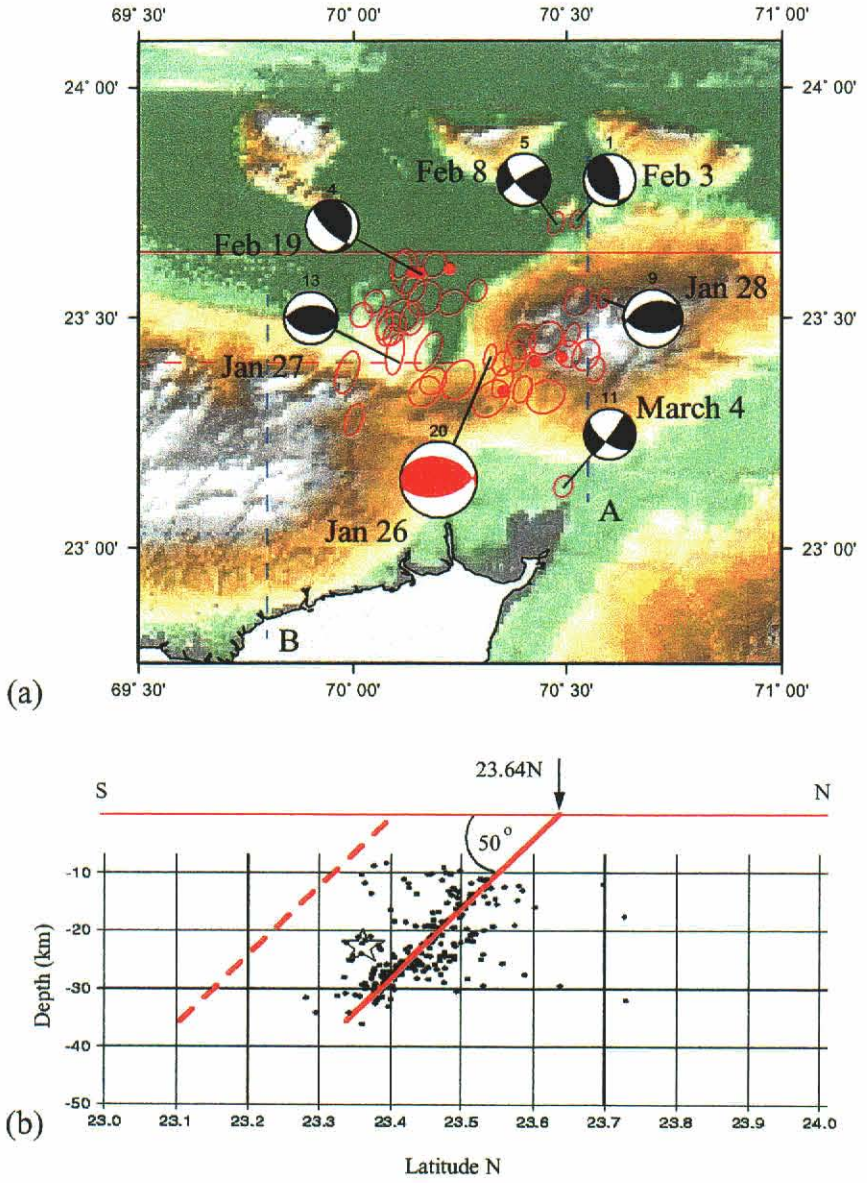
69° 30'
70° 00'
70° 30'
71° 00'
24° 00'
23° 30'
23° 00'
Feb 8
Feb 3
Feb 19
Jan 28
Jan 27
March 4
Jan 26
A
B
(a)
23.64N
S
N
50°
Depth (km)
-10
-20
-30
-40
-50
23.0
23.1
23.2
23.3
23.4
23.5
23.6
23.7
23.8
23.9
24.0
Latitude N
(b)

Figure 2:

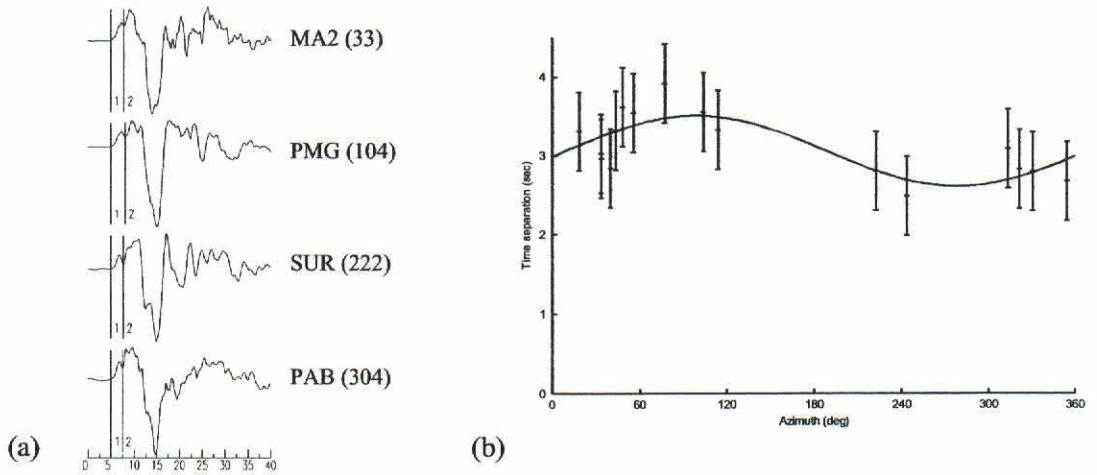
MA2 (33)
PMG (104)
SUR (222)
PAB (304)
1 2
0 5 10 15 20 25 30 35 40
(a)
(b)
Time separation (sec)
Azimuth (deg)
0 1 2 3 4
0 60 120 180 240 300 360

Figure 3:

St/Dp/Rk = 281/42/107 degrees

Depth = 20 km M0 = 2.3e20 Nm

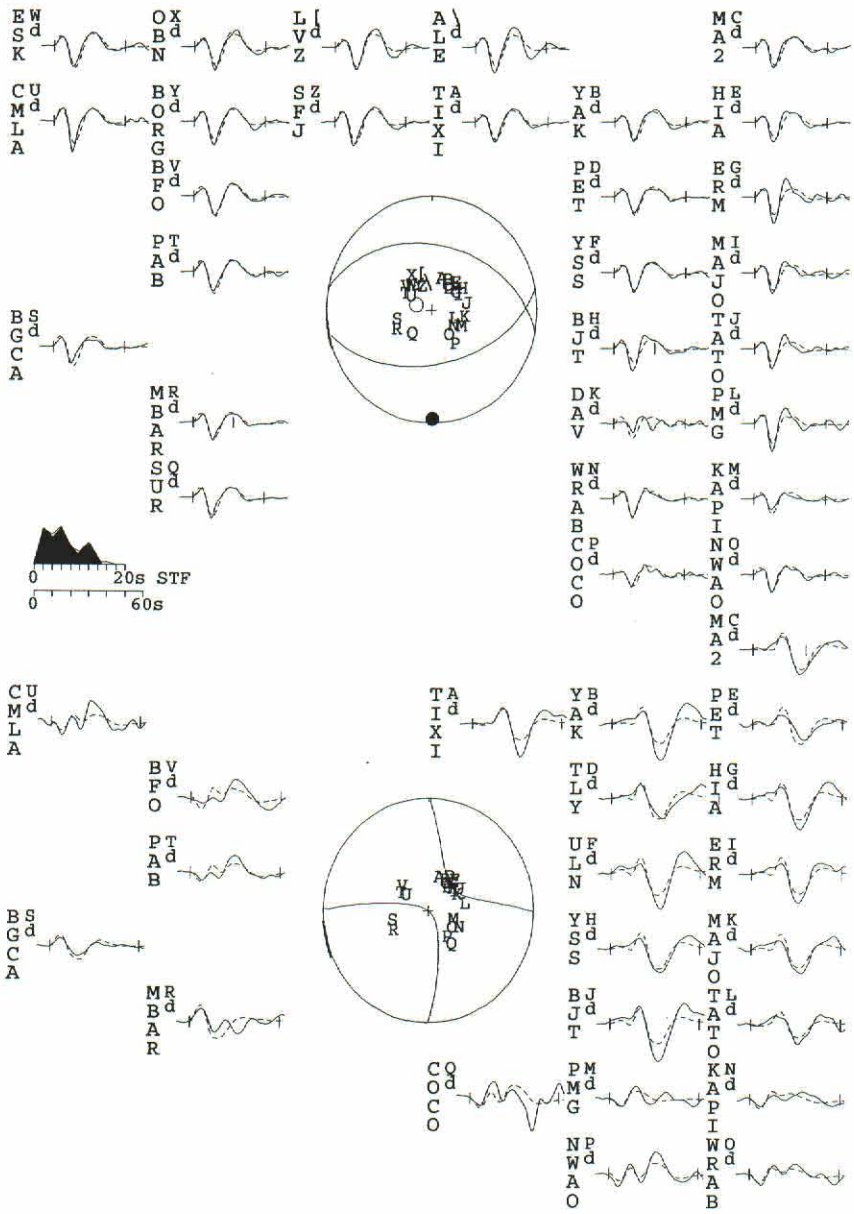

Figure 4:

Bhuj mainshock (26 January, 2001) — South dipping plane

Moment = 0.28E21 Nm Mw = 7.6 (Strike / Dip / Rake) = (78/56/81)

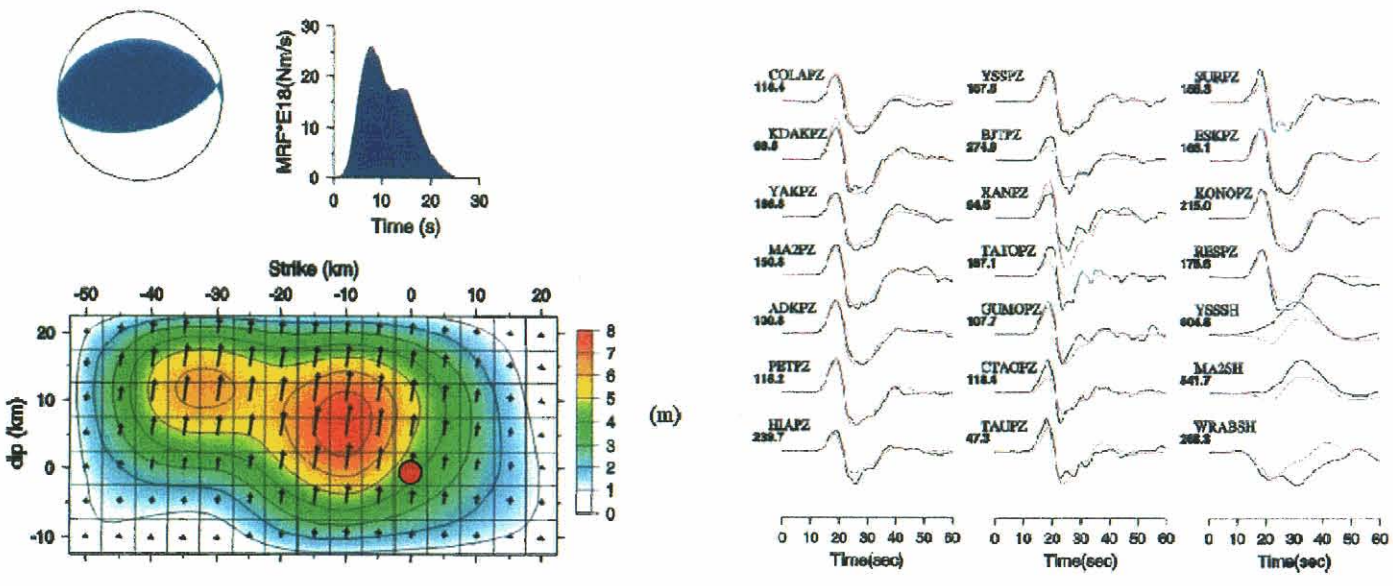

Figure 5:

St/Dp/Rk = 81/50/87 degrees

Depth = 9 km M0 = 4.9e17 Nm

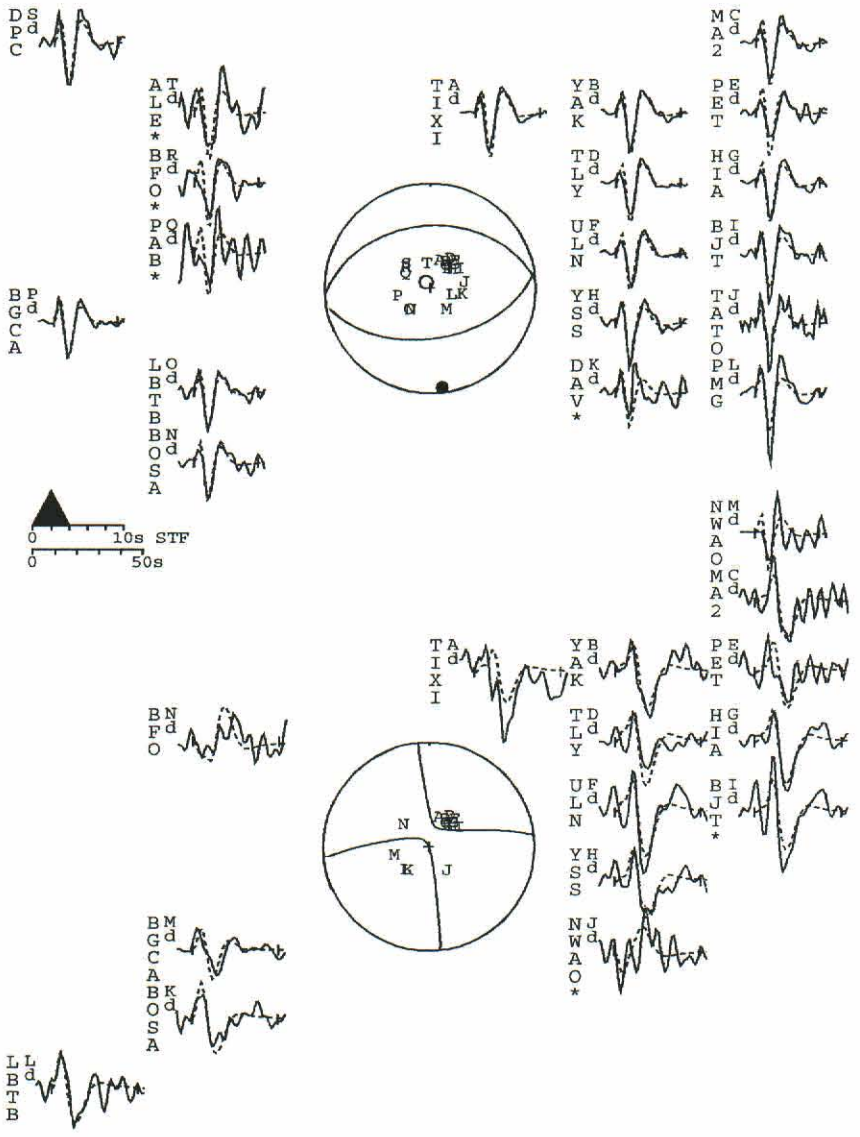

Figure 6:

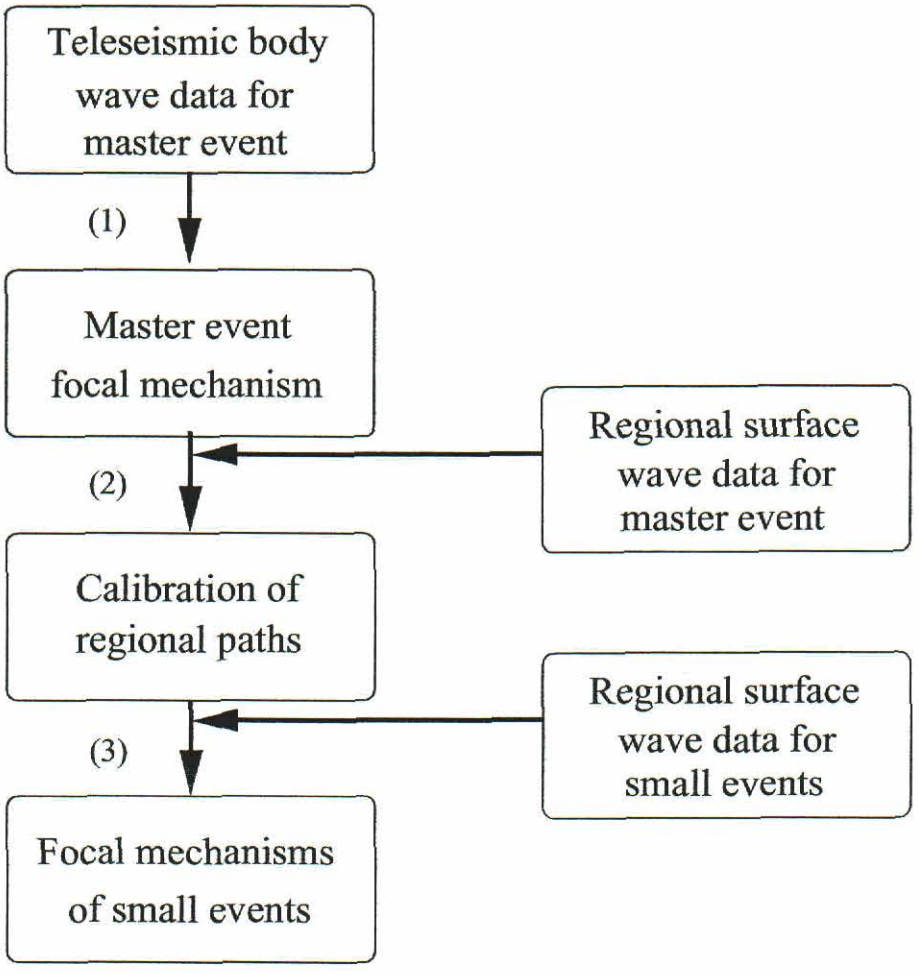
Teleseismic body wave data for master event
(1)
Master event focal mechanism
Regional surface wave data for master event
(2)
Calibration of regional paths
Regional surface wave data for small events
(3)
Focal mechanisms of small events

Figure 7:

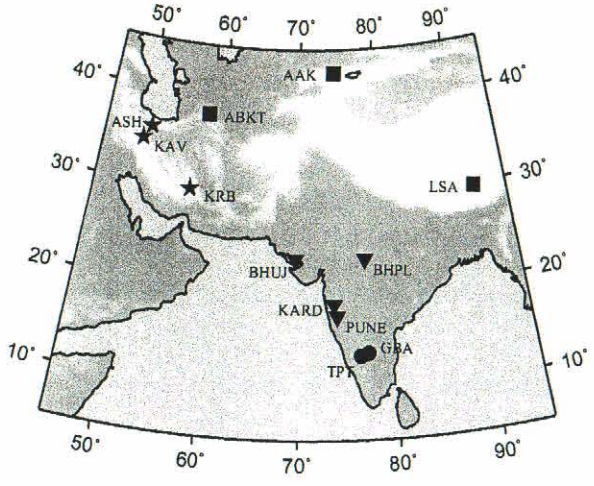
50°
60°
70°
80°
90°
40°
30°
20°
10°
AAK
ABKT
ASH
KAV
KRB
LSA
BHUJ
BHPL
KARD
PUNE
GBA
TPT

(a)

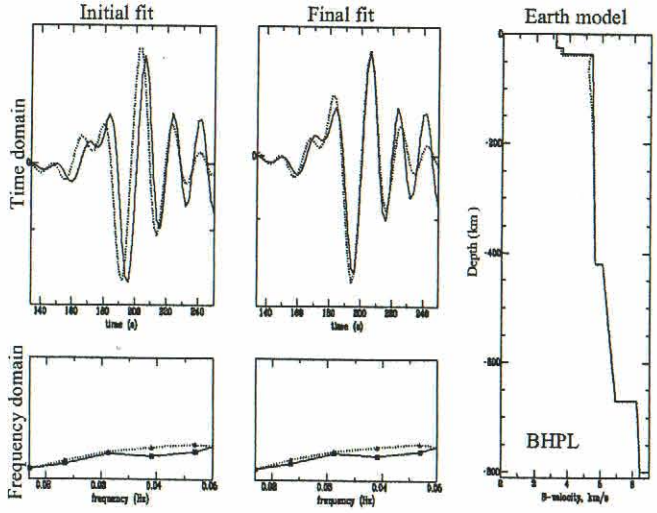
Initial fit
Final fit
Earth model
Time domain
Frequency domain
Depth (km)
BHPL

(b)

Figure 8:

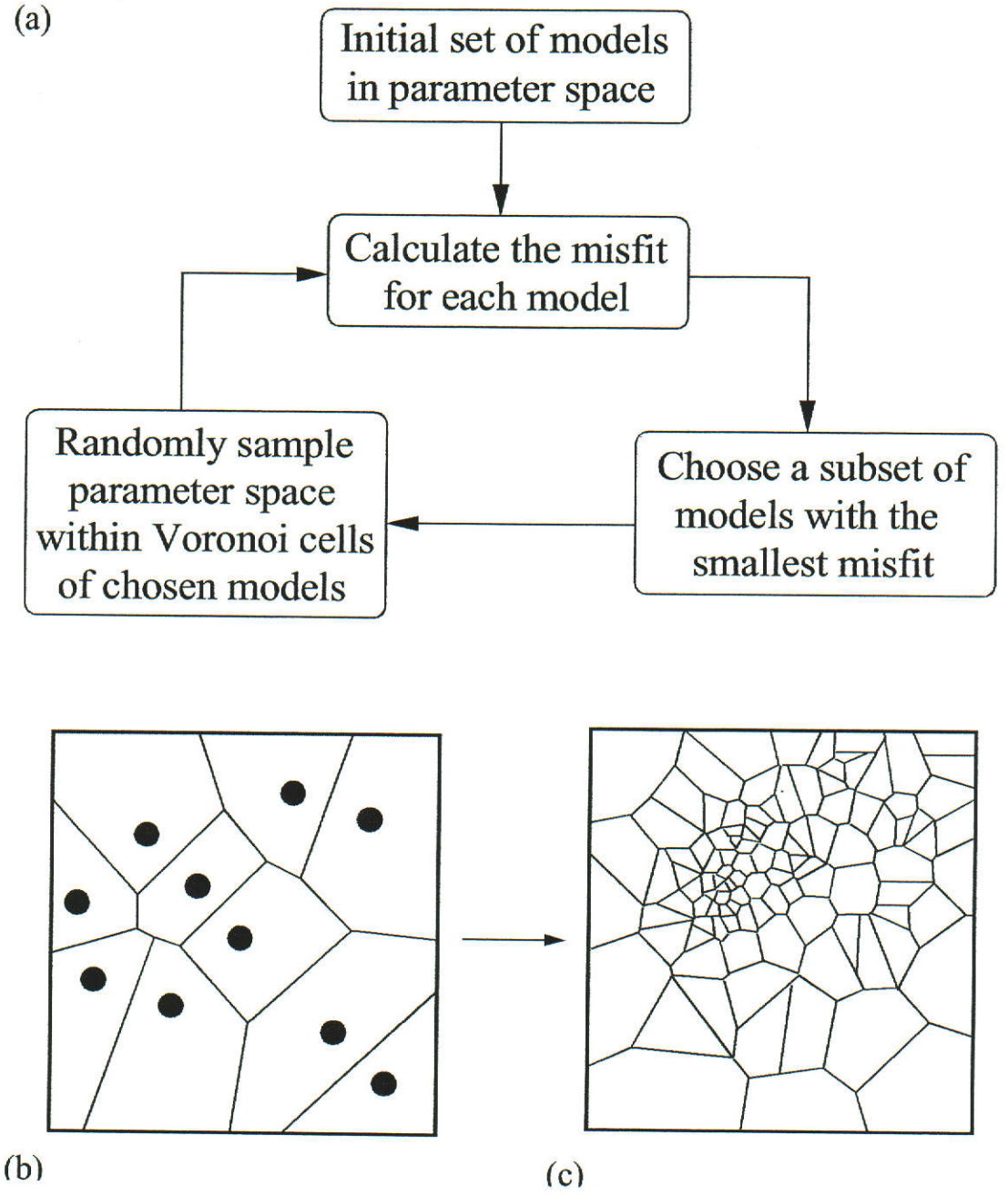
(a)
Initial set of models in parameter space
Calculate the misfit for each model
Choose a subset of models with the smallest misfit
Randomly sample parameter space within Voronoi cells of chosen models
(b)
(c)

Figure 9:

28 January 2001 (Mw 5.7)

Strike = 96 – Dip = 48 – Rake = 107 – Depth = 9

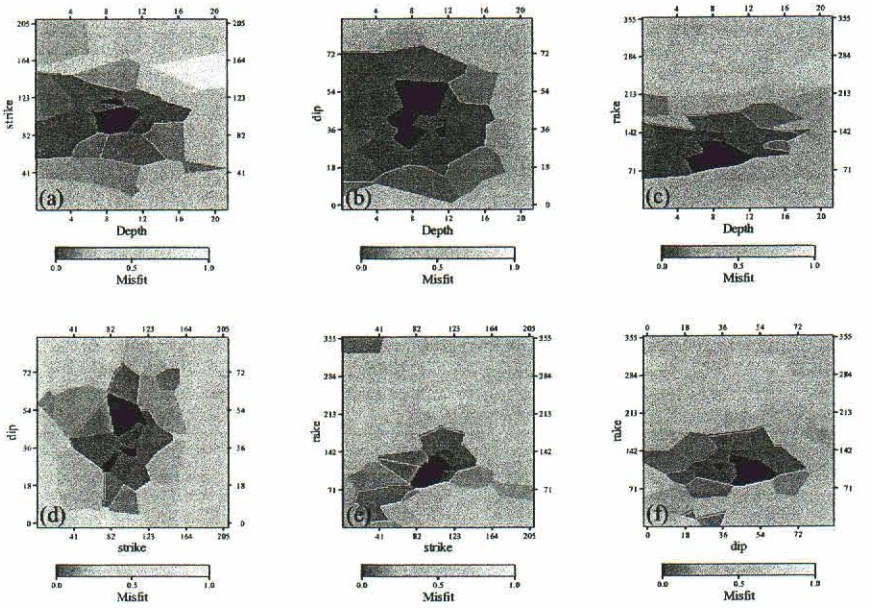

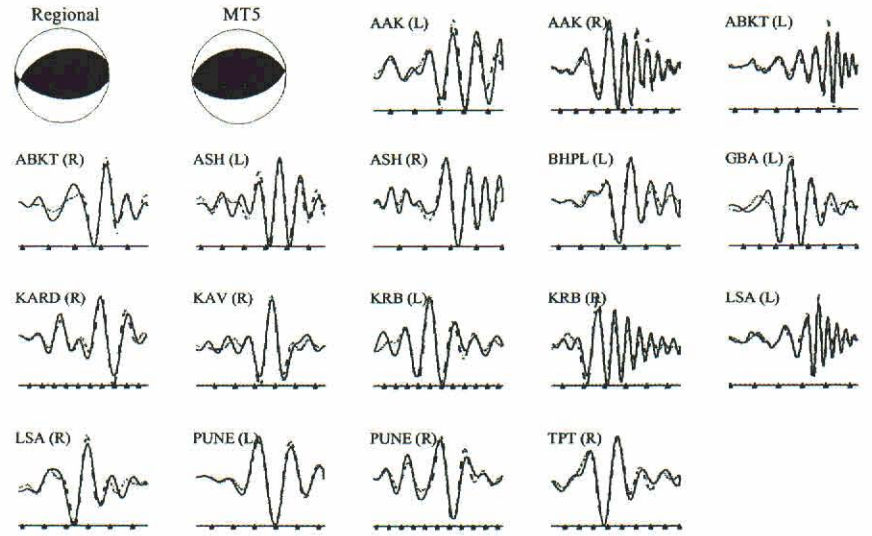

Figure 10:

27 January 2001 (Mw 5.2)

Strike = 104 – Dip = 39 – Rake = 105 – Depth = 13

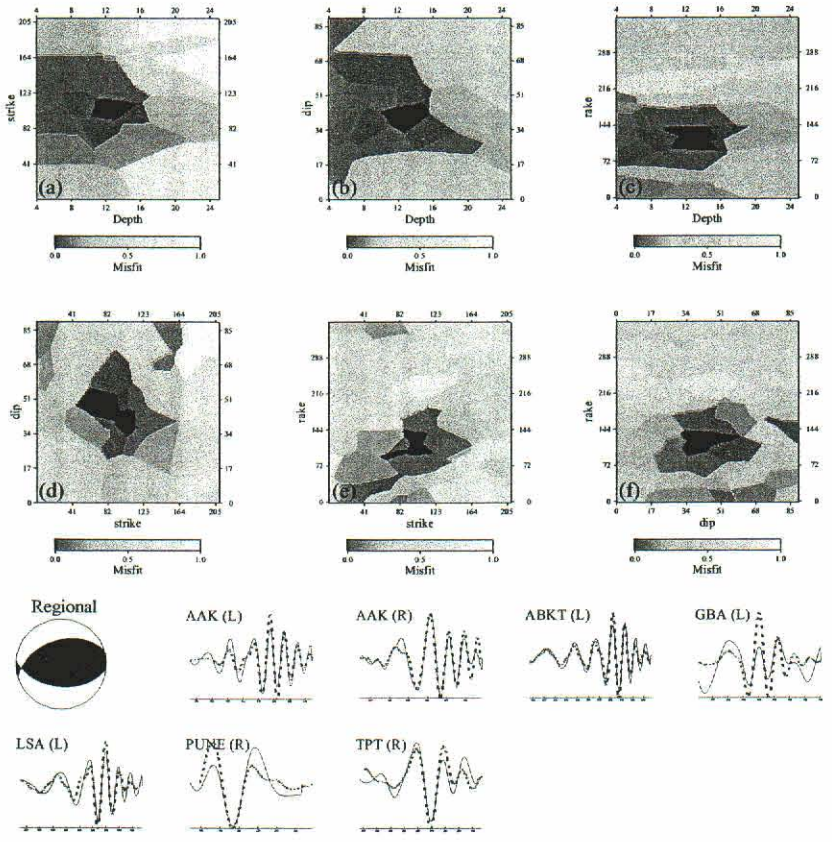

Figure 11:

3 February 2001 (Mw 5.1)

Strike = 127 – Dip = 33 – Rake = 56 – Depth = 1

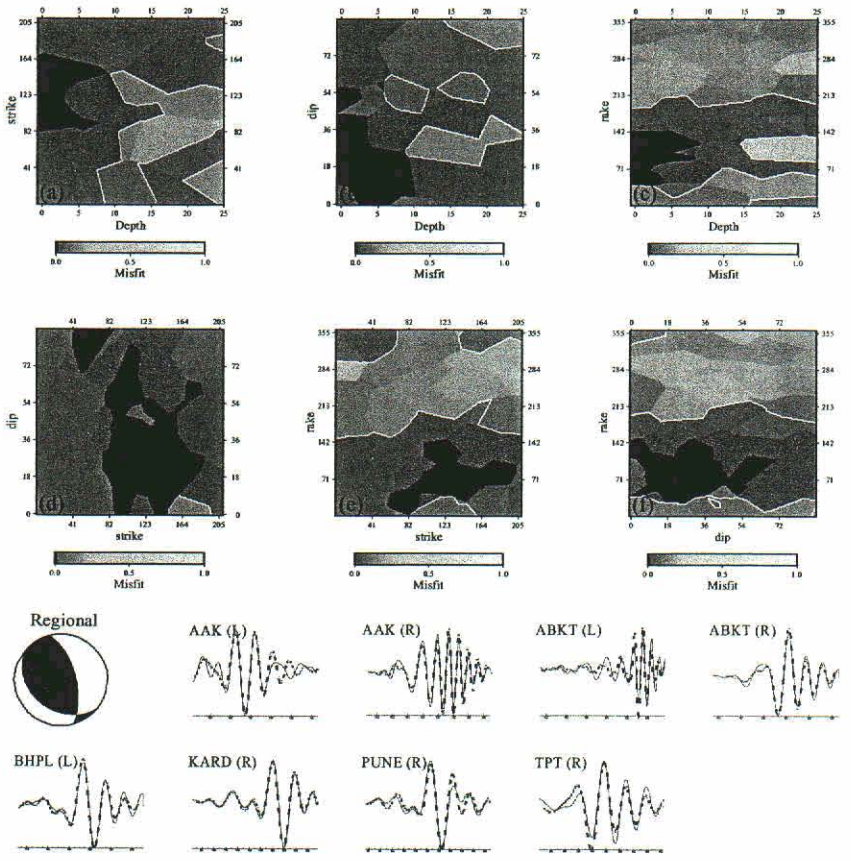

Figure 12:

8 February 2001 (Mw 5.2)

Strike = 141 – Dip = 65 – Rake = 167 – Depth = 5

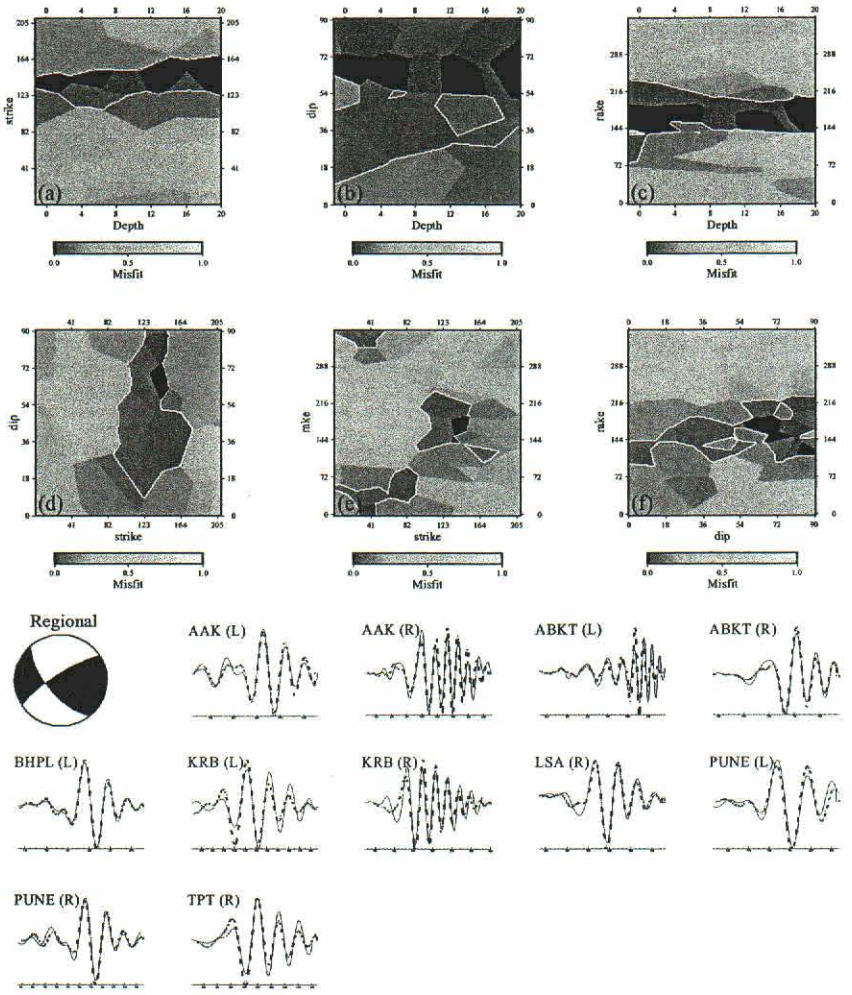

Figure 13:

19 February 2001 (Mw 5.2)

Strike = 4 – Dip = 28 – Rake = 136 – Depth = 4

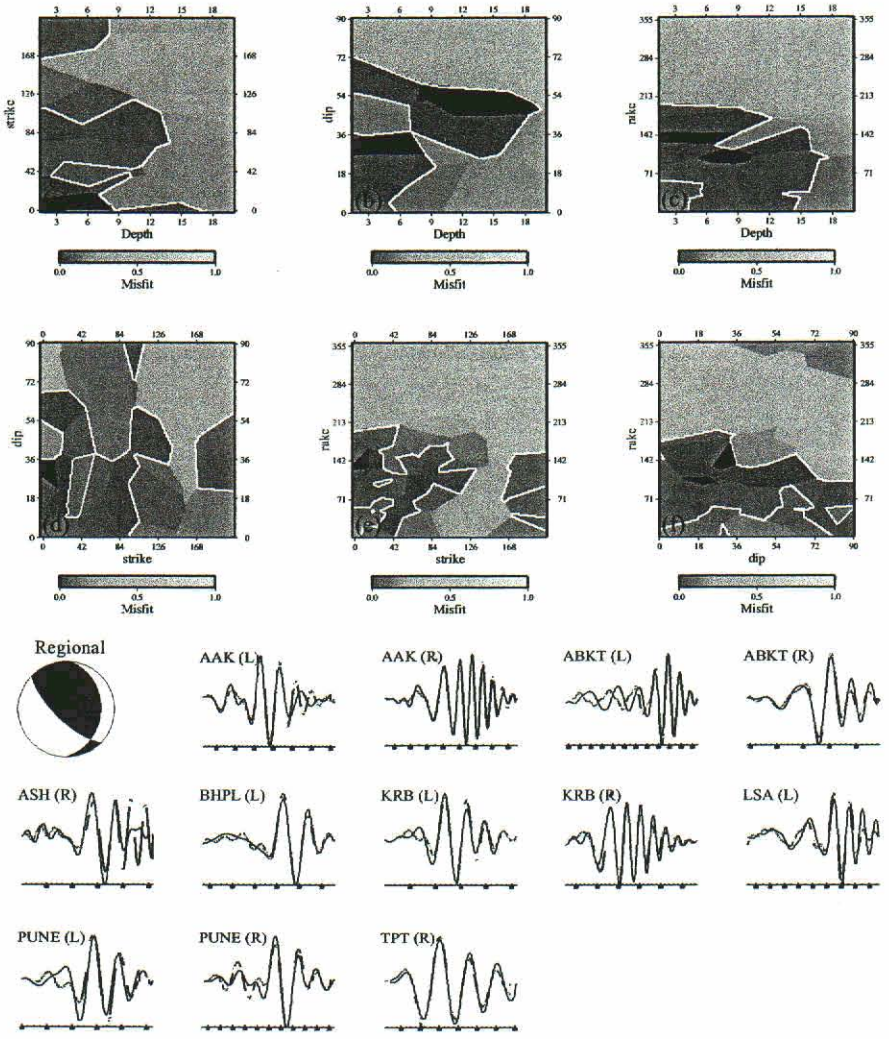

Figure 14:

19 February 2001 (Mw 5.2)

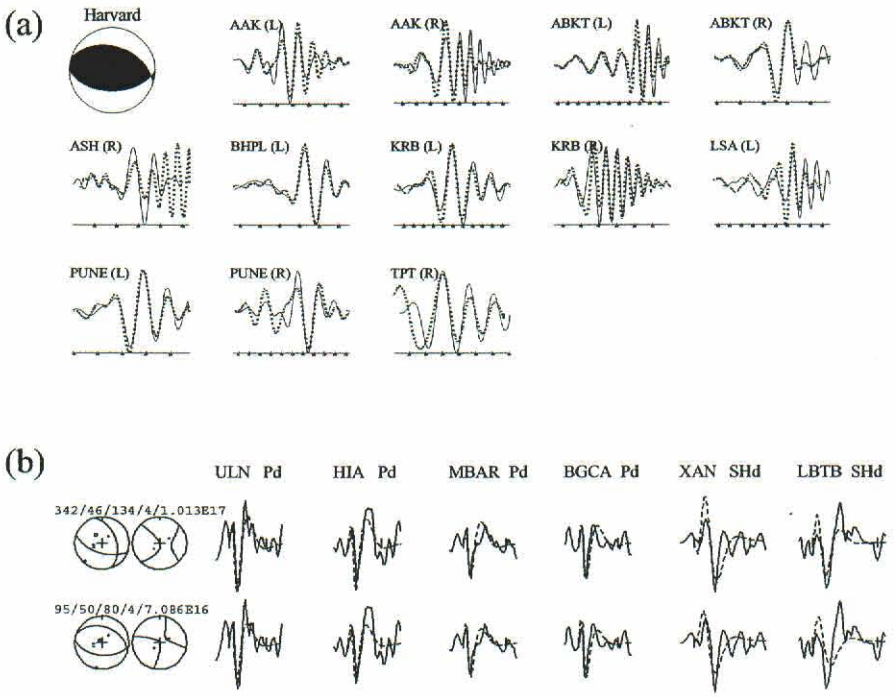

Figure 15:

4 March 2001 (Mw 5.0)

Strike = 36 – Dip = 86 – Rake = 332 – Depth = 11

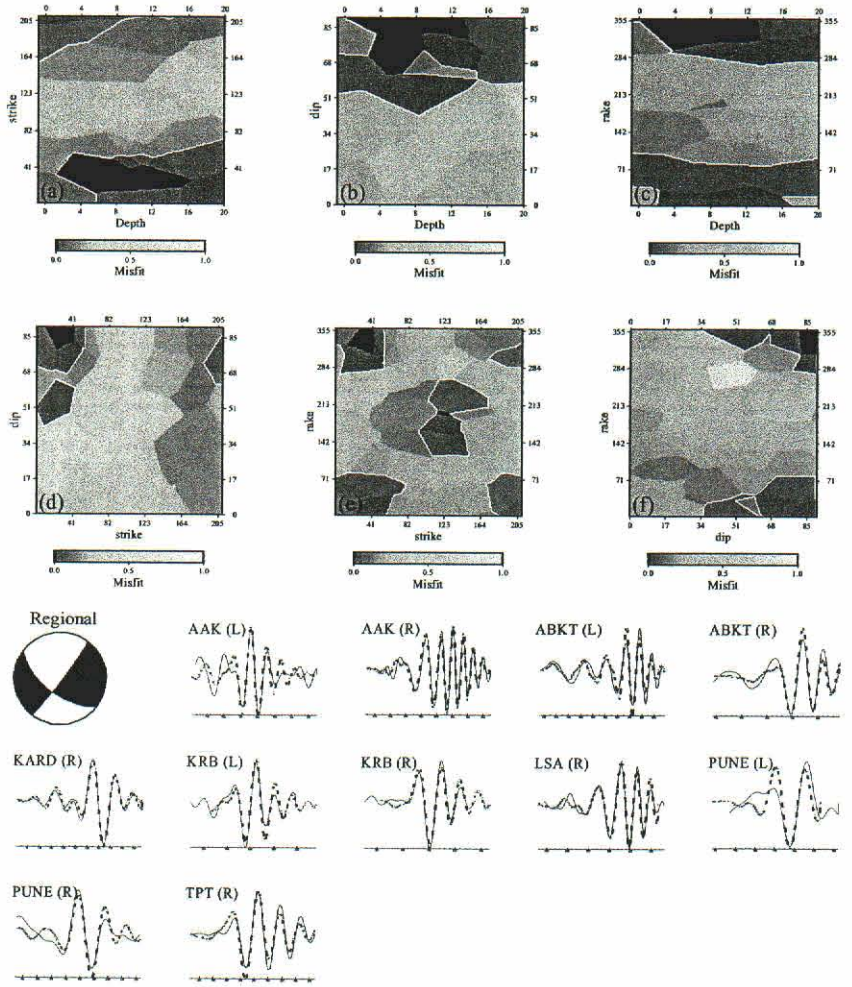

Figure 16:

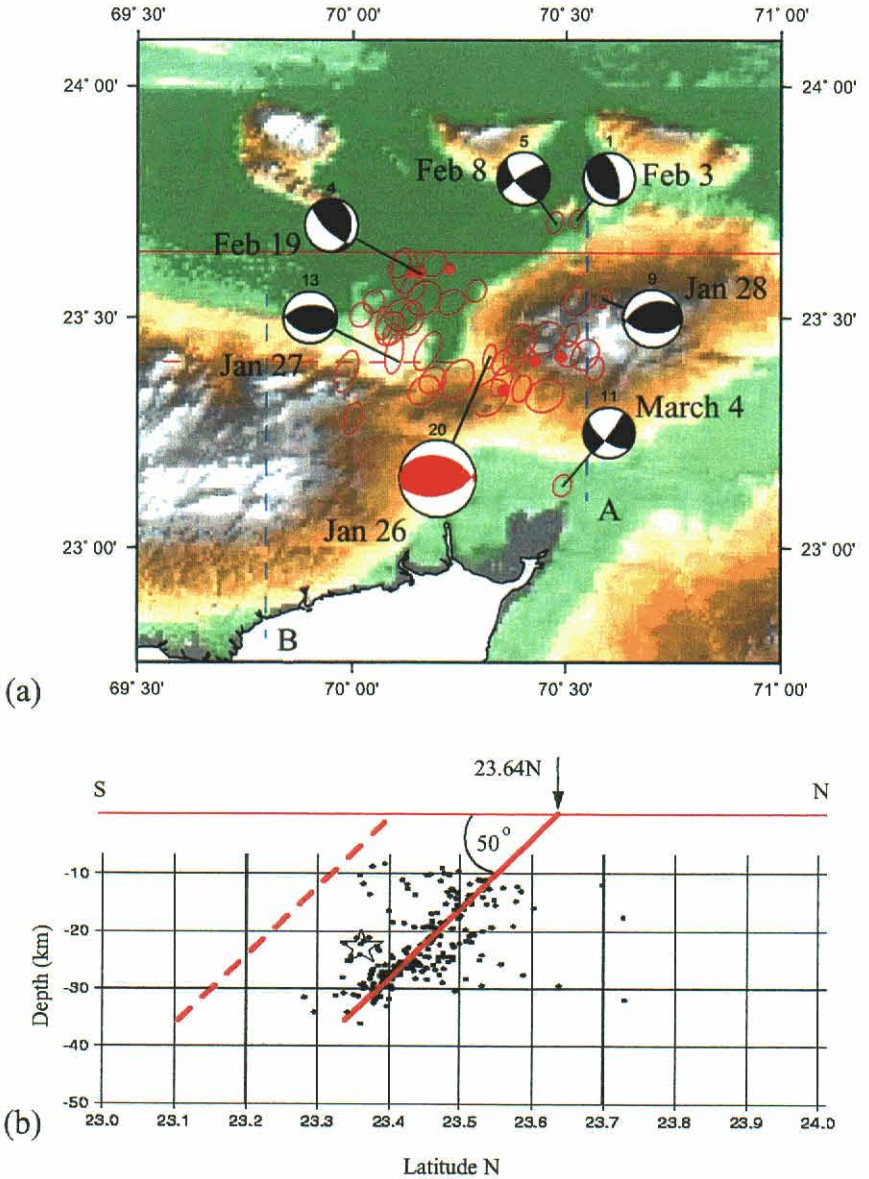
69° 30'
70° 00'
70° 30'
71° 00'
24° 00'
23° 30'
23° 00'
Feb 8
Feb 3
Feb 19
Jan 28
Jan 27
March 4
Jan 26
A
B
(a)
23.64N
S
N
50°
Depth (km)
-10
-20
-30
-40
-50
23.0
23.1
23.2
23.3
23.4
23.5
23.6
23.7
23.8
23.9
24.0
Latitude N
(b)

Figure 17:

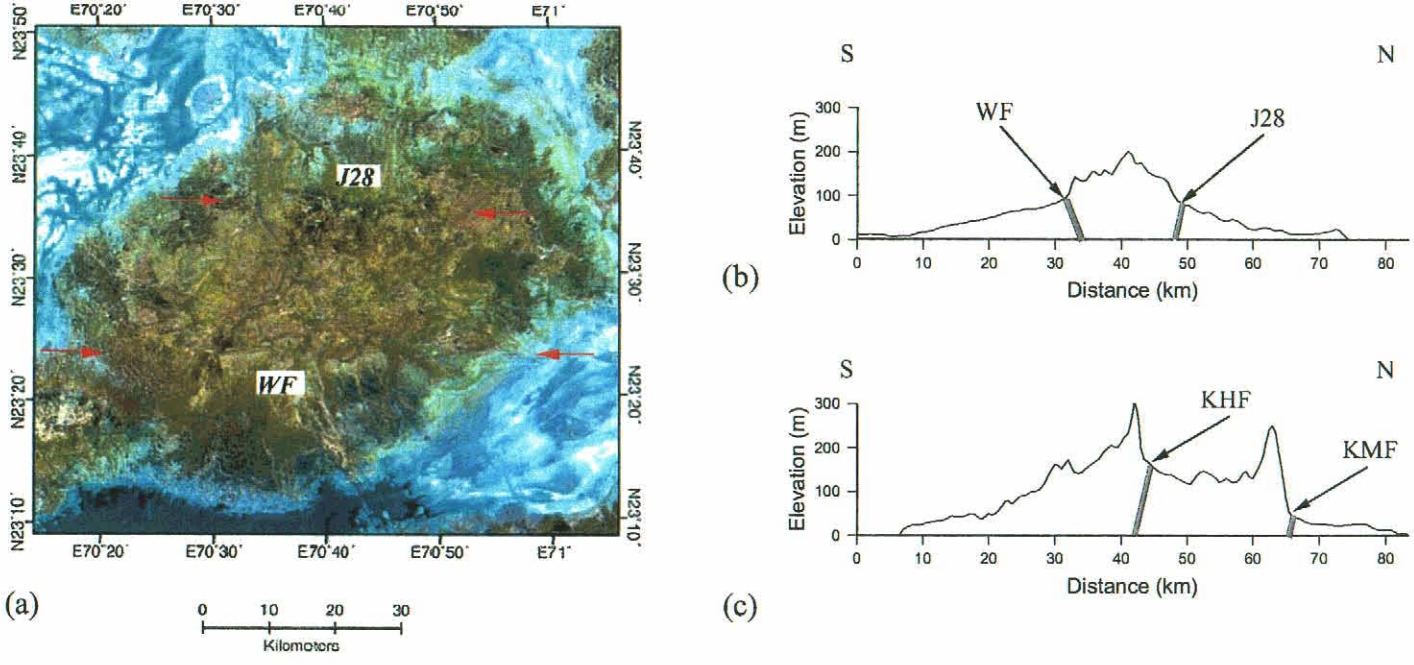
E70°20'
E70°30'
E70°40'
E70°50'
E71°
N23°50'
N23°40'
N23°30'
N23°20'
N23°10'
J28
WF
0 10 20 30
Kilometers
(a)
S
N
WF
J28
Elevation (m)
Distance (km)
(b)
S
N
KHF
KMF
Elevation (m)
Distance (km)
(c)

Figure 18:

Crustal shear velocity structure of the south Indian shield

S. S. Rai,[1] Keith Priestley,[2] K. Suryaprakasam,[1] D. Srinagesh,[1] V. K. Gaur,[3,4] and Z. Du[5]

Received 21 January 2002; revised 2 August 2002; accepted 30 October 2002; published 11 February 2003.

[1] The south Indian shield is a collage of Precambrian terrains gathered around and in part derived from the Archean-age Dharwar craton. We operated seven broadband seismographs on the shield along a N-S corridor from Nanded (NND) to Bangalore (BGL) and used data from these to determine the seismic characteristics of this part of the shield. Surface wave dispersion and receiver function data from these sites and the Geoscope station at Hyderabad (HYB) give the shear wave velocity structure of the crust along this 600 km long transect. Inversion of Rayleigh wave phase velocity measured along the profile shows that the crust has an average thickness of 35 km and consists of a 3.66 km s^{-1}, 12 km thick layer overlying a 3.81 km s^{-1}, 23 km thick lower crust. At all sites, the receiver functions are extremely simple, indicating that the crust beneath each site is also simple with no significant intracrustal discontinuities. Joint inversion of the receiver function and surface wave phase velocity data shows the seismic characteristics of this part of the Dharwar crust to be remarkably uniform throughout and that it varies within fairly narrow bounds: crustal thickness (35 ± 2 km), average shear wave speed (3.79 ± 0.09 km s^{-1}), and V_p/V_s ratio (1.746 ± 0.014). There is no evidence for a high velocity basal layer in the receiver function crustal images of the central Dharwar craton, suggesting that there is no seismically distinct layer of mafic cumulates overlying the Moho and implying that the base of the Dharwar crust has remained fairly refractory since its cratonization. *INDEX TERMS:* 7203 Seismology: Body wave propagation; 7205 Seismology: Continental crust (1242); 7255 Seismology: Surface waves and free oscillations; *KEYWORDS:* continental crust, Archean crust, receiver function, Indian shield

Citation: Rai, S. S., K. Priestley, K. Suryaprakasam, D. Srinagesh, V. K. Gaur, and Z. Du, Crustal shear velocity structure of the south Indian shield, *J. Geophys. Res.*, *108*(B2), 2088, doi:10.1029/2002JB001776, 2003.

1. Introduction

[2] Precambrian shields and platforms account for ~70% of the continental crust. The seismic characteristics of these regions provide insightful clues for discriminating between various contending hypotheses of crustal growth, whether by steady state or by evolutionary processes governed by the thermal history of the mantle. Three specific crustal seismic parameters provide strong constraints to be imposed on models of crustal evolution: (1) the thickness of the crust; that is, depth to the seismic Mohorovicic discontinuity, (2) the presence or absence of a basal cumulate layer in which the shear velocity increases from about 4.0 to 4.35 km s^{-1} and, if present, its thickness, and (3) the Poisson's ratio σ or V_p/V_s of the crust. Knowledge of the lateral variation of these three properties provides critical input for modeling seismic wave propagation in the crustal waveguide, which has strong influence on quantification of regional seismic hazards and of the source characteristics of earthquakes.

[3] In this study, we discuss the results of an experiment designed to determine the shear velocity structure and thickness of the crust beneath a 600 km long N-S transect of the relatively poorly studied south Indian shield, a collage of Precambrian terrains gathered around and in part derived from the Archean-age Dharwar craton (Figure 1). A large expanse of the northern Dharwar craton lies buried beneath the cover of Deccan flood basalts (65 Ma); elsewhere, the south Indian shield is dominated by the ubiquitous Peninsular Gneisses (3.3–2.6 Ga) that surround and separate the shield's variegated components, including some of its oldest relics (3.6 Ga) of migmatitic and gneissic rocks. The Closepet granite, which evolved by anatexis of its host, divides the Dharwar craton longitudinally. To the south, the rocks of the south Indian shield pass through a narrow gradational zone and into the high-grade granulites of late Archean metamorphism (2.6 Ga). Further south, across the Noyil-Kaveri shear zone (Figure 1), the high-grade granulites are joined to the metamorphic terrains of Pan African orogeny. The latter cover the entire southern peninsula, alternately exposing a migmatitic complex and the granulite massifs of Palni, Kodaikanal, and Periyakulum as well as

[1]National Geophysical Research Institute, Hyderabad, India.
[2]Bullard Laboratories, University of Cambridge, Cambridge, United Kingdom.
[3]Centre for Mathematical Modeling and Computer Simulation, Bangalore, India.
[4]Indian Institute of Astrophysics, Bangalore, India.
[5]Institute of Theoretical Geophysics, University of Cambridge, Cambridge, United Kingdom.

0148-0227/03/2002JB001776$09.00

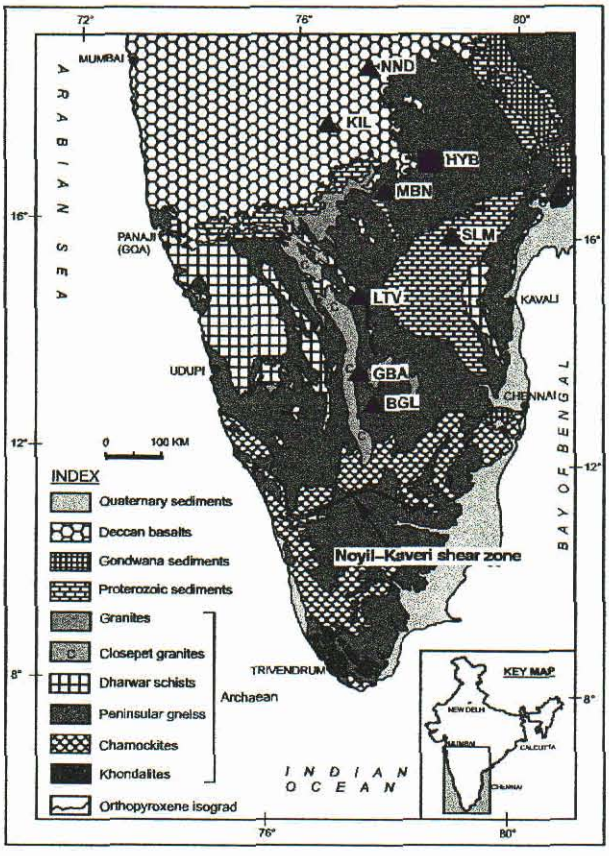

Figure 1. Principle geologic units of the south Indian shield. The seven sites with broadband seismographs operated by NGRI and the Indian Institute of Astrophysics, jointly with the University of Cambridge, are designated by solid triangles. The location of the Geoscope station at Hyderabad is denoted by the solid square.

intrusives, of which the Proterozoic alkaline complex of Sivamalai is the most prominent.

[4] Little research has been done on the seismic structure of the south Indian shield. *Dube et al.* [1973] analyzed travel times of crustal phases from aftershocks of the 1967 m_b 6.7 Koyna earthquake and inferred from these a two-layer crust consisting of a 20 km thick granitic layer (V_p 5.78 km s^{-1}, V_s 3.42 km s^{-1}), a 18.7 km thick basaltic lower crust (V_p 6.58 km s^{-1}, V_s 3.92 km s^{-1}) and a P_n and S_n velocity of 8.19 and 4.62 km s^{-1}, respectively. Our transect, which will be discussed below, is crossed about midway by the 600 km long ENE-WSW refraction seismic profile [*Kaila and Krishna*, 1992] from Kavali on the east coast to Uduppi on the west coast (Figure 1). These refraction data show an upper crust with P wave velocity of 6.4 km s^{-1}, a Moho depth varying from 34 km in the east to 41 km in the west, and high P_n velocities of 8.4–8.6 km s^{-1}.

[5] Crustal structure in the vicinity of Gauribidnaur (GBA) (Figure 1) near the southern end of our transect is discussed by *Krishna and Ramesh* [2000] who inverted the seismic wave field from mine tremors and explosions recorded on the GBA short period vertical seismograph array. They interpreted the group velocity and coda lengths of the seismograms as indicating a laminated upper crustal waveguide at 5–15 km depth. They find the Moho depth beneath GBA to be 34–36 km, the P_n velocity to be 8.2 km s^{-1}, and a value of 0.24 (V_p/V_s = 1.71) for the Poisson's ratio just below the Moho. *Krishna et al.* [1999] analyzed travel times and waveforms of aftershocks of the Latur earthquake to determine a 1-D, P and S wave crustal model near KIL (Figure 1). Their model contains alternating low velocity layers (~7% velocity reduction) for both P and S waves in the upper crust at depths between 6.5–9.0 and 12.3–14.5 km and a lower crustal low velocity layer at 24–26 km depth. The arrival times of S_mS phases (the S wave reflection from the Moho) indicated a Moho depth of 35–37 km, while the Poisson's ratio was found to be 0.21 (V_p/V_s = 1.65) for the upper crust and 0.226 (V_p/V_s = 1.68) for the lower crust.

[6] Little is known about the S wave structure of the south Indian shield. *Gaur and Priestley* [1997] used receiver function analysis of 11 events with the highest signal-to-noise ratio occurring in two compact clusters during the period 1989–1996 to determine the shear wave structure of the crust beneath the Geoscope station at Hyderabad (HYB) (Figure 1). Their study showed that the crust beneath the HYB granites is quite simple, possesses a thickness of 36 ± 1 km, and consists of a 10 km thick upper layer in which the shear velocity is 3.54 ± 0.07 km s^{-1} underlain by a 26 ± 1 km thick lower crust in which the shear wave velocity varies uniformly with a small gradient of 0.02 s^{-1}. The shear wave velocity at the base is 4.1 ± 0.1 km s^{-1} just above the Moho transition zone, which is constrained to be less than 4 km thick and overlies a 4.74 ± 0.1 km s^{-1} half-space. *Saul et al.* [2000] used a data set of 297 events recorded at HYB and confirmed these basic findings: a seismically transparent crust beneath HYB and a shallow Moho (33 ± 2 km). *Zhou et al.* [2000] also analyzed HYB broadband data from 38 events by constraining the shear wave velocity in the crust from a joint analysis of receiver function and Rayleigh wave dispersion measured over a broad region of India by *Hwang and Mitchell* [1987] and *Bhattacharya* [1992]. Their analysis also indicates a low average shear velocity for the HYB crust (3.58 ± 0.01 km s^{-1}), a shallow Moho (32 ± 2 km), and a Poisson's ratio of 0.26 ± 0.01. *Singh et al.* [1999] measured group velocity dispersion from seismograms of the 1997 Jabalpur earthquake at several stations on the Indian shield. Inversion of the group velocity data gave an average crustal model consisting of a two-layer crust (H_1 13.8 km, V_{p1} 5.68 km s^{-1}, V_{s1} 3.55 km s^{-1}; H_2 24.9 km, V_{p2} 6.16 km s^{-1}, V_{s2} 3.85 km s^{-1}) overlying an upper mantle with V_{pn} 8.01 km s^{-1} and V_{sn} 4.65 km s^{-1}. *Kumar et al.* [2001] find a crustal thickness of 36.5 km, average shear velocity of 3.7 km s^{-1} and Poisson's ratio of 0.26 at two sites on the Deccan basalt flows to the west of HYB. At these sites, the Deccan basalts are likely to form a thin veneer overlying rocks of the west Dharwar craton.

2. Data and Methodology

[7] In this study we examine the crustal shear wave structure of the south Indian shield along a 600 km long N-S transect from Nanded (NND) in the north to Bangalore (BGL) in the south (Figure 1). This transect lies along the

Table 1. Surface Wave Analysis Summary

Date	Origin Time (UTC)	Latitude (°N)	Longitude (°E)	Full Profile	North Section	South Section
1999/01/16	1044:39.4	56.2	−147.4		NND–KIL (9.0)[a]	SLM–GBA (6.5) SLM–BGL (1.0)
1999/01/24	0037:04.6	30.6	131.1			SLM–LTV (9.5)
1999/01/24	0800:08.5	−26.5	74.5	HYB–BGL (7.0)		
1999/01/28	0810:05.4	52.9	−169.1		NND–KIL (1.0)	SLM–GBA (3.5)
1999/02/01	1635:31.1	−6.5	104.7		SLM–KIL (2.5)	
1999/02/03	0635:56.6	−6.2	104.2		SLM–KIL (2.0)	
1999/03/20	1047:45.9	51.6	−177.7			SLM–GBA (6.5)
1999/03/21	1616:02.2	55.9	110.2		NND–KIL (6.0)	SLM–GBA (6.5)
1999/03/28	1905:11.0	30.5	79.4	BGL–NND (8.5) GBA–LTV (10.0) GBA–NND (7.5)		
1999/08/01	1247:50.1	51.5	−176.3		NND–KIL (4.5)	
1999/12/29	0519:46.9	18.2	−101.4		NND–MBN (7.5)	LTV–BGL (6.5)

[a]Numbers in brackets following the two station pairs used for the interstation phase velocity measurement denote the difference in azimuth between the great circle path joining the stations and the great circle path joining the stations and the epicenter.

western boundary of the eastern Dharwar craton and approximately parallels the Closepet granitic intrusion. We deployed seven broadband digital seismographs (Figure 1) along this profile and operated these stations for about 15–18 months. Stations BGL, GBA, LTV, and MNB all lie on Archean crystalline outcrops of the Dharwar craton; KIL and NND lie on a thin veneer of Deccan basalt flow (~350 m) below which lie rocks of the Dharwar craton; and SLM is situated on the northeastern part of the Cuddappah Basin. Seismograms from these seven sites and from the Geoscope station at HYB (Figure 1) provide the data for our study. We analyze teleseismic receiver functions and surface wave phase velocity from these data to constrain the average crustal shear wave velocity, the Moho depth, the V_p/V_s ratio of the crust, the velocity gradient in the crust–mantle transition zone and Moho sharpness beneath this part of the south Indian shield.

2.1. Surface Wave Dispersion Analysis

[8] Crustal structure has previously been determined at three points along the NND–BGL transect (Figure 1): near KIL [*Krishna et al.*, 1999], near GBA [*Krishna and Ramesh*, 2000], and between GBA and LTV [*Kaila and Krishna*, 1992]. All show a similar crustal thickness of ~35 km but indicate a possible small increase in average P wave speed for the crust from ~6.4 km s^{-1} in the south to ~6.5 km s^{-1} in the north. We first measure the short period (15–35 s) fundamental mode Rayleigh wave phase velocity and invert these dispersion data to determine the average shear wave velocity of the crust beneath the transect.

[9] We measure two-station fundamental mode Rayleigh wave phase velocity from eleven events nearly aligned along the same great circle path (<10°) as station pairs (Table 1), using the transfer function method of *Gomberg et al.* [1988]. This method poses the problem of phase velocity determination as a linear filter estimation problem in which the seismogram at a more distant station from an event is considered the convolution of the seismogram at a close station with the Earth filter (the dispersion curve), which is to be determined. Smoothness constraints are imposed based on an approximate knowledge of the group velocity. We used the results of *Bhattacharya* [1992] as an initial dispersion model. To ensure that the starting dispersion curve was appropriate, we tested a number of variations of the initial dispersion models and smoothing criteria. We determined dispersion curves for the full length of the transect and, separately, curves for the northern (KIL–SLM) and southern (SLM–BGL) halves of the transect. We inverted the dispersion along the transect to provide an average crustal model which could be used as the starting model for the receiver function inversion; we used the dispersion measured for the halves of the profile in the joint receiver function–phase velocity inversion. The dispersion curves were determined simultaneously from multiple station pairs, but we also calculated dispersion curves for all individual two-station paths separately to verify that there were no large outliers among the various two-station combinations.

[10] We invert the Rayleigh wave phase velocity measured along the full transect using the stochastic least squares routine of *Hermann* [1994]. This expresses the least squares problem in terms of eigenvalues and eigenvectors and uses singular value decomposition to invert the matrix giving the solution vector, the variance–covariance matrix, and the resolution matrix. The starting model for the inversion is from the average crustal model for the Indian shield of *Singh et al.* [1999] and the 4.72 km s^{-1} S_n velocity measurement of *Huestis et al.* [1973]. The starting model has been parameterized in terms of 2 km thick layers over a half-space upper mantle. After the initial inversion, adjacent thin layers with nearly the same velocities were grouped into thicker layers, resulting in a coarser model; we repeat the inversion to find the minimum number of crustal parameters which explain the observed dispersion. The final inversion model (Figure 2b) and the fit of the dispersion curve for this model to the observed dispersion (Figure 2a) show that the average crustal structure beneath the profile consists of two layers: an upper 12 km thick layer with V_s 3.65 km s^{-1}, and a lower 23 km thick layer with V_s 3.81 km s^{-1}, overlying an upper mantle with S_n velocity 4.61 km s^{-1}.

2.2. Receiver Function Analysis

[11] The teleseismic P wave coda contains S waves generated by P-to-S conversions at significant velocity contrasts in the crust and upper mantle below the seismograph site. Receiver functions are radial and transverse waveforms created by deconvolving the vertical component from the radial and transverse components of the seismogram to isolate the receiver site effects from the other

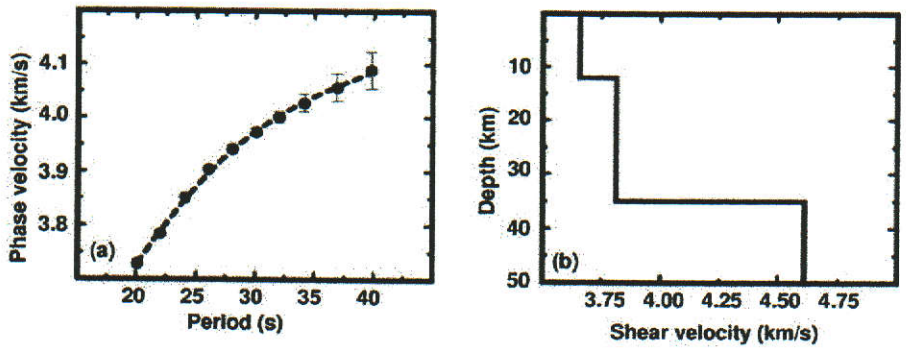

Figure 2. (a) Average fundamental mode Rayleigh wave phase velocity curves measured along the N-S transect. (b) Two layer crustal model from inversion of the Rayleigh wave dispersion data.

information contained in a teleseismic *P* wave. The use of receiver functions to determine crust and upper mantle velocity structure beneath three-component broadband seismographs is now a well-established seismological technique; various approaches for interpreting receiver functions have been discussed in the literature [*Owens et al.*, 1984; *Priestley et al.*, 1988; *Zandt et al.*, 1995; *Sheehan et al.*, 1995; *Zhu and Kanamori*, 2000]. We follow the procedure of *Ammon et al.* [1990] and compute true amplitude radial and tangential receiver functions [*Ammon*, 1991] and low-pass filter these at 1.2 Hz. The resulting receiver functions consist of wavelengths greater than 5–6 km; therefore, the minimum resolvable model layer thickness is approximately 2–3 km.

[12] Those receiver functions whose averaging functions [*Ammon*, 1991] resembled a narrow Gaussian pulse and which emanated in a limited back azimuth and epicentral distance range were stacked, and the ±1 standard deviation (σ) bounds calculated. These bounds were used to evaluate how well particular phases of the waveform are determined. We obtain a shear wave crustal model using the linearized inversion procedure of *Ammon et al.* [1990] as modified to include the joint surface wave phase velocity constraint [*Du and Foulger*, 1999]. A starting model is parameterized as a stack of thin horizontal layers to a depth of 60 km. The *S* wave velocity is the free parameter in the inversion, the *P* wave velocity is set assuming a Poisson's ratio of 0.25 and the layer thicknesses are fixed. The radial receiver function is inverted by minimizing the difference between the observed receiver function and synthetic receiver functions computed from the model, while simultaneously constraining the model smoothness.

[13] We illustrate the details of our analysis procedure using the data from BGL and then summarize the results for the remaining sites. BGL is situated on the western edge of the eastern Dharwar craton close to its contact with the Closepet granitic intrusion (Figure 1). An important assumption in the receiver function analysis procedure we employ is that the crustal structure is laterally homogeneous beneath the seismograph site. The validity of this assumption can be checked by examining the azimuthal variation in the *Ps* phase and the amplitude of any arrivals in the tangential receiver function which should be zero for flat-lying, isotropic layers. Figure 3 shows BGL receiver functions for a range of back azimuths. The eastern quadrant is well sampled, but there is only one event from the west. The small variation in the *Ps* converted phase (4.2 ± 0.1) and the small amplitude of the tangential receiver function relative to the amplitude of the radial receiver function justify modeling the crust beneath BGL as 1-D.

[14] Figure 4 shows one of the receiver function stacks for BGL, consisting of 10 events (Δ 76 ± 7° and back azimuth 99 ± 3°). The receiver function stack shows a large amplitude positive arrival at ~4 s followed by a prominent positive arrival at ~14 s and a negative arrival at 16–18 s. We identify these as the *Ps*, PpS_ms + PsP_ms and arrivals, respectively. The *Ps* arrival is a prominent phase in all of the

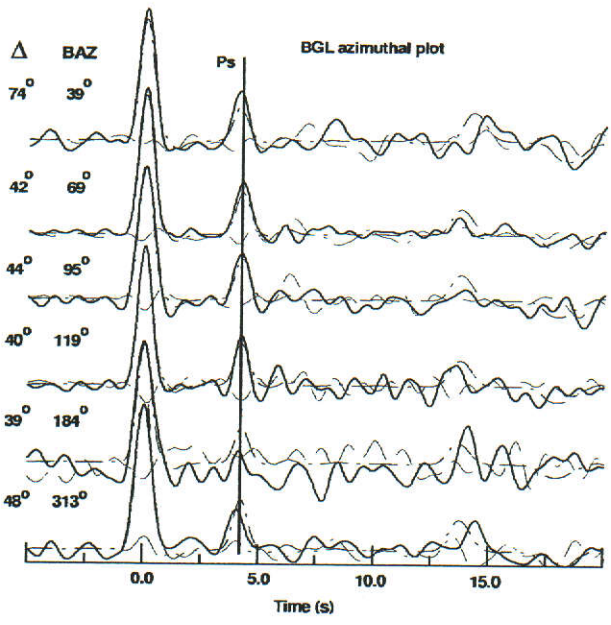

Figure 3. BGL receiver functions as a function of back azimuth. The numbers to the left of the direct *P* wave arrival are the epicentral distance and the back azimuth in degrees, respectively. The solid line denotes the radial receiver function, the dashed line the tangential receiver function, and the dash-dot line the theoretical receiver function computed for the BGL crustal model derived from the joint receiver function–surface wave dispersion inversion.

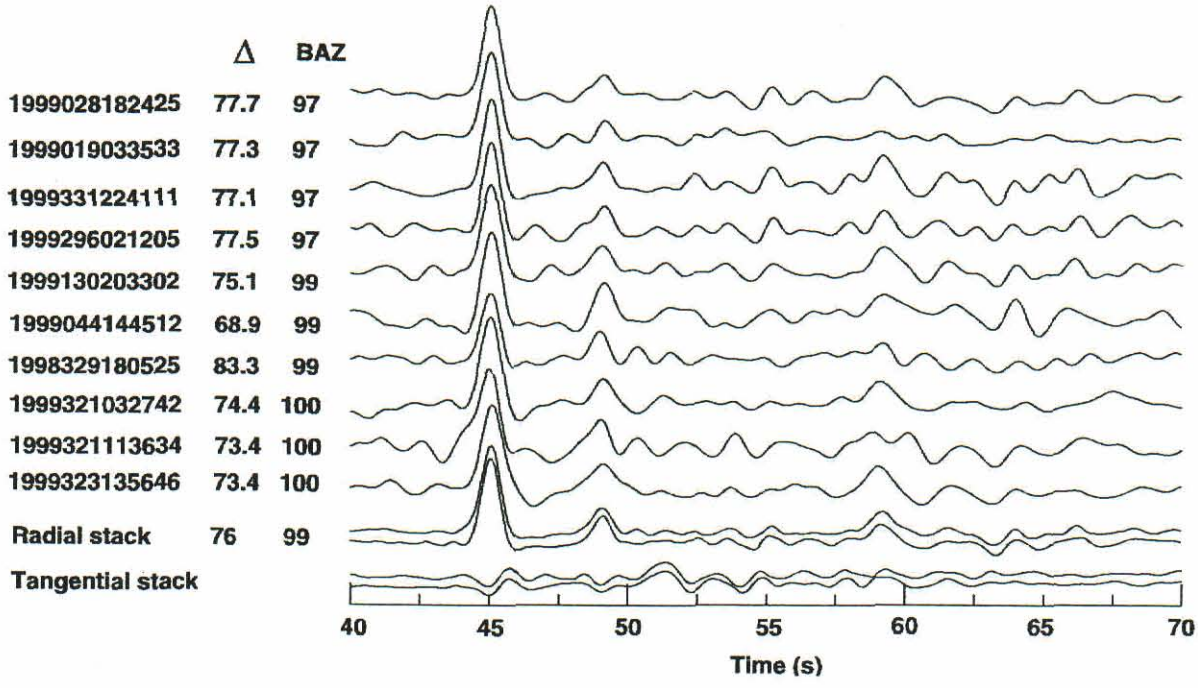

Figure 4. BGL receiver function stack Δ 76°, back azimuth 99° cluster. Individual event receiver functions are shown above the receiver function stack (±1 standard deviation bounds) at the bottom. The number to the left of the direct arrivals is the event designation, the epicentral distance in degrees and the back azimuth in degrees for the individual events, and the average distance and back azimuth of the stack.

individual receiver functions (Figure 4). There are no arrivals in the receiver function which suggest either a significant low velocity zone or interfaces within the crust. Below the radial stack is the stacked tangential receiver function; amplitudes of the tangential arrivals are small in comparison to those of the radial arrivals.

[15] Crustal thickness H and V_p/V_s can be estimated from the relative timing of the conversions and reverberations [*Zandt et al.*, 1995; *Zhu and Kanamori*, 2000]. The $Ps - Pp$ time difference depends on the average V_p/V_s ratio of the crust and the crustal thickness. The $PpP_ms - Ps$ time is the two-way P wave travel time and the $\{PpP_ms + PsP_ms\} - Pp$ time is the two-way S wave travel time through the crust. The ratio of the $Ps - Pp$ to $PpP_ms - Ps$ time is independent of crustal thickness but weakly dependent on V_p; the ratio of the $PpP_ms - Ps$ to $\{PpP_ms + PsP_ms\} - Pp$ time is proportional to the V_p/V_s ratio and independent of crustal thickness. The crustal reverberations are prominent in some of the stacked receiver functions and apparent in some of the individual receiver functions. We measure H and V_p/V_s using the stacking procedure of *Zhu and Kanamori* [2000] with the Ps, PpP_ms and $PpP_ms + PsP_ms$ phases being weighted 0.7, 0.2, and 0.1, respectively. The values in Figure 5 and Table 2 are estimated using the P wave speed of 6.45 km s^{-1}, the average P wave velocity of the crust measured by refraction profiling in the vicinity of our transect [*Kaila and Krishna*, 1992; *Krishna et al.*, 1999; *Krishna and Ramesh*, 2000].

[16] The details of the crustal structure beneath BGL are determined from inversion of the receiver function stacks. The average crustal model from the surface wave analysis discussed above was used as the starting velocity model in the inversion. Receiver function inversions are sensitive to the velocity–depth product but contain weak information on velocity. Inversion of receiver function data with no other

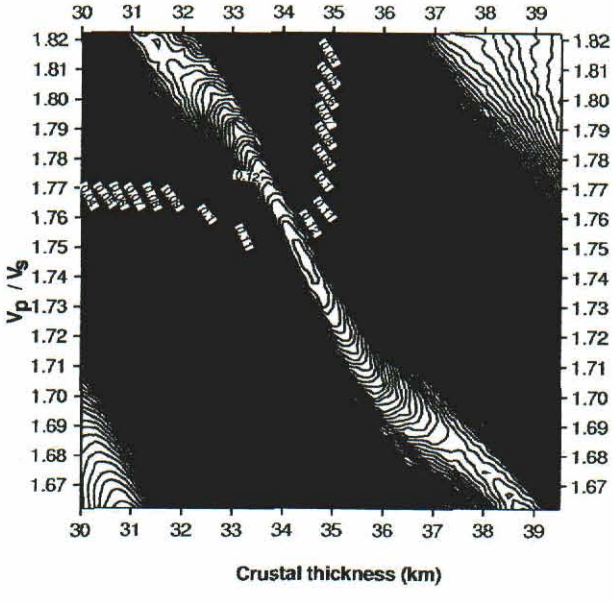

Figure 5. The V_p/V_s ratio versus crustal H stack for station BGL. The best estimate of V_p/V_s is 1.741 and for H is 34.7 km.

Table 2. Station Data

Station	Latitude (°N)	Longitude (°E)	N	P_s (s)	H^a (km)	$V_p/V_s{}^a$	H^b (km)	$\langle V_s \rangle^b$ (km s^{-1})
BGL	13.021	77.570	48	4.2	34.7±1.5	1.741 ± 0.038	35 ± 2.0	3.74
GBA	13.564	77.357	57	4.3	34.5 ± 1.1	1.748 ± 0.031	36 ± 2.0	3.75
LTV	14.926	77.280	23	4.2	34.4 ± 1.8	1.745 ± 0.063	34 ± 2.0	3.70
SLM	16.101	78.894	13	4.3	33.4 ± 2.2	1.776 ± 0.064	35 ± 2.0	3.67
MBN	16.871	77.657	48	4.2	34.1 ± 1.4	1.745 ± 0.039	35 ± 2.0	3.80
HYB	17.417	78.553	216	4.0	33.3 ± 0.7	1.728 ± 0.020	35 ± 2.0	3.86
KIL	18.069	76.598	32	4.4	36.4 ± 1.5	1.739 ± 0.047	37 ± 2.0	3.92
NND	19.106	77.287	44	4.5	36.2 ± 1.7	1.747 ± 0.054	36 ± 2.0	3.86

[a]From receiver function stacking [*Zhu and Kanamori*, 2000].
[b]From receiver function inversion [*Ammon et al.*, 1990].

constraint on the velocity may lead to highly nonunique velocity models. Surface waves constrain the average velocity but weakly constrain velocity discontinuities and strong velocity gradients. Therefore, the strengths of one type of data set compensate for the weaknesses of the other and the joint inversion of both receiver function and surface wave dispersion data provide much more stringent constraints on the crustal velocity structure than does the inversion of either data separately. However, it is important that the two data sets sample the same structure as closely as possible. We inverted the receiver function and surface wave dispersion data jointly but did not use the average Rayleigh wave phase velocity measured along the transect (Figure 2); instead, we split the profile at station SLM (Figure 1) and calculated separately the dispersion for the north and south sections of the transect. The result of the joint inversion with a velocity model parameterized in terms of many thin layers is shown in Figures 6a–6c (heavy solid lines).

[17] We then simplified the crustal model by grouping adjacent model layers with similar wave speeds to form a more coarsely parameterized starting model and reinverted the receiver function. We repeated this procedure until we found the velocity model with the minimum number of parameters which fit both the main features of the receiver function and the short period surface wave phase velocity. The simplified inversion model (Figures 6a–6c, dotted lines) shows that the BGL receiver function can be fit by a single main crustal layer with a thin low velocity layer at the surface and a gradational Moho at 34–36 km depth.

[18] Finally, we tested the main features of the crustal model (e.g., thickness of the low velocity surface layer, thickness of the gradational layer at the base of the crust, Moho depth, etc.) using forward modeling (Figures 6e and 6f) to estimate how well these features of the velocity model are constrained by arrivals in the observed receiver function. All forward modeling results were also required to

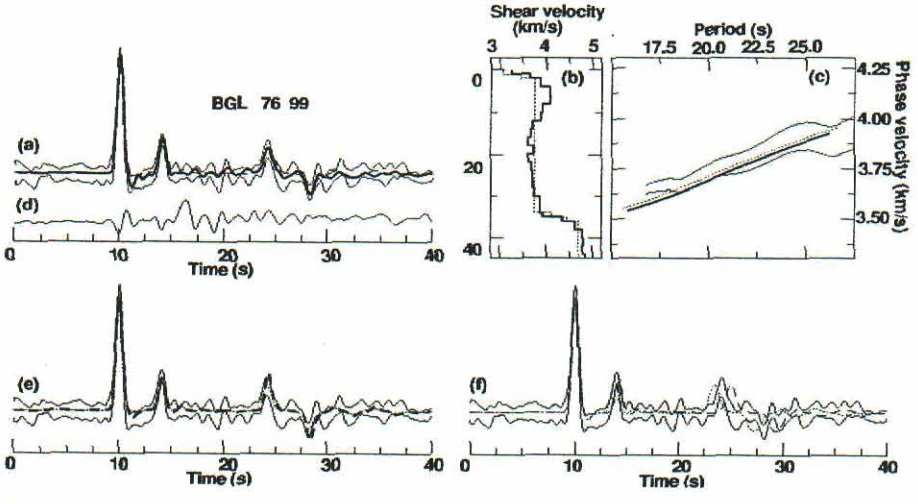

Figure 6. Inversion results for the 76–99 BGL receiver function stack. (a) Match of the ±1 standard deviation bounds of the observed (light solid lines) and synthetic receiver functions calculated for the velocity models shown in (b). (c) Fit of the theoretical Rayleigh wave phase velocity curves calculated for the velocity in (b) to the ±1 standard deviation bounds of observed (light solid lines) Rayleigh wave phase velocity. In (a), (b), and (c), the heavy solid line is for the initial inversion with the fine layer parameterization and the dotted line is for the simplified velocity model. (d) Stacked tangential for the 76–99 BGL receiver functions. (e) Forward modeling test of the low velocity surface layers (dotted line) and the gradient (dashed line) above the Moho. The removal of either feature does not significantly reduce the match of the synthetic and observed receiver function. (f) Forward modeling test of the Moho depth. Neither a Moho at 33 km (dotted line) nor 37 km (dashed line) depth fit the observed receiver function.

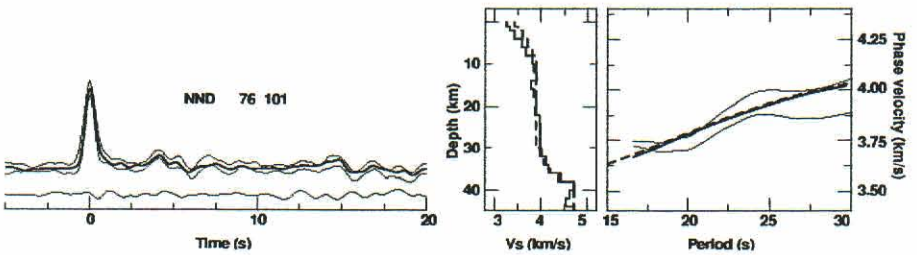

Figure 7. Results for NND. The leftmost panel shows the observed radial receiver function stack bounds (upper) and the mean tangential receiver function (lower). The conversions and reverberation phase amplitudes at NND are not as prominent as at some of the other sites, but the *Ps* and PpP_ms phases are relatively clear at 4–5 and 14–15 s, respectively. The heavy solid line is the synthetic radial receiver function computed for the fine layer parameterization joint receiver function–surface wave inversion model denoted by the solid line in the middle panel. The dotted line in the middle panel denotes the average coarse layer parameterization inversion result. The rightmost panel shows the fit of the Rayleigh wave phase velocity curves computed for the two inversion models (solid line: fine layer inversion, dashed line: coarse layer inversion). The forward modeling test for NND indicates the lower velocity, near-surface layer is significant and that the thickness of the crust–mantle transition zone can be as thin as 2 km. The Moho is at 36 ± 2 km depth.

agree with the observed dispersion curves. The final velocity model has a thin (~2 km), low velocity ($V_s \sim 3.26$ km s^{-1}) surface layer, an almost uniform velocity crust (~3.76 km s^{-1}), and a Moho discontinuity at 35 ± 2 km depth with the Moho transition zone ~2 km thick.

[19] Figure 3 compares the synthetic receiver function for the BGL crustal model and the observed receiver functions as a function of azimuth. This excellent match supports our assumption of a laterally homogeneous crust about BGL. A small systematic variation in the $Ps - P$ time might exist in the azimuthal plot and may not be clear because of the poor sampling of events to the west. If this is the case, the variation is small, ~0.1 s. If such a variation results from crustal velocity variation which is spread through the whole 35 km thickness of the crust, it would correspond to a ±0.1 km s^{-1} variation in shear wave velocity. If such a variation is due to a systematic azimuthal variation in the Moho depth, this corresponds to a ±1 km lateral variation in the Moho depth about BGL.

3. Crustal Structure of the East Dharwar Craton

[20] The receiver function and surface wave data for the other seven stations of the transect were analyzed in an identical manner. The results for each station are shown in Figures 7–13 and are summarized in Table 2 and Figure 14.

[21] Figure 14 compares the receiver function stacks for each of the eight stations for a similar distance (79 ± 1°) and azimuth (99 ± 1°) and the crustal models derived from the analysis of the receiver function and surface wave dispersion data for each site. Figure 14a shows that there is little variation in the receiver functions along the transect. The *Ps* delay time is nearly constant for the eight receiver functions (4.06 ± 0.15 s), but there is more variation in the delay time of the crustal reverberations (PpP_ms 14.22 ± 0.50 s, PpS_ms + PsP_ms 18.24 ± 0.96 s). There is little signal in the interval between *Pp* and *Ps* except in the SLM receiver function.

[22] All of the sites except for SLM lie over and are surrounded by the granite–gneisses of the Dharwar craton, although the two northernmost stations NND and KIL nominally lie on a veneer of Deccan volcanics. At KIL, boreholes in the region indicate that the thin veneer of volcanics overlying the Dharwar is ~350 m thick, and it is thought that the volcanics have a similar thickness at NND about 75 km further north. LTV lies about 50 km west of the western margin of the intracratonic Cuddappah Basin, and the basin structure may affect the crustal reverberations of the LTV receiver function. The simplicity of the receiver

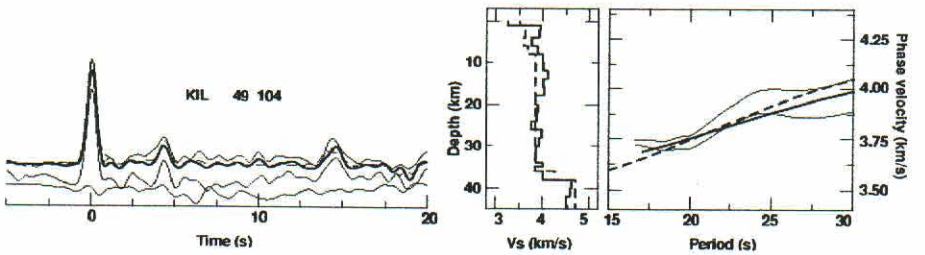

Figure 8. Results for KIL. The *Ps*, PpP_ms, and $PpS_ms + PsP_ms$ phases are prominent in the KIL receiver function stack at 4–5, 14–15, and 18–19 s, respectively. The KIL crust has a thin, low velocity, near-surface layer and an almost constant shear wave speed crust. The crust–mantle transition zone is 0–3 km thick and the Moho is at 37 ± 2 km depth. Same format as Figure 7.

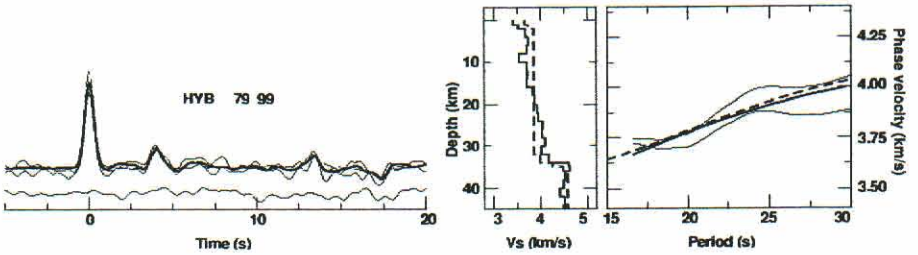

Figure 9. Results for HYB. The *Ps*, PpP_ms, and $PpS_ms + PsP_ms$ phases are prominent in the HYB receiver function stack at ~4, ~13, and ~15 s respectively. The HYB crust has a thin, near-surface, low velocity layer, a nearly uniform shear wave speed layer between 2 and 16 km depth and a positive gradient between 16 km depth and the Moho at 34 km depth. However, the HYB receiver function is almost as well fit by a uniform shear wave speed layer between 2 and 33 km depth and a 3 km thick crust–mantle transition zone. Same format as Figure 7.

functions (Figure 14a) indicates that the crust beneath each site is uncomplicated. The average Moho depth is 35 ± 2 km, the average shear wave velocity of the crust is 3.79 ± 0.09 km s^{-1} and the average V_p/V_s ratio of the crust is 1.746 ± 0.014.

[23] These values are similar to those found by *Gaur and Priestley* [1996] for HYB and compatible with refraction observations along the transect. *Kumar et al.* [2001] found similar values from receiver function analysis of data from PUNE and KARD to the northwest of our transect. However, *Zhou et al.* [2000] found a slightly shallower Moho (32 ± 2 km) and a lower average shear wave velocity (3.58 ± 0.10 km s^{-1}) for the crust in their receiver function study of HYB. A possible reason for this difference is that Zhou et al. used surface wave dispersion measured over a broad region around India which included northern India where other geophysical studies suggest the crust is thicker and where the thick sediment of the Indo-Gangetic plane [*Chatterjee*, 1971] affects the observed phase and group velocities. In contrast, the phase velocity values we jointly invert with the HYB receiver function are measured in the immediate vicinity of HYB. To be consistent, the two data for the joint receiver function–surface wave inversion must sample the same medium. The surface wave dispersion constrains the average shear wave velocity of the crust, and the receiver function constrains the interfaces. If the average shear wave velocity of the crust is too low (3.58 versus 3.79 km s^{-1}), the Moho will be too shallow (30–32 versus 34–36 km).

[24] SLM lies on shales and sandstones younger than 1700 ma, on the northeastern margin of the Proterozoic Cuddappah Basin. This spectacular crescent-shaped basin is filled with over 10 km thick clastic sediments that are virtually undeformed except at its eastern margin. The basin is thought to have developed over the upturned and eroded Archean basement, as evidenced by the Great Eparchaean Unconformity which spans 800 Ma and which marks its northern, western and southern contacts with the craton. The deeper crustal structure beneath this site is therefore expected to be a piece of the larger Dharwar craton. The SLM receiver function is somewhat more complex than the receiver functions from the other sites (Figure 14a), and there is stronger evidence for a midcrustal discontinuity in the SLM crustal model (Figure 14b).

4. Discussion and Conclusions

[25] The seismic characteristics of the central Dharwar craton, presented above, demonstrates the remarkable similarity of crustal structure and composition all along this transect. Specifically, the receiver functions at all sites are characterized by a weak (~10%) transverse component and a simple *P* coda with clear *Ps*, PpP_ms and $PpS_ms + PsP_ms$ phases. The first attribute is an expression of the near-horizontal layering that provides adequate justification for assuming a 1-D model of the crust in the receiver function inversions. The second attribute is a measure of the seismic transparency of the crust, implying no significant intracrustal discontinuities. The relatively clear conversions and reverberations of the simple *P* coda provide accurate time intervals to determine the value of the V_p/V_s ratio which imposes a tighter constraint on crustal petrology than

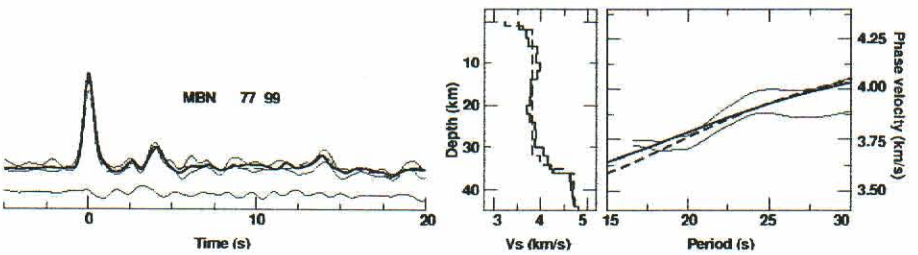

Figure 10. Results for MBN. The MBN receiver function stack has prominent *Ps* and PpP_ms phases at ~4 and ~13 s and a weak $PpS_ms + PsP_ms$ phase at 16–17 s. The crust–mantle transition zone is ~4 km thick and the Moho is at 35 ± 2 km depth. Same format as Figure 7.

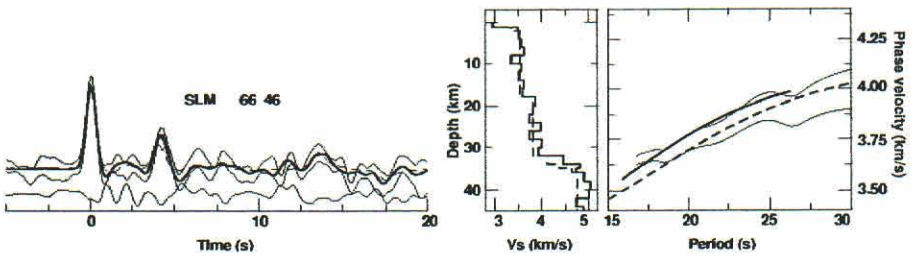

Figure 11. Results for SLM. The SLM receiver function is the most complex of any of the receiver functions observed along the transect. The large amplitude *Ps* phase at ~4.5 s is clear, but the PpP_ms and $PpS_ms + PsP_ms$ phases at 13–14 and 17–18 s, respectively, are not as prominent due to other large amplitude arrivals in the SLM receiver function. The SLM tangential receiver function has significant amplitude arrivals between the direct *P* and *Ps* phases and overall has larger amplitudes than are seen on any of the other transverse receiver functions observed along the transect. The crustal shear wave speed model has the lowest, near-surface velocities of the eight crustal models. The deeper crust consists of two layers, one with $V_s \sim 3.5$ km s^{-1} that extends from 2 to 18 km depth, presumably corresponding to the lower wave speed material infilling the basin, and a second layer with $V_s \sim 3.8$ km s^{-1} which extends from 18 to 32 km depth, presumably corresponding to the underlying rocks of the east Dharwar Craton. The crust–mantle transition is 2–3 km thick and the Moho is at 35 ± 2 km depth. Same format as Figure 7.

is possible to obtain from either compressional or shear velocities alone. However, all strategies to determine crustal thickness from travel times are essentially nonunique because of the tradeoff with crustal velocity. Consequently, we have further constrained the reliability of our inverse solutions by jointly inverting the receiver function measurements with fundamental mode Rayleigh wave phase velocity measurements along the profile. The two data are sensitive to different features of the crustal structure; hence, their joint inversion provides a more unique model of the crustal structure.

[26] The receiver functions show the seismic characteristics of the Dharwar crust to be remarkably uniform throughout and varying within fairly narrow bounds: crustal thickness (35 ± 2 km), average shear wave speed (3.79 ± 0.09 km s^{-1}), and V_p/V_s ratio (1.746 ± 0.014). These values are within the gross estimates of crustal thicknesses and velocities determined by earlier investigators for HYB [*Gaur and Priestley*, 1996; *Saul et al.*, 2000; *Zhou et al.*, 2000], KIL [*Krishna et al.*, 1999], GBA [*Krishna and Ramesh*, 2000], and the intersection of the BGL–NND transect with the E-W refraction profile [*Kaila and Krishna*, 1992; *Reddy and Rao*, 2000]. However, a straightforward comparison of the details of the crustal models determined from receiver function and refraction analysis cannot be made for several reasons. First, the conversions and reverberations analyzed in the receiver function study sample the crust in a restricted region (~35 km) around the seismograph site whereas the refraction/wide-angle reflection arrivals sample the crust over a broader region (~200 km) and hence the two methods average different spatial domains. Second, the frequency content of the receiver function arrivals is centered at about 0.2 Hz whereas the refraction/wide-angle reflection arrivals are 1–2 Hz and because of the different frequency content, the two data sample the details of the crustal layering in a different manner. Third, the receiver function arrivals primarily constrain the shear wave speed structure of the crust whereas the refraction/wide-angle reflection arrivals primarily constrain the crustal compressional wave speed structure.

[27] The simple nature and nearly uniform thickness (~35 km) of the central Dharwar craton crust and its felsic character are similar to the crust found for other Archaean

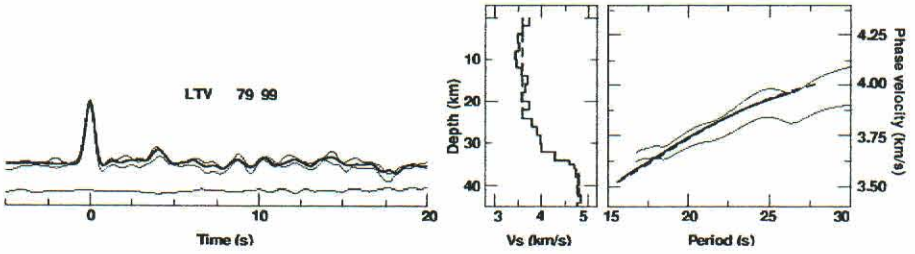

Figure 12. Results for LTV. The Moho conversion and reverberations are weak in the LTV receiver function but the *Ps*, PpP_ms, and $PpS_ms + PsP_ms$ can be seen at ~4, ~14, and 17–18 s, respectively. The near-surface, low velocity layer is absent beneath LTV and the upper 24 km of the crust have nearly a uniform shear wave speed of 3.4. There is a pronounced positive gradient in the lower crust starting at 24 km depth and extending to the Moho at 34–36 km depth. The existence of this strong gradient is substantiated in the forward modeling tests. The Moho is at 34 ± 2 km depth. Same format as Figure 7.

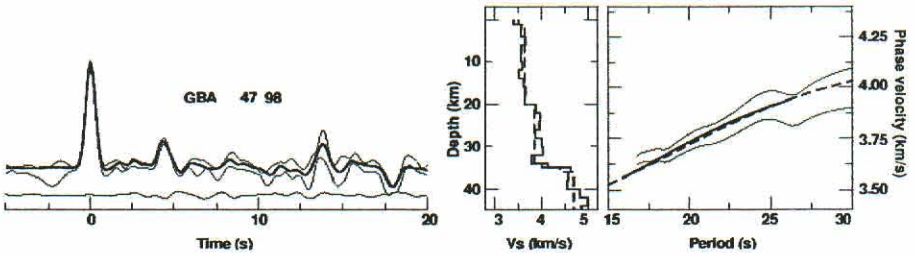

Figure 13. Results for GBA. The GBA receiver function has prominent *Ps*, PpP_ms, and $PpS_ms + PsP_ms$ phases at ~4, 13–14, and 18 s, respectively. The GBA crust consists of two layers: an upper layer with V_s ~3.4 km s^{-1} extending from near the surface to 20 km depth, and a second layer with $V_s \sim 3.9$ km s^{-1} extending from 20 to 35 km depth. The crust–mantle transition is sharp beneath GBA and the Moho is at 36 ± 2 km depth. Same format as Figure 7.

cratons that have remained largely stable since cratonization. The two largest Archaean terrains of western Australia (the Pilbara and the Yilgarn cratons) have a predominantly felsic [*Chevrot and van der Hilst*, 2000] crust which in their central undisturbed regions is 33–36 km thick [*Clitheroe at al.*, 2000] and underlain by a sharp Moho. The cores of Archaean Kaapvaal and Zimbabwe cratons of southern Africa also have crustal thicknesses clustering between 34 and 37 km [*Nguuri et al.*, 2001], and a sharp Moho that produces clear and large amplitude *Ps* signals. Sites over the

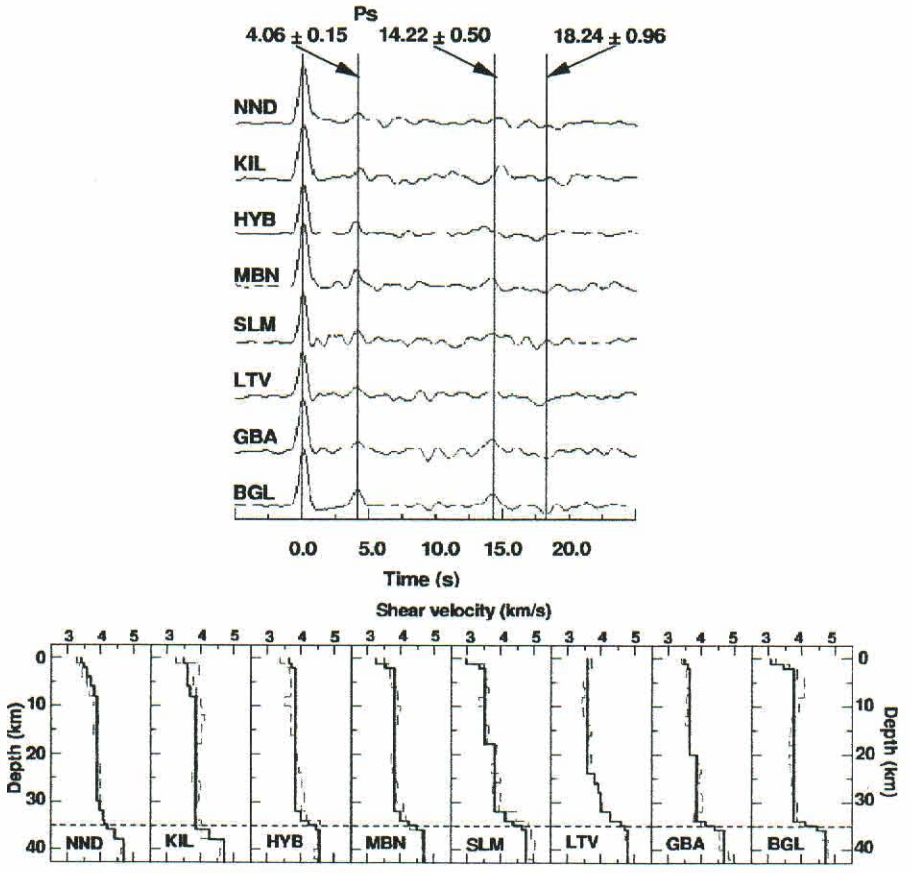

Figure 14. Summary of the crustal structure for the south Indian shield. (a) Comparison of stacked receiver functions observed at each station for nearly a common distance (79°) and back azimuth (99°) cluster. To the left of the direct arrivals are the station names. Lines denote the average *Ps*, PpP_ms, and $PpS_ms + PsP_ms$ delay times. (b) Average crustal shear wave models beneath each site. The models from the fine layer parameterization joint inversion and the coarse layer parameterization inversion are denoted by the solid and dashed lines, respectively. The dotted line across the plot is at 35 km depth and is for reference.

Slave craton in northwest Canada that contain the oldest known rocks on Earth also show clear *Ps* phases without significant arrival time variations [*Bank et al.*, 2000], yielding an average crustal thickness of 38 km. Receiver functions at three sites on the central Sao Francisco craton in the southeast Brazilian shield show a similar ~35 km thick (estimated from the $Ps - P$ intervals of 4–4.3 s), transparent crust which is felsic (V_p/V_s = 1.70) with no significant intracrustal features [*Assumpcao et al.*, 2002].

[28] Furthermore, there is no evidence for any high velocity basal layer in the receiver function crustal images of the central Dharwar craton, suggesting that there is no seismically distinct layer of mafic cumulates overlying the Moho. This implies that the base of the Dharwar crust has remained fairly refractory since its cratonization. Corroborating evidence for the absence of mafic underplating in the Dharwar craton is also provided by the average Poisson's ratio of the crust (0.256 ± 0.006), indicating that the crust is essentially intermediate-to-felsic in composition. This conclusion supports the evolutionary hypothesis for the growth of continental crust; that is, the crustal formation processes in the Archean were different from those that dominated since the Archean [*Durrheim and Mooney*, 1991]. Indeed, the uniform low heat flow and the occurrence of diamonds in the Dharwar craton lend weight to this hypothesis.

[29] Heat flow throughout this corridor is 25–50 mW m^{-2} [*Roy and Rao*, 2000]. In fact, the mantle heat flow is reduced to a remarkably uniform value of around 12–18 mW m^{-2}, when the quite variable heat generation of the surficial crustal layers is accounted for, discounting any suggestion that there are substantial spatial variations in heat from the mantle into the lower crust. The eastern Dharwar craton is also diamondiferous, with some of the well-known pipes being quite close to LTV west of the Cuddappah Basin. These diamonds, which are yet to be dated, occur in the kimberlites of much younger ages (1100 Ma). South African kimberlites of similar age contain Archean-age diamonds [*Richardson et al.*, 1984].

[30] The diamonds found on the Dharwar craton may also belong to the Archean (2500 Ma) when the cratonization of Dharwar was complete, with an undercarriage of a colder, thicker lithosphere that had entered the diamond stability field. A puzzling feature of the Dharwar craton, however, is that its bulk composition does not appear to have a komatiitic origin but is possibly of tholeiitic and picritic composition, with some component of ultramafic rocks.

[31] The above picture, strictly speaking, characterizes only the central Dharwar craton whose 3-D structure must await similarly extended investigations to its east and west. The E-W refraction profile [*Reddy and Rao*, 2000], however, indicates that the crust of the western Dharwar craton across the Closepet granite is thicker (>40 km) and of lower velocity. However, based on its geology, the Dharwar craton is widely regarded to be composed of two different terrains sutured longitudinally by the Closepet granite, and very elaborate proposals [*Hanson et al.*, 1986] have been suggested as evidence of a plate tectonic-type of activity having operated as far back as the Archean. Nevertheless, these hypotheses are equivocal and if, as we believe, a similar evolutionary process was responsible for both the western and eastern Dharwar craton, the differences in crustal thickness and isotopic signatures are a result of subsequent tectonic processes. Therefore, we should be encouraged to investigate the western Dharwar craton for the possible existence of diamondiferous kimberlites and auriferous schists and not declare the western craton to be barren.

[32] In conclusion, we note that seismically, the central Dharwar craton over the 600 km long transect is remarkably transparent and is therefore an excellent window for imaging the mantle beneath. The Dharwar craton appears to be a classical representative of primitive cratons and constitutes a significant sample of early Earth processes that evolved with the thermodynamic evolution of the mantle.

[33] **Acknowledgments.** This project was supported in part by a grant from the Department of Science and Technology, Government of India, and by Bullard Laboratories of the University of Cambridge. Considerable logistic support was provided by the directors of the National Geophysical Research Institute at Hyderabad, Centre for Mathematical Modeling and Computer Simulation, and the Indian Institute of Astrophysics at Bangalore. VKG is especially thankful to Cowsik, Leelanandam, R. Srinivasan, and RUM Rao for stimulating discussions. KP would like to thank Denis Hatzfeld for arranging a CNRS summer professorship and providing computing facilities at Universite Joseph Fourier, where most of the computations were done. This is Cambridge University Department of Earth Sciences contribution 7145.

References

Ammon, C. J., The isolation of receiver effects from teleseismic P waveforms, *Bull. Seismol. Soc. Am.*, *81*, 2504–2510, 1991.

Ammon, C. J., G. E. Randall, and G. Zandt, On the non-uniqueness of receiver function inversions, *J. Geophys. Res.*, *95*, 15,303–15,318, 1990.

Assumpcao, M., D. James, and A. Snoke, Crustal thicknesses in SE Brazilian Shield by receiver function analysis: Implications for isostatic compensation, *J. Geophys. Res.*, *107*(B1), 2006, doi:10.1029/2001JB000422, 2002.

Bank, C.-G., M. G. Bostock, R. M. Ellis, and J. F. Cassidy, A reconnaissance teleseismic study of the upper mantle and transition zone beneath the Archean Slave craton in NW Canada, *Tectonophysics*, *319*, 151–166, 2000.

Bhattacharya, S. N., Crustal and upper mantle velocity structure of India from surface wave dispersion, in *Seismology in India: An Overview*, edited by H. K. Gupta and S. Ramaseshan, *Curr. Sci.*, *62*, Suppl., 94–100, 1992.

Chatterjee, S. N., On the dispersion of Love Waves and crust–mantle structure in the Gangetic Basin, *Geophys. J. R. Astron. Soc.*, *23*, 129–138, 1971.

Chevrot, S., and R. D. van der Hilst, The Poisson ratio of the Australian crust: Geological and geophysical implications, *Earth Planet. Sci. Lett.*, *183*, 121–132, 2000.

Clitheroe, G., O. Gudmundsson, and B. L. N. Kennett, The crustal thickness of Australia, *J. Geophys. Res.*, *105*, 13,697–13,713, 2000.

Du, Z. J., and G. R. Foulger, The crustal structure of northwest Fjords, Iceland, from receiver functions and surface waves, *Geophys. J. Int.*, *139*, 419–432, 1999.

Dube, R. K., J. C. Bhayana, and H. M. Chaudhary, Crustal structure of the Peninsular India, *Pure Appl. Geophys.*, *109*, 1718–1727, 1973.

Durrheim, R. J., and W. D. Mooney, Archean and Proterozoic crustal evolution: Evidence from crustal seismology, *Geology*, *19*, 606–609, 1991.

Gaur, V. K., and K. Priestley, Shear wave velocity structure beneath the Archean granites around Hyderabad, inferred from receiver function analysis, *Proc. Indian Acad. Sci. Earth Planet. Sci.*, *105*, 1–8, 1996.

Gaur, V. K., and K. F. Priestley, Shear wave velocity structure beneath the Archean granites around Hyderabad, inferred from receiver function analysis, *Proc. Indian Acad. Sci. Earth Planet. Sci.*, *106*, 1–8, 1997.

Gomberg, J. S., K. Priestley, T. G. Masters, and J. N. Brune, The structure of the crust and upper mantle of northern Mexico, *Geophys. J. R. Astron. Soc.*, *94*, 1–20, 1988.

Hanson, G. N., E. J. Krogstad, V. Rajamani, and S. Balakrishnan, The Kolar schist belt: A possible Archean suture zone, in *Workshop on Tectonic Evolution of Greenstone Belts*, edited by M. J. de Wit and L. D. Ashwal, LPI Tech Rep. 86-10, pp. 111–113, Lunar and Planet. Inst., Houston, Tex., 1986.

Herrmann, R. B., *Computer Programs in Seismology*, version 3.15, St. Louis Univ., St. Louis, Mo., 2002.

Huestis, S., P. Molnar, and J. Oliver, Regional *Sn* velocities and shear velocity in the upper mantle, *Bull. Seismol. Soc. Am.*, *63*, 469–475, 1973.

Hwang, H. J., and B. J. Mitchell, Shear velocities, Q_β, and frequency dependence of Q_β in stable and tectonically active regions from surface wave observations, *Geophys. J. R. Astron. Soc.*, *90*, 575–613, 1987.

Kaila, K. L. and V. G. Krishna, Deep seismic sounding studies in India and major discoveries, in *Seismology in India: An Overview*, edited by H. K. Gupta and S. Ramaseshan, *Curr. Sci.*, *62*, Suppl., 117–154, 1992.

Krishna, V. G., and D. S. Ramesh, Propagation of crustal waveguide trapped P_g and seismic velocity structure in the south Indian shield, *Bull. Seismol. Soc. Am.*, *90*, 1281–1296, 2000.

Krishna, V. G., C. V. R. K. Rao, H. K. Gupta, D. Sarkar, and M. Baumbach, Crustal seismic velocity structure in the epicentral region of the Latur earthquake (September 29, 1993), southern India: Inferences from modelling of the aftershock seismograms, *Tectonophysics*, *304*, 241–255, 1999.

Kumar, M. R., J. Saul, D. Sarkar, R. Kind, and A. Shukla, Crustal structure of the Indian shield: New constraints from teleseismic receiver functions, *Geophys. Res. Lett.*, *28*, 1339–1342, 2001.

Nguuri, T. K., J. Gore, D. E. James, S. J. Webb, C. Wright, T. G. Zengeni, O. Gwavava, and J. A. Snoke, Crustal structure beneath southern Africa and its implications for the formation and evolution of the Kaapvaal and Zimbabwe cratons, *Geophys. Res. Lett.*, *28*, 2501–2504, 2001.

Owens, T. J., G. Zandt, and S. R. Taylor, Seismic evidence for an ancient rift beneath the Cumberland Plateau, Tennessee: A detailed analysis of broadband teleseismic P waveforms, *J. Geophys. Res.*, *89*, 7783–7795, 1984.

Priestley, K., G. Zandt, and G. Randal, Crustal structure in eastern Kazakh, USSR from teleseismic receiver functions, *Geophys. Res. Lett.*, *15*, 613–616, 1988.

Reddy, P. R., and V. Vijaya Rao, Structure and tectonics of the Indian Peninsular shield: Evidences from seismic velocities, *Curr. Sci.*, *78*, 899–906, 2000.

Richardson, S. H., J. J. Gurney, A. J. Erlank, and J. W. Harris, Origin of diamonds in old enriched mantle, *Nature*, *310*, 198–202, 1984.

Roy, S., and R. Rao, Heat flow in the Indian shield, *J. Geophys. Res.*, *105*, 25,587–25,604, 2000.

Saul, J., M. R. Kumar, and D. Sarkar, Lithospheric and upper mantle structure of the Indian shield, from teleseismic receiver functions, *Geophys. Res. Lett.*, *27*, 2357–2360, 2000.

Sheehan, A. F., G. A. Abers, C. H. Jones, and A. L. Lerner-Lam, Crustal thickness variation across the Colorado Rocky Mountains from teleseismic receiver functions, *J. Geophys. Res.*, *100*, 20,391–20,404, 1995.

Singh, S. K., R. S. Dattatrayam, N. M. Shapiro, P. Mandal, J. F. Pacheco, and R. K. Midha, Crustal and upper mantle structure of peninsular India and source parameters of the 21 May 1997, Jabalpur earthquake (Mw = 5,8): Results from the new regional broadband network, *Bull. Seismol. Soc. Am.*, *89*, 1631–1641, 1999.

Zandt, G., S. C. Myers, and T. C. Wallace, Crust and mantle structure across the Basin and Range–Colorado Plateau boundary at 37°N latitude and implementation for Cenozoic extensional mechanism, *J. Geophys. Res.*, *100*, 10,529–10,548, 1995.

Zhou, L., W.-P. Chen, and S. Ozalaybey, Seismic properties of the Central Indian shield, *Bull. Seismol. Soc. Am.*, *90*, 1295–1304, 2000.

Zhu, L., and H. Kanamori, Moho depth variation in southern California from teleseismic receiver functions, *J. Geophys. Res.*, *105*, 2969–2980, 2000.

Z. Du, Institute of Theoretical Geophysics, University of Cambridge, Cambridge, UK. (du@esc.cam.ac.uk)

V. K. Gaur, Centre for Mathematical Modeling and Computer Simulation, NAL Belur Campus, Bangalore 560037, India. (gaur@cmmacs.ernet.in)

K. Priestley, Bullard Laboratories, University of Cambridge, Madingley Rise, Madingley Road, Cambridge, CB3 0EZ, UK. (keith@esc.cam.ac.uk)

S. S. Rai, D. Srinagesh, and K. Suryaprakasam, National Geophysical Research Institute, Hyderabad 500007, India. (postmast@csngri.ren.nic.in)

The nature of the crust in southern India: Implications for Precambrian crustal evolution

Sandeep Gupta, S. S. Rai, K. S. Prakasam, and D. Srinagesh
National Geophysical Research Institute, Hyderabad, India

B. K. Bansal
Department of Science and Technology, New Delhi, India

R. K. Chadha
National Geophysical Research Institute, Hyderabad, India

Keith Priestley
Bullard Laboratories, University of Cambridge, Cambridge, UK

V. K. Gaur
Indian Institute of Astrophysics, Bangalore, India

Received 15 December 2002; revised 19 February 2003; accepted 11 March 2003; published XX Month 2003.

[1] We present crustal thickness and Poisson's ratio determinations from receiver function analyzes at 32 sites on the Archaean and Proterozoic terrains of South India. The crustal thickness in the late Archaean (2.5 Ga) Eastern Dharwar Craton varies from 34–39 km. Similar crustal thickness is observed beneath the Deccan Volcanic Province and the Cuddapah basin. The most unexpected result is the anomalous present-day crustal thickness of 42–51 km beneath the mid-Archaean (3.4–3.0 Ga) segment of the Western Dharwar Craton. Since the amphibolite-grade metamorphic mineral assemblages (5–7 Kbar paleopressures) in this part of Western Dharwar Craton equilibrated at the depths of 15–20 km, our observations suggest the existence of an exceptionally thick (57–70 km) crust 3.0 Ga ago. Beneath the exhumed granulite terrain in southernmost India, the crustal thickness varies between 42–60 km. The Poisson's ratio ranges between 0.24–0.28 beneath the Precambrian terrains, indicating the presence of intermediate rock type in the lower crust. These observations of thickened crust suggest significant crustal shortening in South India during the Archaean. *INDEX TERMS:* 7203 Seismology: Body wave propagation; 7205 Seismology: Continental crust (1242); 7299 Seismology: General or miscellaneous. **Citation:** Gupta, S., S. S. Rai, K. S. Prakasam, D. Srinagesh, B. K. Bansal, R. K. Chadha, K. Priestley, and V. K. Gaur, The nature of the crust in southern India: Implications for Precambrian crustal evolution, *Geophys. Res. Lett.*, *30*(0), XXXX, doi:10.1029/2002GL016770, 2003.

1. Introduction

[2] The South India shield is an amalgamation of several crustal blocks formed by geodynamic processes operating from mid-Archaean to Neo-Proterozoic time. The main geological provinces in southern India are shown in Figure 1.

0094-8276/03/2002GL016770$05.00

The Dharwar Craton is an Archaean continental fragment with a continuously-exposed crustal section from low-grade gneisses and greenstone basins in the north to granulites in the south. At the surface, the craton is divided into the Western Dharwar Craton (WDC) and Eastern Dharwar Craton (EDC) by the 2.5 Ga Closepet granite. The WDC has a more stable ensialic portion with 3.4 to 3.0 Ga basement gneisses [*Beckinsale et al.*, 1980; *Rogers*, 1986]. The central part of WDC hosts 3.4 Ga greenstone belts while the northern part constitutes the 2.6 Ga Dharwar Basins [*Taylor et al.*, 1984].

[3] The EDC crust consists largely of granitoid rocks, all juvenile additions to the continental crust from 2.6–2.5 Ga. To the east the EDC is wrapped by the Proterozoic Cuddapah Basin (CB) and the Eastern Ghat granulite terrain. The northern part of EDC and the Bastar Craton are separated by the Proterozoic Godavari Graben (Figure 1). The 65 Ma flood basalt province of the Deccan Volcanic Province (DVP) covers the NW part of Dharwar craton. It is not clear whether rocks of the WDC or EDC form the basement of the flood basalt province.

[4] The most important feature of the Dharwar craton is the transition from the low- to medium-grade granite - greenstone terrain in the north to the high-grade granulite terrain in the south, the Southern Granulite Terrain (SGT). The paleopressures gradually increase from 3 Kbar in the north to 5–7 Kbar in the center and 9–10 Kbar in the south of the Dharwar craton, corresponding to an erosion level of 6–8 km in the north to ~30 km in the south [*Harris and Jayaram*, 1982]. The granulite evolution is thought to have occurred at around 2.5 Ga [*Grew and Manton*, 1984], coeval with the Closepet granite emplacement.

[5] South India has undergone a complex terrain accretion since the mid-Archean and has poorly-defined tectonic boundaries at depth. The growth of the South Indian continental crust will be better understood once the variation in crustal structure across South India is known. In this study, we present constraints for crustal thickness and composition (from the Poisson's ratio) in South India

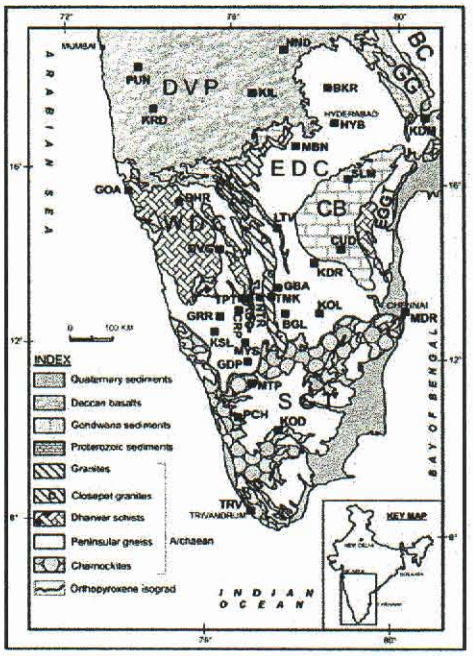

Figure 1. Generalized geotectonic map of south India. Important geological blocks include EDC - Eastern Dharwar Craton, WDC - Western Dharwar craton, DVP - Deccan Volcanic Provinces, SGT - Southern Granulite Terrain, CB - Cuddapah Basin, GG - Godavari Graben, EGGT - Eastern Ghat Granulite Terrain and BC - Bastar Craton. Location of broadband seismic stations are indicated by filled squares.

derived from receiver function analyzes of teleseismic waveforms.

2. Data and Methodology

[6] We analyze seismograms from 32 broadband seismographs in South India (Figure 1). The number of high signal-to-noise receiver functions varied from at least 20 to more than 100 for individual stations. Stacked receiver functions (5° distance and azimuth bins) for individual stations arranged by geologic provinces are shown in Figure 2. This plot shows significant variation in *Ps* arrival times, reflecting variations in crustal thickness and/or Poissons's ratio (σ). We estimated the crustal thickness and σ using the stacking procedure of *Zhu and Kanamori* [2000], with *Ps*, *PpPms*, *PsPms* + *PpSms* being weighted 0.7, 0.2 and 0.1 respectively. We used the average crustal *P*-wave speed of 6.45 km s^{-1} [*Kaila and Krishna*, 1992] in making the crustal thickness vs. V_p/V_s stacks. Figure 3 shows the contour plots for crustal thickness and V_p/V_s for several stations. The average error is ±0.5 km and ±0.015 for the crustal thickness and V_p/V_s, respectively.

3. Results

[7] Figure 4 is a Moho depth map for South India which combines the results from the 32 receiver function measurements and 14 estimates from seismic refraction studies employing ray tracing analysis [*Krishna et al.*, 1989; *Sarkar et al.*, 2001; *Reddy et al.*, 2003]. The crust beneath the EDC, DVP and CB is remarkably similar in both receiver function waveforms and crustal parameters with a fairly transparent crust containing no marked apparent mid-crustal interfaces. The crustal thickness varies from 34 to 36 km (except at KDR ~39 km) and the Poisson's ratio ranges from 0.24 to 0.27. *Gaur and Priestley* [1996], *Kumar et al.* [2001], and *Rai et al.* [2003] report similar observations from sparser receiver function measurements in South India.

[8] Surprising results come from the mid-Archean WDC where the receiver functions are more complex and crustal thickness varies between 42–51 km. The Poisson's ratio at most stations in the WDC varies from 0.25 to 0.27, similar to that in the EDC. The thickest crust (~60 km) is observed beneath MTP located near the Nilgiri Hills (elevation 2.7 km) in the SGT. The other highly elevated station, KOD (2.4 km), has a 43 km-thick crust. The average crustal thickness in SGT is about 40–50 km and σ ~0.25–0.26 with the exception of MTP (H ~60 km, σ = 0.28). The crust beneath KDM in the Proterozoic Godavari Graben is 44 km-thick.

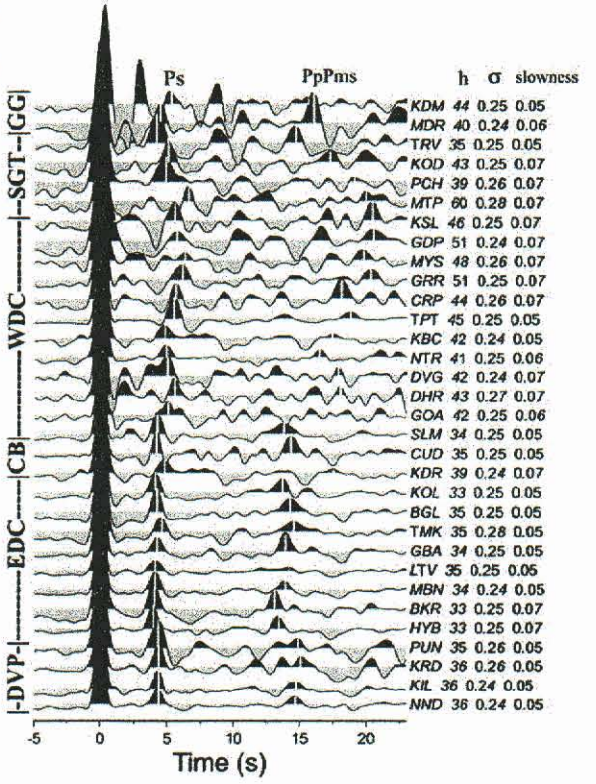

Figure 2. Stacked radial receiver functions organized according to geological provinces. The Moho conversion and reverberations are indicated on the receiver functions. The geological provinces are denoted to the left of the receiver functions and the crustal thickness, the average Poisson's ratio, and average slowness for the stack are given to the right of the receiver function. A clear time shift in the *Ps* phase is visible for stations in the WDC and SGT compared to stations in the EDC.

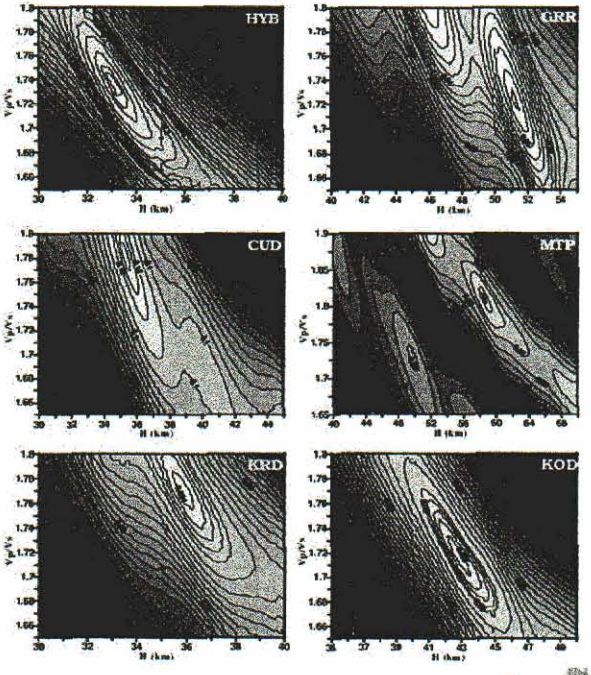

Figure 3. Vp/Vs ratio vs crustal thickness (H) stack for six stations in South India.

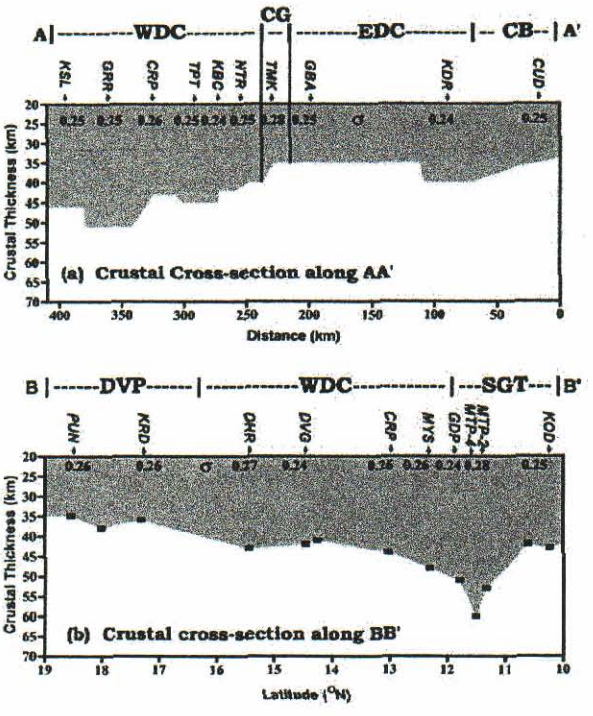

Figure 5. Cross-section depicting Crustal thickness and Poisson's ratio variation across: (a) SW-NE profile across the Western Dharwar craton (WDC), the Closepth granite (CG), the Eastern Dharwar craton (EDC) and the Cuddapah Basin (CB), (b) NW-SE profile across the Deccan Volcanic Province (DVP), the Western Dharwar craton (WDC) and the Southern Granulite Terrain (SGT). The locations of the profiles are indicated on Figure 4. In cross-section AA′ the crustal thickness is projected at depth with horizontal offset in the direction of the earthquakes. The azimuth ranges used are SW-W, NE-E and the entire 360° azimuthal sector.

[9] Figure 5 shows the variability of the Moho depth along two crustal cross-sections across South India: AA′ from the CB across the EDC to WDC (Figure 5a) and BB′ from DVP across the WDC to the SGT (Figure 5a). The cross-section locations are shown on Figure 4. Figure 5a shows that the crust thickness beneath the EDC varies from 34–39 km, but beneath the WDC the crustal thickness ranges from 42–51 km. To discern the nature of the Moho depth variations, we examined the receiver functions at individual stations for a systematic delay of the *Ps* phase with azimuth and distance, but we do not observe significant variations in the arrival times or amplitudes of converted and multiples as expected for a dipping Moho. This suggests that the Moho is essentially horizontal and that the offsets occur at rather sharp boundaries which seem to coincide with major N-S shear zones [*Drury et al.*, 1984]. The thickest WDC crust (51 km) occurs beneath the mid-Archaean (3.4 Ga) greenstone belt - the nucleus of the Dharwar craton - a major low-strain zone which has not been subjected to any severe compressive deformation [*Chadwick et al.*, 1989]. In addition, this area is characterized by high *P*- and *S*-wave velocities [*Gupta et al.*, 2001] and lower mantle heat flow [*Gupta et al.*, 1991]. The crustal Poisson's ratio for both the EDC and WDC crust is 0.25 ± 0.1 except beneath TMK ($\sigma = 0.28$), which is situated on the K-rich mantle-derived Closepet granite. The cross-section AA′ from station CRP to KSL is representative of the

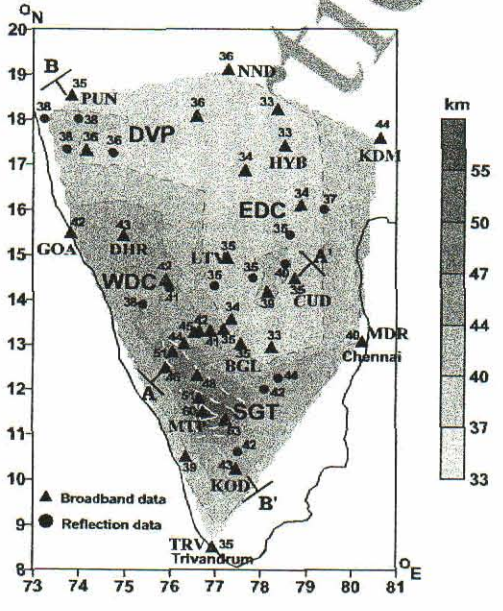

Figure 4. Crustal thickness map for South India derived from the receiver function analysis reported here and published reflection/refraction results. Numbers denote Moho depth. The locations of the two crustal cross-sections (AA′, BB′) shown in Figure 5 are indicated.

amphibolite-grade metamorphic rocks whose paleopressures range between 5–7 Kbar, consistent with a 15–20 km erosion level, indicating that the Archaean crust in this part of the WDC may have been 57–70 km thick 3.4–3.0 Ga ago.

[10] Cross-section BB′ (Figure 5b) shows the Moho topography from undeformed Archaean crust beneath the DVP and northern WDC to the area of late Archean to Proterozoic deformation responsible for the evolution and exhumation of granulite facies rocks in the southern parts of India. In Figure 5b MTP-2 and MTP-4 refer to crustal thickness inferred beneath the station for events from 90–180° and 270–360° azimuths, respectively. Although the receiver functions for the two azimuthal ranges indicate a difference in crustal thickness, the transition between the two regions must be relatively sharp since there is no indication in the tangential receiver function of a dipping Moho. The DVP is underlain by 35–38 km thick crust, similar to the crustal thickness beneath the adjoining EDC. Progressive thickening with an increasing grade of metamorphism is observed southward across the WDC. The northern part of the WDC (DHR and DVG) consists of granite-gneisses terrain (paleopressures 3–4 Kbar) with a crustal thickness of 42–43 km, while the amphibolite grade central part (pressure 5–7 Kbar, CRP, MYS) thickens to 44–48 km. At MTP in the Nilgiri Hills, which consist of hornblende granulite facies rock, the present-day Moho is about 60 km deep. Since the exhumed granulite rocks were once buried to a depth of 25-30 km (10 Kbar paleopressure), the crustal thickness during the Precambrian could have been ~90 km. However, since the 2.5 Ga-old granulite terrain rocks are overprinted by the 550 Ma Pan-African event, it is difficult to determine when the crust attained this anomalous thickness. Further south, the crustal thickness decreases with decreasing paleopressure. Our observations are consistent with the significant crustal thickening seen in similar metamorphic belts [*Percival et al.*, 1989; *Nguuri et al.*, 2001].

4. Discussion

[11] The significant findings of the broadband teleseismic experiment in South India assre: (i) very similar crustal architecture (thickness ~35 km, σ ~0.25) beneath the 2.5 Ga EDC, the DVP and the CB; (ii) significant crustal thickening (42–51 km) beneath the southern part of the WDC, (iii) a 42–60 km crustal thickness beneath the SGT, and (iv) that the Closepet granite forms the crustal divide at depth between the EDC and WDC. The average Poisson's ratio for the South Indian crust has values of 0.24–0.27 which are at the lower end of the global average [*Zandt and Ammon*, 1995] for the Archaean shields (0.27–0.31), implying felsic-to-intermediate composition. No significant differences are observed between the Archaean and Proterozoic crustal blocks as suggested elsewhere [*Durrheim and Mooney*, 1991].

[12] The overly-thick (>50 km) crustal block of the WDC coincides with >3.36 Ga amphibolite grade greenstone belt (5–7 Kbar pressure,) suggesting the existence of a 57–70 km thick crust during the mid-Archaean. The preservation of such an overly-thickened crust could only be possible where the crust is shielded from high mantle heat flow by a thick, insulating layer of lithosphere. The presence of such a thick, cool lithospheric root beneath this region has been demonstrated by *Srinagesh and Rai* [1996], *Gupta et al.* [1991], and *Gupta et al.* [2003]. Our crustal thickness observations are at odds with those of *Durrheim and Mooney* [1991] who proposed that the Archaean crust is thinner than Proterozoic crust. The northern part of granulite terrain, which is characterized by high paleopressures (8–10 Kbar), is conspicuous by the presence of the thickest crust (50–60 km). The fact that these 2.5 Ga rocks were exhumed from depths of 25–30 km indicates anomalous crustal thickening (75–90 km) during the Archean, similar to that observed in the high Himalayan and Indus Tsangpo Suture Zone and suggestive of a possible Himalayan-type geodynamic event for granulite evolution in South India.

[13] **Acknowledgments.** The deep continental studies program of the Department of Science and Technology supported the South India broadband project. We acknowledge the support provided by NGRI and are grateful to the Indian Meteorological Department for providing data from its network. S. Singh, T. V. Kumar, R. Sarma and Y. Satyanarayana provided the necessary field support during field deployment. KP acknowledges travel support from the University of Cambridge.

References

Beckinsale, R. D., S. A. Drury, and R. N. Holt, 3.360 Myr old gneisses from South Indian Craton, *Nature*, *283*, 469–470, 1980.

Chadwick, B., M. Ramakrishnan, V. N. Vasudev, and M. N. Vishwanathan, Facies distribution and structures of a Dharwar volcano-sedimentary basin: Evidence for late Archean transpression in southern India, *J. Geol. Soc. London*, *146*, 825–834, 1989.

Drury, S. A., N. B. Harris, R. W. Holt, G.J. Reeves-Smith, and R. T. Wightman, Precambrian tectonics and crustal evolution in south India, *J. Geol.*, *92*, 3–20, 1984.

Durrheim, R. J., and W. D. Mooney, Archean and Proterozoic crustal evolution: Evidence from crustal seismology, *Geology*, *19*, 606–609, 1991.

Gaur, V. K., and K. Priestley, Shear wave velocity structure beneath the Archean granite around Hyderabad, inferred from receiver function analysis, *Proc. Indian Acad. Sci. Earth Planet. Sci.*, *106*, 1–8, 1996.

Grew, E. S., and W. F. Manton, Age of allarite from Kabbldurga Quarry, Karnataka, *J. Geol. Soc. India*, *25*, 193–195, 1984.

Gupta, M., S. R. Sharma, and A. Sundar, Heat flow and heat generation in the Archaean Dharwar cratons and implications for the Southern Indian Shield Geotherm and Lithospheric thickness, *Tectonophysics*, *194*, 107–122, 1991.

Gupta, S., D. Srinagesh, S. S. Rai, V. K. Gaur, K. Priestley, and Z. Du, The thick early Archean crust-Teleseismic results from Dharwar Craton, *Eos Trans. AGU*, *82*(47), Fall Meet. Suppl., S11D-03, 2001.

Gupta, S., S. S. Rai, K. S. Prakasam, D. Srinagesh, R. K. Chadha, K. Priestley, and V. K. Gaur, First evidence for anomalous thick crust beneath mid-Archean western Dharwar Craton, *Curr. Sci*, in press, 2003.

Harris, N. B. W., and S. Jayaram, Metamorphism of cordierite gneisses from the Bangalore region of the Indian Archean, *Lithos*, *15*, 89–98, 1982.

Kaila, K. L., and V. G. Krishna, Deep seismic sounding studies in India and major discoveries, in *Seismology in India—An Overview*, edited by H. K. Gupta and S. Ramasheshan, *Curr. Sci.*, *62*, 117–154, 1992.

Krishna, V. G., K. L. Kaila, and P. R. Reddy, Synthetic seismogram modeling of crustal seismic record sections from the Koyna DSS profiles in the western India, in *Properties and Processes of Earth's Lower Crust*, *Geophys. Monogr. Ser.*, vol. 51, edited by R. F. Mereu, S. Mueller, and D. M. Fountain, pp. 143–158, AGU, Washington, D. C., 1989.

Kumar, M. R., J. Saul, D. Sarkar, R. Kind, and A. Shukla, Crustal structure of the Indian shield: New constraints from teleseismic receiver functions, *Geophys. Res. Lett.*, *28*, 1339–1342, 2001.

Nguuri, T. K., J. Gore, D. E. James, S. J. Webb, C. Wright, T. G. Zengeni, O. Gwavava, and J. A. Shoke, Crustal structure beneath South Africa and its implications for the formation and evolution of the Kaapvaal and Zimbabwe cratons, *Geophys. Res. Lett.*, *28*, 2501–2504, 2001.

Percival, J. A., A. G. Green, B. Milkereit, F. A. Cook, W. Geis, and G. F. West, Seismic reflection profiles across deep continental crustal exposed in the Kapuskasing uplift structure, *Nature*, *342*, 416–419, 1989.

Rai, S. S., K. Priestley, K. Suryaprakasam, D. Srinagesh, V. K. Gaur, and Z. Du, Crustal shear velocity structure of the south Indian shield, *J. Geophys. Res.*, *108*(B2), 2088, doi:10.1029/2002JB001776, 2003.

Reddy, P. R., B. Rajendra Prasad, V. Vijaya Rao, K. Sain, P. Prasad Rao, P. Khare, and M. S. Reddy, Deep seismic reflection and refraction/wide-angle reflection studies along kuppam-palani transect in the southern granulite terrain, *Mem. Geol. Soc. India*, in press, 2003.

Rogers, J. J. W., The Dharwar craton and the assembly of Peninsular India, *J. Geol.*, *94*, 129–144, 1986.

Sarkar, D., K. Chandrakala, P. Padmavathi Devi, A. R. Sridhar, K. Sain, and P. R. Reddy, Crustal velocity structure of western Dharwar craton, South India, *J. Geodyn.*, *31*, 227–241, 2001.

Srinagesh, D., and S. S. Rai, Teleseismic tomographic evidence for contrasting upper mantles in South Indian Archean terrains, *Phys. Earth Planet. Inter.*, *97*, 22–41, 1996.

Taylor, P. N., S. Moorbath, B. Chadwick, M. Ramakrishna, and M. N. Viswanatha, Petrography, chemistry and isotopic ages of peninsular gneisses, dharwar acid volcanic, *Precambrian Res.*, *23*, 349–375, 1984.

Zandt, G., and C. J. Ammon, Continental crust composition constrained by measurements of crustal Poisson's ratio, *Nature*, *374*, 152–154, 1995.

Zhu, L., and H. Kanamori, Moho depth variation in southern California from teleseismic receiver functions, *J. Geophys. Res.*, *105*, 2969–2980, 2000.

B. K. Bansal, Department of Science and Technology, New Mehrauli Road, New Delhi 110 016, India.

R. K. Chadha, S. Gupta, K. S. Prakasam, S. S. Rai, and D. Srinagesh, National Geophysical Research Institute, Hyderabad 500 007, India. (ssrai_ngri@rediffmail.com)

V. K. Gaur, Indian Institute of Astrophysics, Bangalore 560 034, India.

K. Priestley, Bullard Laboratories, Madingley Rise, Madingley Road, Cambridge CB3 0EZ, UK. (keith@esc.cam.ac.uk)

Geophys. J. Int. (2000) **143**, 629–661

A re-assessment of focal depth distributions in southern Iran, the Tien Shan and northern India: do earthquakes really occur in the continental mantle?

A. Maggi, J. A. Jackson, K. Priestley and C. Baker

University of Cambridge, Department of Earth Sciences, Bullard Laboratories, Madingley Road, Cambridge, CB3 0EZ, UK.
E-mails: maggi@esc.cam.ac.uk; jackson@esc.cam.ac.uk; keith@esc.cam.ac.uk

Accepted 2000 May 30. Received 2000 May 16; in original form 1999 December 7

SUMMARY

We investigate the depth distribution of earthquakes within the continental lithosphere of southern Iran, the Tien Shan and northern India by using synthetic seismograms to analyse *P* and *SH* body waveforms. In the Zagros mountains of southern Iran, earthquakes are apparently restricted to the upper crust (depths of <20 km), whereas in the Tien Shan and northern India they occur throughout the thickness of the continental crust, to depths of $\sim$40–45 km. We find no convincing evidence for earthquakes in the continental mantle of these regions, in spite of previous suggestions to the contrary, and question whether seismicity in the continental mantle is important in any part of the world. In some regions, such as Iran, the Aegean, Tibet and California, seismicity is virtually restricted to the upper continental crust, whereas in others, including parts of East Africa, the Tien Shan and northern India, the lower crust is also seismically active, although usually less so than the upper crust. Such variations cannot reliably be demonstrated from published catalogue or bulletin locations, even from ones in which depth resolution is generally improved. In contrast to the oceanic mantle lithosphere, in which earthquakes certainly occur, the continental mantle lithosphere is, we suggest, virtually aseismic and may not be significantly stronger than the lower continental crust. These variations in continental seismogenic thickness are broadly correlated with variations in effective elastic thickness, suggesting that the strength of the continental lithosphere resides in the crust, and require some modification to prevalent views of lithosphere rheology.

Key words: continental mantle lithosphere, earthquakes, lithosphere rheology.

1 INTRODUCTION

The distribution of earthquake focal depths within the lithosphere is one of the most accessible indicators of its likely mechanical properties. In the continents, and away from obvious subduction zones, seismicity is usually concentrated in the upper 10–20 km of the crust and the lower crust is usually much less active or even completely aseismic (e.g. Chen & Molnar 1983; Chen 1988). These observations, combined with a clear correlation between the depth of the deepest oceanic intraplate earthquakes and the age of the oceanic lithosphere in which they occur (e.g. Wiens & Stein 1983), are usually taken to indicate that temperature is the dominant control on seismicity, with earthquakes restricted to regions of relatively low temperature (e.g. Brace & Byerlee 1970). Chen & Molnar (1983) estimated the limiting temperatures for earthquakes in crustal and mantle materials to be about 350 ± 100 °C and 700 ± 100 °C respectively, the different temperatures reflecting their contrasting compositions. Chen & Molnar (1983) and Chen (1988) also emphasized the occurrence of rare continental earthquakes close to probable Moho depths and perhaps in the uppermost continental mantle. These earthquakes were taken to indicate an important strength contrast between the lower crust and the mantle. The observations summarized above are largely responsible for a view of the continental lithosphere in which a lower crust of relatively low strength, where aseismic ductile deformation predominates, is sandwiched between relatively strong upper crustal and uppermost mantle seismogenic regions. This view has had an enormous influence on our views of continental tectonics.

This study re-examines the depth distribution of the seismicity in four regions: the Zagros and Makran of Iran, the Tien Shan of central Asia, and northern India. It was motivated by three developments.

(i) The first was the discovery that not all areas were as simple as the picture summarized earlier. In parts of the East African rift system, usually near or within Archaean shields, earthquakes occur throughout the thickness of the continental crust to depths of approximately 35 km, prompting a re-examination of the likely rheology of those regions (e.g. Nyblade & Langston 1995; Zhao *et al.* 1997; Foster & Jackson 1998). Earthquakes to depths of 30–40 km have also been found around the Shillong Plateau (Chen & Molnar 1990), near Lake Baikal in Siberia (Déverchère *et al.* 1991), and around the margins of the Caspian Sea (Priestley *et al.* 1994).

(ii) The second development was the relocation by Engdahl *et al.* (1998) of earthquakes in the International Seismological Centre (ISC) catalogue between 1964 and 1995 (subsequently updated to 1998) using an improved velocity model and also including the arrival times of additional phases, particularly teleseismic depth phases *pP*, *pwP* and *sP*, to supplement the direct *P* arrival times in the relocation procedure. In principle, these relocations (which we refer to as the EHB catalogue) should be better than the original ISC locations, and Engdahl *et al.* (1998) demonstrated that this is the case in several subduction zones, where improved depths give a sharper image of the descending slabs. The EHB catalogue shows a number of earthquakes deeper than 50 km in the Zagros, where previously none had been confirmed below 20 km, and, in the light of the Africa, Baikal and Caspian experiences, we wanted to see whether these were genuine.

(iii) A third recent development was the re-assessment of effective elastic thicknesses on the continents using gravity and topography by McKenzie & Fairhead (1997). Their general conclusion that the effective elastic thickness (T_e) on the continents is probably close to the thickness of the seismogenic crust (T_s) allows the simple interpretation that the strength of the lithosphere resides in that layer, although they were unable to estimate the depth to the top of any elastic layer. Since McKenzie & Fairhead's (1997) study, more information on T_e variations in Asia is now available (Maggi *et al.* 2000), and we wanted to see how these variations correlated with variations in T_s.

This study thus has two aims. One is to see whether the undoubted general improvement in locations shown by the EHB catalogue (Engdahl *et al.* 1998) is sufficiently good to reveal anomalies in the usual pattern of earthquake depth distribution on the continents. The second, and more important, is to see whether our rheological views of the continental lithosphere based on earthquake focal depths need modification in the light of the large amount of extra data now available since the original studies of 15–20 years ago.

We focus on four main regions: the Zagros and Makran of Iran, the Tien Shan, and northern India. The Zagros mountains form a linear intracontinental fold-and-thrust belt trending NW–SE between the Arabian shield and central Iran (Fig. 1). The belt is seismically very active, with frequent reverse faulting earthquakes of up to M_s7.0. Early studies used the presence of earthquakes deeper than 50 km in the ISC or USGS catalogues to postulate subduction of the continental Arabian shield beneath Iran in the Zagros (Nowroozi 1971; Bird *et al.* 1975), a view sometimes repeated more recently (e.g. Moores & Twiss 1995). However, neither local seismograph networks nor the modelling of teleseismic body waves from the larger earthquakes have found any focal depths deeper than 15–20 km (e.g. Jackson & Fitch 1981; Ni & Barazangi 1986; Baker *et al.* 1993). Moreover, in an earlier study Jackson (1980) showed that the apparently deep earthquakes were mostly poorly recorded by relatively few stations, which increases the trade-off between origin time and depth. Thus it appeared that there was no

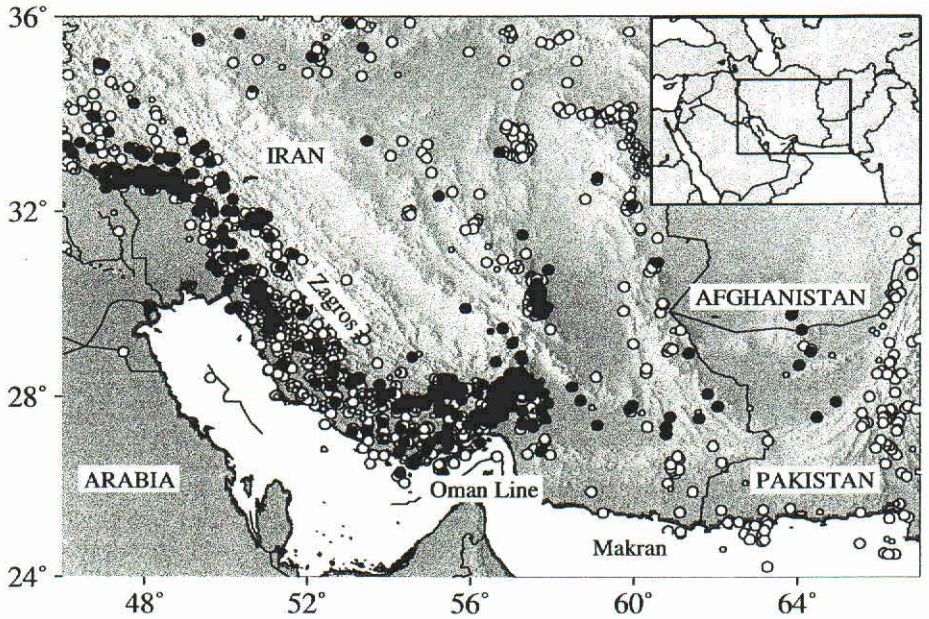

Figure 1. Seismicity in southern Iran from the Engdahl *et al.* (1998) catalogue (EHB) for 1964–1998. Events reported as shallower than 50 km are shown in white, while those reported at 50 km or deeper are shown in black. Large circles are those events whose depths were freely determined (flag DEQ) while small circles are events whose depth was fixed by the operator (flag FEQ; see text). The EHB catalogue is complete down to M_w5.2, although the magnitude range extends down to M_w4.5. The geographical location of the region is shown in the inset map.

evidence in the seismicity for subduction of continental crust, and shortening appeared to be accommodated by crustal thickening instead, with seismicity confined to the upper 20 km. However, more recently, the EHB catalogue and both the Harvard and USGS Centroid Moment Tensor (CMT) catalogues have reported depths as great as 80 km, even for quite large earthquakes whose waveforms can be studied in detail (Fig. 1 and Table 1). These depths, if correct, would require a re-assessment of our current views of the active tectonics.

At its southeastern end, the continent–continent collision zone in the Zagros merges along strike with the subduction of the Arabian Sea floor beneath the Makran coast. The change from continent to ocean occurs near 57°E in a region of complicated structure known as the Oman Line (Fig. 1). The Makran subduction zone is known to produce earthquakes to depths of approximately 200 km (Jackson & McKenzie 1984; Laana & Chen 1989; Byrne *et al.* 1992). Again, we re-examined earthquakes in the CMT and EHB catalogues to see whether the tectonic change associated with the Oman Line is revealed in an abrupt or gradual change in the earthquake depth distribution. In addition we wanted to see how depths obtained from body wave modelling compared with EHB depths in a region of known subcrustal seismicity.

We then re-examined published focal depths in the Tien Shan, another intracontinental collision belt, this time in central Asia (Fig. 12). This range has been influential in our views of continental tectonics because of the confirmed presence of earthquakes at depths of 40–50 km, near the probable depth of the Moho, in addition to the more common earthquakes at depths of 10–20 km (Chen & Molnar 1983; Nelson *et al.* 1987). The region has attracted considerable interest from seismologists, mainly because of international treaties related to nuclear testing, and we were anxious to see whether the additional data now available required any modification of these earlier views. We were conscious of the African experience, where seismicity occurs throughout the continental crust and is not restricted to the upper crust and the mantle.

Finally we looked at focal depths in north India and the Himalaya (Fig. 14). In the Shillong Plateau and southern Nepal, earthquakes at ~50 km depth have been interpreted to be in the mantle (Chen & Molnar 1990; Chen & Kao 1996), and others near the Himalayan front with depths of 50 km or more reported by the Harvard CMT or EHB catalogues apparently support this view. We re-examine the evidence for mantle focal depths in these and other earthquakes in the region, making use of the fact that we now have much better estimates of Moho depths, mostly from receiver function studies, than were available to Chen & Molnar (1983). The question of whether we can confirm that some earthquakes occur in the uppermost continental mantle is one of particular interest.

Table 1. The Zagros–Makran events analysed in this study. Published depths are listed from the EHB, Harvard CMT and USGS CMT catalogues, together with waveform-determined centroid depths. In the EHB column * indicates a depth which was fixed by the operator (flag FEQ), whereas all other EHB depths were freely determined in the EHB inversion (flag DEQ; see text). In the HRV column † indicates a depth that was fixed prior to the CMT inversion. Multiple events are indicated by an 'm' in the M_w column. In the method column, 'a' refers to full *P* and *SH* waveform inversion and 'b' to inversion for depth only. For class 'a' events, the strike, dip, rake and moment are from the minimum-misfit solution. For class 'b' events, the scalar moment is that published in the Harvard CMT catalogue. The events of 1985.02.02, 1985.03.27, 1992.03.29 and 1994.07.31 are discussed in the main text. Details of the other inversions are in the Appendix.

Date	Time	Lat. N	Lon. E	M_w	M_0	Depth (km)				Fault Plane			Method	Region
						EHB	HRV	USGS	*P/SH*	Strike	Dip	Rake		
1977 04 26	16:25	32.65	48.90	5.5	2.0e17	23	20		20				b	Zagros
1980 10 19	17:24	32.70	48.58	5.6	3.2e17	18	15		17	327	19	120	a	Zagros
1983 02 18	07:40	27.91	53.82	5.2	6.9e16	26	15†		6				b	Zagros
1985 02 02	20:52	28.36	52.97	5.6	2.8e17	16	22		11	128	37	91	a	Zagros
1985 03 27	02:06	31.59	49.92	5.1	7.3e16	53	84	150	15				b	Zagros
1988 08 30	17:30	29.96	51.72	5.1	3.0e16	24	15†		16				b	Zagros
1990 11 06	18:45	28.32	55.46	6.5	7.1e18	10	15	4	7	275	30	101	a	Zagros
1993 03 29	15:20	28.00	52.74	5.2	7.3e16	43	40		13				b	Zagros
1993 06 22	16:32	30.18	50.83	5.2	9.1e16	43	15		5	301	44	65	a	Zagros
1994 06 20	09:09	29.05	52.67	5.8	6.0e17	15	15	7	9	255	74	−3	a	Zagros
1994 07 31	05:15	32.69	48.42	5.5	2.0e17	41	18		14	288	17	90	a	Zagros
1998 08 21	05:13	34.30	48.20	4.9	3.3e16	22*	22		9				b	Zagros
1999 05 06	23:00	29.54	51.93	6.1	1.9e18		17	38	7	44	82	−6	a	Zagros
1977 03 22	11:57	27.60	56.42	6.0	1.5e18	15	10		12	77	34	112	a	Oman line
1977 12 10	05:46	27.68	56.60	5.6	2.9e17	13	15†		18	291	28	138	a	Oman line
1983 07 12	11:34	27.61	56.40	5.9	1.0e18	20	47	20	17	227	50	75	a	Oman line
1987 04 29	01:45	27.42	56.11	5.6	3.7e17	9	15		10	265	41	112	a	Oman line

2 METHODS

Although the confinement of seismicity to the upper continental crust had been known in California for some time, it was not until the study by Chen & Molnar (1983) that its more general pattern was demonstrated. The reason for this was the difficulty in obtaining reliable focal depths outside dense local networks of seismic stations. Locations based on the arrival times of teleseismic *P* waves alone, the method routinely employed by the ISC, the USGS and its predecessors, suffer notoriously from a trade-off between origin time and depth, which can cause errors in focal depth of several tens of kilometres or even more. This effect arises because of the limited range of teleseismic ray parameters, with ray paths illuminating only a small part of the lower focal sphere (e.g. Jackson 1980). By the early 1980s the common use of teleseismic synthetic seismogram techniques, which can estimate centroid depths to typically ± 4 km, and the increasing number of temporary local seismic surveys allowed Chen & Molnar's (1983) compilation to be made. It is those synthetic seismogram techniques that we exploit here. Two types of analyses were performed, depending on the quality of the available waveform data.

2.1 Inversion for source parameters and depth

Where possible we used long-period *P* and *SH* waveforms to constrain the earthquake source parameters. We took digital broad-band records from stations of the Global Digital Seismographic Network (GDSN), deconvolved the station response from the records and then reconvolved them with the response of the old World Wide Standard Seismic Network (WWSSN) 15–100 long-period instruments, which have a bandwidth that is well suited for the resolution of shallow, moderate-sized events (e.g. McCaffrey & Nábělek 1987). Where broad-band data were not available, we used the original long-period digital data. Onset arrival times were measured either from the original broad-band data or from short-period records.

We then used the MT5 version of McCaffrey & Abers' (1988) algorithm, which inverts *P* and *SH* waveform data to obtain the strike, dip, rake, centroid depth, seismic moment and source time function. We always constrained the source to be a double couple. The procedure assumes that the source can be represented as a point (the centroid) in space, but not in time. The time history of displacement on the fault is represented by a source time function made up of a series of overlapping isosceles triangles. The seismograms are formed by the combination of direct *P* or *SH* waves with the surface reflections *pP*, *sP* and *sS* and near-source multiples. Amplitudes are corrected for geometrical spreading, and for anelastic attenuation using a Futterman *Q* operator with a value for t^* of 1.0 s for *P* and 4.0 s for *SH* waves. Uncertainties in t^* lead to uncertainties in source duration and seismic moment, but have only a small effect on centroid depth and source orientation. To avoid upper mantle triplications and interference from core phases, *P* waveforms are used in the distance range 30°–90° and *SH* waves in the range 30°–75°.

The inversion procedure adjusts the relative amplitudes of the source time function elements, the centroid depth, the seismic moment and the source orientation (strike, dip, rake) to minimize the misfit between observed and synthetic seismograms. We refer to this solution as the minimum-misfit solution. The covariance matrix associated with this solution usually underestimates the true uncertainties associated with the source parameters. A better estimate of the uncertainties is found by fixing some of the source parameters at values close to but different from those of the minimum-misfit solution, and seeing whether the match of observed to synthetic seismograms deteriorates (e.g. Molnar & Lyon-Caen 1989; Taymaz *et al.* 1991). We use this type of sensitivity analysis here. Changes in the depth and/or source time function will influence the width of the first pulse and the presence or absence of later pulses, while changes in the focal mechanism will influence the polarity and relative amplitudes of the pulses. The focal mechanism of an event is best constrained by stations that plot close to the nodal planes on the *P* or *SH* focal sphere.

Uncertainties in the seismic moment and centroid depth arise from errors in the source velocity model. Detailed velocity models are rarely known in the source regions of the earthquakes studied here. In general we used a velocity with an average *P* velocity of 6.0 km s^{-1} above the source and 6.8 km s^{-1} below the source, unless (in the case of a few earthquakes in the Makran, for example) the events were found to be genuinely subcrustal, in which case we used a 35 km crust of average *P* velocity 6.8 km s^{-1}, and a half-space mantle of *P* velocity 8 km s^{-1}.

2.2 Inversion for depth only

For some earthquakes there was insufficient good digital data for a full inversion for source orientation, depth, source time function and moment. In these cases we concentrated on constraining the depth by fixing the strike, dip and rake to suitable values (usually those given by the corresponding Harvard CMT solution) and allowing the depth, source time function and moment to vary.

In cases where only the depth was being investigated, we used the broad-band or short-period records when possible, as the depth phases are more easily distinguishable than in long-period records. In these cases we performed forward modelling of the vertical-component seismograms using the program WKBJ3 (Chapman *et al.* 1978). This program traces rays through a 1-D spherical earth using the WKBJ approximation for turning rays, allowing for the interference of rays and geometric spreading. We used the AK135 earth model (Kennett *et al.* 1995) for the generation of synthetics, and included only *P*, *pP* and *sP* waves. The synthetics were convolved with the responses of the individual broad-band or short-period stations, and corrected for attenuation using a Futterman operator with $t^*=1$ before being compared with the data.

3 THE ZAGROS–MAKRAN REGION

We analysed a total of 24 events in the Zagros–Makran region (Table 1), 12 of them with $M_w > 5.5$. Of these, 16 had digital data of sufficient quality for a complete inversion of *P* and *SH* waveforms, and eight were analysed only to determine their depths. The EHB catalogue reported depths greater than 30 km for nine of the events we studied (of which four were in the Zagros with depths apparently greater than 40 km). The EHB catalogue contains a qualification of the earthquake depth determination. Locations in which the depth is free in the inversion are marked DEQ. Poorly determined depths are flagged XEQ, while other depths are fixed either by the inversion program (LEQ) or by the operator (FEQ). All nine of the

events reported deeper than 30 km were of type DEQ. The minimum-misfit fault plane solutions and depths for the events whose *P* and *SH* waveforms were inverted for source parameters, and our re-assessed depths for the others, are tabulated in Table 1. Details of the inversions and waveforms of events not discussed in the main text are contained in the Appendix.

Below we present a detailed description of four events in the Zagros region, partly to illustrate the data quality and techniques, and partly because these are particularly interesting earthquakes. The first and second examples (1994.07.31 and 1993.03.29) are of earthquakes that we re-determine as shallow (14 and 13 km) but which were reported to be much deeper (41 and 43 km) by the EHB catalogue. We analyse the first event using long-period *P* and *SH* waveform inversion, and the second using forward modelling of *P* waveforms. The third and fourth examples (1985.02.02 and 1985.03.27) were both reported by the Harvard CMT catalogue as normal faulting events, which are extremely unusual mechanisms to find in the Zagros fold-and-thrust belt. For the third event *pP* arrivals corresponding to a depth of 122 km were reported by the ISC, while the fourth event was reported at 53 km depth by the EHB catalogue and at 84 km by the Harvard CMT catalogue. We analyse the third event by long-period waveform inversion, and discover that it is a multiple event composed of two thrusting earthquakes. We use forward modelling of long-period *SH* waves to determine the depth of the fourth earthquake (15 km), and find some evidence for it possibly being a thrust faulting event.

3.1 1994 July 31, NW Zagros (M_w5.5)

All the observed *P* and *SH* waveforms used in the inversion for this event are shown in Fig. 2, along with the best-fit synthetic waveforms. Although available stations are restricted to the northern half of the focal sphere, they are well distributed within that, and the combination of *P* and *SH* waveforms constrains the inversion solution quite tightly, as we show

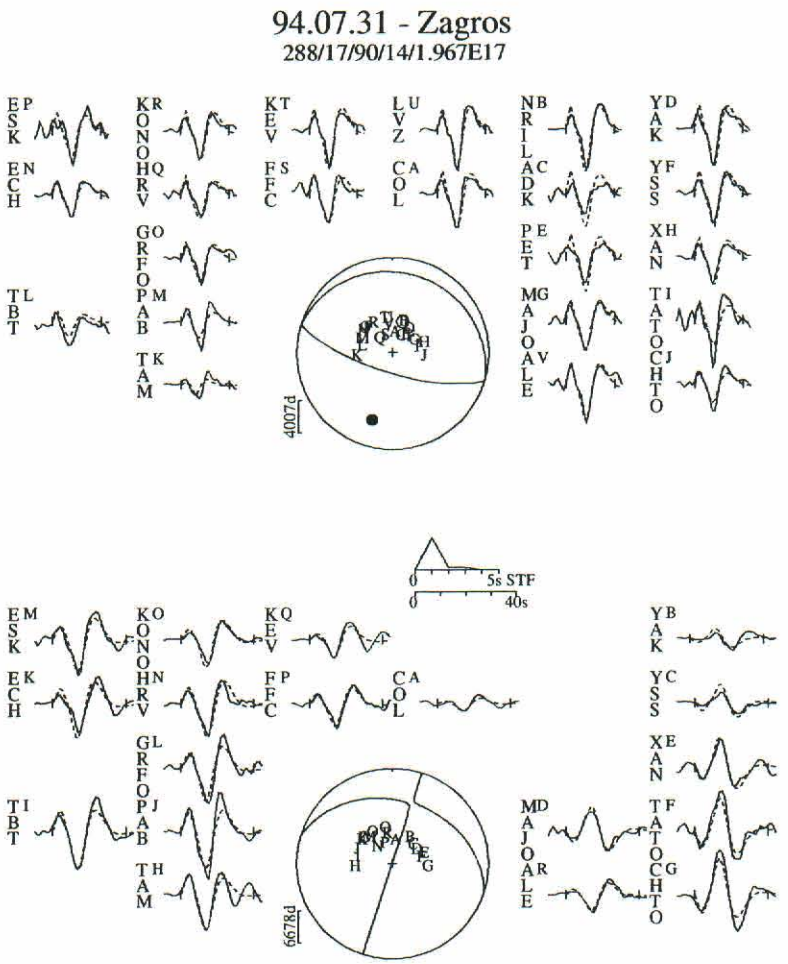

Figure 2. Minimum-misfit solution for the event of 1994 July 31 in the Zagros. The values beneath the event header give strike, dip, rake, depth in km and seismic moment in N m. This solution was calculated using a velocity model consisting of a 10 km thick layer with V_P=6.0 km s^{-1}, V_S=3.45 km s^{-1}, ρ=2.78 g cc^{-1} over a half-space with V_P=6.8 km s^{-1}, V_S=3.92 km s^{-1} and ρ=2.91 g cc^{-1}. The upper sphere shows the *P*-wave radiation pattern and the lower sphere that for *SH*. Both are lower-hemisphere projections. The station code by each waveform is accompanied by a letter corresponding to its position in the focal sphere. These are ordered clockwise by azimuth. The solid lines are the observed waveforms; the dashed lines are the synthetic waveforms. The inversion window is marked by solid bars at either end of the waveform. P and T axes within the sphere are represented by solid and open circles respectively. The source time function is shown below the *P* focal sphere, with the waveform timescale below it.

below. Synthetics were calculated for a 10 km thick layer with velocity $V_p=6.0$ km s^{-1} over a half-space of $V_p=6.8$ km s^{-1}, as described above. The minimum-misfit solution shows a thrust faulting mechanism with a simple time function of about 2 s duration and a depth of 14 km. The low dip (17°) of the shallow-dipping nodal plane is unusual in the Zagros, where high-angle (40–60°) reverse faults are common, but is similar to that of two other events nearby (1977.04.26 and 1980.10.19), also studied here (see Table 1).

The quality of the solution in Fig. 2 was assessed by tests, illustrated in Fig. 3, which shows the observed and synthetic *P* and *SH* seismograms at selected stations. The top line contains the minimum-misfit solution in Fig. 2. In line two the depth was held fixed at 41 km (as reported in the EHB catalogue) while all the other source parameters were allowed to be free to change in the inversion, which was started at the published CMT best-double-couple orientation (strike 309°, dip 41°, rake 114°). The result is a minimum in dip, depth, source time function and moment space, but is very much a worse fit than the minimum-misfit solution shown in the first line. In particular, there is no evidence in the *P* waveforms for the separation of the direct *P* and surface reflections, which would certainly be apparent if the depth were really 41 km (and which the inversion has attempted to minimize by rotating the nodal planes). The third and fourth lines show inversions in which the depth is held fixed at 18 and 10 km, while all other source parameters are free. At 18 km (line 3) the fits at LVZ (*P*), TATO (*SH*) and PAB (*SH*) in the third line are significantly worse than in line 1. The fits in line 4 (depth 10 km) are not significantly worse than in line 1, but the inversion has compensated for the shallow depth by requiring a double pulse to the source time function, which is possible but not very likely for an event of this size (M_w5.5). If the time function is required to be short as well as the depth fixed at 10 km (line 5), the fit at all stations deteriorates. We conclude that the uncertainty in our estimate of the centroid depth for this earthquake (14 km) is unlikely to be greater than ± 4 km.

This earthquake, therefore, is significantly shallower than reported by the EHB catalogue (14 ± 4 versus 41 km). Note that for an earthquake of this size ($M_0=2\times10^{17}$ N m) the source dimension is unlikely to exceed $\sim$5 km, which would be the maximum allowable difference between the position of rupture nucleation detected at short periods and the centroid position estimated at long periods. The difference between the EHB depth and our re-determined centroid far exceeds that.

3.2 1993 March 29, S Zagros (M_w5.2)

The teleseismic waveform data available for this relatively small (M_w5.2) event were insufficient for complete body waveform inversion, so we performed forward modelling of the broad-band records directly using WKBJ3. We assumed a source orientation given by the Harvard CMT mechanism, which was a thrust with strike 104°, dip 28°, rake 72° , similar in orientation to many other known earthquakes nearby (e.g. Baker *et al.* 1993). As the earthquake was relatively small we expect a time function of only 1–2 s duration. To generate synthetic seismograms we used an impulse time function, but

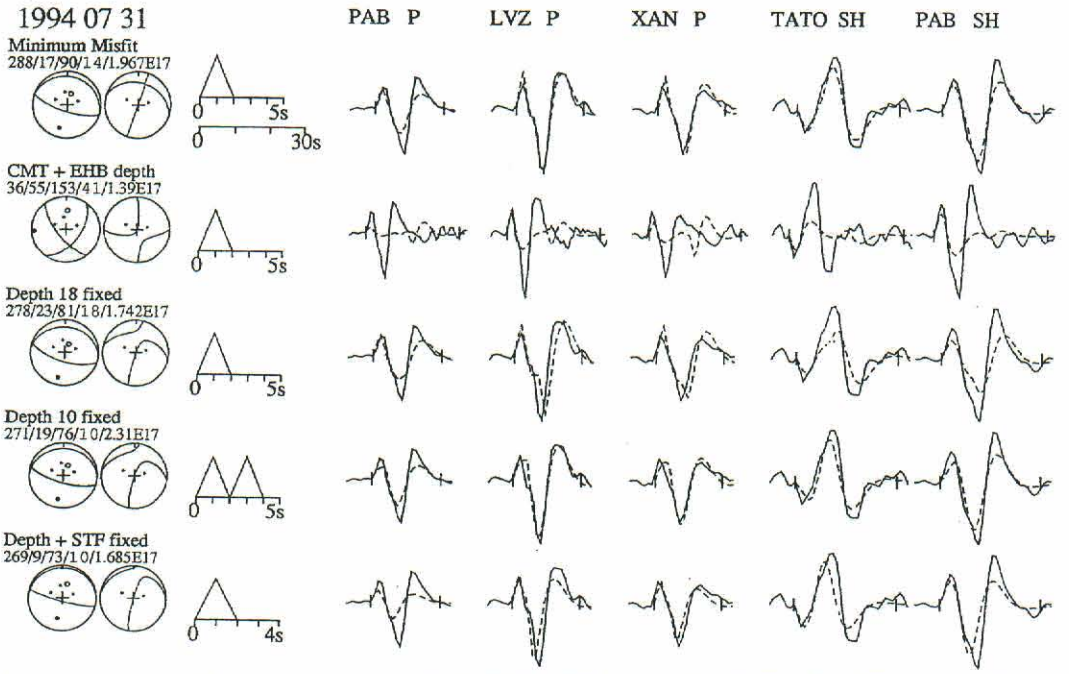

Figure 3. Comparisons between different inversion solutions for the 1994 July 31 Zagros earthquake. The *P* and *SH* radiation patterns are shown in the first column, with the strike, dip, rake, depth in km and scalar moment in N m above the two focal spheres. The source time function for each solution is in the second column, followed by the observed and synthetic waveforms. Line 1: the minimum-misfit solution; line 2: the result of an inversion started from the published Harvard CMT solution with the fixed EHB depth of 41 km; lines 3–5: tests for the uncertainty in the depth; in all these inversions the depth was held fixed and all other parameters were free to change. In line 5 the duration of the source time function was also held fixed.

with the addition of attenuation (a Futterman operator with $t^*=1$ s for P waves) the effect on the synthetic seismograms is equivalent to a time function of ~1 s.

Fig. 4 shows the comparison between data and synthetics for two stations, XAN (Δ 48°, Az 068°) and YSS (Δ 70°, Az 047°). In order to use records as similar as possible to those on which the station operators had identified their reported phases, we transformed the original broad-band records into records with the WWSSN short-period response. The seismograms are aligned on the first prominent trough in the waveforms after the P arrival time published by the ISC. The synthetics calculated for a depth of 13 km (our preferred depth, see Table 1) mirror the essential features of the short-period seismograms above them. One early peak that is present at both stations (~2 s after the P arrival at XAN and ~4 s after the P arrival at YSS) is not fitted by the synthetic seismograms. We cannot fit both this early peak and the group we are currently fitting by using only P, pP and sP rays. Also shown in Fig. 4 are synthetics calculated for the EHB reported depth of 43 km. The position of the pP peak in the synthetic corresponds to a pP arrival time identified by the ISC at XAN. A depth of 43 km for this event would, however, ignore the more prominent arrivals at ~15–18 s at both stations, arrivals that had been reported to the ISC, but not identified as depth phases.

Despite the poor quality of the data available, we conclude that this earthquake was shallow (~13±3 km) rather than at ~40 km depth as reported by both the EHB and HRV catalogues.

3.3 1985 February 2, S Zagros (M_w5.6)

This earthquake has a wide range of depths reported for it: 16 km by the EHB catalogue, 22 km by the Harvard CMT catalogue and 44 km by the ISC, who also report a depth of 122 km based on pP–P arrival times. In addition, Harvard give a CMT solution that is nearly a pure double-couple source (eigenvalues of 1.81, 0.03 and −1.85, all $\times 10^{17}$ N m) indicating normal faulting in the crust (22 km depth) with a strike parallel to the fold-and-thrust belt, which would be extremely interesting if it were confirmed. Finally, several stations in the ISC bulletin quote S-wave arrivals with unusually large traveltime residuals of between +20 and +30 s.

In our analysis below we show that this earthquake was probably a double event, consisting of a small foreshock followed around 25 s later by a larger, thrust-faulting earthquake in roughly the same place. Both subevents are at shallow depths. We suspect that the S phase reported with a +20 to +30 s residual is actually from the second subevent, and that it is the P arrival from the second subevent that was mistaken for the pP arrival for the first subevent, explaining the apparent depth of 122 km from pP–P times.

Observed P and SH seismograms and synthetics from our preferred inversion solution are shown in Fig. 5. The amplitudes of the observed P onsets are comparable with the noise level in the long-period waveforms, so the arrival times indicated by the arrows were taken from short-period records, which were clear. Baker (1993) showed that on the stacked short-period array data at Eskdalemuir (EKA), Yellowknife (YKA) and Warramunga (WRA), the P onsets are impulsive and unambiguously compressional. These polarities conflict with the expected dilatational first motions at these stations if the focal mechanism was indeed normal faulting, but are compatible with a thrust parallel to the regional strike of the Zagros folds nearby. At all stations there is a large pulse about 25 s after the initial P onset time, and this pulse has the characteristic inverted W shape of a shallow (~10 km depth) reverse faulting earthquake of magnitude ~6 (e.g. Jackson & Fitch 1981).

In our waveform modelling the mechanism of the first subevent was fixed with the nodal planes in the same orientation as the Harvard CMT solution, but with the rake changed so that the mechanism is now a thrust (compatible with the compressional onsets at ESK, YKS and WRA). The first event is very small, with a moment less than a tenth of that of the second subevent, so it makes only a very small contribution to the form of the synthetic seismograms. The second subevent

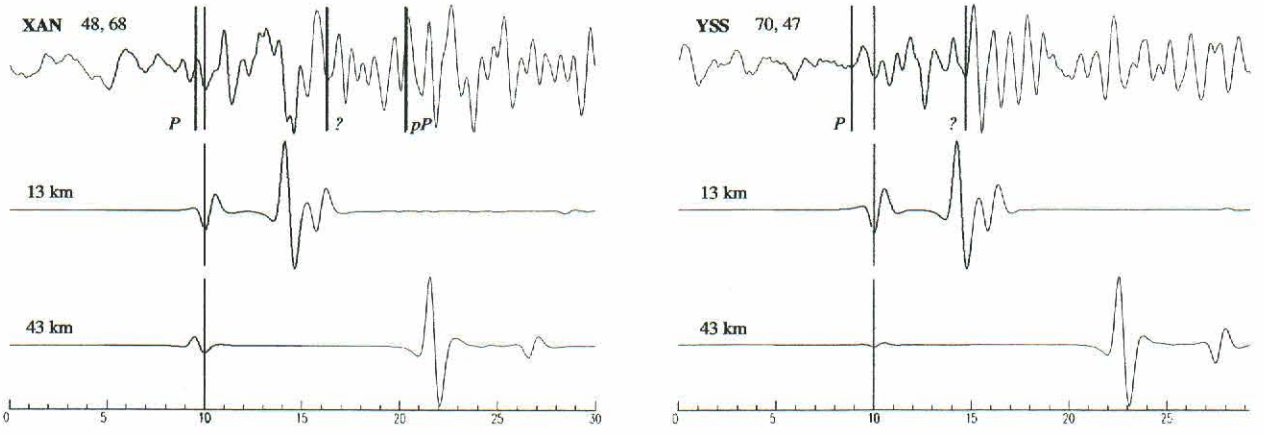

Figure 4. Forward modelling of the focal depth for the 1993 March 29 Zagros earthquake using WKBJ3 for (a) station XAN (Δ 48° and Az 068°) and (b) station YSS (Δ 70° and Az 047°). For both stations the first trace is the broad-band vertical record, which has been transformed to one with the WWSSN short-period response, with the ISC time picks shown as thick black lines. The ISC phase identifications for the picks are also shown, with unidentified phases shown by question marks. The second trace is a synthetic computed for a depth of 13 km, and the third trace is a synthetic computed for the EHB reported depth (43 km).

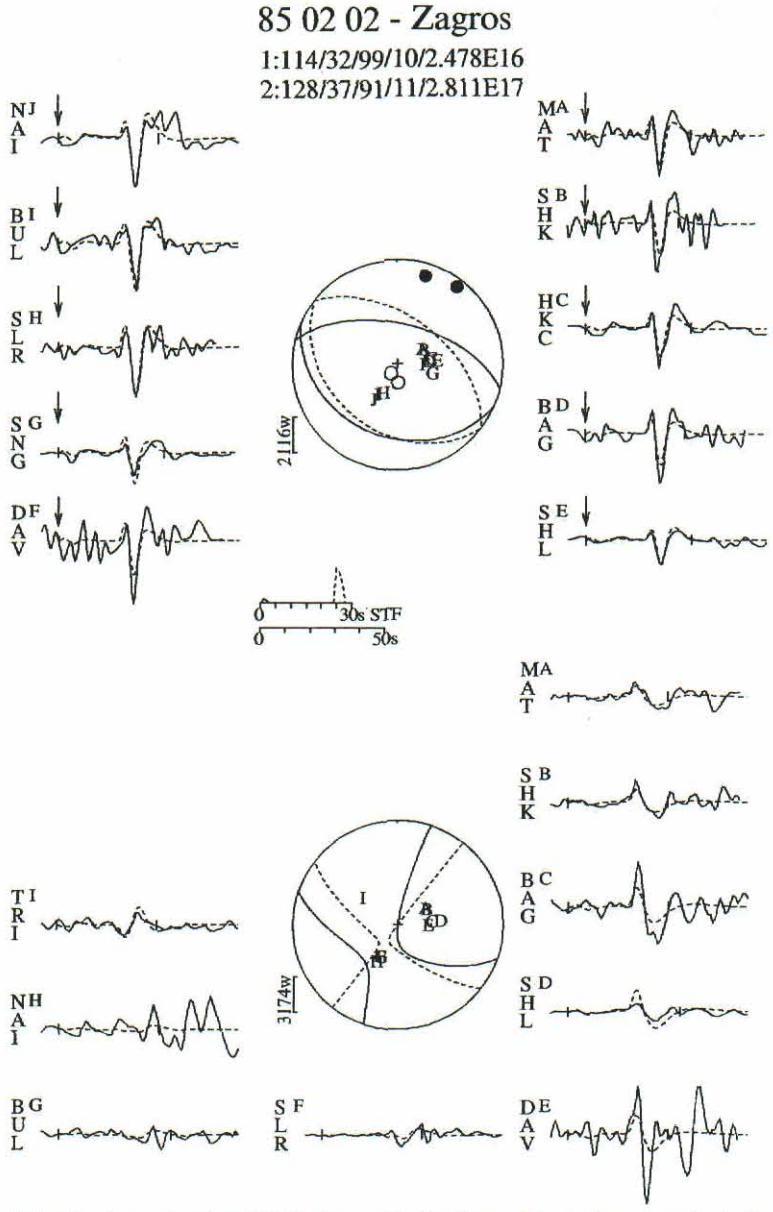

Figure 5. Minimum-misfit solution for the earthquake of 1985 February 2 in the Zagros. The display convention is the same as in Fig. 2. There are two subevents in this case. The two mechanisms are printed under the header and the second source is represented as a dashed line within the focal sphere. The source time function indicates two distinct ruptures, the second occurring ~22 s after the onset of the first. Arrows mark the *P* arrival time determined from short-period records.

was modelled from the data, inverting for source orientation, moment, depth and origin-time offset from the first subevent. This gives a thrust mechanism for the second event with planes that dip at similar angles to the CMT solution, but with the slip vector rotated clockwise by about 15°. We obtained this solution using a velocity model consisting of a 7 km layer (V_p 6.0 km s^{-1}) over a half-space (V_p 6.8 km s^{-1}).

Fig. 6 shows tests to illustrate the robustness of our modelling. The top line shows the fit of *P* and *SH* waveforms at selected stations obtained for our preferred solution in Fig. 5. The second line shows the fit obtained for the Harvard CMT solution. The first-motion amplitudes are much larger than those actually observed and this mechanism fails to account for the second pulse seen at all stations on the *P* waveforms. The solution in the third line fixes the fault orientation at that of the Harvard CMT solution and investigates the possibility that the second pulse is the result of the surface-reflected phases *pP*, *sP* and *sS*. We have allowed the depth and moment to vary in this inversion. The plots show that, for a depth of about 85 km, it is possible to obtain a second pulse with the correct polarity and onset time for the *P* waveforms. However, the amplitudes of the first motions are larger than observed, and the fit is

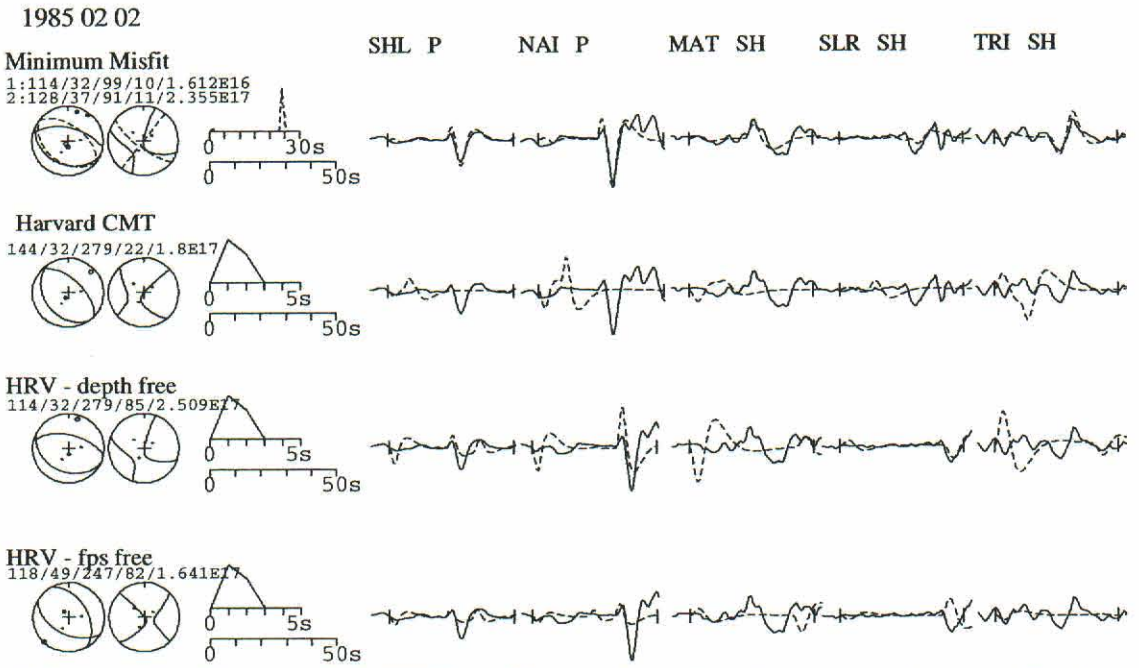

Figure 6. Comparison of possible solutions for the 1985 February 2 Zagros earthquake. The display convention is the same as in Fig. 3. Line 1 shows the minimum-misfit solution in Fig. 5. Line 2 shows a solution in which the source orientation and depth were fixed to the Harvard CMT solution. In line 3 the source orientation was held fixed at the Harvard CMT solution, but the depth was free to change. In line 4 both the source orientation and depth were allowed to vary from the Harvard starting model.

also noticeably less good for the *SH* waveforms (the onsets at MAT and TRI are much larger than are observed and the *sS* phases are smaller than those required to match the observed waveforms). The fourth line shows the results of a similar test where the fault orientation is also allowed to vary. This results in a better fit to the amplitudes of the first motions but fails to provide an adequate fit to the second pulse.

Therefore, we believe that this earthquake consists of two subevents with shallow depths. The mechanism of the first is too small to be modelled using body waves, but compressional arrivals on stacked array data suggest thrusting, not normal faulting. The second subevent occurred 25 s after the first. Its mechanism can be constrained by the modelling of body waves, which confirms a thrust mechanism and a depth of $\sim$11 km, comparable with the EHB depth of 16 km. The first event was too small to determine formal errors; for the second event, the uncertainty in depth is about $\pm$4 km. In our interpretation neither the fault type or depth(s) of this earthquake are unusual in the Zagros.

3.4 1985 March 27, NW Zagros (M_w5.1)

The Harvard CMT catalogue reports a reasonably good double-couple solution for this event (eigenvalues of 5.50, 0.81 and -6.35, all $\times 10^{16}$ N m), indicating normal faulting and a centroid depth of 84 km, both of which would be extremely surprising in the Zagros if they were to be confirmed. The EHB catalogue reports a depth of 53 km.

The long-period *P* waveforms for this event were barely detectable above the noise, but the long-period *SH* waveforms had roughly double the amplitude of *P*, and could be used for forward modelling and testing of various source geometries. Fig. 7 shows synthetic and observed *SH* waveforms in order to compare three different source models for this earthquake. The first model (a) is that reported in the Harvard CMT catalogue. The synthetics fit the amplitude and width of the first peak at four out of the six stations, and also try to fit a smaller, second peak, most visible at RSON, as an *sS* arrival. It is this second peak at RSON that lends support to the Harvard CMT depth of 84 km. However, the second peak is not matched at eastern stations (SHIO, CHTO, NWAO), nor are the amplitudes and widths of the first pulses matched at CHTO and NWAO. The second model (b) in Fig. 7 retains the Harvard CMT normal faulting mechanism but at a shallower depth of 15 km. In this model the amplitude and width of the first peak are fitted well at all stations, and any later arrivals are ignored. The third model (c) is a thrusting mechanism (strike 115°, dip 65°, rake 65°, similar to other focal mechanisms nearby) at a depth of 15 km. Once again the first pulse is well fitted both in amplitude and width at all stations, and the second pulse is ignored.

Given the level of noise in these records (approximately half the *SH*-wave amplitude), it is quite possible that the second pulses at RSNO, RSNY and GRFO are due either to noise or to some phase other than *sS*. To investigate this further, we show in Fig. 8 three vertical-component array stacks for this earthquake, taken from Baker (1993). The noise level in these stacks is significantly lower than that for the single seismograms, which means that the *P*-wave onsets are visible. The expected *pP* and *sP* arrival times for a depth of 84 km are shown on the traces and do not correspond to significant features in the seismograms. Therefore, we conclude that this event is more likely to have had a shallow depth, occurring at $\sim$15 km.

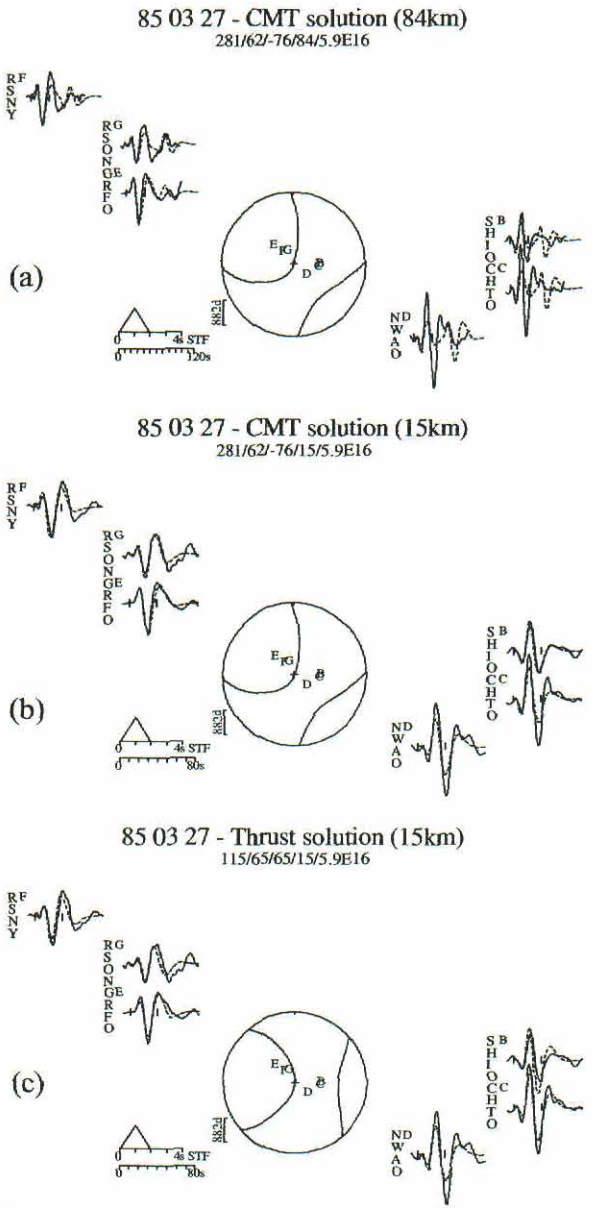

Figure 7. Forward modelling comparison of three solutions for the 1985 March 27 earthquake in the Zagros. Only the *SH* focal spheres are shown. The display convention is the same as in Fig. 2. (a) The CMT focal mechanism (a normal faulting earthquake) at the CMT-determined depth of 84 km. (b) The same normal faulting mechanism at 15 km depth. (c) A thrusting mechanism also at 15 km depth. Note that the timescales in (b) and (c) are different from (a).

As Fig. 7(c) shows, the long-period *SH* data can be fitted just as well by a thrust as by a normal faulting mechanism. The first arrivals on the stacked array data are all compressional (Fig. 8), which is consistent with a thrust but not with a normal fault. The available data do not allow us to constrain the source parameters tightly, but seem to us to favour a thrust faulting mechanism with a shallow (10–15 km) depth, which would not be at all unusual, rather than a deep normal faulting event, which would be unique in the NW Zagros.

3.5 The Zagros–Makran region: summary

The results of our investigations in this region are summarized in Table 1 and Figs 9 and 10, and when combined with other studies of additional earthquakes using the same techniques (Table 2) can be used to form a clearer picture of the focal depth distribution. Of the five Zagros earthquakes in Tables 1 and 2 reported with depths of greater than 40 km by the EHB catalogue, all are shown to have shallow depths of approximately 15, 13, 5, 14 and 7 km. Two of these earthquakes were also given depths of 40 and 84 km by the Harvard CMT catalogue. The two apparently normal faulting events reported by the Harvard CMT catalogue (1985.02.02 and 1985.03.27, discussed above) are more likely to have had thrust faulting mechanisms. There is no evidence in the events studied here or by others using the same methods (Table 2) for earthquakes significantly deeper than 20 km in the Zagros, in agreement with local microearthquake surveys. It is clear that significant mislocations in depth can occur in the EHB catalogue, even amongst good-quality hypocentres. We discuss possible reasons for these discrepancies later (Section 6.1). Although the EHB catalogue reports other small Zagros earthquakes with depths greater than 50 km (Fig. 1), we view these depth determinations with scepticism. Our image of the depth distribution in the Zagros is thus unchanged from the days of Chen & Molnar (1983), with earthquakes largely confined to the upper crust (Fig. 10a) and no evidence in the form of mantle earthquakes for active subduction.

Near the Oman line there is some indication that the seismicity extends to greater depths in the crust, but the sample is quite small (Fig. 10b). More significant is one earthquake whose depth of 28 km, deeper than any in the Zagros, was confirmed by long-period *P* and *SH* waveforms. We show a selection of those waveforms in Fig. 11 to emphasize how different they are from the more common earthquakes at 10–15 km (compare with Fig. 2). One genuine shallow normal faulting event (1987.12.18 at 10 km depth) near the Oman Line has also been confirmed by *P* and *SH* waveforms (Fig. 9c; Baker 1993). The earthquake of 1970.11.09 at 100 km depth (Fig. 9c) probably occurred in the subducting slab beneath the Makran, and is discussed below.

It has been known for some time that the Makran region experiences earthquakes with depths genuinely deeper than 50 km. Of interest here is how the EHB and CMT depths compare with those confirmed by waveform modelling. Tables 1 and 2 list nine earthquakes whose depths are estimated to be in the range 50–170 km by the EHB catalogue. For eight of these events, waveform analysis, either by *P* and *SH* modelling or by the identification of *pP* and *sP* on short-period records (relatively easy at these depths), confirms the depths to be within ± 10 km of the EHB estimates. Only in one case (1994.12.10) is the discrepancy greater (17 km). The Harvard CMT catalogue estimates two depths to be greater than 100 km, both of which are similarly confirmed to within ± 15 km (Table 1). The tectonic view of the Makran expounded by Jackson & McKenzie (1984), Laana & Chen (1989) and Byrne *et al.* (1992) is thus unmodified by these results, with earthquakes in the upper crust and also within a subducting slab dipping north at $\sim 26°$ (Figs 9b and 10c and d). The deep earthquake of 1970 November 9 (100 km) appears to lie on the down-dip projection of this slab, at its western edge (Fig. 10d).

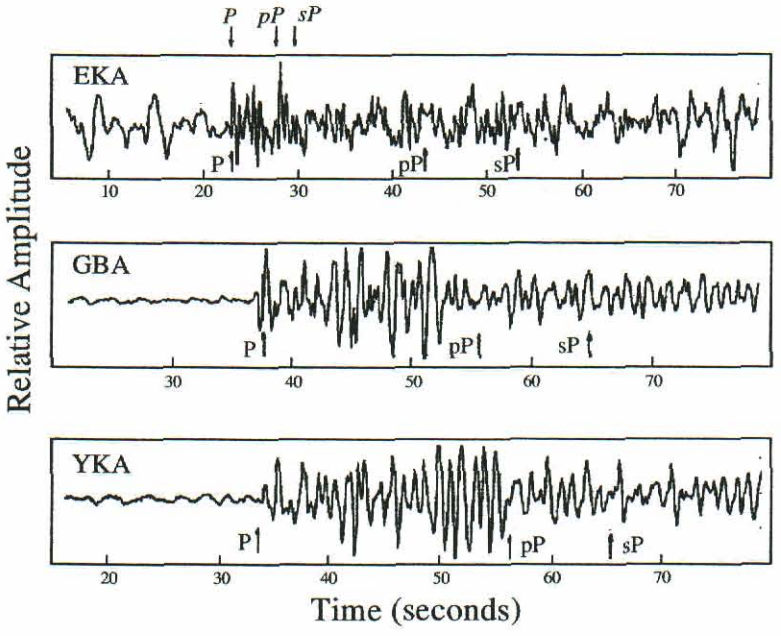

Figure 8. Stacked array seismograms for the 1985 March 27 Zagros event. The arrows show the expected *P*, *pP* and *sP* arrival times for an event depth of 84 km (in bold, below each trace) and 15 km (in italics, above the top trace). This figure was modified from Baker (1993).

4 THE TIEN SHAN REGION

The Tien Shan form an active intracontinental mountain belt within central Asia. In this study we concentrate on the region north of 40°N, away from the deep mantle seismic zones of the Pamir and Karakoram that represent subducted slabs penetrating to ~300 km (e.g. Fan *et al.* 1994; Pegler & Das 1998). The EHB catalogue shows few earthquakes with good-quality hypocentres deeper than 50 km in this region (Fig. 12), in contrast to the Zagros (Fig. 1). Nevertheless, the Tien Shan has been influential in our views of focal depth distribution on the continents because of confirmed depths that are certainly greater than 20 km, again in contrast to the Zagros. Chen & Molnar (1977) found two earthquakes (1965.11.13 and 1973.06.02) at ~50 and ~30 km by identifying *pP* reflections on long-period WWSSN records. These were later confirmed at

Table 2. Zagros–Makran events whose source parameters have been determined by *P* and *SH* waveform inversion in other studies. In the HRV column † indicates a depth that was fixed prior to the CMT inversion. Multiple events are indicated by an 'm' in the M_w column. The references are to: JQ79, Jacob & Quittmeyer (1979); JM84, Jackson & McKenzie (1984); BJP93, Baker *et al.* (1993); B93, Baker (1993); LC89, Laana & Chen (1989).

Date	Lat. N	Lon. E	M_w	Depth (km)			Region	Ref.
				P/SH	EHB	HRV		
1968 06 23	29.75	51.26	5.5	9	32		Zagros	BJP93
1971 04 06	29.78	51.88	5.2	6	5		Zagros	BJP93
1972 04 10	28.39	53.74	6.7 m	9	6		Zagros	BJP93
1974 12 02	28.09	55.86	5.2	7	49		Zagros	B93
1976 04 22	28.69	52.12	5.6	7	23	15†	Zagros	BJP93
1977 04 06	31.96	50.67	5.9	6	11	10	Zagros	B93
1985 08 07	27.86	53.04	5.4	17	11	15†	Zagros	B93
1986 07 12	29.91	51.56	5.5	4	7	33†	Zagros	BJP93
1986 12 10	29.88	51.56	5.3	8			Zagros	BJP93
1988 08 11	29.95	51.57	5.5	7	15	15	Zagros	BJP93
1988 08 11	29.89	51.66	5.8	9	15	15†	Zagros	BJP93
1988 12 06	29.89	51.63	5.6	10	12	37	Zagros	BJP93
1987 12 18	28.15	56.66	5.8	10	21	15	Oman line	B93
1968 08 02	27.55	60.90	5.7 m	74	67		Makran	JQ79
1969 11 07	27.81	59.98	6.1 m	62	75		Makran	JQ79
1970 11 09	29.50	56.79	5.5	100	98		(Makran)	B93
1972 11 17	27.37	59.11	5.4 m	65	64		Makran	JM84
1983 04 18	27.77	62.06	6.6	65	63	51	Makran	LC89
1990 09 26	29.07	60.89	5.5	8	5	15†	Makran	B93

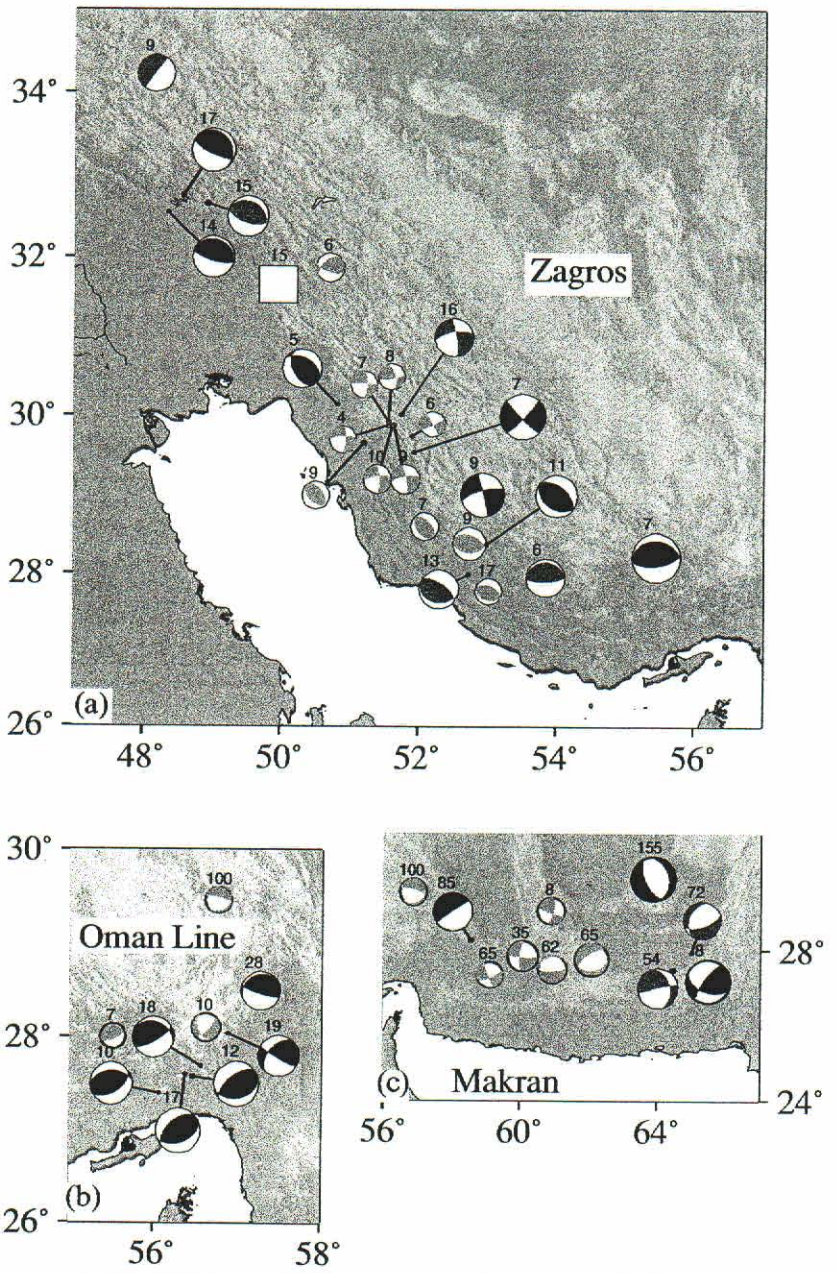

Figure 9. Fault plane solutions for earthquakes with well-determined depths in (a) the Zagros, (b) the Oman Line and (c) the Makran regions. Black symbols correspond to events for which *P* and *SH* waveform inversion was performed in this study. Dark grey symbols refer to events for which only the depth was determined in this study; the mechanisms shown for these events are those published in the Harvard CMT catalogue. Light grey symbols refer to events whose mechanism and depth were determined by *P* and *SH* waveform inversion in other studies (see Table 2). The white square represents the 1985 March 27 earthquake (see text for details). The depth in km of each event is shown above the corresponding symbol. The 100 km deep 1970.11.09 event is shown in both (b) and (c).

Table 3. Tien Shan events with waveform-determined depths of 20 km or more in the Tien Shan. In the EHB column * indicates a depth that was fixed by the operator (flag FEQ), whereas all other EHB depths were freely determined in the EHB inversion (flag DEQ; see text). In the method column 't' refers to teleseismic waveform inversion and 'r' refers to regional waveform inversion. References are to: FNW94, Fan *et al.* (1994); GHA98, Ghose *et al.* (1998); NMM87, Nelson *et al.* (1987).

Date	Lat. N	Lon. E	M_w	Depth (km) *P/SH*	Depth (km) EHB	Ref.	Method
1965 11 13	43.84	87.76	6.3	44	51	NMM87	t
1973 06 02	44.14	83.59	5.5	26	22	NMM87	t
1979 09 25	45.09	76.98	5.4	40	41	NMM87	t
1982 05 06	40.14	71.53	5.5	20	30	NMM87	t
1988 01 06	39.68	75.50	5.3	37	26	FNW94	r
1991 10 31	40.14	72.82	5.1	31	19	GHA98	r
1993 09 20	42.57	76.05	3.8	21		GHA98	r
1995 02 20	41.18	72.40	4.9	22	40	GHA98	r
1995 11 03	40.17	73.77	4.4	20	48	GHA98	r
1996 06 01	41.35	76.97	4.2	22	26*	GHA98	r

(Mangino *et al.* 1999; Kosarev *et al.* 1993; Bump & Sheehan 1998). Thus, at least in some parts of the Tien Shan, there is no doubt that the lower continental crust is seismically active, although with relatively few earthquakes. However, there is no clear evidence of earthquakes in the continental mantle lithosphere north of 40°N. The two deepest known earthquakes remain those of 1965.11.13 (44 km, close to station WMQ) and 1979.09.25 (40 km) confirmed by Nelson *et al.* (1987), and we were unable to find any more recent examples with comparable depth. The focal depth distribution in the Tien Shan is clearly different from that in the Zagros.

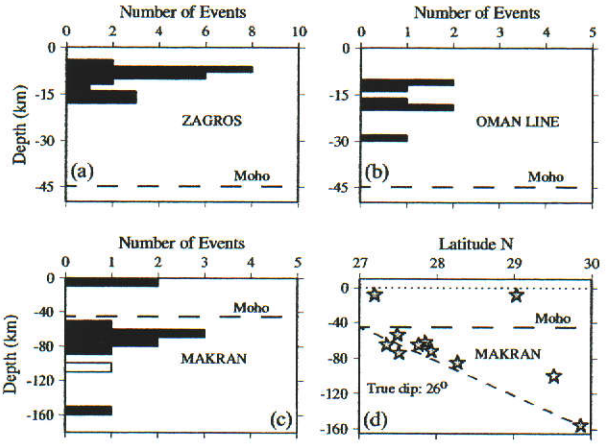

Figure 10. Histograms showing the focal depth distributions of earthquakes in Tables 1 and 2 in (a) the Zagros, (b) the Oman Line and (c) the Makran regions. (d) A N–S cross-section of the Makran showing the extrapolated position of the slab. The approximate Moho depths are shown in all figures, based on receiver function studies in the southern Zagros (K. Priestley, personal communication, 1999). The white symbols in (c) and (d) refer to the 1970.11.09 event, which we interpret as lying on the western edge of the subducting slab.

5 NORTHERN INDIA

Our main interest in this region is in whether there is unequivocal evidence for earthquakes within the mantle lithosphere of the Indian shield. There is certainly evidence for seismicity in the lower crust. The 1997.05.21 earthquake at Jabalpur, on the Indian shield south of the Ganges basin (Figs 14 and 15c and Table 4), had a well-determined centroid depth of 35 km, with many aftershocks also at depths of

Table 4. Earthquakes with waveform-determined depths of 20 km or more in peninsular India, the central Himalayas and southern Tibet. In the method column 'd' refers to depths determined from short-period depth phases, while 't' and 'r' are depths determined from teleseismic or regional waveforms. References are to: C81, Chen *et al.* (1981); MC83, Molnar & Chen (1983); E87, Ekström (1987); CM90, Chen & Molnar (1990); CK96, Chen & Kao (1996); ZH96, Zhu & Helmberger (1996).

Date	Lat. N	Lon. E	M_w	Depth (km) *P/SH*	Depth (km) EHB	Ref.	Region	Method
1973 08 01	29.60	89.13	4.9	85	93	MC83	Tibet	t
1976 09 14	29.78	89.53	5.9	90	103	C81	Tibet	t
1991 12 21	27.89	87.96	4.7	70	45	ZH96	Tibet	r
1992 03 07	29.62	89.19	4.2	80	79	ZH96	Tibet	r
1992 04 04	28.14	87.96	4.8	80	49	ZH96	Tibet	r
1968 08 18	26.41	90.60	5.1	29	28	CM90	Himalaya	d
1971 07 17	26.39	93.16	5.5	36	43	CM90	Himalaya	t
1980 11 19	27.39	88.79	6.0	44	44	E87	Himalaya	t
1963 06 19	24.97	92.06	6.0	52		CM90	Shillong	d
1963 06 21	25.13	92.09	6.0	38		CM90	Shillong	d
1968 06 12	24.83	91.89	5.3	41	44	CM90	Shillong	d
1988 02 06	24.68	91.51	5.9	31	30	CM90	Shillong	t
1988 08 20	26.73	86.59	6.7	51	61	CK96	Nepal	t
1996 04 01	31.50	73.44	5.5	38	92	Here	Nilore	t
1997 05 21	23.10	80.12	6.0	35	39	B97	Jabalpur	t

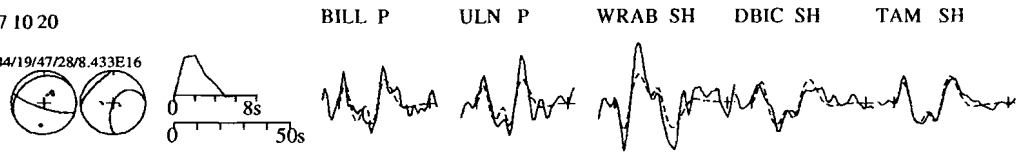

Figure 11. Selected waveforms from the minimum-misfit solution for the earthquake of 1997 October 20 at a depth of 28 km near the Oman Line (Fig. 9b). The full solution is given in the Appendix.

35–40 km (Battacharya *et al.* 1997; Acharyya *et al.* 1998). The Moho in the Jabalpur region is known to be at 40–44 km from wide-angle reflection and refraction studies (Murty *et al.* 1998). An earthquake on 1996.04.01 in the Punjabi foreland of the NW Himalaya had a centroid depth determined at 38 km (Fig. 15a) and occurred less than 200 km south of the GDSN station at Nilore (NIL), where receiver functions indicate a Moho depth of 50–54 km (Fig 15b).

Chen & Kao (1996) reported an earthquake at 51 km near Udaypur in Nepal on 1988.08.20 (Fig. 14), suggesting that it occurred in the uppermost mantle of the Indian shield. With the better information on crustal thickness now available at Jabalpur and Nilore we suspect that this may in fact have occurred in the lower crust. If the relatively undeformed Indian shield near Jabalpur has a Moho depth of 40–44 km, then 500 km further north, beneath the frontal thrusts of the Himalaya where the shield has certainly been bent down to form the Ganges basin (e.g. Lyon-Caen & Molnar 1983; McKenzie & Fairhead 1997), it seems probable to us that the Moho could quite easily be at 50–55 km, especially since that is the Moho depth determined at Nilore.

A similar argument applies to the earthquakes reported by Chen & Molnar (1990) beneath the Shillong Plateau (Fig. 14), where the Precambrian basement of the Indian shield is uplifted 1000 m above the foreland of the eastern Himalayas. Several focal depths in the range 30–40 km are constrained by teleseismic waveforms (Chen & Molnar 1990) and microearthquakes are largely confined to the range 15–35 km (Kayal & Zhao

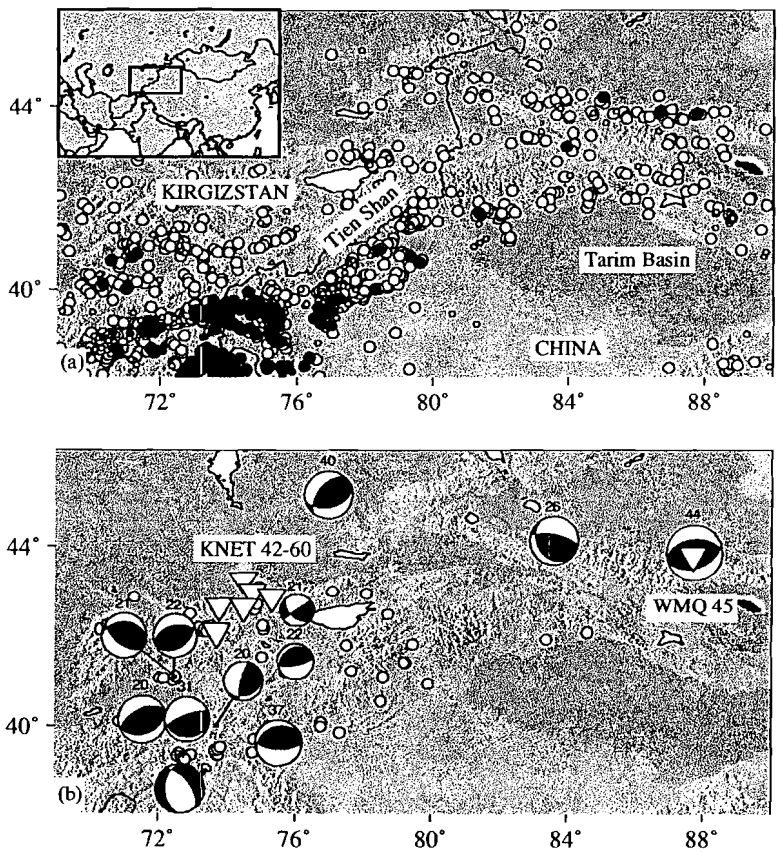

Figure 12. The Tien Shan region. (a) Seismicity taken from the EHB catalogue, with events reported to be at 50 km depth or deeper shown in black. Large circles are those events whose depths were freely determined (flag DEQ), while small circles are events whose depth was fixed by the operator (flag FEQ; see text). The geographical location of the region is shown in the inset map. (b) Fault plane solutions of earthquakes with depths greater than 20 km analysed by waveform inversion methods in other studies (Table 3). The depths in km are shown above the focal mechanisms. Events from the same studies with depths less than 20 km are shown as white circles. White triangles show the position of broad-band seismometers in the KNET array and at Urumqi (WMQ), under which Moho depths of 42–60 km and 45 km have been determined from receiver functions (Bump & Sheehan 1998; Kosarev *et al.* 1993; Mangino *et al.* 1999).

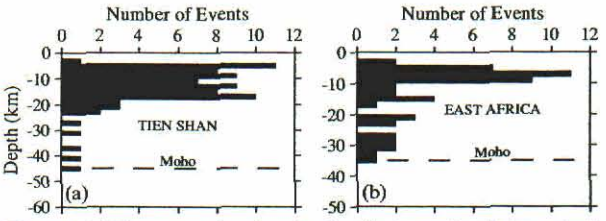

Figure 13. Histograms showing the distributions of well-determined focal depths in (a) the Tien Shan and (b) East Africa. The Tien Shan histogram contains all the events plotted in Fig. 12, while the East Africa histogram contains all the continental events discussed by Foster & Jackson (1998). The Moho is shown at 45 km (Mangino *et al.* 1999) in (a) and at 35 km (Zhao *et al.* 1997; Foster & Jackson 1998) in (b).

1998). Chen & Molnar (1990) reported one focal depth at ~52 km, based on the identification of *pP* and *sP* on short-period records. The Moho depth beneath the Shillong Plateau is not well known. The EGM96 gravity field (Lemoine *et al.* 1996) shows that the plateau is mostly compensated, with a flexural gravity low in front of it indicating a relatively small elastic thickness in this part of the foreland (see Plate 5 of McKenzie & Fairhead 1997). If the undeformed crustal thickness of the Indian shield is 40–44 km, as at Jabalpur, then beneath the 1 km high Shillong Plateau we believe it could reach 50–55 km, and that all of these earthquakes could have been in the lower continental crust. However, as Chen & Molnar (1990) pointed out, there is some residual uncertainty about whether the crust underlying the Bengal basin south of the plateau, and over which the Shillong Plateau is being thrust, is old (Cretaceous?) oceanic crust, rather than continental crust.

In a different category from the earthquakes discussed so far is a group that occurred at depths of 70–90 km beneath the Higher Himalaya and southern Tibet (Fig. 14). These earthquakes appear to be just beneath the Moho depth of 70–80 km determined by receiver functions (Kind *et al.* 1996) and therefore in the mantle. Various authors have argued that these are not in material originally attached to India and that has

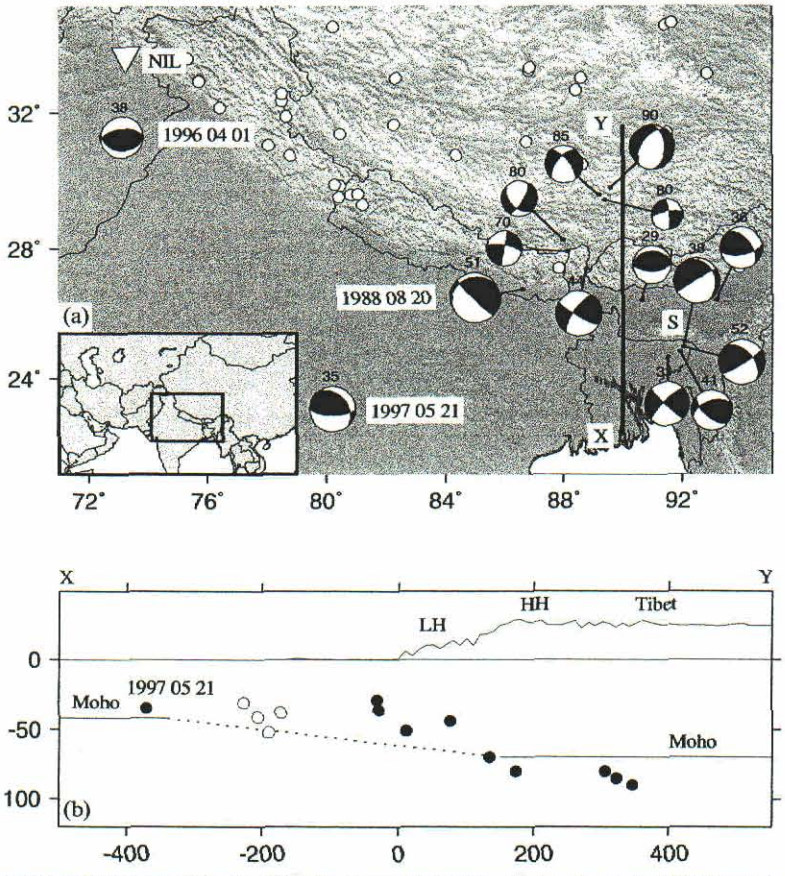

Figure 14. (a) Earthquakes with well-determined depths of 20 km or more in northern India, the central Himalayas and southern Tibet (Table 4). Numbers above the focal spheres refer to depths in km. Small circles are earthquakes whose depths of <20 km have also been well determined by the authors listed in Table 4. The white triangle represents the broad-band seismic station at Nilore (NIL). The Shillong Plateau is marked by S. X and Y mark the limits of the cross-section in (b). (b) Cross-section along 90°E showing the distribution of the deeper earthquakes in (a). LH marks the lesser Himalaya and HH the higher Himalaya. Events from the Shillong Plateau are marked by open circles. The depth of the Jabalpur earthquake of 1997.05.21, which is a long way west of the section, is marked to illustrate the depth of the probable Moho beneath the undeformed Indian shield (see text), and the 1996.04.01 event near Nilore is not shown. The Moho is shown to deepen from ~40 km south of the Ganges basin to reach a depth of ~70 km beneath Tibet and the high Himalaya (Kind *et al.* 1996), but whether it does so in the regular way indicated by the dotted line in unknown. The distances and depths on the cross-section are in km, and the elevation is exaggerated five times.

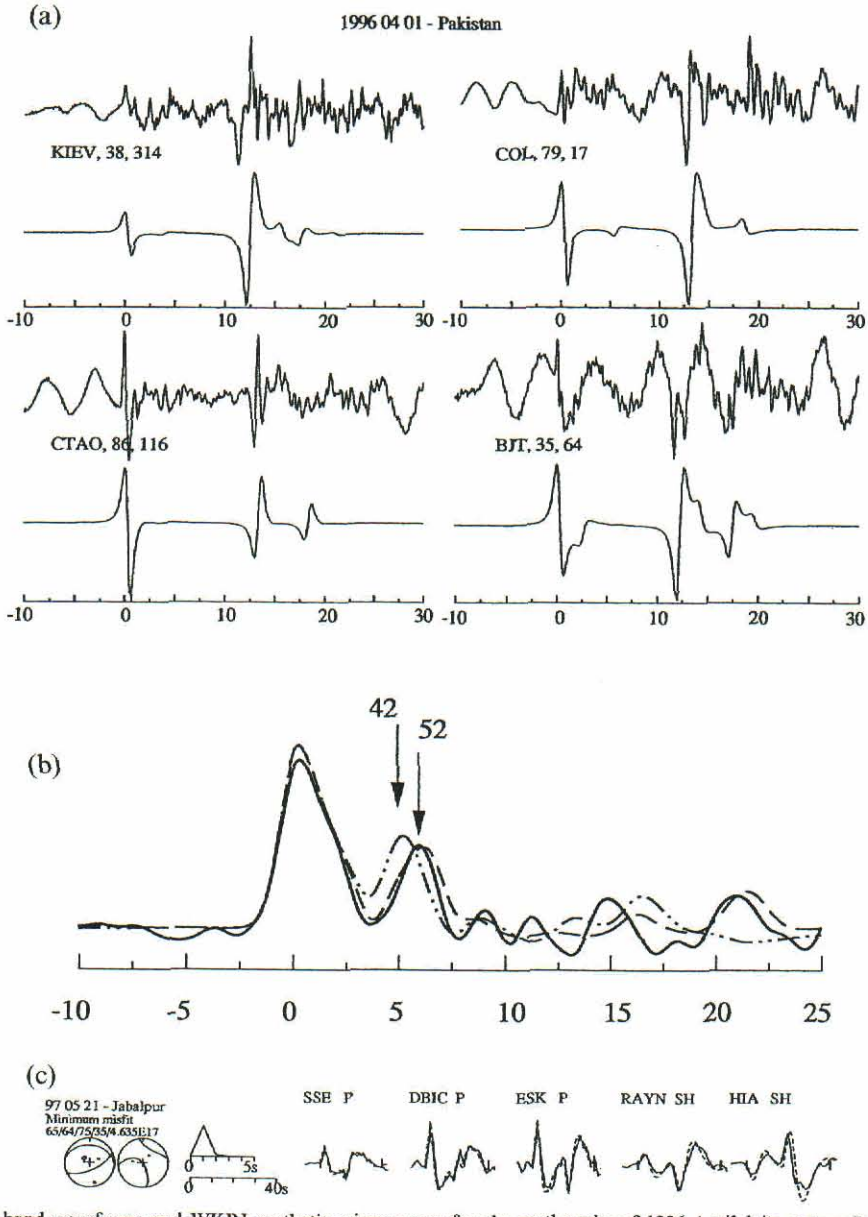

Figure 15. (a) Broad-band waveforms and WKBJ synthetic seismograms for the earthquake of 1996 April 1 in eastern Pakistan (see Fig. 14a). Synthetics were calculated using a depth of 38 km and a crustal velocity structure determined from the NIL receiver function in (b) below. The name of each station is followed by its distance and azimuth from the epicentre. (b) Receiver functions (Langston 1979) for the GDSN station at NIL. The solid line is the stacked receiver function formed from three earthquakes in the distance range 40°–45°. The dashed line is the synthetic receiver function for a crust 52 km thick, determined from inversion of the observed receiver function. The dot-dashed line is a synthetic receiver function calculated for a 42 km thick crust. The second prominent pulse is the *P*-to-*S* conversion at the Moho. From these observations we estimate the crustal thickness at NIL to be 52±2 km. (c) Selected waveforms from the minimum-misfit inversion solution for the 1997 May 21 Jabalpur earthquake (see Fig. 14a). The display convention is the same as in Fig. 3, and the full solution is given in the Appendix.

underthrust Tibet, mainly because their focal mechanisms are neither those expected at intermediate depths in slabs nor low-angle thrusts, but instead they resemble the normal and strike-slip mechanisms seen at upper crustal depths in the same place (e.g. Chen *et al.* 1981; Chen & Kao 1996; Zhu & Helmberger 1996). Thus, one interpretation of these events is that they represent the response of the uppermost continental mantle to whatever is also deforming the upper continental crust, where focal depths are generally restricted to the top 15 km (Molnar & Lyon-Caen 1989). We are suspicious of this interpretation for three reasons: (1) these anomalously deep earthquakes are apparently restricted to this region of southern Tibet, whereas the shallow strike-slip and normal faulting is widespread; (2) their locations are close to an extrapolation of

the Indian shield northwards; and (3) there is the possibility that the Indian shield reaches this far north (e.g. Nelson *et al.* 1996) and exerts a basal traction that is transmitted throughout its overlying material (McCaffrey & Nabelek 1998). In short, while a case can be made for these earthquakes at 70–90 km being in the mantle, it is not clear to us that it has to be continental mantle originally beneath the Indian shield or Tibet rather than mantle belonging to a piece of originally oceanic lithosphere (a point made also by Chen & Molnar 1983).

To summarize, there is abundant evidence for lower crustal seismicity in the Indian shield, but no unequivocal evidence for seismicity in the continental mantle beneath that shield.

6 DISCUSSION

6.1 Bulletin and catalogue focal depth determinations

Our experience in the Zagros–Makran and Tien Shan shows that, although there is an undoubted general improvement in locations shown by the EHB catalogue over the ISC catalogue (see Engdahl *et al.* 1998), important errors in depth can still occur for shallow crustal earthquakes in some regions. Of the better-located depths (i.e. those labelled DEQ) reported as deeper than 30 km in the Zagros by the EHB catalogue and which were big enough for us to check with waveform analysis, none was deeper than 20 km, and we found discrepancies with the EHB depths as great as 40 km. Figs 16(a) and (c) compare the discrepancies between EHB depths and the centroids determined by body waves. There is a suggestion that the discrepancy decreases for genuinely deeper events, particularly for events deeper than about 60 km, and for larger events ($M_w > 5.5$). This effect is not surprising, given that the EHB depth determinations are based on reported high-frequency (~ 1 s) regional and teleseismic *P* and *S* phases, *PKP* phases, and the teleseismic depth phases *pP*, *pwP* and *sP*. At depths greater than ~ 50 km, when the *pP*–*P* time separation is ~ 15 s, the surface reflections are often clear and easily recognized, and source time functions are often simple and quite impulsive. At shallow depths, *pP* and *sP* can easily be misidentified on short-period records and confused with other phases arising from near-source structure, complicated source time functions or multiple subevents. For small-magnitude events in particular, waveforms at teleseismic distances may have small signal-to-noise ratios, making it hard to pick out the depth phases. The signal-to-noise ratios generally improve at regional distances, but here the often complex structure through which the seismic waves are propagating causes the seismograms themselves to be rather complex, which again makes finding and identifying depth phases rather difficult. Furthermore, in the absence of stations within the inflection point of the traveltime curve, EHB depth phase identifications can be highly dependent on the starting depth of the EHB location. When the EHB inversions were started at the depth we obtained from waveform modelling (E. R. Engdahl, personal communication, 2000), the discrepancies between the new EHB depths and our waveform depths were in all cases reduced to less than 20 km, as shown in Figs 16(b) and (d). There is little evidence for a correlation between depth discrepancy and either depth or magnitude for the new EHB depths (Figs 16c and d).

Our analysis of the 1985.02.02 (Section 3.3) and 1985.03.27 (Section 3.4) earthquakes in the Zagros suggests that serious

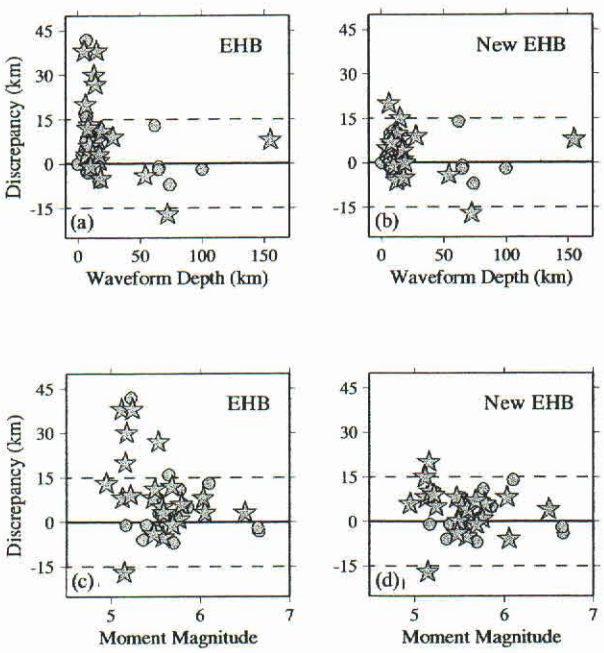

Figure 16. Comparison between the EHB depths and those obtained by waveform inversion in the Zagros–Makran. (a) Depth discrepancy (i.e. the EHB depth minus the waveform depth) against the depths determined by waveform analysis for all the events in Tables 1 and 2. (b) Discrepancy between the depths obtained by starting the EHB inversions at the waveform-determined depths and these same depths, plotted against depth. (c), (d) Depth discrepancies plotted against moment magnitude. Stars refer to events whose depths were determined in this study.

errors in depth and focal mechanism can also arise in long-period CMT determinations such as those published by Harvard. These solutions are determined using low-pass-filtered long-period body and mantle waveform data and the moment tensor inversion method described by Dziewonski *et al.* (1981). If the depth is not perturbed during the inversion, it is fixed to be consistent with the waveform matching of reconstructed broad-band body waves (Ekström 1989). Depths for most crustal earthquakes are poorly determined by the Harvard method and are usually fixed at an arbitrary, but sensible, depth of 15 km in the CMT catalogue. Table 1 also shows discrepancies in depth with those provided by the USGS. The USGS moment tensor inversions are based on long-period vertical-component *P* waveforms obtained from digital recording stations (Sipkin 1982, 1986a,b). The source depth that gives the smallest normalized mean-square error is a byproduct of the inversion, but for crustal earthquakes these depths are also poorly resolved.

It therefore seems clear to us that unverified catalogue depths are insufficiently accurate to resolve the relatively subtle differences in focal depth distribution within the crust that are of interest to us here. We conclude that in the Zagros, seismicity is confined to the upper 20 km of the crust whereas in the Tien Shan it occurs throughout a crustal thickness of 40 km. This contrast could not have been determined with confidence from bulletin or catalogue locations, nor, in particular, should unverified catalogue depths of 50–100 km be used as evidence for seismicity in the mantle lithosphere or for subduction.

6.2 Earthquakes in the continental mantle lithosphere?

Chen & Molnar (1983) concluded that in many regions of continental convergence the uppermost mantle is seismically active. It is worth examining how that evidence looks today, and for this purpose we ignore unverified depths reported by bulletins and catalogues based on arrival time data. In the Zagros, Tien Shan and Indian shield there is no unequivocal evidence for mantle seismicity. Certainly in the Tien Shan, Indian shield and parts of East Africa (Zhao *et al.* 1997; Foster & Jackson 1998) there are earthquakes whose waveform-determined centroids are very close to the Moho and, given the uncertainty in their depths and the crustal thickness, could have occurred in the uppermost mantle. However, they could just as well have occurred in the lower crust, which other earthquakes nearby show is definitely seismogenic in all three places. We would feel more confident about assigning seismicity to the continental mantle if there were earthquakes with depths definitely beneath the Moho, not just close to it on the crustal side. The remaining areas where Chen & Molnar (1983) suggested that seismicity in the continental mantle might occur split into two groups: those near places where subduction is occurring now or has occurred within the recent past, and those that have no plausible association with subduction.

The first group includes earthquakes at ~100 km under the Karakoram in central Asia and the high Atlas in north Africa. As with the earthquakes at 70–90 km in southern Tibet that were discussed above, Chen & Molnar (1983) thought it unlikely that these occurred within downgoing slabs of lithosphere, mainly because their focal mechanisms do not fit into the usual pattern of P or T axes aligned down the dips of likely potential slabs, yet both the Karakoram and the Atlas are sites where oceanic lithosphere is very likely to have been subducted into the mantle in the late Tertiary. The problem then is in proving that these mantle events did not occur in lithosphere of oceanic origin (as Chen & Molnar 1983 pointed out).

The second group consists of isolated anomalies. Marks & Lindh (1978) reported two small (M_L1.1) events at depths of about 40 km beneath the foothills of the Sierra Nevada in California, where most seismicity is shallower than 20 km. In this region, which is one of present-day extension rather than shortening, the Moho depth is in the range 30–40 km (Spieth *et al.* 1981), so these earthquakes could conceivably be in the lowermost crust. In the Baikal region, Déverchère *et al.* (1991) found some microearthquakes at ~40 km, but the rather large seismograph station spacing and lack of knowledge of Moho depths must cast doubt as to whether these were actually in the mantle. Assumpção & Suárez (1988) determined a focal depth of ~45 km for an earthquake in the Brazilian shield near Manaus, in a region where the crustal thickness is unknown. Finally, Zandt & Richins (1979) reported a small (M_L3.8) isolated strike-slip earthquake at 90±5 km in northern Utah, which must be in the mantle.

There is, of course, no doubt that in the oceanic lithosphere numerous intraplate earthquakes occur within the mantle (e.g. Chapple & Forsyth 1979; Wiens & Stein 1983). There are also other places, besides those discussed explicitly here, where seismicity occurs at depths greater than 20 km in the continental crust, and these are summarized in Table 5. However, the only earthquake we know of that must have occurred in the continental mantle is the small, isolated event at 90 km in Utah, mentioned above. We therefore conclude that there is no compelling evidence to believe that earthquakes in the uppermost mantle of the continental lithosphere are either common or an important indicator of mechanical strength.

Table 5. Summary of locations where earthquakes have been observed deeper than 20 km in the continental crust. The middle column refers to whether the depth determinations are from local or regional seismic networks or from teleseismic waveform analysis.

Location	Type of Analysis	Comments
Gazli, Uzbekistan	local	Earthquakes to 20–25 km (±3 km). Crustal thickness ~40 km (Bossu *et al.* 1996).
Saguenay, Canada	teleseismic and local	Earthquakes, including one of M_w5.8, to ~26 km. Crustal thickness ~43 km (Somerville *et al.* 1990).
Crownpoint, NM	regional and local	Two events at 41±7 km and 44±4 km (regional). Aftershocks mostly at 22–32 km (local). Moho at 45–50 km (Wong *et al.* 1984).
Paradox Basin, UT	local	Seismicity generally to ~40 km. Two isolated events at 53 and 58 km, but errors uncertain: probably ±2–5 km, but may be ±10 km. Moho at 45–50 km (Wong & Humphrey 1989).
Randolph, UT	local	Single event at 90 km, possible second at 55 km. Moho at ~36 km (Zandt & Richins 1979; Zandt, personal communication, 1999).
Laramide Mts., WY	teleseismic	One event of m_b5.3 at 27.5±1 km from modelling reconstituted broad-band waveform at RSNY. Moho at ~41 km (Spence *et al.* 1996).
Ventura Basin, CA	local	39 small events between 20 and 30 km depth. Waveforms show depths are above the Moho at ~32 km (Bryant & Jones 1989).
Sierra Foothills, CA	local	Many small events in the lower crust (Wong & Savage 1983).
Oroville, CA	local	Two small events at ~40 km (Marks & Lindh 1978). Moho at 30–40 km (Spieth *et al.* 1981).
Southern Illinois	teleseismic and local	Earthquakes to 25±3 km, including one of m_b5.5 (Chen & Molnar 1983; Chen 1988).
Manaus, Brazil	teleseismic	Earthquake of m_b4.1 at ~45 km, confirmed by *pP* and *sP*, in Brazilian shield (Assumpção & Suárez 1988). Moho depth unknown.
East Africa (south)	teleseismic and local	Earthquakes of m_b>5.5 to ~35 km depth (teleseismic). Smaller events in lower crust (local). Moho at 36–45 km in Proterozoic and Archaean shields (Zhao *et al.* 1997; Foster & Jackson 1998).
Oman Line (Iran)	teleseismic	Earthquake at ~28 km (this paper, Section 3).
North India	teleseismic and local	Numerous events including m_b>5.5 in the lower crust (this paper, Section 5).
Tien Shan	teleseismic and regional	Numerous events including m_b>5.5 in the lower crust (this paper, Section 4).

6.3 Focal depth distributions and the rheology of the continental lithosphere

It remains true that most continental seismicity is concentrated in the upper crust. In many places, such as most of California (Hill *et al.* 1990), the Aegean (Taymaz *et al.* 1991), Tibet (Molnar & Lyon-Caen 1989) and the Zagros, seismicity is essentially confined to the upper 20 km of the crust and the lower crust is effectively aseismic. In other places (summarized in Table 5), including parts of East Africa (Zhao *et al.* 1997; Foster & Jackson 1998), the Tien Shan, the Indian shield and around Lake Baikal (Déverchère *et al.* 1991), lower crustal seismicity is more important, but is usually less intense than in the upper crust. The major modification since the reviews by Chen & Molnar (1983) and Chen (1988) is the reduced evidence for seismicity in the mantle beneath the continental lithosphere. As Chen (1988) pointed out, in several places there is an apparent concentration of seismicity at depths near the Moho, with mid-crustal levels apparently showing fewer earthquakes. However, it seems to us that the balance of evidence now favours the interpretation that these events occurred in the lower crust rather than in the upper mantle. These lower crustal events are evidently more common in old shield areas (see also Chen 1988).

These observations raise several questions. One is whether the places with thicker seismogenic crust, in which the lower crust is also seismically active, represent stronger continental lithosphere, and whether this can be recognized in the effective elastic thickness variations detected by methods such as that used by McKenzie & Fairhead (1997). Another is what causes such variations in seismogenic thickness within the continental crust, and particularly what can lead to the continental mantle being aseismic under shields whereas the oceanic mantle is clearly capable of producing earthquakes. These questions are beyond the scope of this paper, which has concentrated on seismological evidence, but are discussed in a separate study (Maggi *et al.* 2000). In brief, variations in the seismogenic thickness correlate with variations in the effective elastic thickness (T_e), which is usually the smaller of the two. Thus, T_e in the forelands of the northern Tien Shan and Himalaya is roughly 40 km, whereas it is only about 15–20 km around Iran. While the main control on rheological properties and strength is still likely to be homologous temperature, we believe the other important effect to be the presence (or absence) of volatiles, particularly water, small amounts of which are known to reduce strength dramatically (e.g. Mackwell *et al.* 1998). The young oceanic mantle is essentially dry, whereas the old continental mantle beneath shields slowly accumulates hydrous phases, formed by the crystallization of melts percolating upwards from the asthenosphere (McKenzie 1989; Harte *et al.* 1993). There may be sufficient water to reduce the strength of the old continental mantle but not of the younger oceanic mantle, which has accumulated less in the shorter time available. Similarly, it may be the loss of hydrous granitic melts from the deep continental crust, leaving anhydrous mafic granulites as residues, that is responsible for the increased strength and lower crustal seismicity in some old shield regions (Foster & Jackson 1998).

A final question concerns whether this variation in the thickness and strength of the continental seismogenic layer influences the scale of the structures that form within it. In particular, the seismogenic thickness seems to control the maximum segmentation length of the major dip-slip faults and the width of fault-bounded graben (e.g. Jackson & White 1989; Jackson & Blenkinsop 1997; Scholz & Contreras 1998; Ebinger *et al.* 1999). This question is further discussed by Maggi *et al.* (2000).

7 CONCLUSIONS

Most earthquakes in the continental lithosphere occur in the upper crust (typically <20 km depth) and in some regions, such as southern Iran, the Aegean, Tibet and most of California, they are virtually restricted to this depth. In other places, such as parts of East Africa, the Tien Shan and northern India, earthquakes occur throughout the continental crust to Moho depths as great as $\sim$40–45 km. These variations cannot be reliably detected from published bulletins or catalogues based on teleseismic arrival time data, even from those whose depth resolution is improved, such as the EHB catalogue of Engdahl *et al.* (1998). In the Zagros we found depth errors of up to 40 km in the EHB and Harvard CMT catalogues, and incidentally showed that two earthquakes with unusual CMT mechanisms showing normal faulting probably involved thrust faulting instead. Except for a single, small (M_L3.8), isolated event in Utah, we know of no compelling evidence that the continental mantle lithosphere is seismically active anywhere, although the oceanic mantle is certainly known to produce earthquakes. Thus there is little support in earthquake focal depth distributions for the idea that the uppermost mantle is significantly stronger than the lower crust in continental regions. The simplest interpretation of these observations is that the strength of the continental lithosphere resides in the crust and varies regionally, with an effective elastic thickness approximately corresponding to the seismogenic thickness.

ACKNOWLEDGMENTS

We are especially grateful to Dr E. R. Engdahl for a particularly generous, detailed and careful review that went far beyond the obligations of duty. Not only did he correct several errors and misconceptions in our assessment of the EHB catalogue, but he also carried out (and allowed us to quote) tests in which 'new EHB' locations in Figs 16(b) and (d) were determined in inversions using starting depths corresponding to those obtained from waveform modelling. His comments clarified our understanding of teleseismic depth determinations significantly, although we emphasize that we alone are responsible for any remaining misconceptions. We thank Dan McKenzie and Peter Molnar for helpful reviews, and W.-P. Chen for guiding us to some obscure literature. This is Cambridge Earth Sciences contribution ES 5939.

REFERENCES

Acharyya, S.K., Kayal, J.R., Roy, A. & Chaturvedi, R.K., 1998. Jabalpur earthquake of May 22, 1997: constraint from aftershock study, *J. geol. Soc. India*, **51**, 295–304.

Assumpção, M. & Suárez, G., 1988. Source mechanism of moderate-size earthquakes and stress orientation in mid-plate South America, *Geophys. J. Int.*, **92**, 253–267.

Baker, C., 1993. The active seismicity and tectonics of Iran, *PhD thesis*, University of Cambridge, Cambridge.

Baker, C., Jackson, J. & Priestley, K., 1993. Earthquakes on the Kazerun Line in the Zagros Mountains of Iran: strike-slip faulting within a fold-and-thrust belt, *Geophys. J. Int.*, **115**, 41–61.

Battacharya, S.N., Ghose, A.K., Suresh, G., Baidya, P.R. & Saxena, R.C., 1997. Source parameters of Jabalpur earthquake of 22 May 1997, *Current Sci.*, **73,** 855–863.

Bird, P., Toksöz, M. & Sleep, N., 1975. Thermal and mechanical models of continent-continent convergence zones, *J. geophys. Res.*, **80,** 4405–4416.

Bossu, R., Grasso, J.R., Plotnikova, L.M., Nurtaev, B., Frechet, J. & Moisy, M., 1996. Complexity of intracontinental seismic faultings: the Gazli, Uzbekistan, sequence, *Bull. seism. Soc. Am.*, **86,** 959–971.

Brace, W.F. & Byerlee, J.D., 1970. California earthquakes: why only shallow focus?, *Science,* **168,** 1573–1576.

Bryant, A.S. & Jones, L.M., 1989. Anomalously deep earthquakes in the crust beneath the Ventura basin, southern California, *EOS, Trans. Am. geophys. Un.*, **70,** 1209–1210.

Bump, H.A. & Sheehan, A.F., 1998. Crustal thickness variations across the northern Tien Shan from teleseismic receiver functions, *Geophys. Res. Lett.*, **25,** 1055–1058.

Byrne, D.E., Sykes, L.R. & Davis, D.M., 1992. Great thrust earthquakes and aseismic slip along the plate boundary of the Makran subduction zone, *J. geophys. Res.*, **97,** 449–478.

Chapman, C.H., 1978. A new method for computing synthetic seismograms, *Geophys. J. R. astr. Soc.*, **54,** 481–518.

Chapple, W.M. & Forsyth, D.W., 1979. Earthquakes and bending of plates at trenches, *J. geophys. Res.*, **84,** 6729–6749.

Chen, W.-P., 1988. A brief update on the focal depths of intra-continental earthquakes and their correlations with heat flow and tectonic age, *Seism. Res. Lett.*, **59,** 263–272.

Chen, W.-P. & Kao, H., 1996. Seismotectonics of Asia: some recent progress, in *The Tectonic Evolution of Asia,* pp. 37–62, eds Yin, A. & Harrison, M., Cambridge University Press, Palo Alto, CA.

Chen, W.-P. & Molnar, P., 1977. Seismic moments of major earthquakes and the average rate of slip in Central Asia, *J. geophys. Res.*, **82,** 2945–2969.

Chen, W.-P. & Molnar, P., 1983. Focal depths of intracontinental and intraplate earthquakes and their implications for the thermal and mechanical properties of the lithosphere, *J. geophys. Res.*, **88,** 4183–4214.

Chen, W.-P. & Molnar, P., 1990. Source parameters of earthquakes and intraplate deformation beneath the Shillong Plateau and northern Indoburman ranges, *J. geophys. Res.*, **95,** 12 527–12 552.

Chen, W.-P., Nabelek, J.L., Fitch, T.J. & Molnar, P., 1981. An intermediate depth earthquake beneath Tibet: source characteristics of the event of September 14, 1976, *J. geophys. Res.*, **86,** 2863–2876.

Déverchère, J., Houdry, F., Diament, M., Solonenko, N.V. & Solonenko, A.V., 1991. Evidence for a seismogenic upper mantle and lower crust in the Baikal rift, *Geophys. Res. Lett.*, **18,** 1099–1102.

Dziewonski, A.M., Chou, T.A. & Woodhouse, J.H., 1981. Determination of earthquake source parameters from waveform data for studies of global and regional seismicity, *J. geophys. Res.*, **86,** 2825–2852.

Ebinger, C., Jackson, J.A., Foster, A.N. & Hayward, N.J., 1999. Extensional basin geometry and the elastic lithosphere, *Phil. Trans. R. Soc. Lond.*, **A357,** 741–765.

Ekström, G.A., 1987. A broad band method of earthquake analysis, *PhD thesis,* Harvard University.

Ekström, G.A., 1989. A very broad-band inversion method for the recovery of earthquake source parameters, *Tectonophysics,* **166,** 73–100.

Engdahl, E.R., van der Hilst, R. & Buland, R., 1998. Global teleseismic earthquake relocation with improved travel times and procedures for depth determination, *Bull. seism. Soc. Am.*, **88,** 722–743.

Fan, G., Ni, J.F. & Wallace, T., 1994. Active tectonics of the Pamirs and Karakorum, *J. geophys. Res.*, **99,** 7131–7160.

Foster, A.N & Jackson, J.A., 1998. Source parameters of large African earthquakes: implications for crustal rheology and regional kinematics, *Geophys. J. Int.*, **134,** 422–448.

Ghose, S., Hamburger, M.W. & Ammon, C.J., 1998. Source parameters of moderate-sized earthquakes in the Tien Shan, central Asia, from regional moment tensor inversion, *Geophys. Res. Lett.*, **25,** 3181–3184.

Harte, B., Hunter, R.H. & Kinny, P.D., 1993. Melt geometry, movement and crystallization, in relation to mantle dykes, veins and metasomatism, *Phil. Trans. R. Soc. Lond.*, **A342,** 1–21.

Hill, D.P., Eaton, J.P. & Jones, L.M., 1990. Seismicity, 1980–86, in *The San Andreas Fault system, California,* ed. Wallace, R.E., *USGS. Prof. Pap.*, **1515,** 115–151.

Jackson, J., 1980. Errors in focal depth determination and the depth of seismicity in Iran and Turkey, *Geophys. J. R. astr. Soc.*, **61,** 285–301.

Jackson, J.A. & Blenkinsop, T., 1997. The Bilila-Mtakataka fault in Malawi: an active 100-km long, normal fault segment in thick seismogenic crust, *Tectonics,* **16,** 137–150.

Jackson, J. & Fitch, T., 1981. Basement faulting and the focal depths of the larger earthquakes in the Zagros mountains (Iran), *Geophys. J. R. astr. Soc.*, **64,** 561–586.

Jackson, J.A. & McKenzie, D.P., 1984. Active tectonics of the Alpine-Himalayan belt between western Turkey and Pakistan, *Geophys. J. R. astr. Soc.*, **77,** 185–264.

Jackson, J.A. & White, N.J., 1989. Normal faulting in the upper continental crust: observations from regions of active extension, *J. struct. Geol.*, **11,** 15–36.

Jacob, K. & Quittmeyer, R.C., 1979. The Makran region of Pakistan and Iran: trench-arc system with active plate subduction, in *Geodynamics of Pakistan,* pp. 305–317, eds Farah, A. & DeJong, K.A., Geological Survey of Pakistan, Quetta.

Kayal, J.R. & Zhao, D., 1998. Three-dimensional seismic structure beneath Shillong Plateau and Assam Valley, northeast India, *Bull. seism. Soc. Am.*, **88,** 667–676.

Kennett, B.L.N., Engdahl, E.R. & Buland, R., 1995. Constraints on seismic velocities in the Earth from travel times, *Geophys. J. R. astr. Soc.*, **122,** 108–124.

Kind, R., *et al.*, 1996. Evidence from earthquake data for a partially molten crustal layer in southern Tibet, *Science,* **274,** 1692–1694.

Kosarev, G.L., Petersen, N.V., Vinnik, L.P. & Roecker, S.W., 1993. Receiver functions for the Tien Shan analog broadband network: contrasts in the evolution of structures across the Talasso–Fergana Fault, *J. geophys. Res.*, **98,** 4437–4448.

Laana, J.L. & Chen, W.-P, 1989. The Makran earthquake of 1983 April 18: a possible analogue to the Puget Sound earthquake of 1965?, *Geophys. J. Int.*, **98,** 1–9.

Langston, C.A., 1979. Structure under Mt. Rainier, Washington, inferred from teleseismic body waves, *J. geophys. Res.*, **84,** 4749–4762.

Lemoine, F.G., *et al.*, 1996. The NASA and DMA joint geo-potential model, *EOS, Trans. Am. geophys. Un.*, 77, Fall mtng suppl., F136.

Lyon-Caen, H. & Molnar, P., 1983. Constraints on the structure of the Himalaya from an analysis of gravity anomalies and a flexural model of the lithosphere, *J. geophys. Res.*, **88,** 8171–8191.

Mackwell, S.J., Zimmerman, M.E. & Kohlstedt, D.L., 1998. High-temperature deformation of dry diabase with application to tectonics on Venus, *J. geophys. Res.*, **103,** 975–984.

Maggi, A., Jackson, J.A., Mckenzie, D. & Priestley, K., 2000. Earthquake focal depths, effective elastic thickness, and the strength of the continental lithosphere, *Geology,* **28,** 495–498.

Mangino, S., Priestley, K. & Ebel, J., 1999. The receiver structure beneath the China digital seismograph network stations, *Bull. seism. Soc. Am.*, **89,** 1053–1076.

Marks, S.M. & Lindh, A.G., 1978. Regional seismicity of the Sierran foothills in the vicinity of Oroville, California, *Bull. seism. Soc. Am.*, **68,** 1103–1115.

McCaffrey, R. & Abers, J., 1988. SYN3: A program for inversion of teleseismic body wave form on microcomputers, *Air Force geophys. Lab. Tech. Rept,* **AFGL-TR-88-0099,** Hanscomb Air Force Base, Massachusetts.

McCaffrey, R. & Nábelek, J., 1987. Earthquakes, gravity, and the origin of the Bali Basin: an example of a nascent continental fold-and-thrust belt, *J. geophys. Res.*, **92,** 441–460.

McCaffrey, R. & Nabelek, J., 1998. Role of oblique convergence in the active deformation of the Himalayas and southern Tibet plateau, *Geology*, **26**, 691–694.

McKenzie, D., 1989. Some remarks on the movement of small melt fractions in the mantle, *Earth planet. Sci. Lett.*, **95**, 53–72.

McKenzie, D. & Fairhead, D., 1997. Estimates of the effective elastic thickness of the continental lithosphere from Bouguer and free air gravity anomalies, *J. geophys. Res.*, **102**, 27 523–27 552.

Molnar, P. & Chen, W.-P., 1983. Focal depths and fault plane solutions of earthquakes under the Tibetan plateau, *J. geophys. Res.*, **88**, 1180–1196.

Molnar, P. & Lyon-Caen, H., 1989. Fault plane solutions of earthquakes and active tectonics of the Tibetan plateau and its margins, *Geophys. J. Int.*, **99**, 123–153.

Moores, E.M. & Twiss, R.J., 1995. *Tectonics*, W. H. Freeman, New York.

Murty, A.S.N., Mall, D.M., Murty, P.R.K. & Reddy, P.R., 1998. Two-dimensional crustal velocity structure along Hirapur-Mandla profile from seismic refraction and wide-angle reflection data, *Pure appl. Geophys.*, **152**, 247–266.

Nelson, K.D., *et al.*, 1996. Partially molten middle crust beneath southern Tibet: synthesis of project INDEPTH results, *Science*, **274**, 1684–1688.

Nelson, M.R., McCaffrey, R. & Molnar, R., 1987. Source parameters for 11 earthquakes in the Tien Shan, Central Asia, determined by P and SH waveform inversion, *J. geophys. Res.*, **92**, 12 629–12 648.

Ni, J. & Barazangi, M., 1986. Seismotectonics of Zagros continental collision zone and a comparison with the Himalayas, *J. geophys. Res.*, **91**, 8205–8218.

Nowroozi, A.A., 1971. Seismotectonics of the Persian plateau, eastern Turkey, Caucasus, and Hindu Kush regions, *Bull. seism. Soc. Am.*, **61**, 317–341.

Nyblade, A.A. & Langston, C.A., 1995. East African earthquakes below 20 km depth and their implications for crustal structure, *Geophys. J. Int.*, **121**, 49–62.

Pegler, G. & Das, S., 1998. An enhanced image of the Pamir-Hindu Kush seismic zone from relocated earthquake hypocentres, *Geophys. J. Int.*, **134**, 573–595.

Priestley, K., Baker, C. & Jackson, J., 1994. Implications of earthquake focal mechanism data for the active tectonics of the south Caspian basin and surrounding regions, *Geophys. J. Int.*, **118**, 111–141.

Roecker, S.W., *et al.*, 1993. Three–dimensional elastic wave velocity structure of the western and central Tien Shan, *J. geophys. Res.*, **98**, 15 779–15 795.

Scholz, C.H. & Contreras, J.C., 1998. Mechanics of continental rift architecture, *Geology*, **26**, 967–970.

Sipkin, S.A., 1982. Estimation of earthquake source parameters by the inversion of waveform data, synthetic seismograms, *Phys. Earth planet. Inter.*, **30**, 242–259.

Sipkin, S.A., 1986a. Interpretation of non-double-couple earthquake source mechanisms derived from moment tensor inversion, *J. geophys. Res.*, **91**, 531–547.

Sipkin, S.A., 1986b. Estimation of earthquake source parameters by the inversion of waveform data: global seismicity, 1981–1983, *Bull. seism. Soc. Am.*, **76**, 1515–1541.

Somerville, P., McLaren, J.P., Saikia, C.K. & Helmberger, D.V., 1990. The 25 November 1988 Saguenay, Quebec, earthquake: source parameters and the attenuation of strong ground motion, *Bull. seism. Soc. Am.*, **80**, 1118–1143.

Spence, W., Langer, C.J. & Choy, G.L., 1996. Rare, large earthquakes at the Laramide deformation front—Colorado (1882) and Wyoming (1984), *Bull. seism. Soc. Am.*, **86**, 1804–1819.

Spieth, M.A., Hill, D.P. & Geller, R.J., 1981. Crustal structure in the northwestern foothills of the Sierra Nevada from seismic refraction experiments, *Bull. seism. Soc. Am.*, **71**, 1075–1087.

Taymaz, T., Jackson, J. & McKenzie, D., 1991. Active tectonics of the north and central Aegean Sea, *Geophys. J. Int.*, **106**, 433–490.

Wiens, D.A. & Stein, S., 1983. Age dependence of intraplate seismicity and implications for lithospheric evolution, *J. geophys. Res.*, **88**, 6455–6468.

Wong, I.G. & Humphrey, J.R., 1989. Contemporary seismicity, faulting and the state of stress in the Colorado plateau, *Geol. Soc. Am. Bull.*, **101**, 1127–1146.

Wong, I.G. & Savage, W.U., 1983. Deep intraplate seismicity in the western Sierra Nevada, central California, *Bull. seism. Soc. Am.*, **73**, 797–812.

Wong, I.G., Cash, D. & Jaksha, L., 1984. The Crowpoint, New Mexico, earthquakes of 1976 and 1977, *Bull. seism. Soc. Am.*, **74**, 2435–2449.

Zandt, G. & Richins, W.D., 1979. An upper mantle earthquake beneath the middle Rocky mountains in NE Utah, *Earthq. Notes*, **50**, 69–70 (abstract).

Zhao, M., Langston, C.A., Nyblade, A.A. & Owens, T.J., 1997. Lower-crustal rifting in the Rukwa graben, east Africa, *Geophys. J. Int.*, **129**, 412–420.

Zhu, L.P. & Helmberger, D.V., 1996. Intermediate depth earthquakes beneath the India-Tibet collision, *Geophys. Res. Lett.*, **23**, 435–438.

Zhu, L., Helmberger, D.V., Saikia, C.K. & Woods, B.B., 1997. Regional waveform calibration in the Pamir–Hindu Kush region, *J. geophys. Res.*, **102**, 22 799–22 813.

APPENDIX A: FULL-WAVEFORM INVERSION SOLUTIONS

This appendix contains the minimum-misfit *P* and *SH* waveforms (Figs A1–A14) for the 14 'a' class earthquakes in Table 1 not already discussed in the text, and also for the Jabalpur earthquake (Table 4) (Fig. A15). We used long-period *P* and *SH* waveforms to constrain the earthquake source parameters. The data is in the form of digital broad-band records from stations of the GDSN, which we transformed to records with the WWSSN long-period response. Where broad-band data were not available, we used the original long-period digital data. Onset arrival times were measured either from the original broad-band data or from short-period records. Inversions were performed using the MT5 version of McCaffrey & Abers' (1988) algorithm, which inverts *P* and *SH* waveform data to obtain the strike, dip, rake, centroid depth, seismic moment and source time function. The synthetic seismograms are formed by the addition of direct *P* or *SH* waves with the surface reflections *pP*, *sP* and *sS* and near-source multiples. Amplitudes are corrected for geometrical spreading, and for anelastic attenuation using a Futterman Q operator with a value for t^* of 1.0 s for *P* and 4.0 s for *SH* waves. We used *P* waveforms in the distance range 30°–90° and *SH* waves in the range 30°–75°. Uncertainties in the earthquake focal parameters were estimated according to the procedure described in Section 2.1 of the main text.

Each figure is divided into two parts. (a) The minimum-misfit solution panel, in which the values beneath the event header give strike, dip, rake, depth in kilometres and seismic moment in Newton metres. The upper circle shows the *P*-wave radiation pattern and the lower circle that for *SH*. Both are lower-hemisphere projections. The station code by each waveform is accompanied by a letter corresponding to its position on the focal sphere. These are ordered clockwise by azimuth. The solid lines are the observed waveforms and the dashed lines are the synthetic waveforms. The inversion window is marked by solid

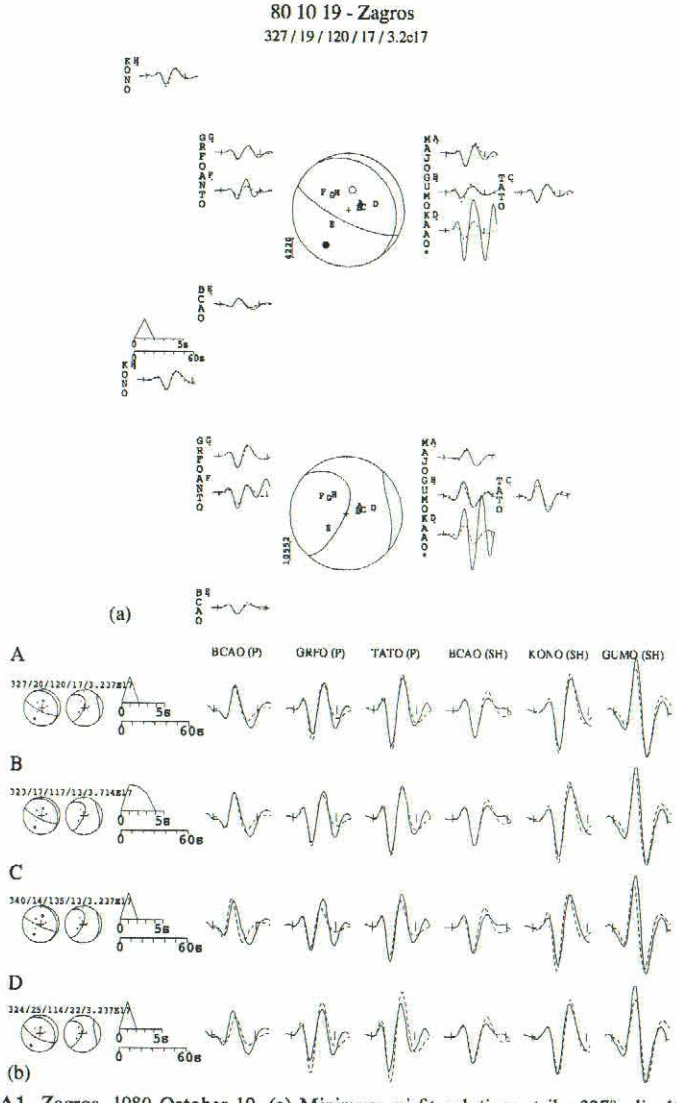

Figure A1. Zagros, 1980 October 19. (a) Minimum-misfit solution: strike 327°, dip 19°, rake 120°, depth 17 km, M_w5.6. The records at KAAO (indicated by *) were not used in the inversion procedure. (b) Sensitivity analysis. A: minimum-misfit solution shown in (a). B: depth fixed at 13 km; the source time function has doubled in length to fit the width of the first pulse. C: depth fixed at 13 km, source time function fixed to its value in A; the width of the first pulse is no longer matched. D: depth fixed at 22 km; the synthetic pulse is too wide. Event depth: 17^{+5}_{-4} km.

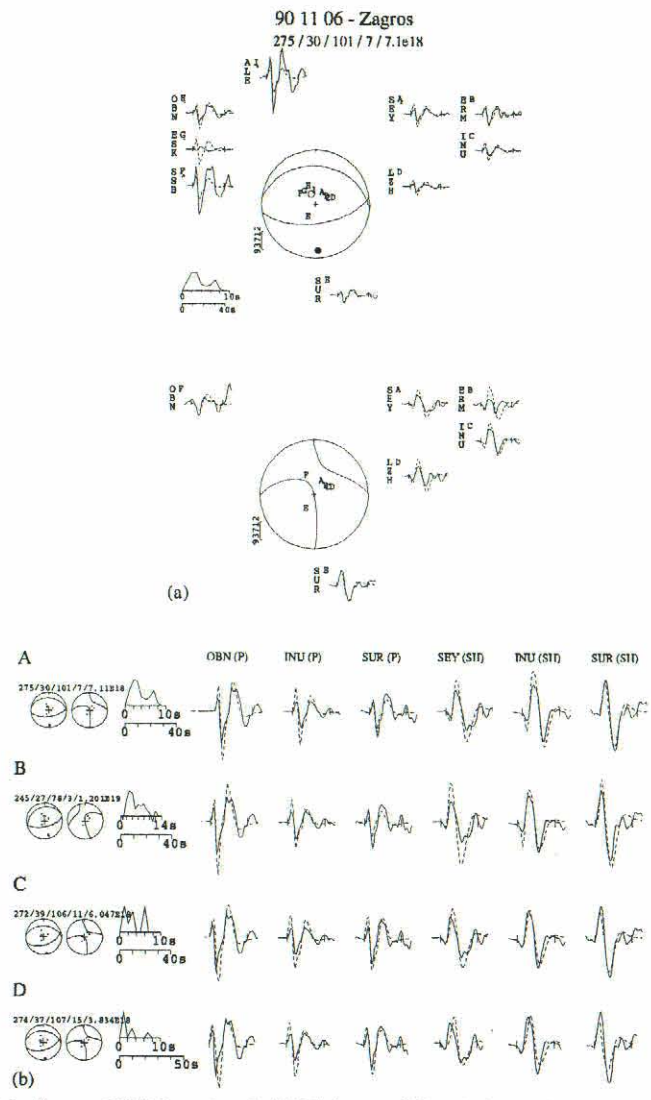

Figure A2. Zagros, 1990 November 6. (a) Minimum-misfit solution: strike 275°, dip 30°, rake 101°, depth 7 km, M_w6.5. (b) Sensitivity analysis. A: minimum-misfit solution shown in (a). B: depth fixed at 3 km; the source time function has expanded from 10 to 14 s duration and has become more complex. C: depth fixed at 11 km; the synthetic pulse is too wide. Event depth: 7 ± 4 km. D: the Harvard CMT solution (strike 274°, dip 37°, rake 107°, depth 15 km); the mechanism is similar to the minimum-misfit solution, but the synthetic waveforms are too broad.

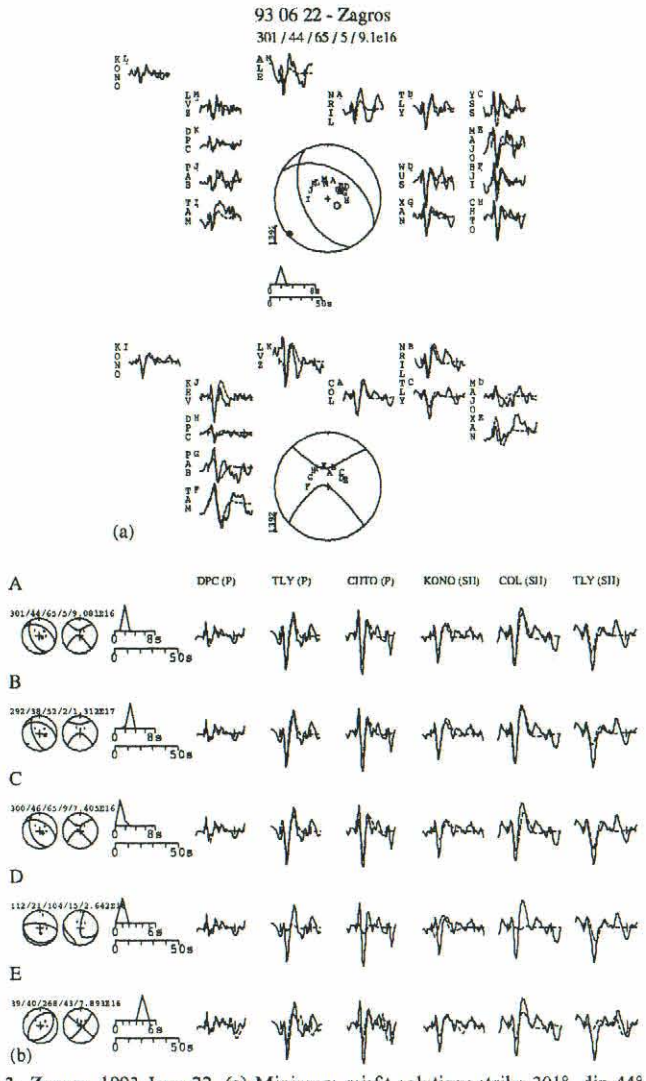

Figure A3. Zagros, 1993 June 22. (a) Minimum-misfit solution: strike 301°, dip 44°, rake 65°, depth 5 km, M_w5.2. (b) Sensitivity analysis. A: minimum-misfit solution shown in (a). B: depth fixed at 2 km; the fit is starting to deteriorate at TLY (*SH*). C: depth fixed at 9 km; the pulse is too broad at COL (*SH*). Event depth: 5^{+4}_{-3} km. D: the Harvard CMT solution (strike 112°, dip 21°, rake 104°, depth 15 km); the stations which should be nodal with this mechanism have non–nodal waveforms. E: best-fit mechanism for a depth fixed at the EHB depth (44 km); the first-motion polarities are now incorrect (showing a normal mechanism perpendicular to the strike of the region).

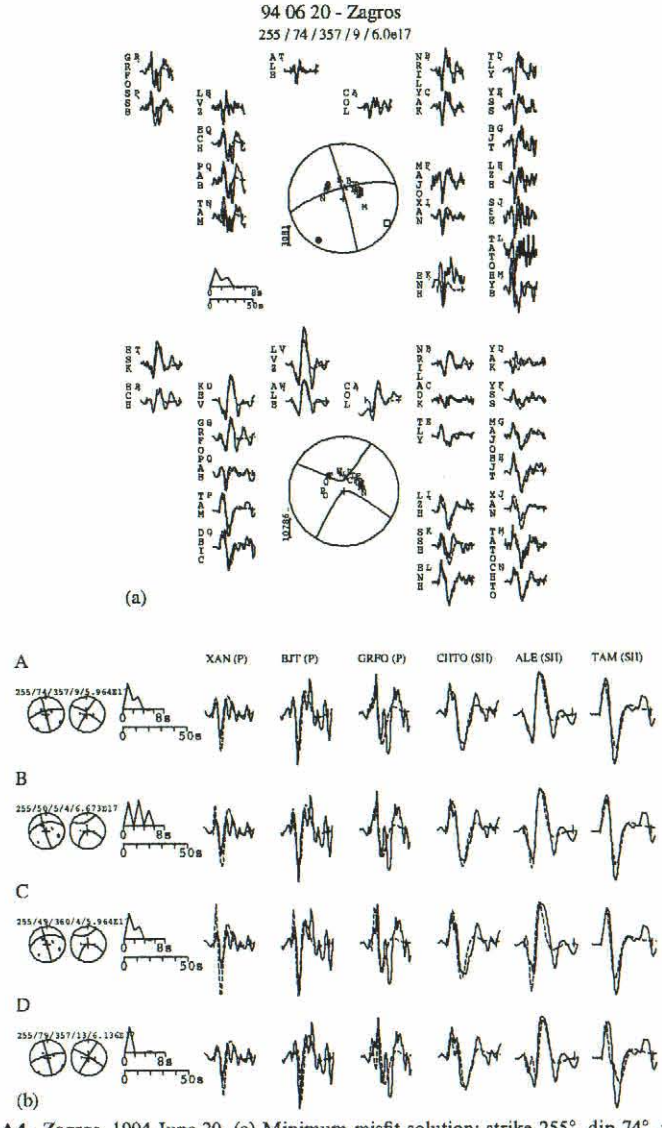

Figure A4. Zagros, 1994 June 20. (a) Minimum-misfit solution: strike 255°, dip 74°, rake 357°, depth 9 km, M_w5.8. (b) Sensitivity analysis. A: minimum-misfit solution shown in (a). B: depth fixed at 4 km; the source time function now shows three pulses. C: depth fixed at 4 km, source time function fixed to value in A; the synthetic waveforms are too narrow. D: depth fixed at 13 km; the synthetics are too broad. Event depth: 9^{+4}_{-5} km.

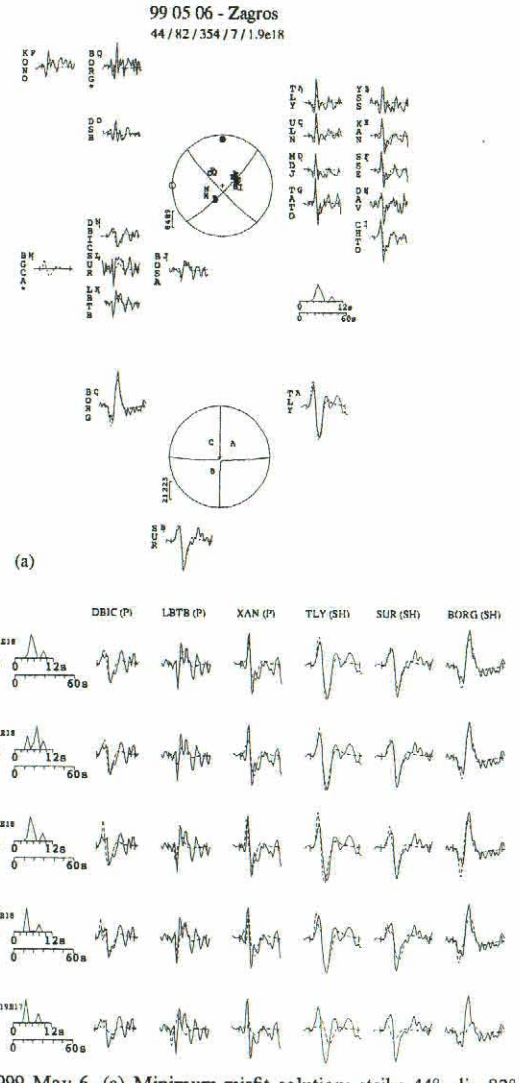

Figure A5. Zagros, 1999 May 6. (a) Minimum-misfit solution: strike 44°, dip 82°, rake 354°, depth 7 km, M_w6.1. The *P*-wave records at BGCA and BORG (indicated by *) were not used in the inversion. (b) Sensitivity analysis. A: minimum-misfit solution shown in (a). B: depth fixed at 3 km; the source time function shows three pulses. C: depth fixed at 3 km, source time function fixed to value in A; the synthetics are too narrow. D: depth fixed at 12 km; the synthetics are too broad. Event depth: 7^{+5}_{-4} km. E: the Harvard CMT solution (strike 324°, dip 68°, rake 190°, depth 17 km); the fit to the *SH* waveforms has deteriorated.

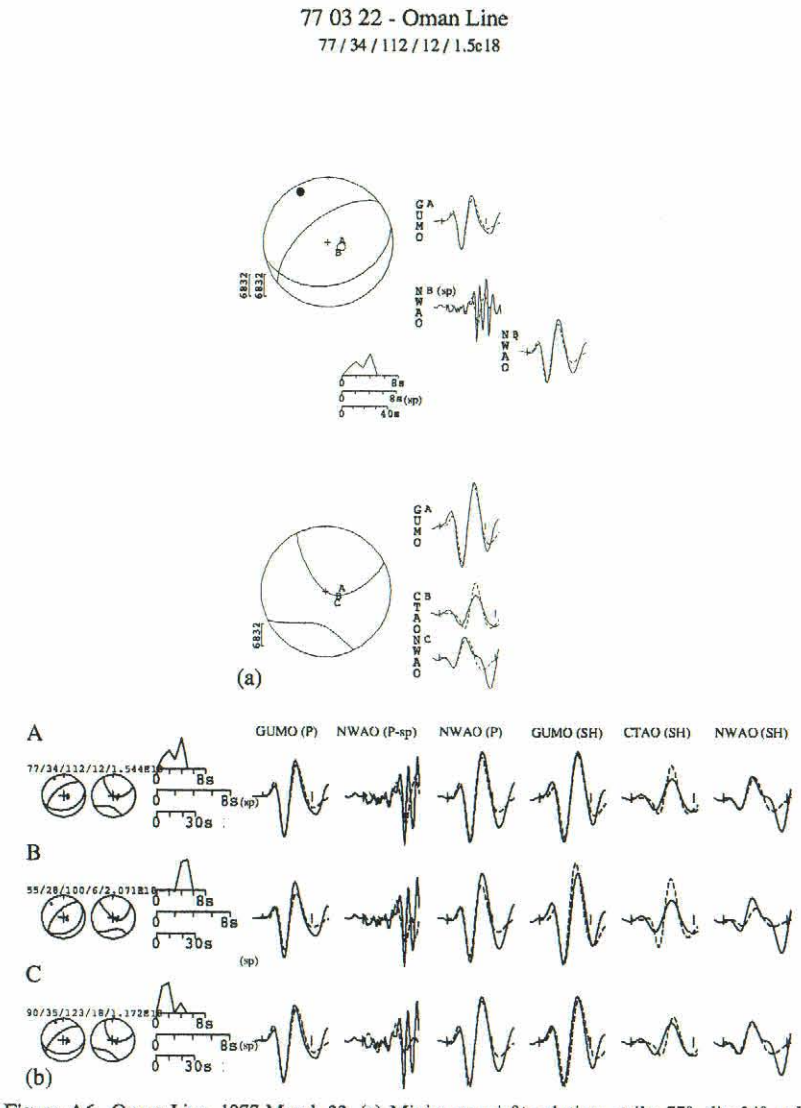

Figure A6. Oman Line, 1977 March 22. (a) Minimum-misfit solution: strike 77°, dip 34°, rake 112°, depth 12 km, M_w6.0. A short-period record at NWAO was included in the inversion. Although few stations were available, the focal mechanism is well constrained by the *SH* waves. (b) Sensitivity analysis. A: minimum-misfit solution shown in (a). B: depth fixed at 6 km; the synthetic pulse is too narrow at GUMO (*SH*), and its amplitude is too large at CTAO (*SH*). C: depth fixed at 18 km; the synthetic waveform is too broad at GUMO. Event depth: 12 ± 6 km.

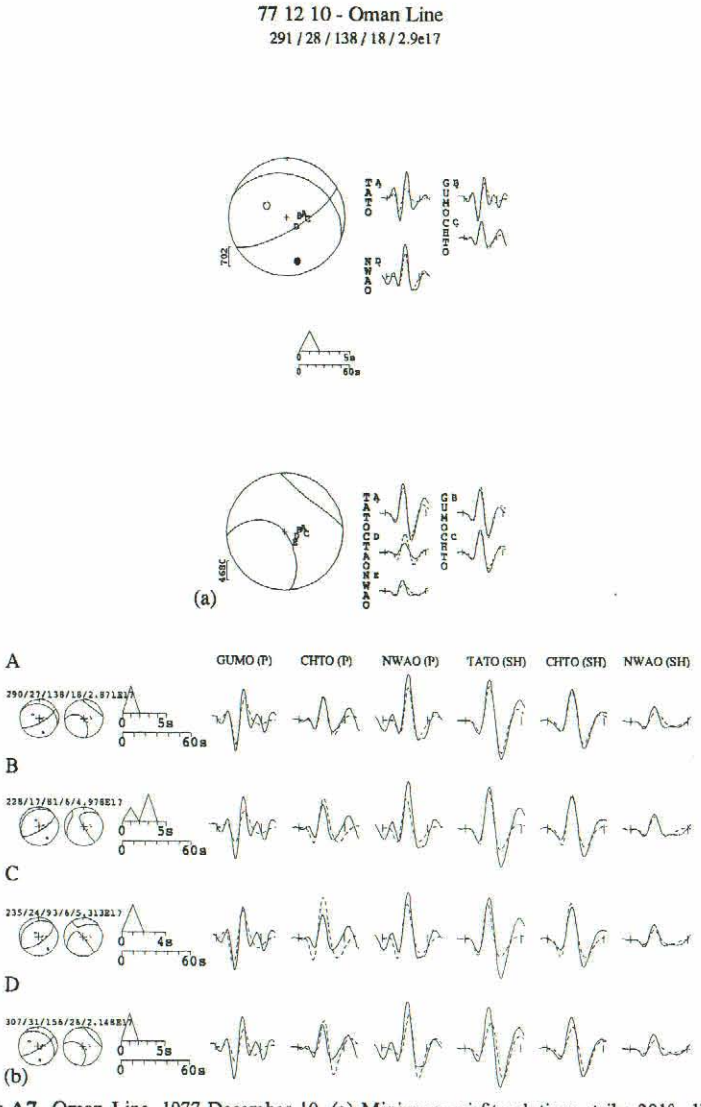

Figure A7. Oman Line, 1977 December 10. (a) Minimum-misfit solution: strike 291°, dip 28°, rake 138°, depth 18 km, M_w5.6. (b) Sensitivity analysis. A: minimum-misfit solution shown in (a). B: depth fixed at 6 km; the source time function has doubled in length. C: depth fixed at 6 km, source time function fixed to its value in A; the synthetics are too narrow, and the amplitude at CHTO (*P*) is too large. D: depth fixed at 26 km; the synthetics are too broad. Event depth: 18^{+8}_{-12} km.

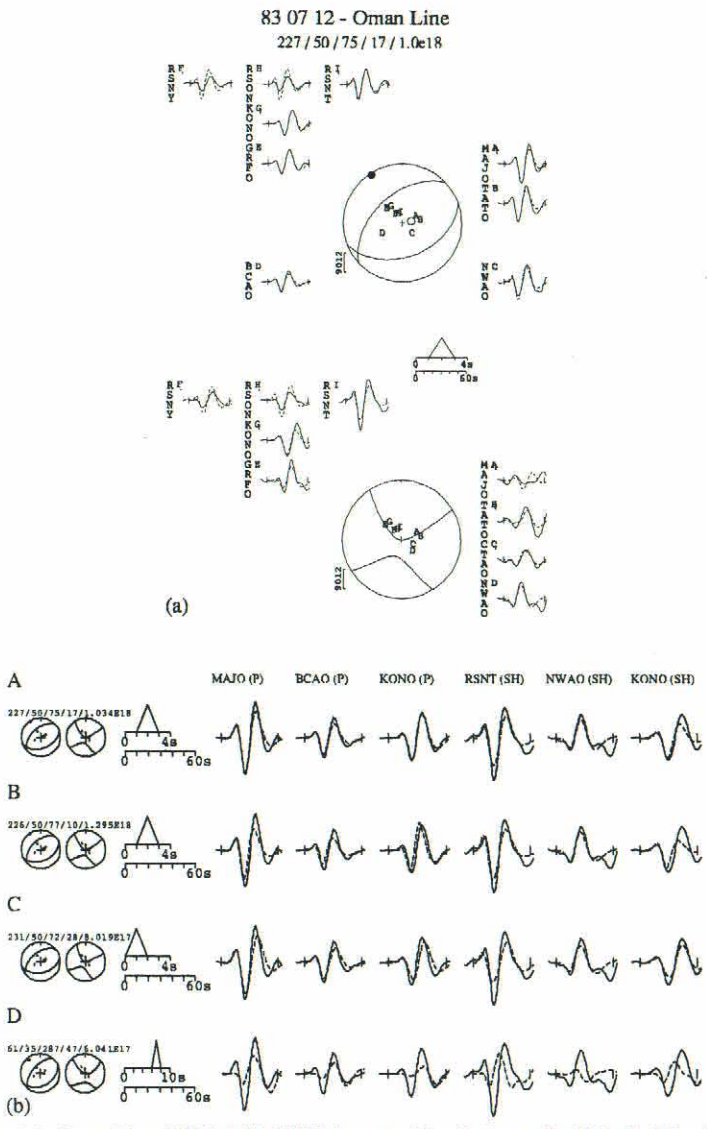

Figure A8. Oman Line, 1983 July 12. (a) Minimum-misfit solution: strike 227°, dip 50°, rake 75°, depth 17 km, M_w5.9. (b) Sensitivity analysis. A: minimum-misfit solution shown in (a). B: depth fixed at 10 km; the synthetics are too narrow. C: depth fixed at 28 km; the synthetics are too broad. Event depth: 17^{+11}_{-7} km. D: the Harvard CMT solution (strike 61°, dip 35°, rake 287°, depth 47 km); the fit has deteriorated at all stations.

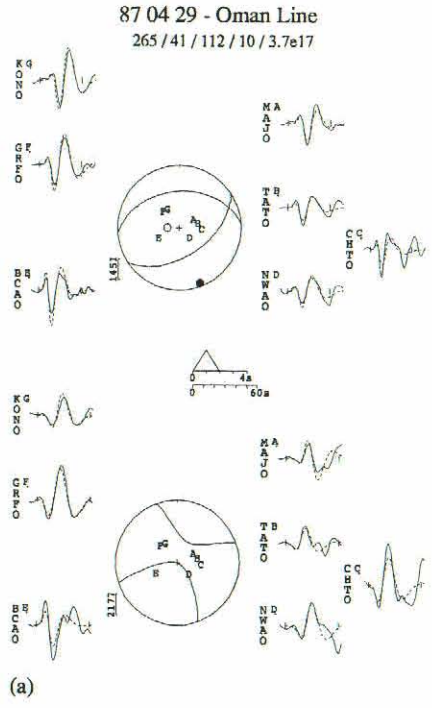

Figure A9. Oman Line, 1987 April 29. (a) Minimum-misfit solution: strike 265°, dip 41°, rake 112°, depth 10 km, M_w5.6. (b) Sensitivity analysis. A: minimum-misfit solution shown in (a). B: depth fixed at 6 km; the synthetic pulse is too narrow at GRFO (*P*) and its amplitude is too small at BCAO (*SH*). C: depth fixed at 17 km; the synthetics are too broad. Event depth: 10^{+7}_{-4} km.

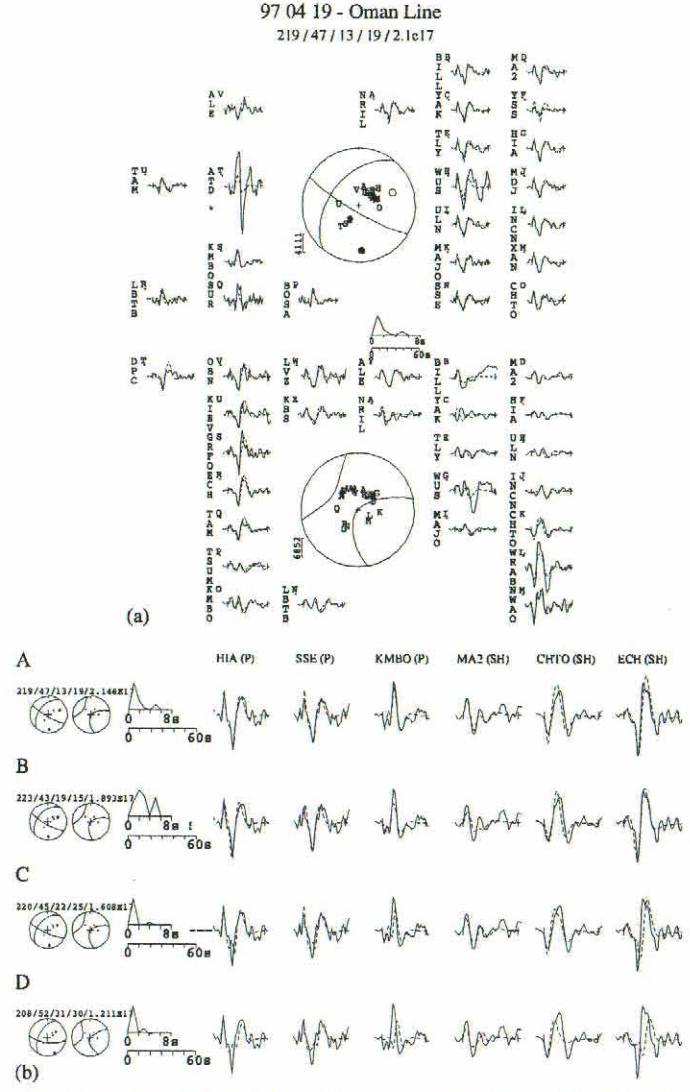

Figure A10. Oman Line, 1997 April 19. (a) Minimum-misfit solution: strike 219°, dip 47°, rake 13°, depth 19 km, M_w5.5. The *P*-wave record at ATD (indicated by *) was not used in the inversion. (b) Sensitivity analysis. A: minimum-misfit solution shown in (a). B: depth fixed at 15 km; the synthetic pulse is too narrow at CHTO (*SH*). C: depth fixed at 25 km; the synthetics are too broad. Event depth: 19^{+6}_{-4} km. D: depth fixed at the EHB value (30 km); the synthetics are too broad to fit the data.

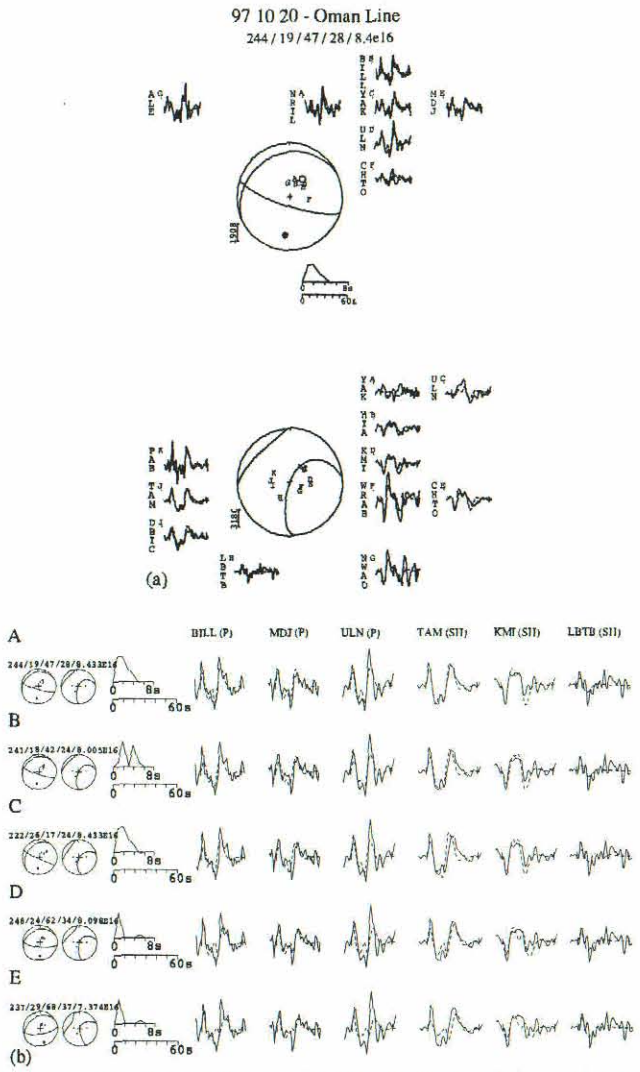

Figure A11. Oman Line, 1997 October 20. (a) Minimum-misfit solution: strike 244°, dip 19°, rake 47°, depth 28 km, M_w5.2. (b) Sensitivity analysis. A: minimum-misfit solution shown in (a). B: depth fixed at 24 km; the source time function has two peaks. C: depth fixed at 24 km, source time function fixed to its value in A; the synthetics are too narrow. D: depth fixed at 34 km; the fit has deteriorated at ULN (*P*) and TAM (*SH*). Event depth: 28^{+6}_{-4} km. E: depth fixed at the EHB value (37 km); the synthetics at BILL (*P*) and MDJ (*P*) no longer have the second trough, and those at ULN (*P*) and TAM (*SH*) are too broad.

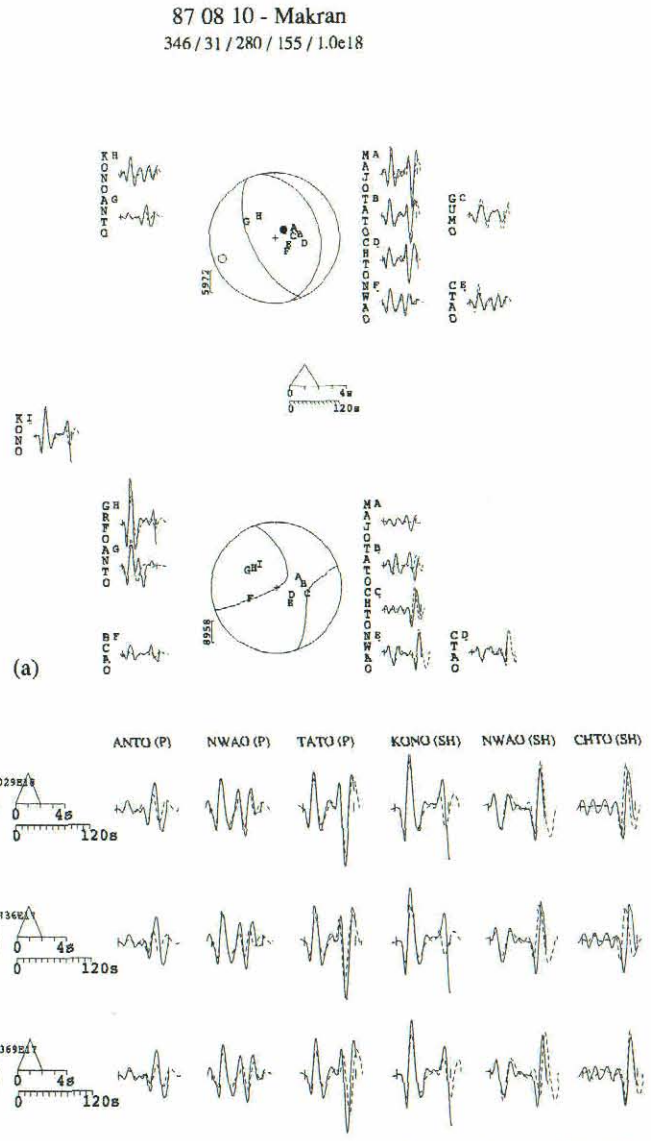

Figure A12. Makran, 1987 August 10. (a) Minimum-misfit solution: strike 346°, dip 31°, rake 280°, depth 155 km, M_w5.9. (b) Sensitivity analysis. A: minimum-misfit solution shown in (a). B: depth fixed at 145 km; the synthetics are too narrow. C: depth fixed at 165 km; the synthetics are too broad. Event depth: 155 ± 10 km.

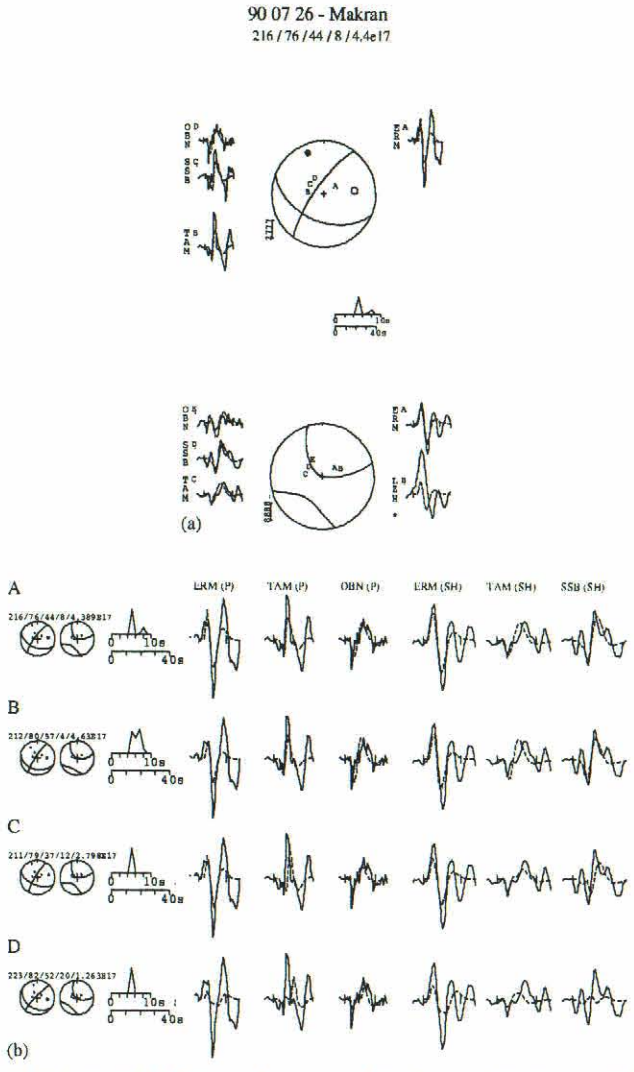

Figure A13. Makran, 1990 July 26. (a) Minimum-misfit solution: strike 216°, dip 76°, rake 44°, depth 8 km, M_w5.7. The *SH* record at LZH (indicated by *) was not used in the inversion. (b) Sensitivity analysis. A: minimum-misfit solution shown in (a). B: depth fixed at 4 km; the synthetics are too narrow at OBN (*P*) and TAM (*SH*). C: depth fixed at 12 km; the synthetics are too broad at TAM (*P*) and SSB (*SH*). Event depth: 8±4 km. D: depth fixed at the EHB value (20 km); the synthetic peak is too late at TAM (*P*) and the amplitudes of the synthetics are too small at most stations.

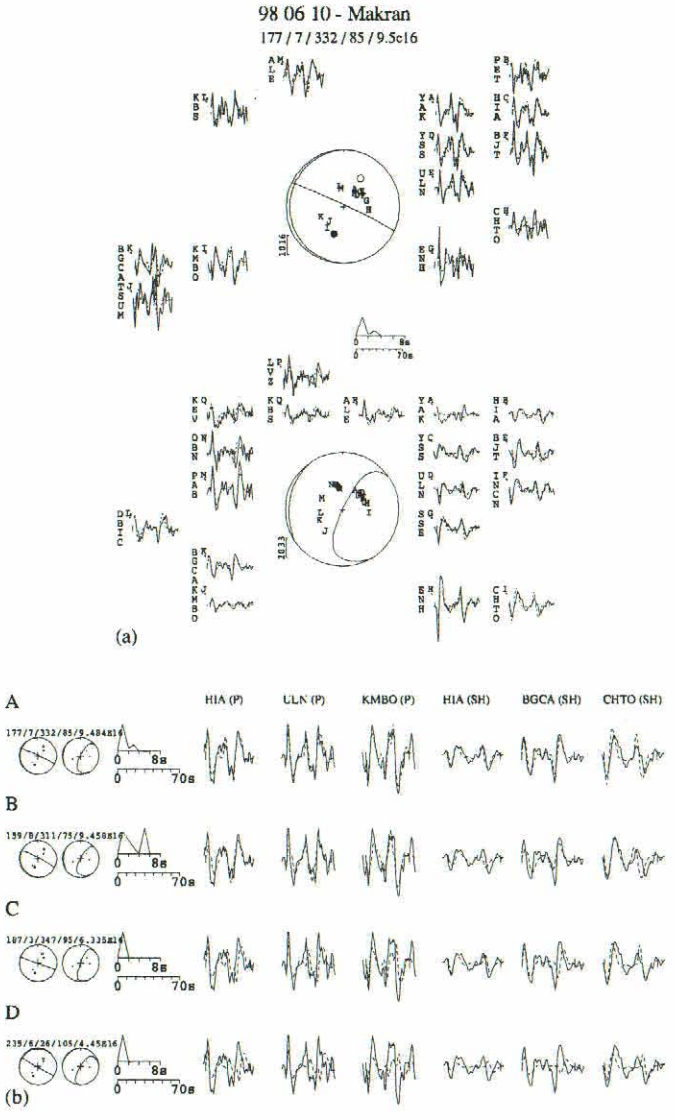

Figure A14. Makran, 1998 June 10. (a) Minimum-misfit solution: strike 177°, dip 7°, rake 332°, depth 85 km, M_w5.3. (b) Sensitivity analysis. A: minimum-misfit solution shown in (a). B: depth fixed at 75 km; the source time function has two peaks. C: depth fixed at 95 km; the synthetic waveforms are too broad. Event depth: 85±10 km. D: the Harvard CMT solution (strike 235°, dip 6°, rake 26°, depth 105 km); the synthetics are too broad to fit the data.

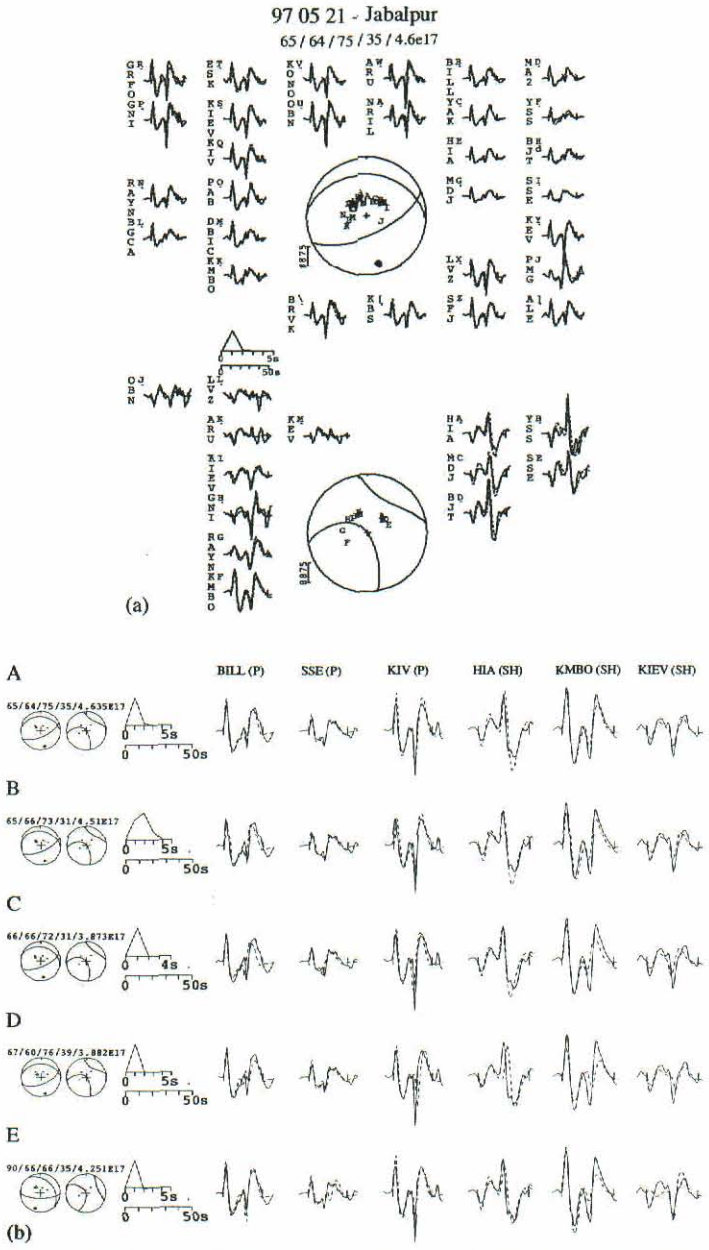

Figure A15. Jabalpur, 1997 May 21. (a) Minimum-misfit solution: strike 65°, dip 64°, rake 75°, depth 35 km, M_w5.7. (b) Sensitivity analysis. A: minimum-misfit solution shown in (a). B: depth fixed at 31 km; the source time function has broadened. C: depth fixed at 31 km, source time function fixed to its value in A; the synthetics are too narrow. D: depth fixed at 39 km; the synthetics are too broad. Event depth: 35±4 km. E: the solution of Battacharya *et al.* (1997), shown for comparison.

bars at either end of the waveform. P and T axes within the sphere are represented by solid and open circles respectively. The source time function (STF) is shown below the P focal sphere, with the waveform timescale below it. (b) The sensitivity analysis, in which each line shows the synthetic waveforms (dashed) generated by the source parameters shown above the focal spheres on the left, and the observed waveforms (solid) at a number of stations. Line A in each plot shows the minimum-misfit solution. Other lines show the effects on the fits of the synthetic waveforms of fixing one or more source parameters at values different from the minimum-misfit ones. A comparison with the Harvard CMT solution is shown, where the depth of the solution lies outside the uncertainties of the minimum-misfit solution; the focal mechanism and depth are set at the Harvard solution, and the moment and source time function shown are those that minimize the misfit to the data.

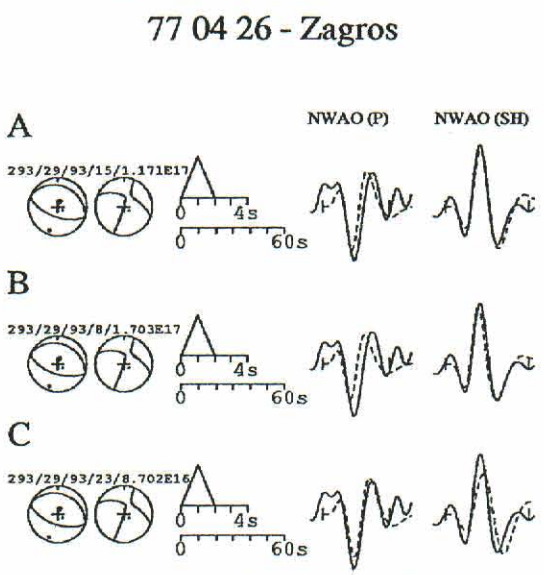

Figure B1. Zagros, 1977 April 26. Good-quality digital records were available only from station NWAO. We used the CMT mechanism (strike 293°, dip 29°, rake 93°) to calculate all the synthetics using MT5. A: best-fit depth: 15 km. B: depth fixed at 8 km; the synthetic pulse is too narrow at NWAO (*P*). C: depth fixed at 23 km; the synthetic pulse is too broad at NWAO (*SH*).

Where the EHB depth is outside the uncertainties of the minimum-misfit solution, we add a line that shows the best possible fit to the data with the depth fixed at the EHB value.

APPENDIX B: FORWARD MODELLING FOR DEPTH ONLY

This appendix contains the depth modelling results (Figs B1–B6) for the six 'b' class earthquakes in Table 1 that are not already discussed in the text. Where more than two broad-band records or only long-period records were available, we used the program MT5 (McCaffrey & Abers 1988) to generate synthetic seismograms with the WWSSN long-period response as described in Section 2.1. For these events, the figures show the fit of the synthetics (dashed lines) to the data (solid lines) at a series of depths; the first line shows the best-fit depth at either the Harvard CMT or the best-fit focal mechanism. In the other cases (Figs B2 and B6) we used the program WKBJ3 (Chapman *et al.* 1978) to generate synthetic seismograms with the WWSSN short-period response as described in Section 2.2. In these figures the synthetics are shown below the short-period record, starting with the synthetic calculated for the best-fit depth at the Harvard CMT mechanism.

In all figures, comparisons with the Harvard CMT or EHB depths are shown only where these depths lie outside the uncertainties in depth of the waveform-determined solution.

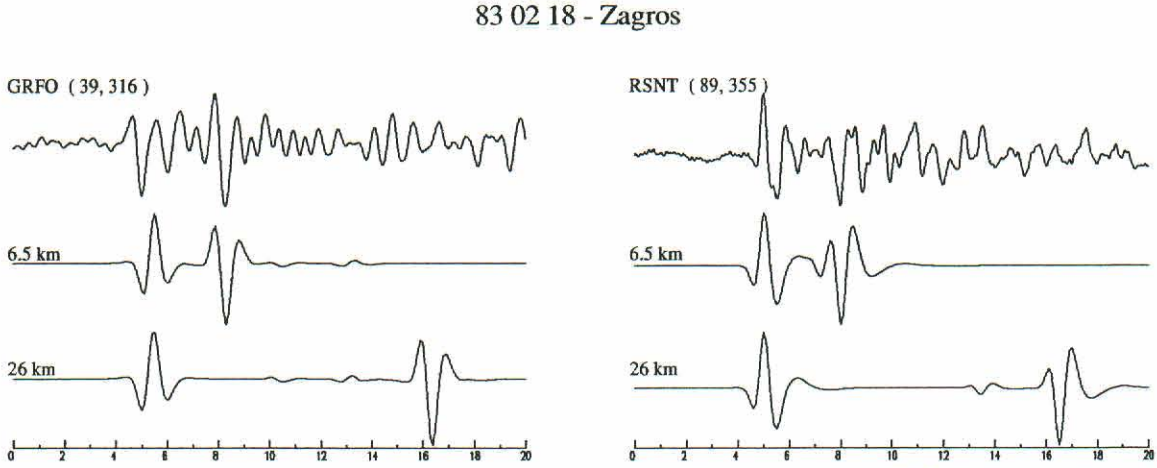

Figure B2. Zagros, 1983 February 18. The first lines show the original short-period records at stations GRFO (Δ 39°, Az 316°) and RSNT (Δ 89°, Az 355°). Synthetics were calculated with WKBJ3 using the CMT focal mechanism (strike 272°, dip 20°, rake 94°). We show synthetics for our best-fit depth (6.5 km) and the EHB depth (26 km).

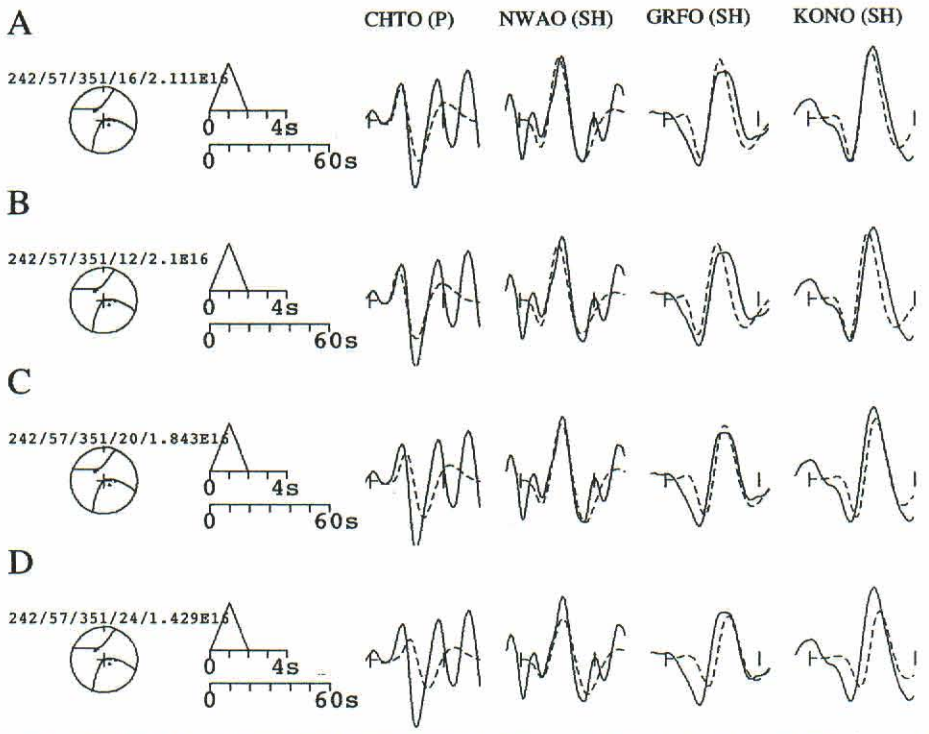

Figure B3. Zagros, 1988 August 30. Only *SH* waveforms had large enough signal-to-noise ratios to be used. All synthetics were calculated with the Harvard CMT focal mechanism (strike 242°, dip 57°, rake 351°) using MT5. A: best-fit depth: 16 km. B: depth fixed at 12 km; the synthetics are too narrow at NWAO, GRFO and KONO. C: depth fixed at 20 km; the synthetics are too broad at CHTO, GRFO and KONO. Event depth: 16±4 km. D: depth fixed at the EHB depth (24 km); the synthetics are too broad at all stations.

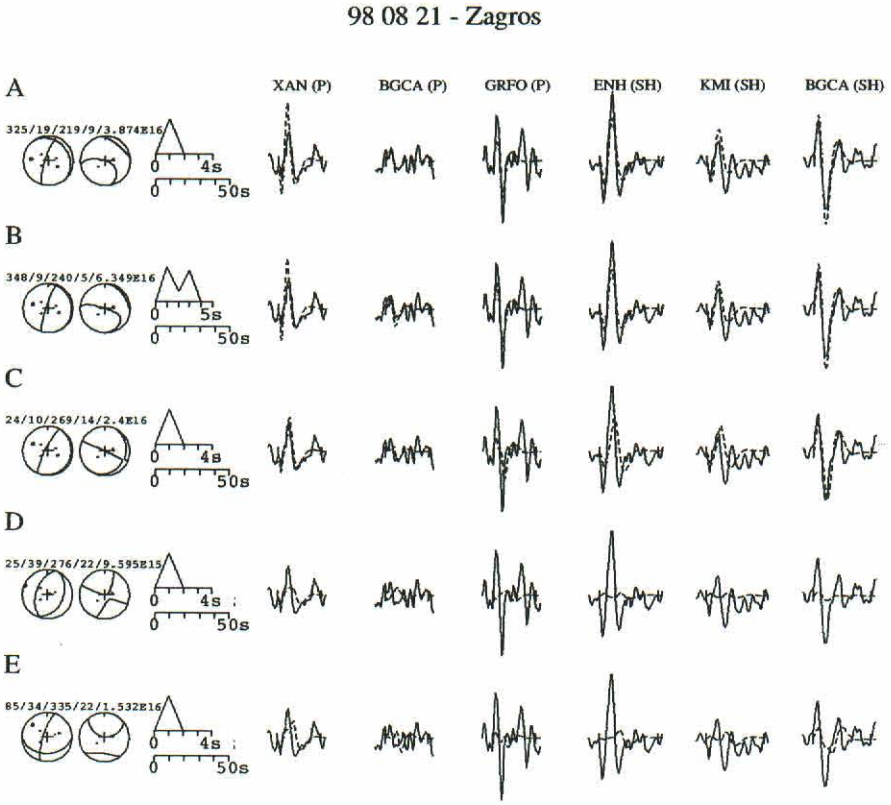

Figure B4. Zagros, 1998 August 21. Synthetics were calculated using MT5. A: best-fit solution: depth 9 km. B: minimum-misfit solution for a depth of 5 km; the source time function has two peaks. C: minimum-misfit solution for a depth of 14 km; the synthetics are too broad at ENH (*SH*) and KMI (*SH*). Event depth: 9^{+5}_{-4} km. D: the Harvard CMT solution (strike 25°, dip 39°, rake 276°, depth 22 km); the nodal planes pass close to stations with non-nodal waveforms. E: minimum-misfit solution for the EHB depth (22 km); the synthetic pulse is too broad at XAN (*P*) and BGCA (*P*), and the amplitudes are too small at the other stations.

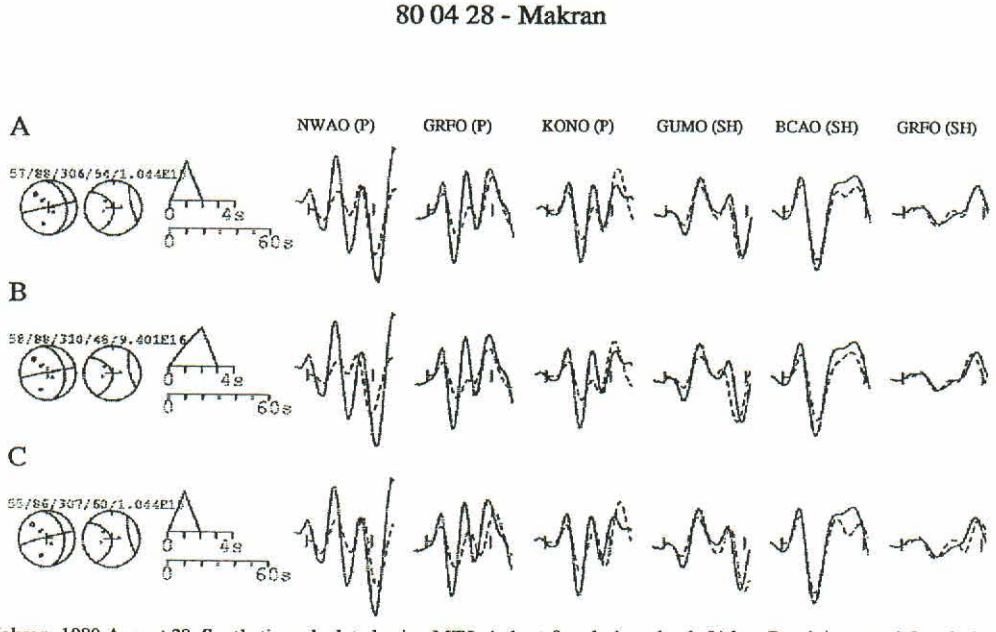

Figure B5. Makran, 1980 August 28. Synthetics calculated using MT5. A: best-fit solution: depth 54 km. B: minimum-misfit solution for a depth of 48 km; the synthetic pulse is too narrow at GUMO (*SH*) and GRFO (*SH*). C: minimum-misfit solution for a depth of 60 km; the synthetic pulse is too broad at GRFO (*P*), GUMO (*SH*) and GRFO (*SH*). Event depth 54 ± 6 km.

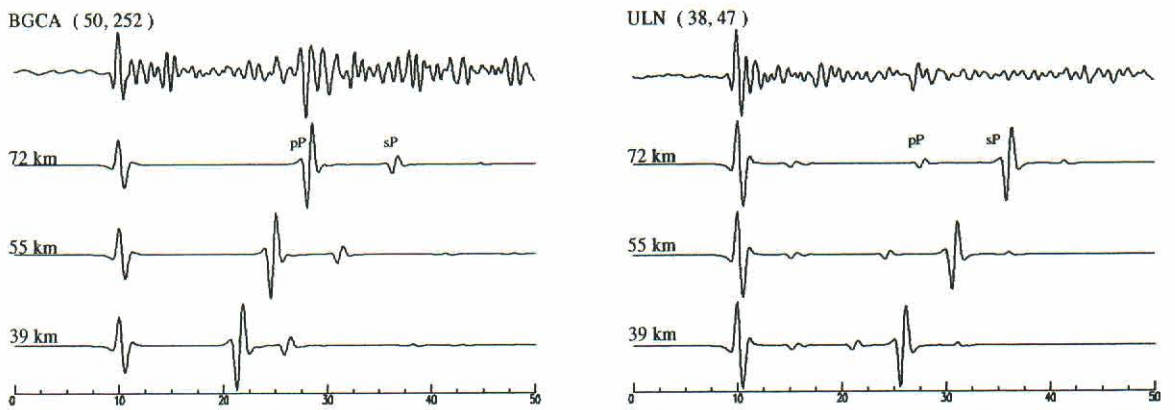

Figure B6. Makran, 1994 December 10. The first lines show WWSSN short-period records at stations GRFO (Δ 39°, Az 316°) and RSNT (Δ 89°, Az 355°). Synthetics were calculated with WKBJ3 using the CMT focal mechanism (strike 204°, dip 37°, rake −130°). We show synthetics for our best-fit depth (72 km), the EHB depth (55 km) and the Harvard CMT depth (39 km).

Crustal Structure Beneath the Foreland Spur in Northeastern India

Supriyo Mitra, Keith Priestley, Bullard Labs, University of Cambridge, UK.
Vinod Gaur, Indian Institute of Astrophysics, Bangalore, India

Northeastern India, one of the most seismically active region of the globe, is wedged between the northern Indo-Tibetan collision zone and the eastern Indo-Burman collision boundary that have jointly carved its remarkably acute angled northeastern extremity. A spur of Precambrian crystalline basement, exposed over a large area in the Shillong plateau and Mikir Hills as well as smaller outcrops in the Brahmaputra valley, is elsewhere covered by gently dipping Tertiary beds that reach prodigious thicknesses of several thousand meters in the eastern Himalayan foreland. We use broadband teleseismic data recorded at 7 sites along a 250 km long N-S profile from stations sited on this foreland spur consisting of the Shillong plateau and other basement exposures across the Brahmaputra, right up to a few km south of the Main Central Himalayan thrust in the region, to glean the seismic characteristics of the crust underneath. Receiver Functions at the above sites show that crustal thickness under the Shillong plateau changes from 40 km at its southern extremity at Cheerapoonji to 35 km at Barapani and Shillong at the center of the plateau. While further north along this profile, at Gauhati, Baihata and Tezpur in the Brahmaputra valley, the crustal thickness is found to be 40-44 km, and the crust appears to gently dip northward reaching a thickness of 50 km in the Lesser Himalaya at Bomdila which is several km north of the Main Boundary thrust(MBT) and a few km south of the Main Himalayan Central thrust in this region.

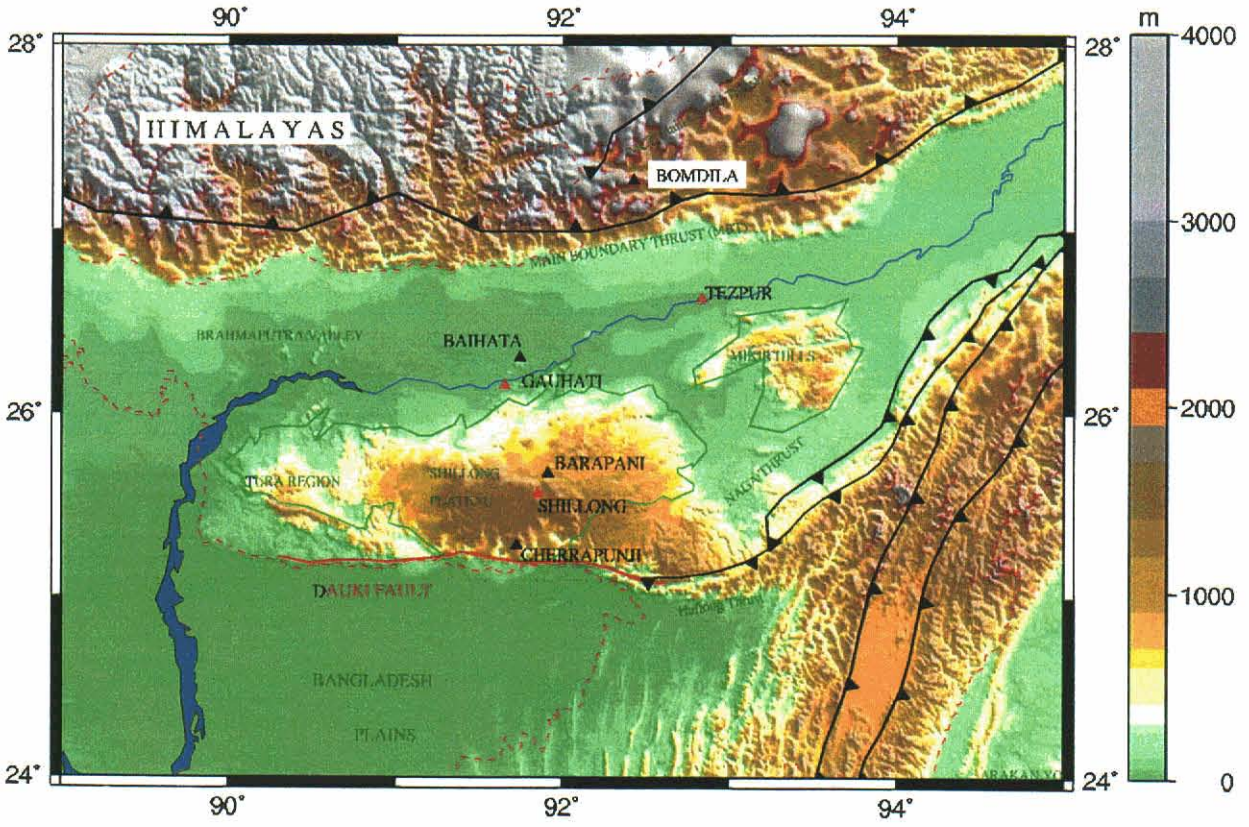

Elevation Map of Northeast India, showing the 7 Broadband stations along a 250 km profile across the Shillong plateau, Brahmaputra Valley and the Lesser Himalayas.

1 Tectonic setting

Northeast India is tectonically one of the most interesting regions of the world being bound by the Himalayan Arc to the north and Burmese arc to the east. The region evolved with the series of complicated geological process that followed the penetration of the Indian continent into Eurasia and later with the wrapping of the Himalayan collision front around its northeastern edge to form the Arakan Yoma ranges. The narrow region intervening between these two ranges is the Brahmaputra valley, confined at its southern edge by the Shillong massif, an elevated Archean Block that rises abruptly above the Bangladesh plains. The region is composed of diverse geological terranes ranging in age from Archean to younger orogenies (Evans, 1964). The plateau is characterized by positive Bouguer and isostatic anomalies (Verma and Mukhopadhyay, 1977; Gaur and Bhattacharji, 1983).

Our present study aims to determine the Crustal thickness and velocity structure along a 250km N-S profile, ranging from the southern edge of the Shillong plateau to a few kilometers south of the Main Central Himalayan thrust(MCT), by measuring and inverting teleseismic receiver functions.

2 Receiver Function Analysis

Receiver functions are time series, computed from three-component seismograms, which show the relative response of Earth structure near the receiver. The waveform is a composite of P-to-S converted waves, at a significant velocity contrast in the crust and upper mantle, that reverberate in the structure beneath the seismometer. Modeling the amplitude and timing of those reverberating waves can supply valuable constraints on the underlying geology.

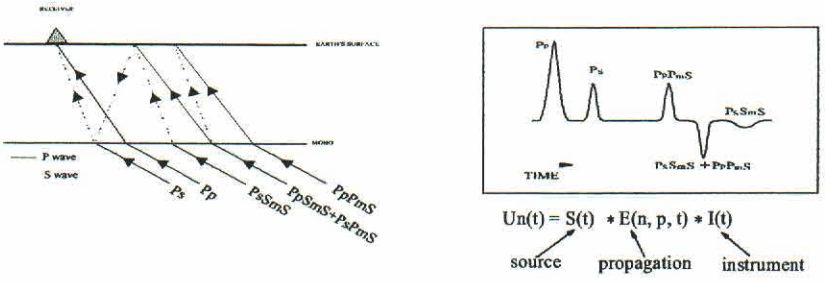

A cartoon showing the reverberations of P-to-S converted waves within the crust. Ray paths are shown on the left and radial receiver functions on the right.

University of Cambridge in collaboration with the Indian Institute of Astrophysics have operated four CMG-3T Broadband seismometers(black triangles in fig-1) in Northeast India in order to

record high quality seismic data for the study of the crustal structure of the region along a N-S profile. We also used data from the NGRI station at Tezpur, IMD station at Shillong and the Gauhati University broadband station(red triangles in fig-1). In our analysis we use teleseismic events recorded at the seven broadband stations along the N-S profile, within a distance range of 30 to 90 degrees from the respective stations.We used events of magnitude 5.7 and above to ensure high signal to noise ratio.

We have used the iterative, time-domain deconvolution approach (Ligorria and Ammon, 1999), to calculate the receiver functions. The foundation of this method is a least-square minimization of the difference between the observed horizontal seismogram and a predicted signal generated by the convolution of an iteratively updated spike train with a vertical component seismogram. Stacked receiver functions calculated with a Gaussian of 2.5 are shown in figure-3, along a NS profile. The stations have been projected back on to the NS profile line. The distances between the traces on the plot represent the relative distance between the stations along the profile.

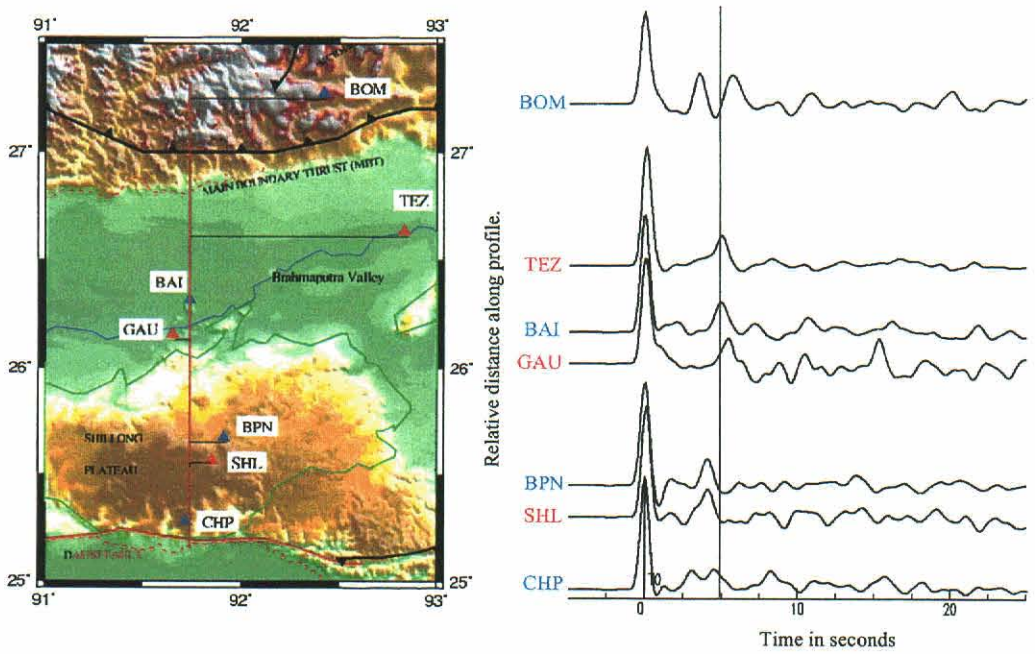

Stacked radial Receiver Functions along the NS profile. Left- Map showing the projection of the seven stations on a NS profile line. Right- Stacked receiver functions from the seven stations along the profile.

In order to model receiver functions, we calculated synthetic seismograms from a velocity model, and then used the iterative deconvolution technique to compute the synthetic receiver functions,

and compare them with the observed ones. The starting Average 1D models for the region is taken from Mukhopadhyay et al., 1997, Rai et al., 1999 and De and Kayal, 1990.

Upper crust: $V_p = 5.9 \pm 0.2\text{kms}^{-1}$, $V_p/V_s = 1.74$

Lower Crust: $V_p = 6.52 \pm 0.6\text{kms}^{-1}$, $V_p/V_s = 1.76$

Upper crust: $Vp = 5.55 \pm 0.4kms^{-1}$, $\frac{Vp}{Vs}ratio = 1.74$

Lower Crust: $Vp = 6.52 \pm 0.6kms^{-1}$, $\frac{Vp}{Vs}ratio = 1.76$

Average Pn velocity $8.5 \pm 0.2kms^{-1}$

We use a grid search algorithm to find the best fit solution between the observed and synthetic receiver functions.

- A grid space is constructed for large range of values of velocity and thicknesses of the layers for the region.
- Synthetic receiver functions are computed for all such node points on the grid.
- The mismatch between the observed and the synthetic receiver function is calculated by least square fit.
- the corresponding model for the minimum misfit synthetic is the solution to the structure beneath the receiver.

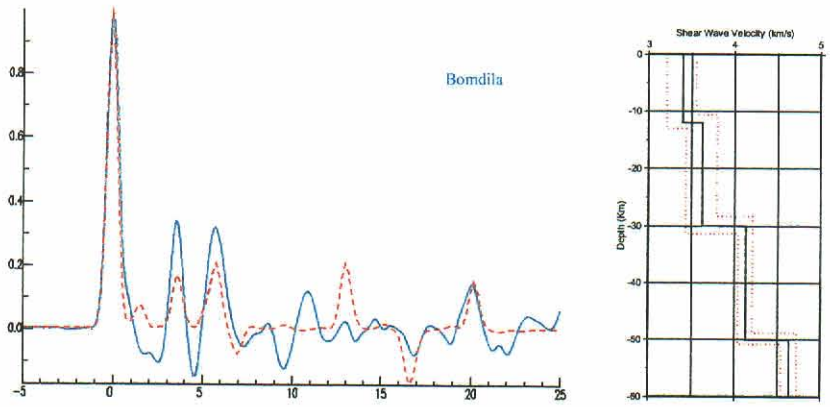

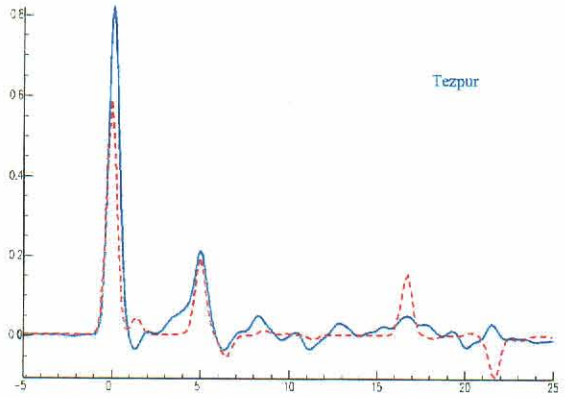
Tezpur

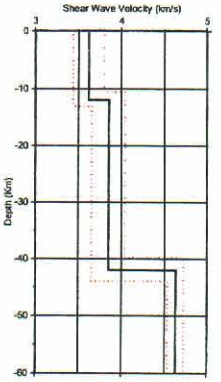
Shear Wave Velocity (km/s)
Depth (Km)

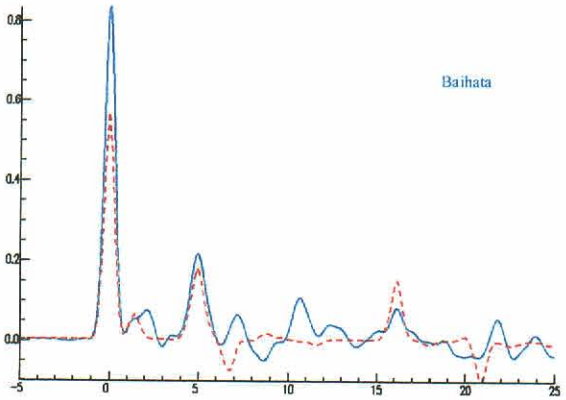
Baihata

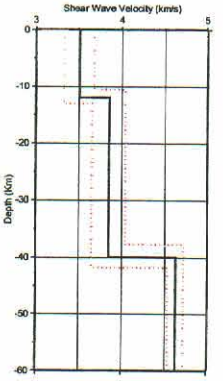
Shear Wave Velocity (km/s)
Depth (Km)

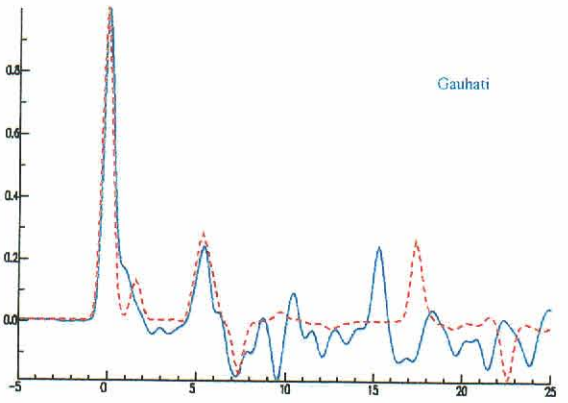
Gauhati

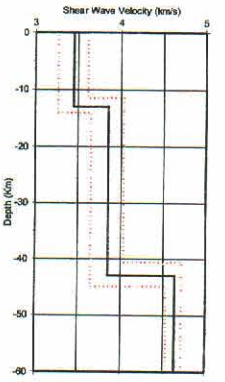
Shear Wave Velocity (km/s)
Depth (Km)

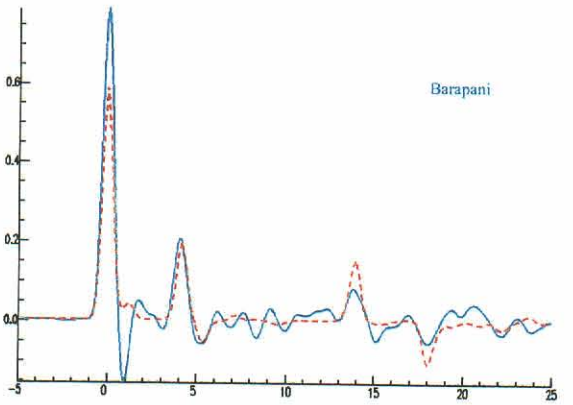
Barapani

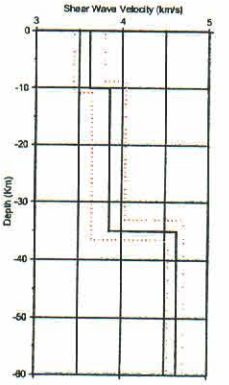
Shear Wave Velocity (km/s)
Depth (Km)

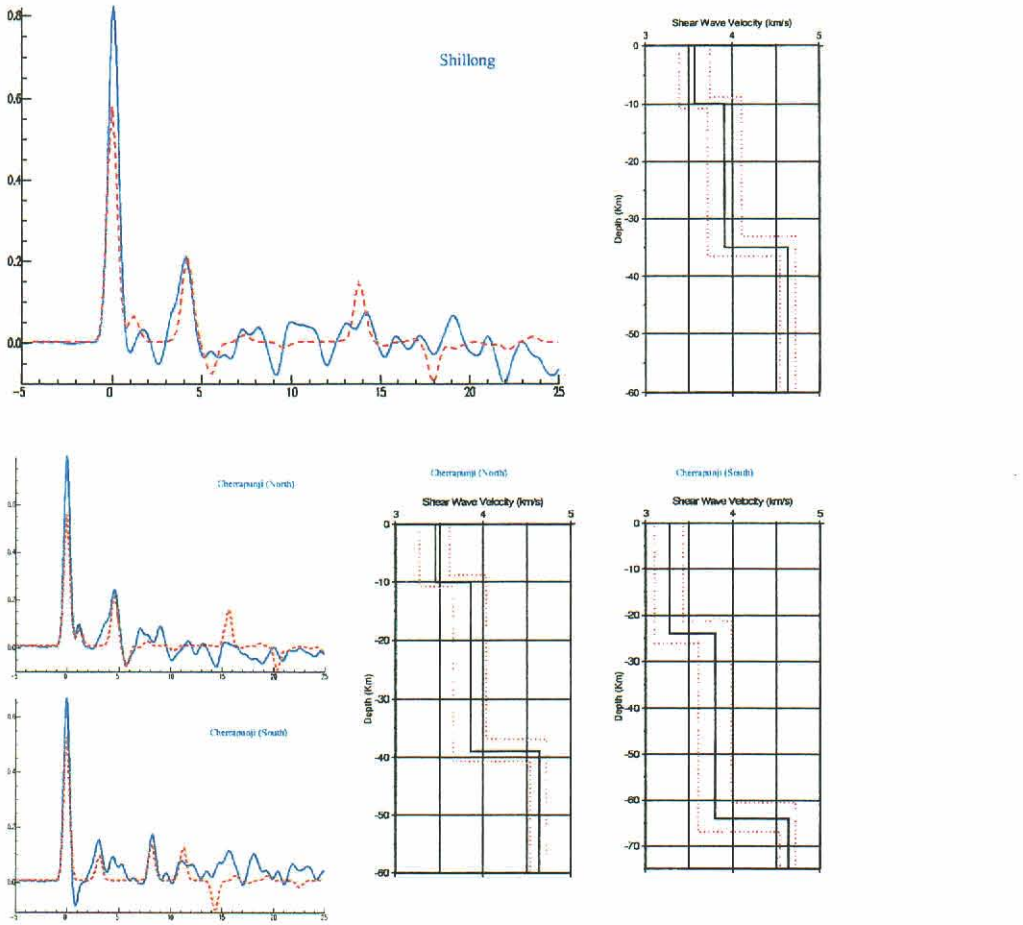

: *Plot showing the radial receiver function and the best fit synthetic generated from the velocity model shown on the right. Left- The blue bold line is the observed data, while the red dotted line is the synthetic. Right- The bold black line is the V_s velocity model used to generate the best fit synthetic, and the red dotted lines(bounds) shows the allowable variation in the model which can produce equally good fit to the data.*

3 Discussion and Conclusion

- Our results show a thinner crust (35km) beneath the Shillong plateau compared to its northern and southern regions, i.e. the Bengal basin and Brahmaputra valley respectively.
- The depth to the Moho obtained by modelling the receiver functions for rays sampling the Bengal basin (south of Cherrapunji) shows a very thick crust (64km). This is consistent with the view that the Archean basement in the Bangladesh plains is about 12km below mean sea level, due to thrusting along the Dawki fault; while the receiver functions for rays sampling the plateau shows a comparatively thinner crust (37km±2), being similar to Barapani and Shillong which are right on the plateau.
- The thickness of the crust in the Brahmaputra valley is 42km±2, and the Moho dips gently towards the north, reaching values of 50km at Bomdila which is beyond the Himalayan Main Boundary Thrust(MBT).
- The thickness of the upper crust is less constrained, due to inadequate data and absolute trade-off between velocity and thickness.

- The thickness of the crust in the Shillong plateau match remarkably well with the results of Bilham and England(Nature, 2001), and could be explained with the plateau pop-up model, showing an uplift of about 5-6kms, due to thrusting along the Dawki and Oldham faults at the edges of the plateau.
- The popped-up crust beneath the Shillong plateau is not fully compensated and hence is thinner compared to the north and south, which agrees with the positive Bouguer gravity anomaly over the plateau region(Gaur and Bhattacharji, 1983).
- The thickness of the crust in the Shillong plateau is fairly similar to the undeformed crust in the stable south Indian shield.

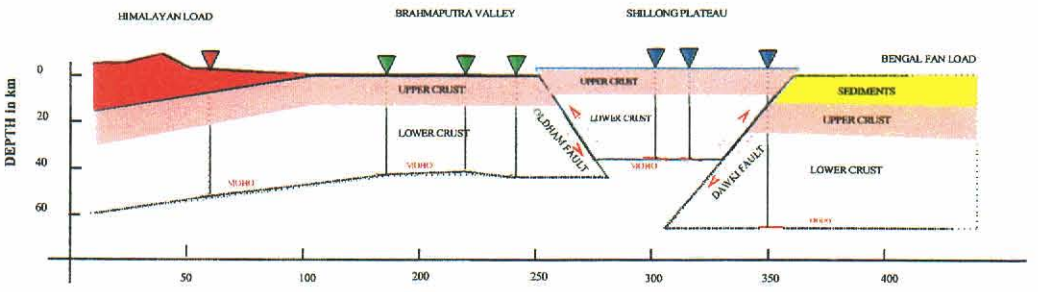

: Schematic N-S profile from the Himalayas to the Bengal basin. The stations are marked with inverted triangles and the depth to the Moho at the 7 sites being used as a guide to interpolate the northward dip and pop-up of the plateau. The basis of the schematic diagram is adopted from Bilham and England, 2001.

4 Acknowledgments

We thank Dr SK Lashkar, Dr Ashoke Kumar, Mr Anjan Kumar Bhattacharya and Mr Nava Kumar Hazarika of Tezpur University, for extending their kind support to maintain the broadband seismometers in northeastern India. We are grateful to Dr Dulal Goswami, Gauhati University, for granting us permission to use their Gauhati broadband data for the analysis. Supriyo Mitra also thanks the Cambridge Commonwealth Trust and the Overseas Research Scholarship for funding my PhD research.

5 References

- Dc R., Kayal J.R., 1990,*Pure Appl. Geophy.* 134 (1), 93-108.
- Evans P., 1964, *J. Geol. Soc. India* 5, 80-96.
- Gaur, V.K. and Bhattacharji, J.C., 1983,*IUGG Assembly*, Hamburg, Germany, August, 15-27.
- Ligorria, J.P. and Ammon, C.J.,1999,*Bull. Seism. Soc. Am.* 89, 1395-1400.
- Mukhopadhyay et al., 1997 *Tectonophysics* 283, 311-330.
- Rai S.S., Prakasam K.S., Agrawal N., 1999,*Proc. Indian Acad. Sc.(Earth Planet. Sc.)* 108(4), 297-304.
- Roger B. and England P., 2001,*Nature* 410, 806-809.
- Verma, R. K., Mukhopadhyay M., 1977,*Tectonophysics* 42, 283-317.

Seismic Characteristics of the Southern Indian Granulite Terrane Around Kodaikanal

Abhishek Rai, Keith F. Priestley, University of Cambridge,UK
Vinod K.Gaur, Indian Institute of Astrophysics,India
D. Srinagesh, National Geophysical Research Institute, India

South-Indian shield is a conglomeration of a variety of metamorphic rocks ranging from low-grade granite-greenstone in the north (Dharwar-craton) to high-grade granulite/charnockite (Granulitic terrain) in the south extending up to Sri-Lanka. Dharwar craton and Granulite terrain are significantly different in their evolution history, crustal properties and chemical composition. We compare the seismological properties around stations at Dharwar craton(BGL), South Indian Granulite terrain(KOD) and Sri-Lankan high-grade terrain(PALK) in terms of crustal thickness, Vp/Vs ratio, shear-wave velocity structure and anisotropy in the crust and upper mantle by the analysis of Moho converted phases and splitting of the shear-waves.

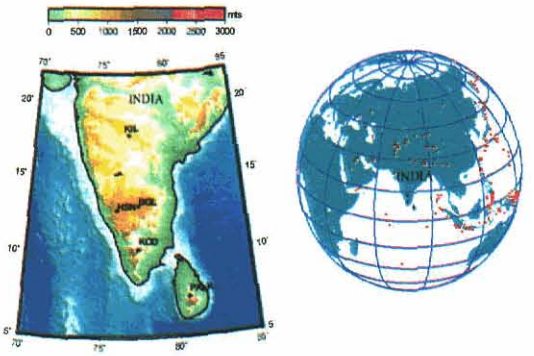

Figure 1: Map of the study area and station locations(left figure); distribution of earthquakes used in the study(right figure).

Receiver Functions

The study of Moho converted Ps phases to constrain the crustal thickness and shear-wave velocity structure is now a well established technique (Ammon C.J.,1991), widely known as receiver-function analysis. The arrival time of Moho converted S-phases with respect to the parent P-phase depends on the crustal thickness and the velocity structure beneath the recording station. While the amplitude of the Ps phase depends on the velocity contrast at the primary and secondary velocity discontinuities. A clear variation of the arrival-times of Moho converted Ps phases on South-Indian receiver-functions indicate changing velocity structures and/or crustal thicknesses around the stations.

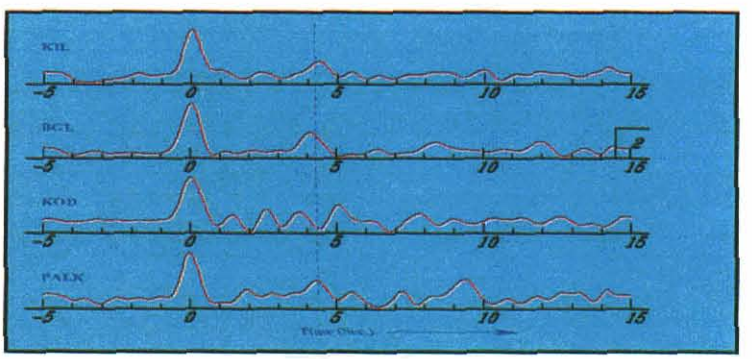

Figure 2: Radial component of receiver-function for the representative stations of Deccan Volcanic province(KIL), Eastern Dharwar craton(BGL), Granulitic terrain(KOD) and Sri-Lankan high-grade terrain(PALK). Relatively simple receiver function for KIL and BGL than KOD and PALK indicate a simpler crustal structure for low-grade Dharwar craton than the high-grade granulite terrains of India and Sri-Lanka in the south.

Crustal thickness and Vp/Vs ratio Study of Vp/Vs ratio along with shear-wave velocity provide an important constraint on the petrology of the rocks. The relative arrival time of the Moho converted Ps phase and the crustal multiples(PpPs, PpSs+PsPs) with respect to the direct P-wave can be used to transform the time domain receiver function to the H-Vp/Vs domain (Zhu and Kanamori,2000). A marked increase in Vp/Vs ratio was observed for high-grade terrain(KOD and PALK), with respect to low-grade rocks of Dharwar craton (BGL). This observation indicates a relatively more mafic composition for the rocks of high-grade granulite terrain than those of the Dharwar craton. Rapid variation in crustal thickness and Vp/Vs ratio may have important implications for the Pan-African orogeny(550Ma) and its impact on the Southern-Indian shield.

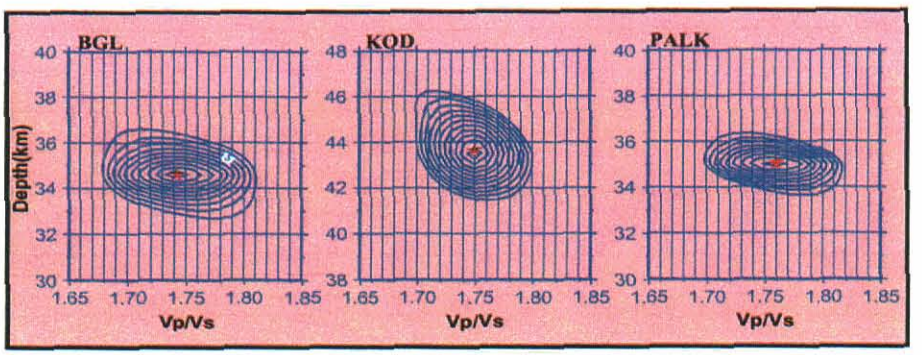

Figure 3: Crustal thickness Vs Vp/Vs ratio for BGL and KOD and PALK. Vp/Vs ratio increases slightly for low-grade to high-grade terrain. The crustal thickness at KOD is 10km more than that at BGL in the north and PALK in the south.

Velocity Structure

We derive our velocity model by inverting the teleseismic receiver functions and subsequently modelling the S to P converted phases (Jordan and Frazer, 1975). Modelling the precursors of S-waves provide an additional constraint to the velocity model derived from receiver function inversion. The final inversion result of the high-grade terrain receiver functions(KOD and PALK) gives a two-layer shear-wave velocity model with a strong mid-crustal velocity discontinuity at a depth of 27km and 22km depth. The crustal thickness varies from 44±1km at KOD to 35±1km at PALK. This indicates a thicker crust beneath KOD than BGL and PALK. The average shear-wave velocity changes from 3.6km/s in the upper crust to 3.95km/s in the lower crust. The smoothed crustal velocity model successfully models the Sp converted phases on the vertical component of the seismogram.

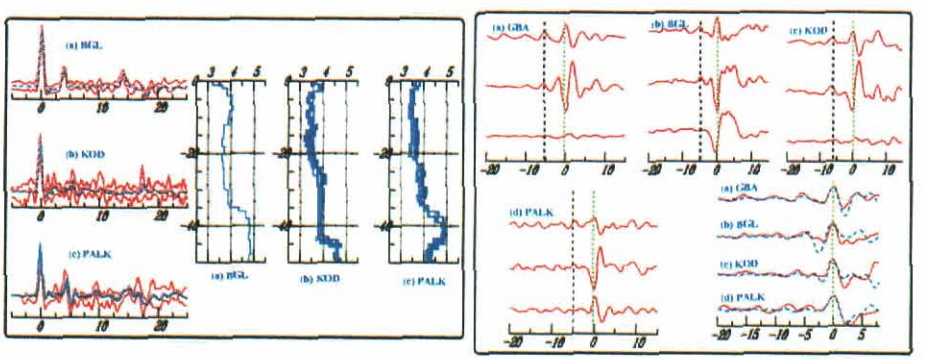

Figure 4: Shear-wave velocity Vs depth plot(the final inversion results) for BGL, KOD and PALK receiver functions(in the left). The right figure is the Z,R,T components indicating Sp phase and modelling of Sp phases on Z component seismogram for four stations of South-Indian shield. A thicker crust below KOD and strong mid-crustal discontinuities below KOD and PALK should be noted.

Variation of Crustal thickness along North-South and East-West Directions

The above observations indicate the rapidly changing crustal properties of the South Indian shield, indicating severe deformation of the shield region in the past.

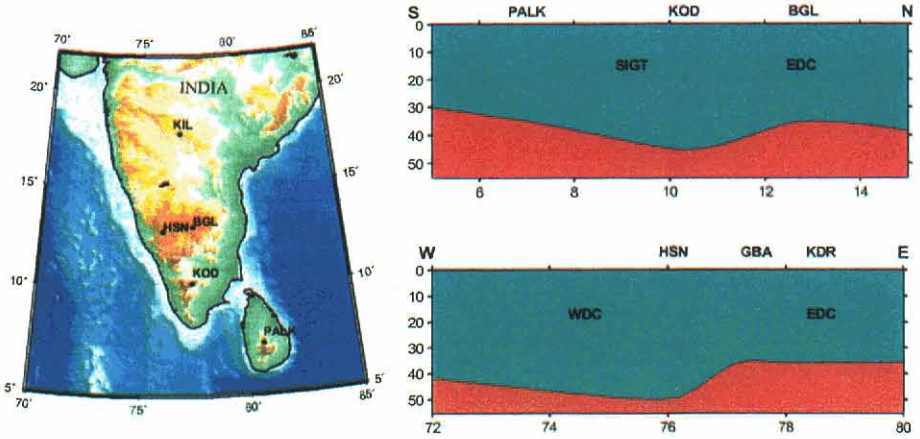

Figure 5: Variation of crustal structure along N-S and E-W profiles. Thicker crust beneath the high-grade terrain station KOD should be noted. There is a rapid change in crustal thickness of Eastern and Western Dharwar craton also.

Heterogeneity in the crust

Observation of the deviation of the teleseismic P-waves from their expected azimuth of arrival indicates scattering of the energy from heterogeneity present in the propagation path of the waves. The large tangential energy could also be a part of scattered energy. Co-variance analysis of the P-wave particle motion determines the true azimuth of the arriving energy at the recording station. The co-variance analysis of P-wave particle motion at higher and lower frequencies does not indicate significant deviation in the arrival azimuth of energy from its expected azimuth, indicating largely homogeneous structure below the South-Indian shield. The results are consistent with the measurements of multi-taper spectral density method.

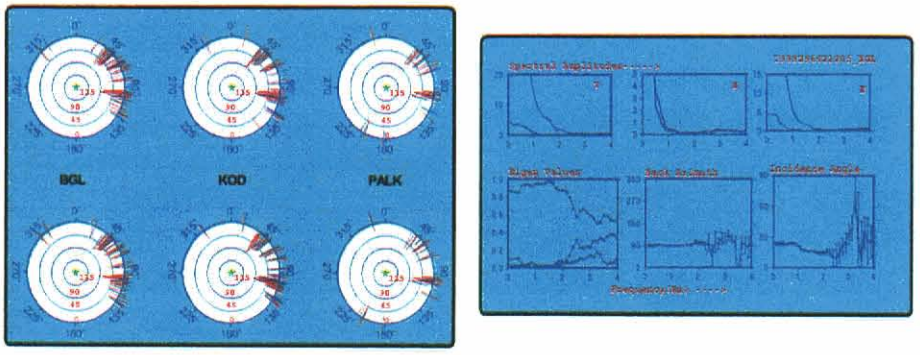

Figure 6: Azimuthal plots for expected and calculated polarization of teleseismic P-wave at lower (0.06-0.20Hz) and higher (0.33-2.0Hz) frequencies(left figure) indicating no significant deviation of energy from its expected path. Results of spectral analysis are shown in the right-hand figure.

An indication of Crustal Anisotropy

Shear wave splitting observed in P to S converted phases (Ps phase) from the Moho indicate velocity anisotropy in the crust (McNamara and Owens,1993). A 0.2sec splitting with fast-axis oriented towards North-South and a 0.25 sec splitting with fast-axis oriented E-W were obtained for most of the stations at Dharwar craton(exp. BGL) and Granulite terrain(KOD and PALK) respectively. These fast directions are in good agreement with the local geologic strike directions.

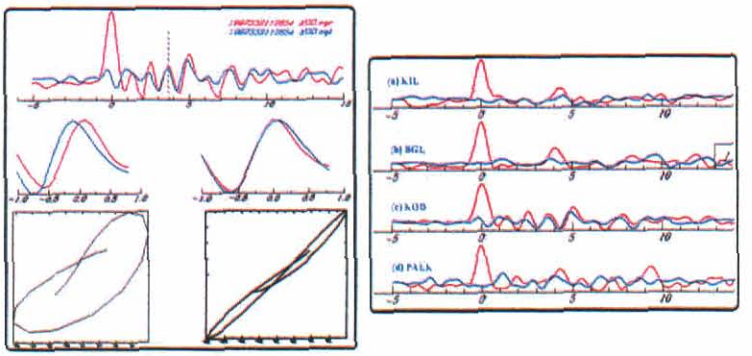

Figure 7: Figure in the left shows examples of splitting of the Moho converted Ps phases for South-Indian stations(BGL,KOD and PALK). The right fig. is the processing of Ps splitting observed at KOD.

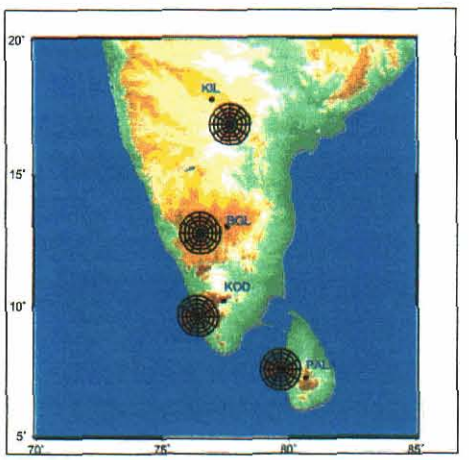

Figure 8: The fast-axis polarization direction of crustal components of anisotropy for Dharwar craton(BGL) and Granulite terrain(KOD and PALK). The fast direction is oriented N-S with a split time of 0.15s for low-grade terrain and E-W with a split time of 0.2s for high-grade terrain.

Teleseismic shear-wave splitting

Strain-Induced lattice preferred orientation(LPO) of olivine due to mantle flow causes anisotropy in the upper mantle. In this case the fast axis orientation of olivine aligns parallel to the flow direction, or to the direction of maximum finite strain and results in seismic velocity anisotropy in the upper mantle. A consequence of seismic anisotropy is the splitting of shear-waves , where an incident shear-wave is polarized into two orthogonal directions travelling at different velocities(Silver and Chan, 1991).
In the case of an isotropic, spherically symmetric earth, teleseismic SKS and S phases are radially polarized and should only be recorded on the radial component of the seismograms. Presence of any detectable energy on the transverse component, SKS_T, indicates deviations from isotropic models. Splitting of SKS waves indicate receiver side anisotropy only, as all the source-side anisotropy is lost due to S to P conversion at the core-mantle boundary.

Summary

- The KOD (SGT) receiver function waveform is more complicated than the BGL (EDC) receiver functions indicating complicated crustal structure beneath the Granulite terrain.
- Significant change in crustal thickness, velocity structure and Vp/Vs ratio between low-grade rocks of Dharwar craton and high-grade rocks of Granulite terrain.
- Vp/Vs ratio for Granulite terrain is higher than that for Dharwar craton, indicating that there is a difference in the chemical composition of the two terrains.

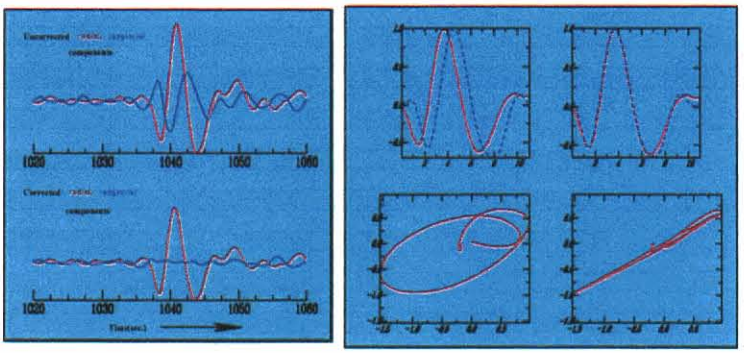

Figure 9: The fig. in the left shows the original radial and tangential component (in the upper half) and corrected radial and tangential components (in the lower half).The right-hand fig. shows the superposed fast and slow components (uncorrected in the left and corrected in the right) and the corresponding particle motion plots.

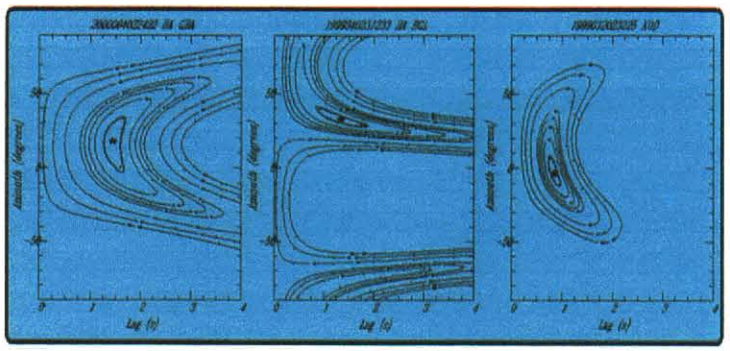

Figure 10: Contour plots of minimum eigenvalue of the corrected matrix of particle motion indicating well constrained splitting parameters for stations at GBA, BGL and KOD.

- Almost homogeneous crust beneath the whole South-Indian shield.
- Indication of crustal anisotropy with fast azimuth parallel to the geologic strike direction.
- Indication of anisotropy in the upper mantle beneath the South-Indian shield indicates fast-axis orientation almost parallel to the plate motion direction.

1 References

- Ammon, C.J., 1991, The isolation of receiver effects from teleseismic P waveforms, BSSA, Vol. 81, 2504-2510.
- McNamara D. E. and T.J. Owens,1993, Azimuthal Shear Wave Velocity Anisotropy in the Basin and Range Province using Moho Ps Converted Phases. Journal of Geophysical Research, Vol. 98, No. B7;12003-12017.
- Jordan, T.H. and L.N. Frazer,1975. Crustal and upper mantle structure from Sp phases. Journal of Geophysical Research., 80, 1504-1518.
- Silver, P. G., and W. W. Chan,1991. Shear-wave splitting and subcontinental mantle deformation, 96, 16,429-16,454.
- Zhu, L. and H. Kanamori,2000. Moho depth variation in southern California from teleseismic receiver functions, JGR, Vol. 105, No. B2, 2969-2980.

FIRST EVIDENCE FOR ANOMALOUS THICK CRUST BENEATH MID -ARCHEAN WESTERN DHARWAR CRATON

**Sandeep Gupta[1], S.S. Rai[1†], K.S. Prakasam[1], D. Srinagesh[1], R.K. Chadha[1]
Keith Priestley[2] and V.K. Gaur[3]**

1. National Geophysical Research Institute, Hyderabad – 500 007, INDIA
2. Bullard Laboratories, University of Cambridge, Cambridge, CB3 0EZ, UK
3. Indian Institute of Astrophysics, Bangalore – 560 034, INDIA

Abstract:

We report an anomalous present day crustal thickness of 43 – 52 km beneath the 3.4 – 3.0 Ga mid-Archean segment of the Western Dharwar Craton (WDC) undisturbed by Proterozoic events. In contrast, adjoining late Archean (2.7 – 2.5 Ga) Eastern Dharwar Craton (EDC) has a 33 – 40 km crustal thickness similar to the Archean global average. Considering that mineral assemblages in the central part of the WDC crust (amphibolite grade metamorphics) equilibrated at a depth of 15 – 20 km, we argue that the Western Dharwar crust 3.0 Ga ago must have been at least 60 – 80 km thick. Both segments of Dharwar craton crust exhibit Poisson's ratio 0.24 – 0.28 suggesting felsic to intermediate average crustal composition. The thickest crust beneath WDC has also underlying high-velocity thicker lithosphere compared to EDC inferred

Key words: Archean, Crust, Dharwar Craton, Receiver function, Teleseismic residual

† Corresponding author. ssrai_ngri@rediffmail.com

from faster arrivals of teleseismic P and S- wave. The contact between WDC and EDC is marked as gradational thinning of crust (42 to 36 km) from Chitradurga thrust to the western part of Closepet granite. These details provide important constraints to model the thermotectonic processes responsible for the formation of Dharwar crust during 3.4 to 2.5 Ga.

Introduction:

The origin and growth of the Archean crust is a subject of intense investigation. The geological, geochemical and geophysical observations suggest a fundamental difference between early and mid- Archean crust with those evolved during and subsequent to the late Archean[1]. Our understanding about the nature of the early crust and it's possible variation through geological time remains incomplete due to insufficient knowledge about the thickness and composition of the undeformed early-mid Archean crust. Global review of seismological data[2,3] suggests that the Precambrian shields have an average crustal thickness of 37 ± 5 km and P-velocity of 6.4 km/s. Also, Durrheim and Mooney[4] observed thicker and mafic crust beneath the Proterozoic terrain than the Archean. Recent analysis of broadband waveforms using receiver function[5-7] suggests bi-modal distribution of V_p/V_s (1.74,1.82) for the Archean terrains. Rudnick and Fountain[3] and Christensen[8] argue for intermediate composition of the average crust with Poisson's ratio $\sigma = 0.265$. For common rock types, σ varies from 0.20 to 0.35. With the increasing silica content σ lowers, while the higher mafic content increases it. For lower crustal rocks, low σ (<0.26), intermediate σ (0.26 – 0.28) and high σ (> 0.28) characterize its felsic, intermediate and mafic composition[9].

To investigate the crust and mantle structure beneath the Dharwar craton, we operated temporary broadband seismic stations during 1999- 2001. The earthquake waveforms were recorded at 20 sps using broadband CMG3T/3ESP sensors and REFTEK data loggers. The location of these stations is depicted in Figure 1.

We present here evidence for the thickest undisturbed mid Archean crust with a felsic to intermediate composition in Western Dharwar Craton through receiver function analysis of earthquake waveforms from teleseismic distance recorded over the network of broadband seismic stations. Along with the crustal character, we also investigate the lithospheric properties underlying the craton to constrain the process responsible for growth of the crust in Dharwar Craton during the Archean.

Tectonic Setting:

The Dharwar craton (Figure 1) is one of the major Archean blocks of the Indian subcontinent. Detailed geology is presented in several publications[10-12]. Geochronological and geochemical studies suggest a > 3.4 to 3.0 Ga continental nucleus in the western part of the Dharwar Craton[13,14] wrapped by 2.7 – 2.5 Ga crustal blocks to the east. Major rock types of craton include gniesses, schist belts and diapiric trondhjemites. The craton is divided into Western and Eastern by a N-S elongated 2.5 Ga Closepet granite. However, an alternative line of contact between EDC and WDC is proposed to be Chitradurga thrust, parallel to and ~ 50 km west of the Closepet granite. The actual boundary between the two cratonic blocks remains debatable. The Western Dharwar Craton (WDC) formed through accretion of terrains[14],

FIG. 1

evolved from the mantle over the period > 3.4 to 3.0 Ga. The > 3.4 Ga old 'nucleus' is a major low strain zone in the craton protected by the severity of compressive deformation[15]. The Dharwar craton has primarily tholeiitic and Picritic composition. The mafic-ultramafic (Komatiites) complexes have been reported from Gorur, Hassan region in WDC and Kolar in EDC. The Eastern Dharwar Craton (EDC) crust contains granitoid rocks, all juvenile addition to the continental crust during 2.6 – 2.5 Ga[16]. The EDC also hosts diamondiferous kimberlite pipes (Figure 1). These diamonds, which are yet to be dated, occur in kimberlites of Proterozoic (1100 Ma) age. To the south, the Dharwar craton passes through narrow gradational zone and into the high-grade metamorphic (2.6 Ga) terrain, while to the east it is wrapped by the Proterozoic Cuddapah basin (CB) and Eastern Ghat granulite terrain (EGGT). The evolutionary history of Cuddapah basin[17] could be traced back to the first igneous activity in the form of lava flow at about 1850 Ma in the SW part of the basin adjoining EDC.

Receiver Function and Crustal Structure:

A teleseismic P-wave propagating to a seismic station generates converted S waves at boundaries with significant impedance contrast beneath the station (Figure 2). Moho is one such most significant boundary. Receiver functions (RF) are waveforms computed by deconvolving vertical component from the radial / tangential components to isolate the converted phases from coda of the P-waves. It contains information related to P and converted and reflected S waves from the seismic discontinuities in the crust and mantle. We follow approach using time domain deconvolution[18] to compute receiver functions.

FIG. 2

The Moho P to S converted wave (P_s) is most dominant on the radial RF and arrives in the time window 4 – 7 sec after the P. In this study, we used earthquake waveforms from teleseismic distances (30° – 95°) recorded over broadband seismic stations in Dharwar craton. Receiver functions were computed at each station for individual earthquakes and stacked in narrow azimuth and delta range to improve S/N ratio. Stacked radial receiver function for individual stations show remarkable spatial coherence of Moho converted P_s phase with the surface geology and compositional boundaries (Figure 3). P_s - P travel time in the EDC is 3.9 – 4.52 while in the WDC it varies from 5.32 – 5.91 indicating significant variation in crustal thickness/ Poisson's ratio. Maximum P_s -P time separation is observed over the oldest crustal block (~3.4 Ga) at GRR.

FIG. 3

To quantify the crustal thickness and Poisson's ratio in the vicinity of each station we modeled the amplitude and travel times of P to S conversions at the Moho (P_s) and its crustal multiples (P_pP_mS and P_pS_mS) in the radial receiver function[19]. For large number of crustal model with varying thickness H (25 – 60 km), V_p/V_s (1.6 – 1.8), we compute corresponding arrival times of P_s, P_pP_mS and P_pS_mS (say t_1, t_2 and t_3) and stack the amplitude of RF through the equation:

$$S(H, V_p/V_s) = w_1 r(t_1) + w_2 r(t_2) - w_3 r(t_3)$$

Where r (t) is the radial receiver function and w_i are weights assigned to RF at time t_i. The H and V_p/V_s providing the maximum amplitude in S is considered the best approximation.

The method requires apriori knowledge of the average crustal P-velocity. Recently, Sarkar *et al.*,[20] modeled an earlier Kavali-Udipi deep

seismic profile measurements[21] across Dharwar Craton and inferred a simple two layer crust with velocity 6.1 km/s in the upper crust (23 km) and 6.9 km/s for the lower crust in both segments of the craton. The inferred Moho depth is ~35 km in the EDC and 40 km for WDC. Inversion of the receiver functions suggests similar average V_s (3.73 ± 0.10 km/s), from EDC[22] and WDC[23]. We computed the average crustal thickness and V_p/V_s for individual stations using stacked receiver function from events in same azimuth and distance range (± 5°) using above equation considering an average 6.45 km/s P-wave crustal velocity. Figure 4 details the H and V_p/V_s computation for a few broadband stations. Detailed result for individual stations is presented in table 1. FIG. 4 TABLE 1

Examination of table 1 suggests that stations in both EDC and WDC exhibit Poisson's ratio varying in a range of 0.24 – 0.28. These observations lie on the lower end of the Archean crust global average[5] of 0.29 ± 0.02 and are in better agreement with Last *et al.*, [6] suggesting a more felsic crustal composition beneath Dharwar Craton. This is also supported by absence of > 7.0 km/s lower crust P- wave velocity in both EDC and WDC from modelling of DSS waveform data. To study the correlation of Moho depth variation with surface geology, we present a crustal cross-section from KSL to CUD (Figure 5). FIG. 5 Moho thicknesses are projected at depth with horizontal offset in the direction of earthquake. Moho depth is computed at individual station due to events from SW-W, NE-E and total. The crustal thickness varies 33 – 40 km beneath the EDC in contrast with 41 – 52 km over WDC. To examine the possibility that these Moho depth variations could be due to dip, we also looked into receiver functions at individual stations with varying distance and azimuth. No significant variation was observed in converted and multiples amplitude and

arrival time as expected for a dipping Moho. We therefore, conclude, that Moho is essentially horizontal and offsets are sharp boundaries. The crustal thickness estimate for the late Archean Eastern Dharwar crust is similar to the global average (30 – 40 km). The mid Archean nucleus in Western Dharwar craton is, however, considerably (>10 km) thicker than that of an average Archean shield. The other Archean terrains with significant crustal thickness (45 – 50 km) include Kapuskasing structural zone[24], Minnesota River Gneiss terrain[25] and Wyoming Province[26]. All these terrains have been subjected to extensive reworking in Proterozoic unlike the WDC where the crustal evolution is primarily during mid Archean (3.4 – 3.0 Ga) and lacks geological signatures of subsequent tectonic perturbations. The contact between EDC and WDC is observed as gradational between the western edge of Closepet granite and Chitradurga thrust where crustal thickness changes by at least 6 km. It is interesting that this zone is also characterized by three east-dipping reflectors inferred from DSS measurements[21]. At station KDR, on the southwestern edge of Cuddapah basin (CB), we observed crustal thickening of 5 km relative to both EDC and CB. The remarkable spatial correlation of observed crustal thickening with 1.8 Ga volcanics in this region requires detailed modelling of waveform at KDR.

Teleseismic Residual and Lithospheric Thickness:

Seismological data suggest strong correlation between upper mantle shear velocity and crustal type. The continents show decrease in heat flow and increase in lithospheric thickness with increasing time interval since the last major thermal or orogenic event[27]. The mapping of lithospheric thickness

beneath EDC and WDC could therefore suggest whether these terrains have been subsequently remobilized during Proterozoic. A compilation of S wave travel time anomalies[28,29] shows progressive increase in vertical travel time from a thick lithosphere craton to a thin one. We investigate the nature of lithospheric variation within the Dharwar craton using teleseismic P and S wave travel times. The predicted P and S wave arrival times were computed using IASP91 tables[30] and then subtracted from observed times to give the travel time residual. This contains the effect of crust, source mislocation, origin time error and heterogeneity along the entire path. The effect of crustal inhomogeneity is considered by computing relative travel time residuals reduced to a common depth of 52 km (maximum observed crustal thickness in EDC and WDC) assuming an average crustal $V_p \sim 6.45$ km/s, $V_s \sim 3.73$ km/s and uppermost mantle P-velocity 8.2 km/s and S-velocity 4.65 km/s. Other contributions to the residual is minimized by subtracting the array average from all other station residuals. The resulting relative residual represents effect of lateral heterogeneity in the upper mantle to a depth approximately equal to the array length (approximately 350 km). The relative residuals corrected for the crust are presented for selected stations in Figure 6 and 7 for earthquakes from different azimuth ranges. Positive residuals indicate travel time delayed for rays due to its passage through a low velocity zone while negative residual represents travel through a high velocity region. Strong azimuthal variation indicates that the causative source is deep seated. It is very clear that the residuals emerge negative for stations in WDC compared to EDC representing faster arrival of seismic waves.

FIG. 6

FIG. 7

To examine the likely cause for systematic variation of the crust corrected residual, we present upper mantle travel time residual across the Dharwar craton (Figures 8 a, b) for earthquakes from NE azimuth (40° – 60°) FIG. 8 coinciding with the profile along stations (KSL-GRR-TPT-TMK-GBA-KDR). For P, WDC stations have 0.3 to 0.6 s. early teleseismic arrivals relative to EDC. Correspondingly, S travel time shows an average of 0.5 to 0.7 s early arrivals for WDC stations. The most likely candidate for the systematic variation of the mantle residual is the variation of depth to the base of the lithosphere. Since the data are relative residual, we can only compute relative thickness variation. The geochemical analysis of Kimberlite xenoliths (1100 Ma) around LTV station in EDC constrains a minimum of 200 km thick lithosphere beneath the EDC during Proterozoic[31]. Using a 0.5 km/s P- wave velocity contrast between lithosphere and asthenosphere, we observe a minimum of 60 – 80 km lithosphere thickening beneath the WDC as compared to EDC (Figure 8c). This supports the view that older continents have thicker and rigid root than the younger ones. This also implies that WDC has not been affected by any major younger tectonothermal event. This is also supported by lower heat flow 30 ± 4 mWm^{-2} in WDC compared to 40 ± 3.4 mWm^{-2} over EDC[32], which gives rise to the observed S delay. Presence of a thicker and rigid lithospheric root beneath WDC could be responsible for its dynamic stability since 3.0 Ga and therefore help preserve its original Moho characteristic.

Conclusion/ Archean Crustal Evolution:

Analysis of teleseismic broadband waveform from an experiment in the east and west Dharwar craton suggests distinct crustal architecture for the two

terrains. The early-mid Archean (3.4 – 3.0 Ga) WDC crust is significantly thicker (43 – 52 km) compared to the global average of 30 – 40 km for Archean crust whilst the late Archean (~2.5 Ga) EDC crust is 33 – 40 km thick similar to those observed elsewhere. The average crustal Poisson's ratio for both the EDC and WDC show similar values 0.24 – 0.28, represent lower end of the global average for Archean shield (0.27 – 0.31), suggesting felsic to intermediate composition. The thicker crust beneath WDC is also underlain by thicker lithosphere root. The crustal thickness increase causes a decrease in gravity and elevation uplift, but the increase in lithosphere thickness has opposite effect on the elevation. This explains why despite thicker crust, WDC nucleus has little topographic expression. The thicker crust beneath WDC nucleus (at GRR) is responsible for a large gravity low (-120 mgal) observed around Gorur-Hassan region of WDC.

It is interesting to note that the over thick (52 km) crustal block coincides with the > 3.36 Ga old Archean gneisses of Gorur – Hassan region bounded to the west and east by mid- late Archean shear belts. Mineral assemblages in this part of WDC represent amphibolite grade metamorphism at about 5 – 7 Kb pressure suggesting that the Archean crust equilibrated at depth of 15 to 25 km. Presence of these high pressure mineral assemblages at surface of continental crust demonstrates that the Archean crust in parts of western Dharwar craton 3.0 Ga ago must have been at least 60 – 80 km thick. Preservance of such an over thickened crust would only be possible in a crust shielded from high mantle heat flow by a thick, insulating layer of subcrustal lithosphere[33] where heat transport was by conduction rather than by convection. Presence of such a thick lithospheric root has been demonstrated

in this study beneath the WDC. Thick and rigid lithosphere found beneath the WDC during early time history probably helped preserving the primitive crustal architecture. Presence of segmented deep crustal blocks with Moho depth 38 – 41 km in WDC was also revealed by DSS data from Kavali – Udipi profile. Within each of these blocks the Moho is essentially horizontal.

We speculate that the crustal blocks inferred from seismological studies and also through field geology[34] represents distinct Archean blocks accreted together to form WDC. Presence of the over thickened Archean crustal blocks of WDC with felsic to intermediate composition suggests that the crustal growth resembles island arc tectonic settings along sites of plate collision. Similar over thickened crust (~ 60 – 80 km) with low σ is also observed in Andean orogenic zone[35]. This, however, assumes that the behaviour of mid Archean lithosphere was also governed by present day plate tectonic processes. A stabilized WDC craton subsequently accreted to the EDC around 2600 Ma along Chitradurga thrust – Closepet granite. Lithospheric thickness show marked reduction to the east of Closepet granite. It is interesting to note that the DSS reflection survey shows prominent east dipping reflectors from Chitradurga thrust to western part of Closepet granite coinciding with our inferred gradation Moho in the zone, which may be an indication of subduction of Western Dharwar Craton to the east.

A detailed modelling of seismic waveform from the broadband experiment currently in progress would soon reveal the untold complex structure and Archean geodynamics of the Dharwar craton.

References:

1. Taylor, S.R., and Mclennan, S.M., 1995, Rev. Geophys., 33, 241 – 266.

2. Christensen, N.I. and Mooney, W.D., 1995, J. Geophys. Res., 100, 9761-9788.

3. Rudnick, R.L. and Fountain, D.N., 1995, Rev. Geophys. 33, 267 – 309.

4. Durrheim, R.J. and Mooney, W.D., 1994, J. Geophys. Res., 99, 15359 – 15374.

5. Zandt, G. and Ammon, C.J., 1995, Nature, 374,152 – 154.

6. Last, R.J., Nyblade, A.A., Langston, C.A. and Owens, T.J., 1997, J. Geophys. Res., 102, 24469- 24483.

7. Chevrot, S. and Van der Hilst, R.D., 2000, Earth and Planet. Sci. Lett. 183, 121 – 132.

8. Christensen, N.I., 1996, J. Geophys. Res., 101, 3139-3156.

9. Holbrook, N.D., Mooney, W.D. and Christensen, N.I., 1992, Continental lower crust, (ed. Fountain, D.M., Arculus, R and Kay, R.) Elsevier, New York, pp. 21-43.

10. Drury, S.A., Harris, N.B.N., Holt, G.J., Reeves – Smith, G.J. and Wightman, R.T, 1984, J. Geol., 92, 3-20.

11. Naqvi, S.M. and Rogers, J.J.W., 1987, Precambrian geology of India, Oxford Univ. Press, 223 pp.

12. Goodwin, A.M., 1996, Principles of Precambrian Geology, Academic Press, London, 327 pp.

13. Beckinsale, R.D., Drury, S.A. and Holt, R.W., 1980, Nature, 283, 469 – 470.

14. Meen, J.K., Rogers, J.J.W. and Fullager, P.D., 1992, Geochemica et Cosmochimica Acta, 56, 2455 – 2470.

Figure Captions:

Figure 1. Map showing the principal segments of Dharwar craton and adjoining geological provinces in South India:
WDC – Western Dharwar Craton, EDC – Eastern Dharwar Craton, CD – Cuddapah Basin, EGGT – Eastern Ghat Granulite Terrain, SGT – Southern Granulite Terrain, DVP – Deccan Volcanic Province, CG – Closepet Granite, CT – Chitradurga Thrust.
Locations of broadband seismic stations are shown as black squares.

Figure 2. (a) Synthetic radial component receiver function for a simple layer over half space model. Main phases and the multiples corresponding the ray path are shown below.
(b) Ray paths for converted P_s phase and major multiples for a simple layer over a half space model.

Figure 3. Stacked radial receiver function for stations in Dharwar craton grouped according to their geological/structural proximity. Note the increase in P_s time for stations in Western Dharwar craton.

Figure 4. The V_p/V_s ratio vs. crustal thickness estimate for selected stations.

Figure 5. A West-East cross-section (from KSL to CUD) of estimated crustal thickness across the Dharwar craton. Average crustal Poisson's ratio is also depicted for individual stations.

Figure 6. Azimuthal variation of crust – corrected teleseismic P-wave relative residual for selected stations.

Figure 7. Azimuthal variation of crust – corrected teleseismic S-wave relative residual for selected stations.

Figure 8. (a, b) Mantle contribution to the teleseismic P and S residual at individual stations across Dharwar craton. Time residual due to earthquakes from azimuth 40° – 60° are averaged for presentations.
(c) Lithospheric thickness variation across Dharwar craton.

Table 1: Station location, Crustal thickness, V_p/V_s and Poisson's ratio

Station Name	*Latitude (°N)*	*Longitude (°E)*	*Elevation (M)*	*P_s - P (Sec)*	*Thickness (Km)*	*V_p/V_s*	*Poisson's Ratio (Σ)*
Cuddapah Basin (CB)							
SLM	16.10	78.89	368	4.07	34.5 – 33.5	1.73 – 1.77	0.25 – 0.26
CUD	14.48	78.77	–	4.16	35.2 – 34.1	1.74 – 1.78	0.25 – 0.26
Eastern Dharwar Craton (EDC)							
MBN	16.87	77.66	417	4.00	34.8 – 33.9	1.71 – 1.74	0.24 – 0.25
LTV	14.93	77.28	402	4.08	35.3 – 33.5	1.71 – 1.77	0.24 – 0.26
KDR	14.18	78.16	453	4.55	39.5 – 40.3	1.71 – 1.72	0.23 – 0.25
KOL	12.95	78.25	803	3.92	33.8 – 33.0	1.72 – 1.77	0.25 – 0.26
BGL	13.02	77.57	791	4.07	35.2 – 34.6	1.73 – 1.74	0.25 - 0.26
GBA	13.56	77.36	681	4.10	34.9 – 33.4	1.73 – 1.78	0.25 - 0.26
Closepet Granite (CG)							
TMK	13.34	77.19	842	4.49	35.0 – 34.2	1.78 – 1.80	0.27 - 0.28
Chitradurga Thrust (CT)							
NTR	13.30	76.90	712	4.72	41.4 – 40.8	1.73 - 1.74	0.25 - 0.26
KBC	13.30	76.65	763	4.90	42.5 – 41.3	1.71 - 1.74	0.24 - 0.25
Western Dharwar Craton (WDC)							
TPT	13.27	76.54	785	5.43	46.1 - 45.4	1.74 – 1.76	0.25 - 0.26
DHR	15.43	74.98	679	5.54	43.5 – 42.4	1.78 – 1.80	0.27 – 0.28
CRP	13.02	76.32	824	5.47	43.3 – 42.2	1.78 – 1.80	0.27 – 0.28
GRR	12.83	76.06	792	5.91	51.9 - 50.8	1.70 – 1.74	0.24 - 0.25
KSL	12.49	75.91	796	5.32	46.6 - 45.6	1.71 – 1.74	0.24 – 0.25

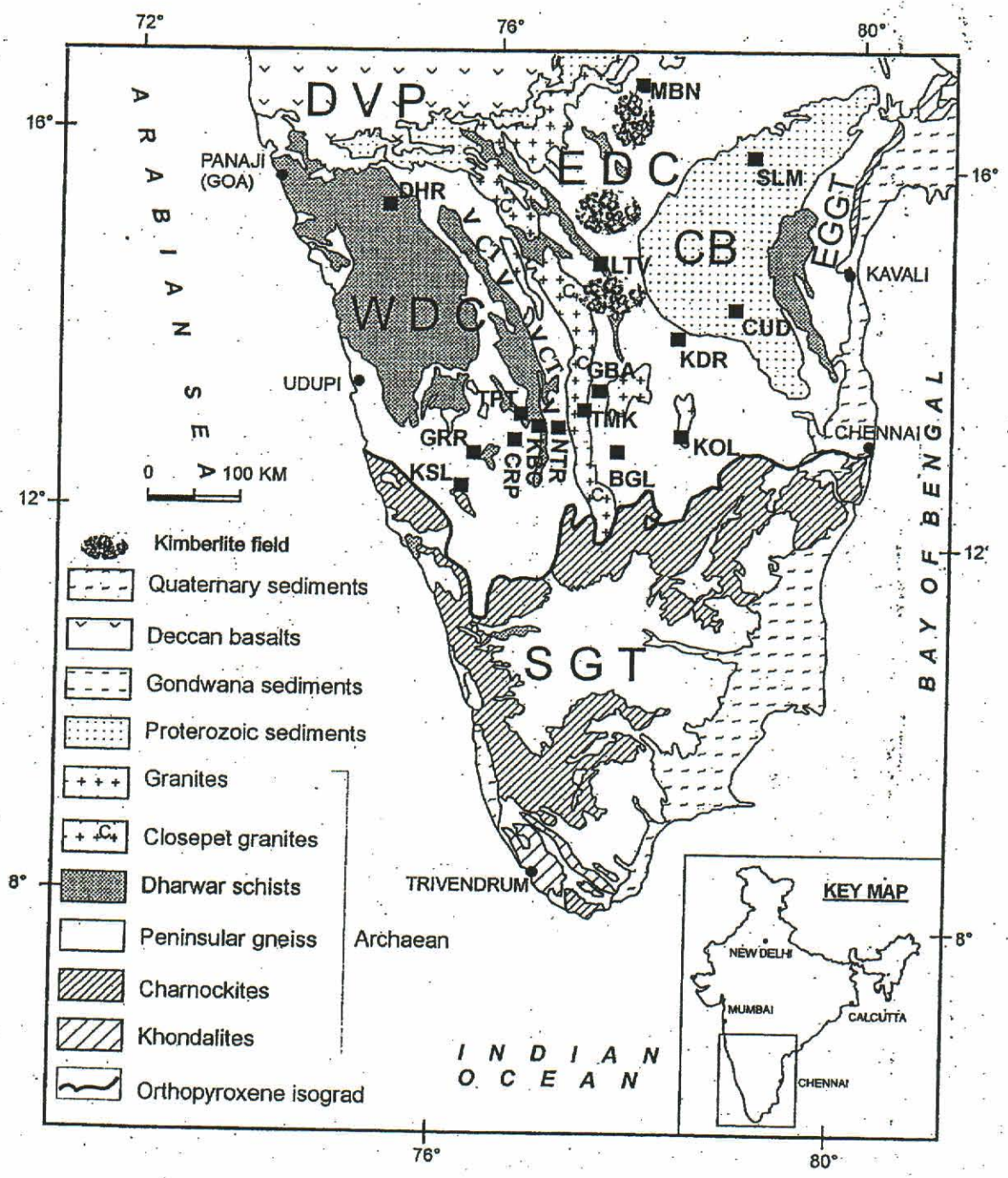
72°
76°
80°
16°
12°
8°
ARABIAN SEA
BAY OF BENGAL
INDIAN OCEAN
DVP
EDC
WDC
CB
SGT
EGGT
PANAJI (GOA)
DHR
MBN
SLM
LTV
KAVALI
CUD
KDR
UDUPI
GBA
TPT
TMK
GRR
KRG
CRP
NTR
KOL
CHENNAI
KSL
BGL
TRIVENDRUM
0 100 KM
Kimberlite field
Quaternary sediments
Deccan basalts
Gondwana sediments
Proterozoic sediments
Granites
Closepet granites
Dharwar schists
Peninsular gneiss
Charnockites
Khondalites
Orthopyroxene isograd
Archaean
KEY MAP
NEW DELHI
MUMBAI
CALCUTTA
CHENNAI

Figure 1

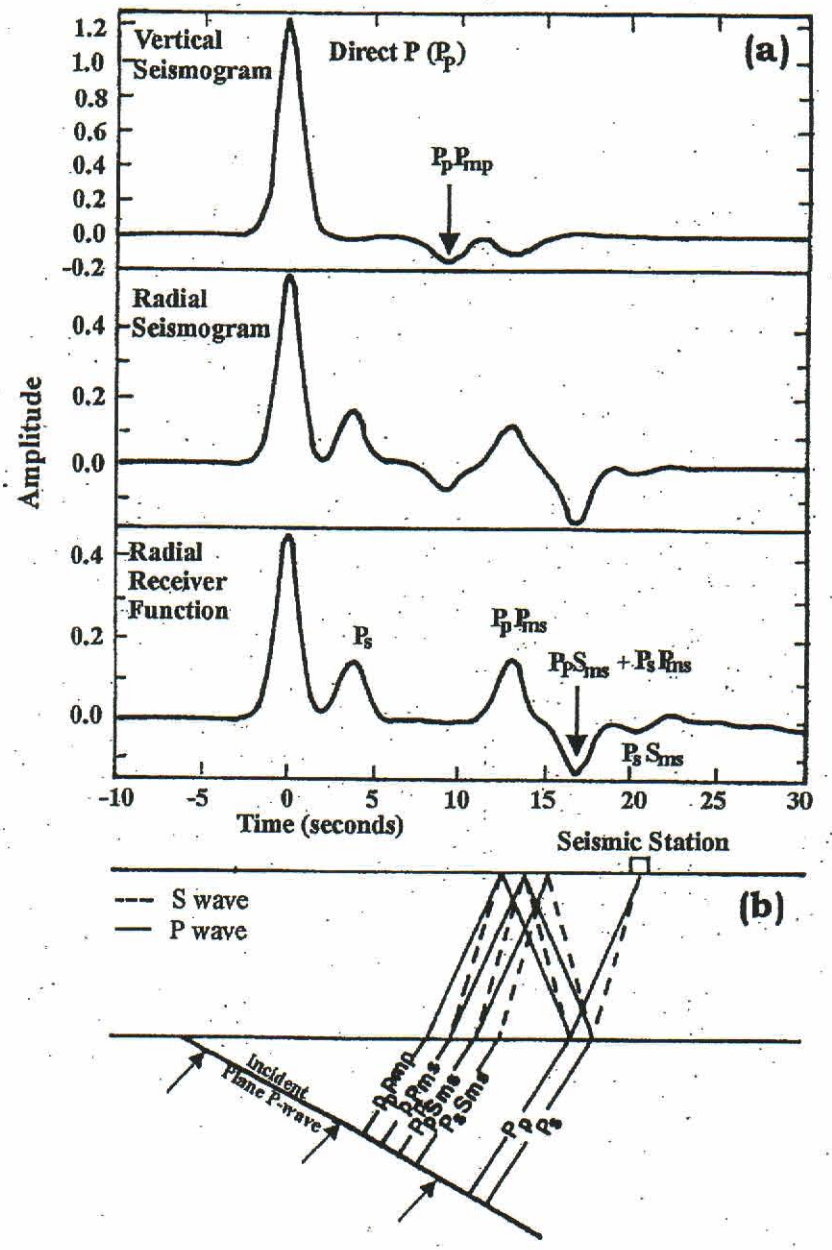
Vertical Seismogram
Direct P (P_p)
(a)
P_pP_{mp}
Radial Seismogram
Amplitude
Radial Receiver Function
P_s
P_pP_{ms}
$P_pS_{ms} + P_sP_{ms}$
P_sS_{ms}
Time (seconds)
Seismic Station
S wave
P wave
(b)
Incident Plane P-wave
P_pP_{mp}
P_pP_{ms}
P_pS_{ms}
P_sS_{ms}
P_pP_p

Figure 2

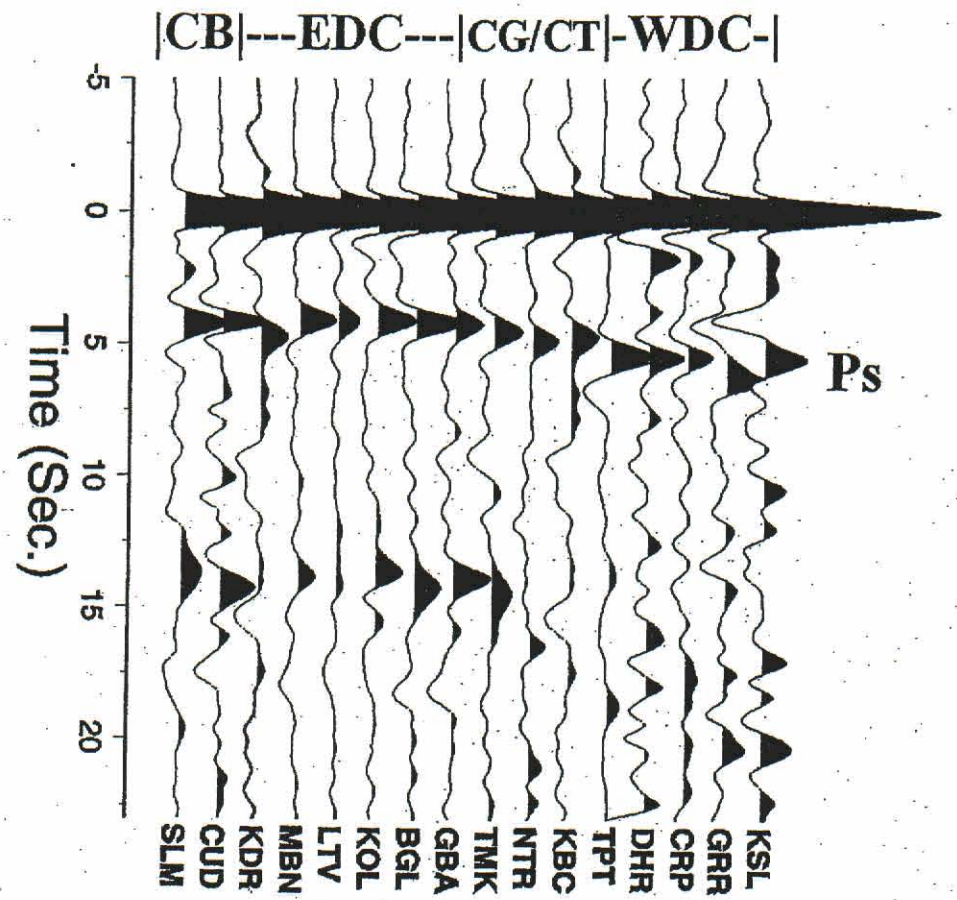
|CB|---EDC---|CG/CT|-WDC-|
-5
0
5
10
15
20
Time (Sec.)
Ps
SLM
CUD
KDR
MBN
LTV
KOL
BGL
GBA
TMK
NTR
KBC
TPT
DHR
CRP
GRR
KSL

Figure 3

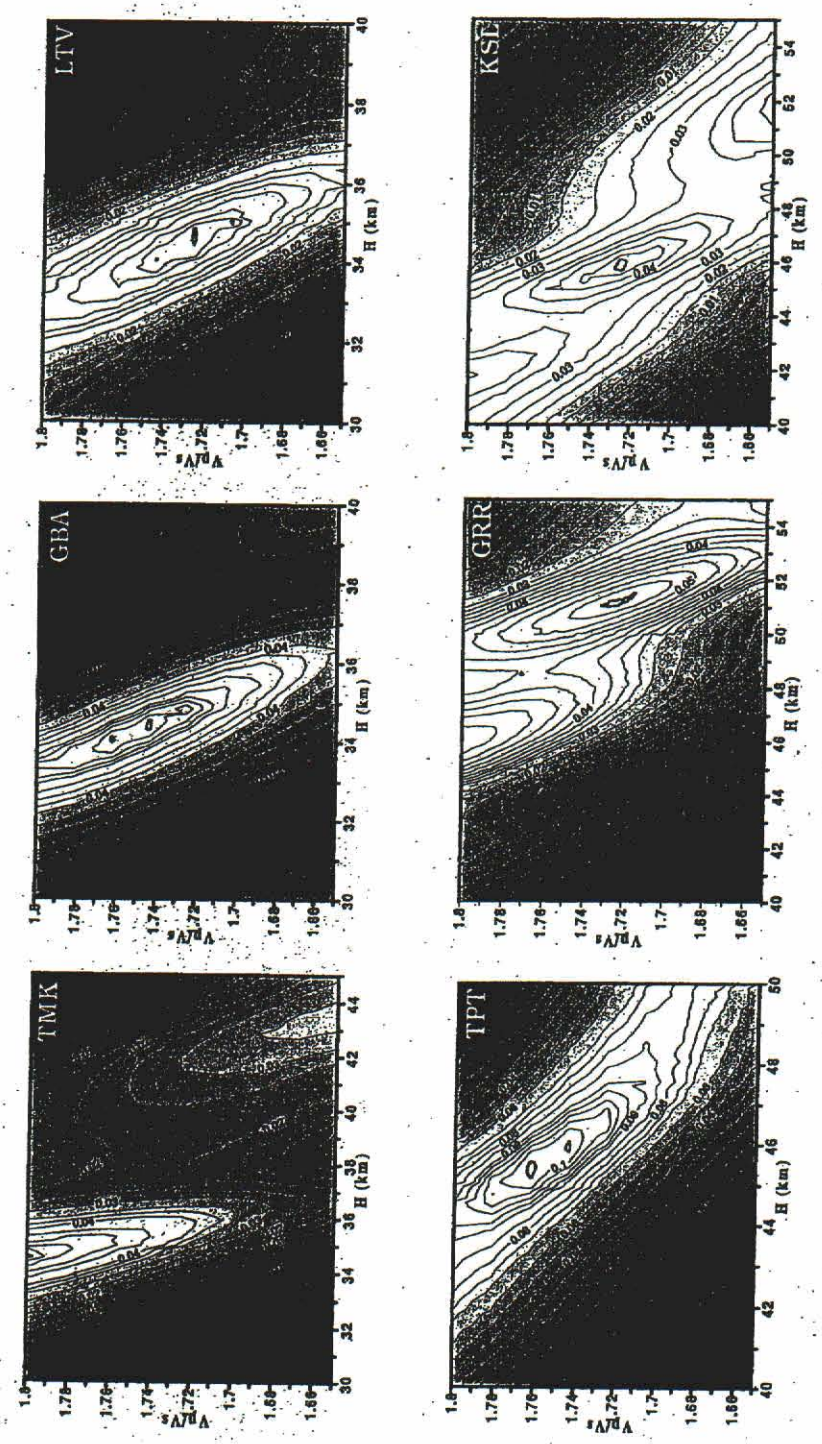

Figure 4

CRUSTAL CROSS-SECTION ACROSS DHARWAR CRATON

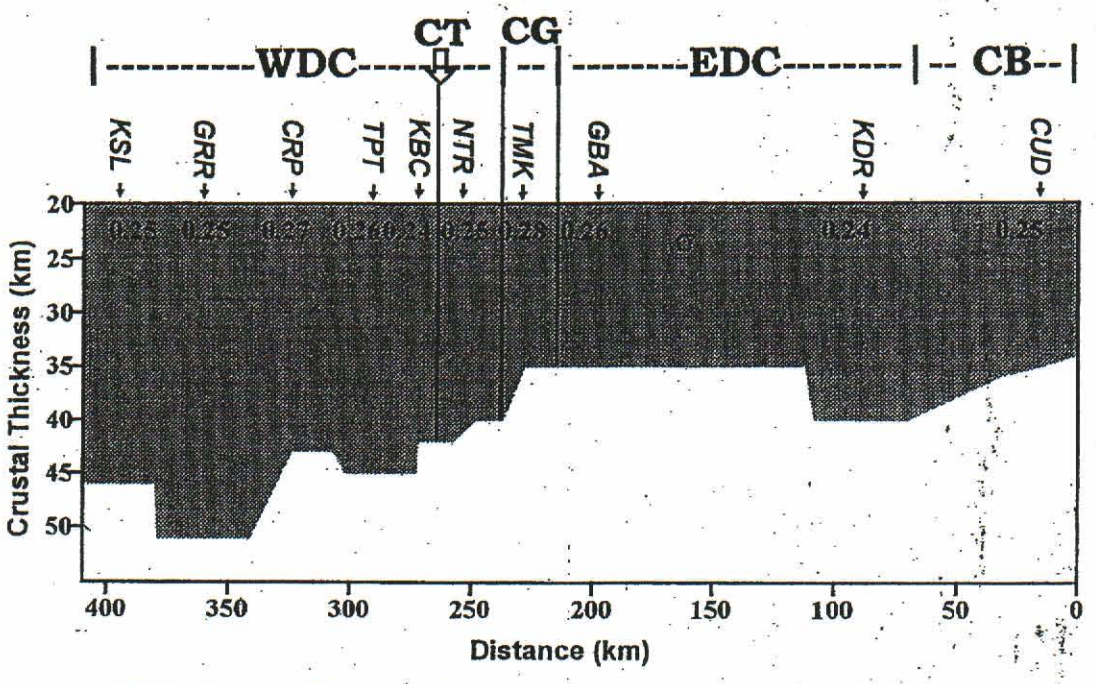

WDC : Western Dharwar Craton
CB : Cuddapah Basin
CT : Chitradurga Thrust
EDC : Eastern Dharwar Craton
CG : Closepet Granite
CUD : Broadband Seismic Station

Figure 5

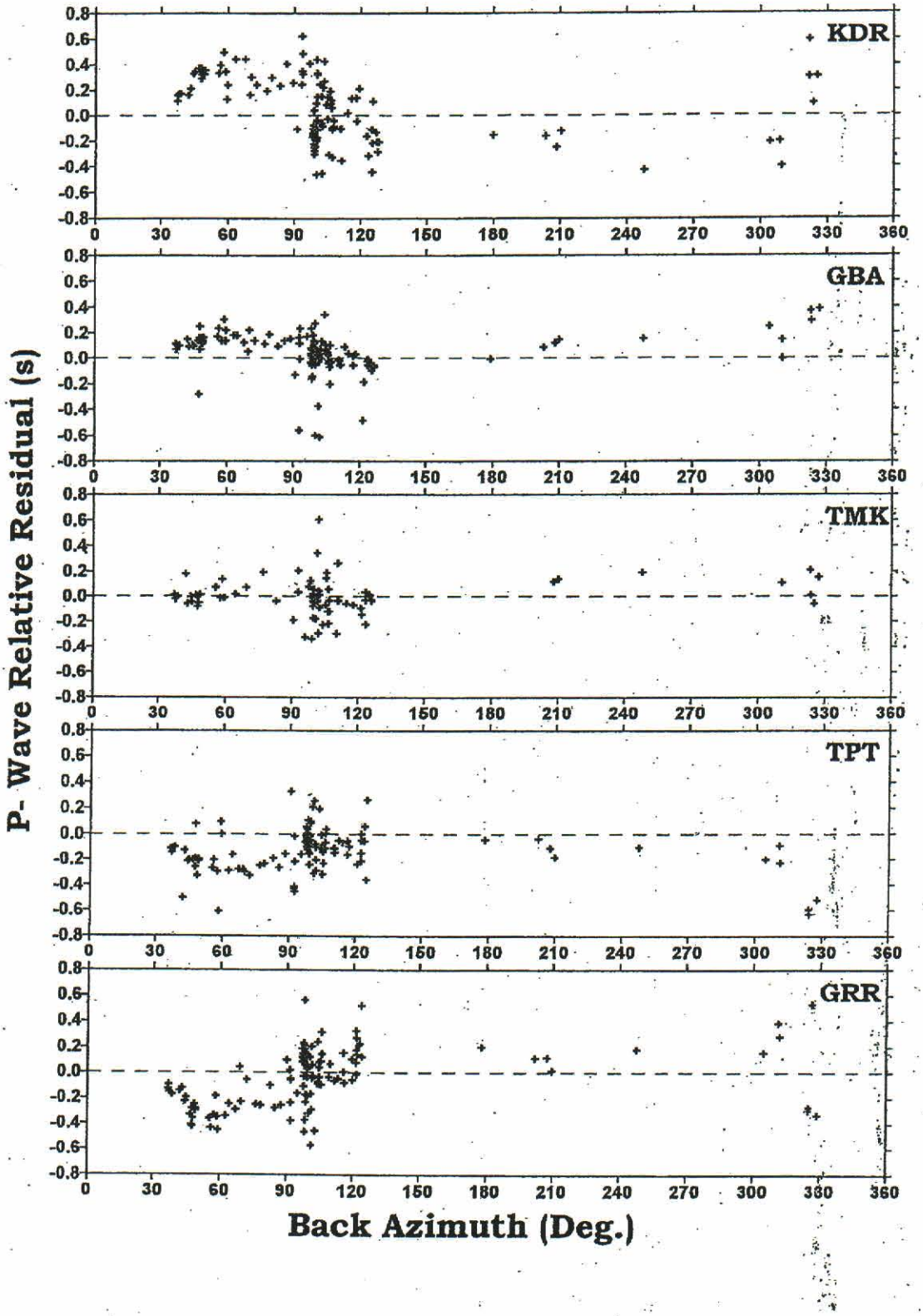
KDR
GBA
TMK
TPT
GRR
P- Wave Relative Residual (s)
Back Azimuth (Deg.)

Figure 6

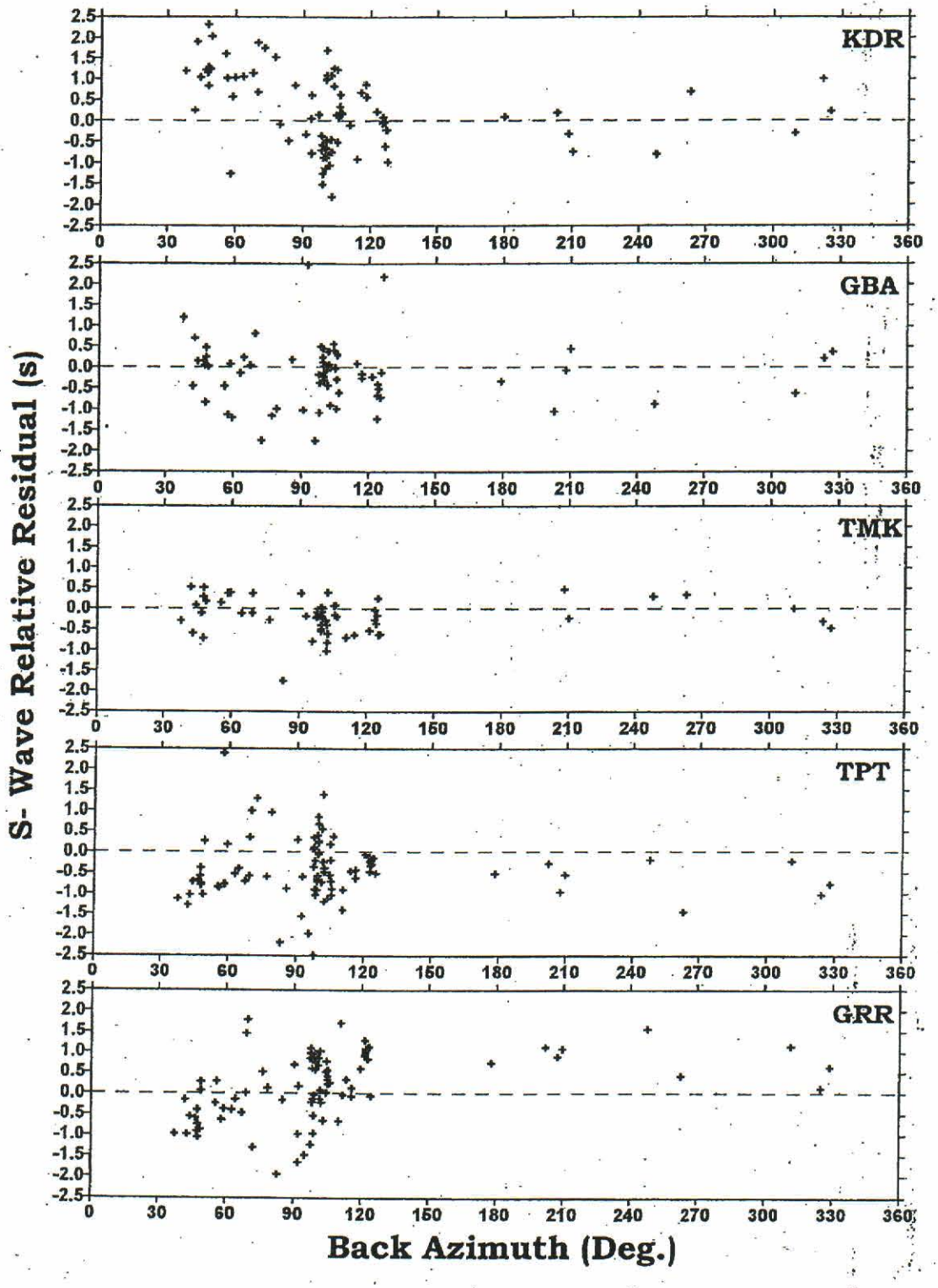
KDR
GBA
TMK
TPT
GRR
S- Wave Relative Residual (s)
Back Azimuth (Deg.)

Figure 7

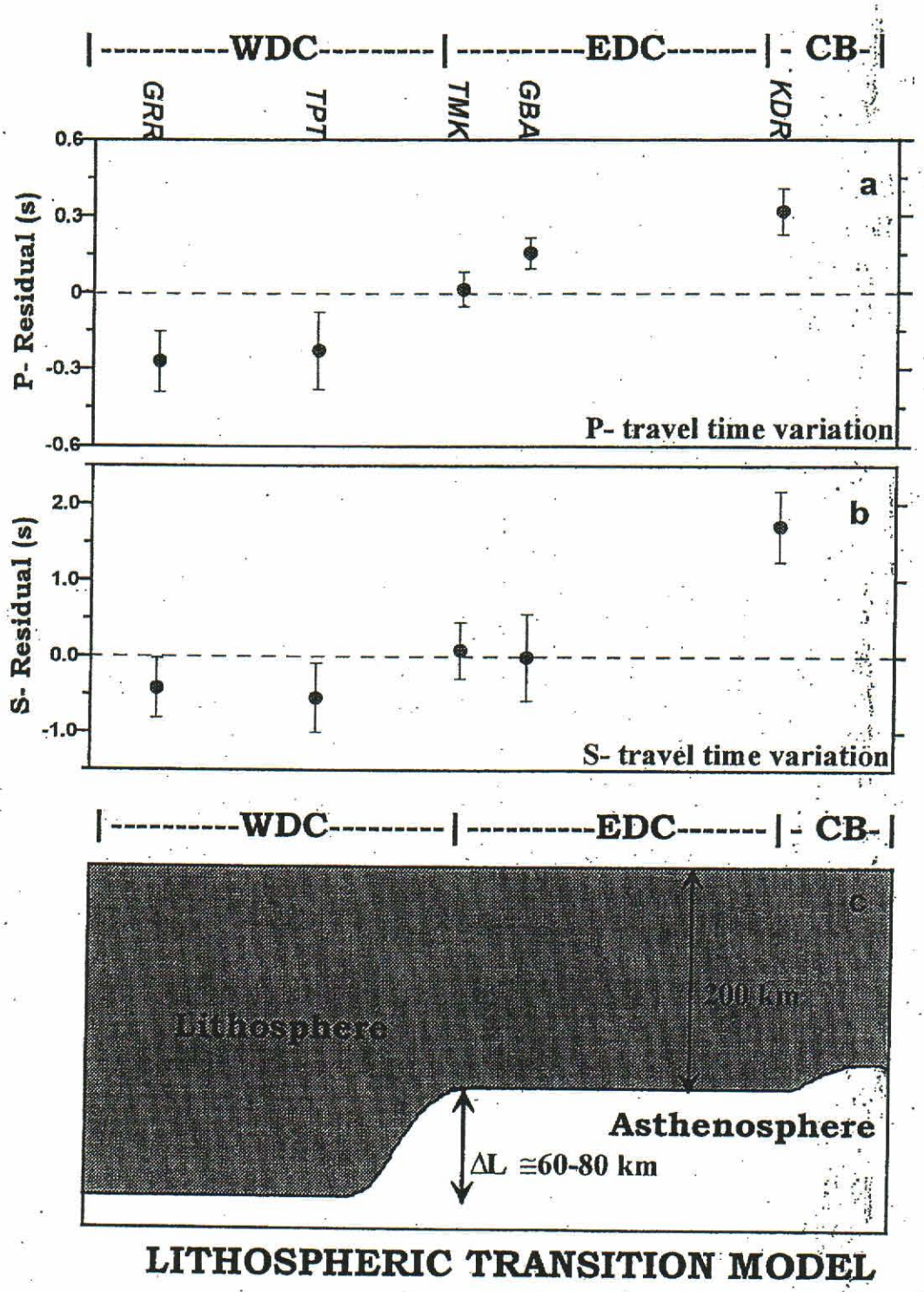

LITHOSPHERIC TRANSITION MODEL

Figure 8

Seismic evidence for a moderately thick lithosphere beneath the Siberian Platform

Keith Priestley
Bullard Laboratories, University of Cambridge, Cambridge, United Kingdom

Eric Debayle
Ecole et Observatoire des Sciences de la Terre, Université Louis Pasteur, Strasbourg, France

Received 21 July 2002; revised 27 September 2002; accepted 12 November 2002; published 6 February 2003.

[1] We have built a *Sv*-wavespeed tomographic model for the upper mantle beneath the Siberian platform and surrounding region derived from the analysis of more than 13,000 fundamental and higher mode regional waveforms. The dense path coverage and rich higher mode content of the data allow building an upper mantle image with an horizontal resolution of a few hundred kilometers extending to ~400 km depth. The high velocity, upper mantle lid or seismic lithosphere is ~200 km thick beneath most of the Siberian platform but may extend to ~250 km depth beneath small areas. A high velocity seismic lid also underlies a large region west of the Siberian platform. Our observation of a ~200 thick seismic lithosphere beneath the Siberian platform on the slow-moving Eurasian plate, similar to the thickness of the seismic lithosphere beneath Precambrian terrains on the fast-moving Australian plate, suggests that a moderately thick seismic lithosphere beneath Precambrian terrains may be more common than previously supposed. *INDEX TERMS:* 7207 Seismology: Core and mantle; 7218 Seismology: Lithosphere and upper mantle; 7255 Seismology: Surface waves and free oscillations. **Citation:** Debayle, E., and K. Priestley, Seismic evidence for a moderately thick lithosphere beneath the Siberian platform, *Geophys. Res. Lett.*, *30*(3), 1118, doi:10.1029/2002GL015931, 2003.

1. Introduction

[2] Eastern Asia is a mosaic of ancient continental fragments separated by mountain ranges and fold belts. The crustal evolution of the largest Archean terrains, the Siberian platform (Figure 1), is thought to have started ~3.5 Ga, but the oldest rocks found thus far are ~3.3 Ga [*Jahn et al.*, 1998]. Initial seismic studies [*Lerner-Lam and Jordan*, 1983] suggest that the tectonically stable parts of northern Eurasia, including the Siberian platform, have a thick, high velocity lid extending to ~400 km depth; recent thermal modeling suggests that the thermal lithosphere [*Jaupart and Mareschal*, 1999] of the Siberian platform is ~350 km thick [*Artemieva and Mooney*, 2001].

[3] In this paper, we present a high-resolution shear velocity model of the upper mantle beneath NE Asia using more than 13,000 Rayleigh wave regional seismograms. The dense path coverage gives the model a lateral resolution of a few hundred kilometers, and the rich higher mode content of the events analyzed provides sensitivity down to ~400 km depth. Our model shows substantial variation in the thickness of the high velocity, upper mantle lid with values less than 100 km thick beneath tectonically active regions and values which may locally exceed 250 km beneath small parts of the Siberian platform. However, for most of the Siberian platform and the stable region to its west, the high velocity lid extends to 200–225 km depth. In this paper we equate the high seismic wavespeed "lid" to a "seismic" lithosphere [*Jaupart and Mareschal*, 1999], likely to be related to processes in the mantle of thermal and/or compositional origin (e.g., via depletion of the cratonic keel).

0094-8276/03/2002GL015931$05.00

2. Development of the 3D Upper Mantle Velocity Model

[4] We construct the 3D upper mantle model using the two-step procedure previously used for Australia [*Debayle and Kennett*, 2000] and eastern Africa [*Debayle et al.*, 2001]. We first use the automated version [*Debayle*, 1999] of the *Cara and Lévêque* [1987] waveform inversion technique to determine a 1D path-average upper mantle velocity model compatible with observed surface waves. We then combine the 1D velocity models in a tomographic inversion using the continuous regionalization algorithm of *Montagner* [1986] to obtain the local *Sv*-wavespeed at each depth (see *Debayle and Kennett* [2000] for the details).

[5] The method is based on the assumptions that the observed surface waveform can be represented by multimode surface waves propagating independently and along the great circle. These assumptions are valid for a smoothly-varying medium without strong lateral velocity gradients [*Woodhouse*, 1974]. *Kennett* [1995] examined the validity of the path average approximation for surface wave propagation at regional continental scale and concluded that it should be suitable for periods between 30 and 100 s and remain valid at longer periods (>50 s) where surface waves cross major structural boundaries, such as the continent-ocean transition. Significant deviations from great-circle propagation have been observed for short periods (<40 s) surface waves [*Levshin and Ratnikova*, 1994; *Alsina and Snieder*, 1996; *Cotte et al.*, 2000], but surface wave ray tracing in Earth models [*Yoshizawa and Kennett*, 2002] similar to ours confirms that off-great circle propagation can reasonably be neglected for the fundamental and first few higher modes at periods greater than ~40 s and for paths less than ~10000 km. (Of the 13055 waveforms used to build our model, 74% have propagation path lengths less

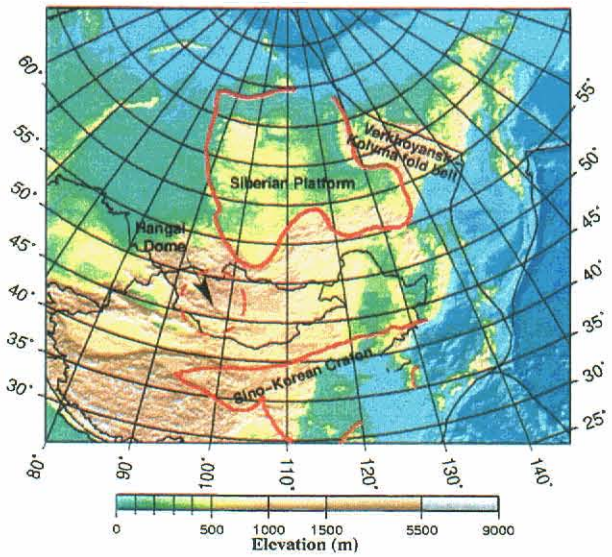

Figure 1. Map showing the tectonic elements of NE Asia discussed in the text. The contour of the cratons is taken from *Goodwin* [1991].

than 6000 km and only 24 waveforms have propagation paths lengths greater than 10000 km.) We therefore restrict our analysis to the fundamental and up to the fourth higher Rayleigh mode in the 50–160 s period band. Sensitivity kernels [see *Debayle et al.*, 2001] show that using the fundamental and up to the fourth higher mode in this period range achieves good sensitivity over the whole upper mantle. In addition, at 50 s period the maximum sensitivity of even the fundamental mode is located below the crust, so that our dataset is primarily sensitive to upper mantle structure.

[6] *Kennett* [1995] also showed that the source contribution is not confined to the immediate neighborhood of the epicenter and the source excitation computation is improved by using a structure specific to the source region. In computing the source excitation, we take the source region velocity structure from the 3D model 3SMAC [*Nataf and Ricard*, 1996] and analyze the seismograms using a smooth version of PREM as the reference and starting model for the upper mantle with a path-specific crustal model determined by averaging the crustal part of 3SMAC along the path. *Cara and Lévêque* [1987] show that for their technique, the final velocity structure is weakly dependent on the reference model. Since we analyze relatively long period surface waves (>50 s), we assume the crustal structure is known and invert for the upper mantle structure. To examine the effect of assuming different crustal models, we inverted a subset of the data assuming the 3SMAC and CRUST2 [*Bassin et al.*, 2000] crustal models; our results show no significant difference in the inversion models below ~100 km.

[7] In the continuous regionalization algorithm, the lateral smoothness of the inverted model is constrained by a horizontal correlation length L_{corr}. We choose L_{corr} = 400 km, thus favoring a smooth model considering our ray density and shortest wavelengths used (about 200 km at 50 s period). We tried various values of L_{corr} but even with L_{corr} = 800 km, the final model was smoother but the features of the model were essentially the same. Synthetic tests show that ray density allows us to resolve structures with horizontal wavelengths of a few hundred kilometers for the uppermost 400 km of the model. This agrees with the lateral resolution that can be expected when considering 'the influence zone of surface wave paths' over which surface waves are coherent in phase and which is identified as approximately one third of the first Fresnel zone [*Yoshizawa and Kennett*, 2002]. In the region lying outside the 'influence zone,' scattering effects can become important [*Spetzler et al.*, 2002] but in general, we did not observe evidence of scattering in the part of the waveforms we analyzed, suggesting that ray theory applies in our period range of analysis. In this paper, our goal is not

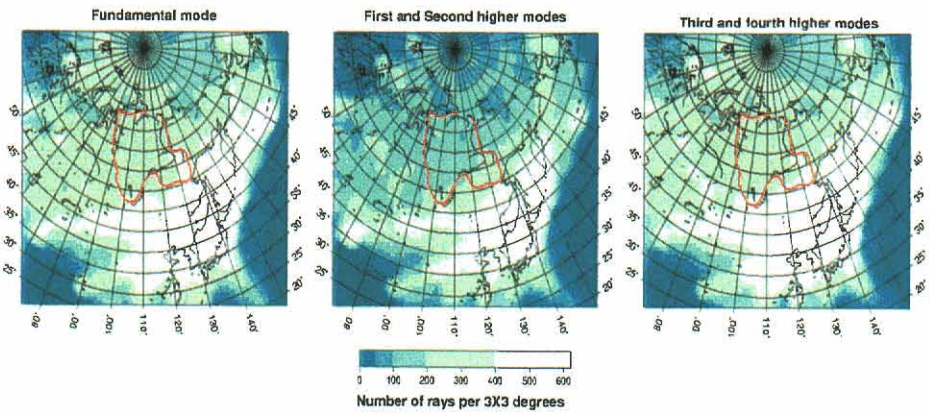

Figure 2. Path coverage maps. The dataset used to build the NE Asian model consists of 13,055 waveforms from 3671 earthquakes recorded at 51 seismographs. Ray density for 3° × 3° cells for the (a) 12310 fundamental mode paths; (b) 4180 first and 4957 second higher mode paths; and (c) 8225 third and 5930 fourth higher mode paths used in constructing the tomographic model. The dense ray coverage of 250–500 rays per 3° × 3° cell, the wide azimuthal distribution of the events, and the rich higher mode content of the data set permits building an image of the seismic lithosphere beneath the Siberian Platform with a horizontal resolution of a few hundred kilometers extending to ~400 km depth.

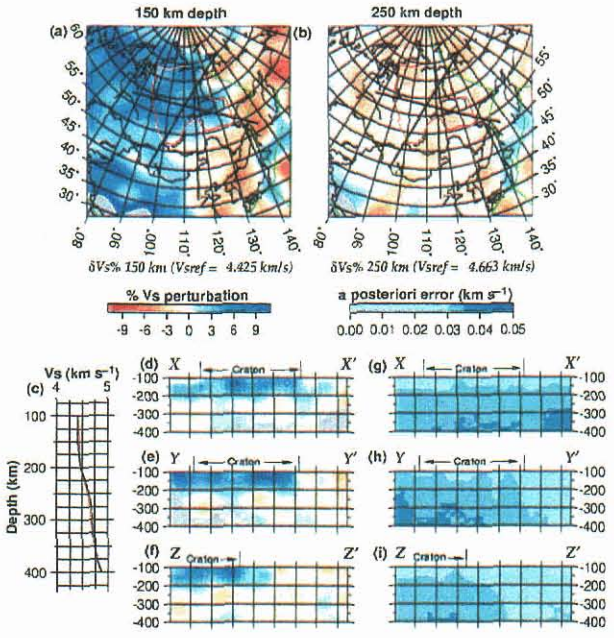

Figure 3. *Sv*-velocity heterogeneity model for NE Asia. (a) and (b) are depth slices through the model at 150 and 250 km depth. *Sv*-velocity perturbations in the depth slices are shown with respect to the PREM velocity at the corresponding depth. (d–f) are cross-sections in the *Sv*-velocity model for the great circles indicated on maps (a–b). The reference velocity for the cross-sections shown in (c) is the average of the seismic velocities of the inverted model at each depth (thick red line). For comparison, our initial smooth PREM reference model (thin black line) is also shown in (c). The cross-section profiles are 4242 km long and the vertical lines across the cross-sections are 500 km apart. The gray areas near the borders of the maps and cross-sections indicate the parts of the model where the a posteriori error is greater than 0.035. (g–i) show the a posteriori corresponding to the *Sv* profiles shown in (d–f). The low a posteriori error (<0.035), obtained compared to the a priori error (0.05), indicates good resolution down to 350–400 km depth for most of the cross-sections.

to interpret short wavelength heterogeneities, and we do not discuss here structures with wavelengths smaller than 1000 km.

3. 3D Model of NE Asia

[8] Figure 2 shows ray density for our model. Of the ~80,000 seismograms analyzed, 13,055 seismograms from 3671 earthquakes recorded at 51 seismographs passed the stringent test of the automated waveform inversion [*Debayle*, 1999]. In a full synthetic experiment but with much lower higher mode coverage than shown in Figures 2b–2c, *Debayle et al.* [2001] demonstrated the ability of the *Cara and Lévêque* [1987] technique to isolate an anomaly located in the transition zone from the shallower and deeper structure. Depths and cross-sections for our model are shown in Figures 3a–3f; the a posteriori error for the cross-sections is shown in Figures 3g–3i.

[9] At 150 km depth (Figure 3a) the *Sv*-wavespeed varies by ±7% with high wavespeed beneath the stable, north-central parts of Asia, and low wavespeed beneath most of Mongolia, northeast China, and northeast Siberia. The lowest wavespeed upper mantle lies beneath the back arc basins to the west of the Kamchatka, Kuriles, and Japan volcanic arcs. The western part of the Sino-Korean Craton is underlain by high *Sv*-wavespeed upper mantle, but low wavespeed upper mantle lies beneath the eastern parts of the craton. Some of these features are noted in previous phase [*Trampert and Woodhouse*, 1995; *Ekstrom et al.*, 1997; *Curtis et al.*, 1998; *van Heijst and Woodhouse*, 1999] and group [*Ritzwoller and Levshin*, 1998] velocity maps of Asia. At 250 km depth (Figure 3b) the range in wavespeed has decreased to ±3% and the strong division between high wavespeed beneath the stable region of north-central Asia and low wavespeed beneath the tectonically active areas has disappeared.

[10] The vertical cross-sections (Figures 3d–3f) show significant lateral variations in the thickness of the high velocity lid. It is well known that in regions where the resolution is low, the a posteriori error nearly equals the a priori error [*Tarantola and Valette*, 1982]. Because of the large number of higher modes included in the analysis, the a posteriori error is low (<0.035 km s^{-1}) compared to the a priori error (set at 0.05 km s^{-1}) over most of the cross-sections (Figure 3g–3i), indicating that we have good resolution to at least 350 km depth. The Hangai Dome in western Mongolia is underlain by a low *Sv*-wavespeed at shallow depth (<125 km) but high *Sv*-wavespeed at greater depths. Using the strongest negative gradient in *Sv*-wavespeed as an indicator for the bottom of the high velocity lid, we estimate the upper mantle lid base to lie between 175 and 225 km depth beneath most of the Siberian platform. However, a thicker lithosphere may exist beneath isolated parts of the Siberian platform.

4. Discussion and Conclusions

[11] *Lerner-Lam and Jordan* [1983] suggest that the tectonically stable part of northern Eurasia, including the Siberian platform, has a thick seismic lithosphere extending to ~400 km depth. *Artemieva and Mooney* [2001] found the thermal lithosphere beneath the Siberian platform to be ~350 km thick. Our model, based on an unprecedented higher mode regional waveform dataset, shows that the seismic lithosphere, as defined by the high velocity lid, is moderately thick beneath most of the Siberian platform, in better agreement with recent global tomography [*Ritsema and van Heijst*, 2000a] which includes higher modes for good vertical resolution, but with weaker horizontal resolution compared to this study. A moderately thick (~200 km) seismic lithosphere agrees well with the thermal structure proposed for the Siberian platform from petrologic modeling of upper mantle nodules from Siberian kimberlites [*Pearson et al.*, 1995]. Isolated high wavespeed anomalies extend down to ~250 km beneath small regions of the Siberian platform and these features may partially reconcile our seismic model with the thermal model of *Artemieva and Mooney* [2001].

[12] High velocity seismic lithosphere, although attenuated, persists to the west of the Siberian platform in our model, similar to that seen in recent global models [*Ritsema and van Heijst*, 2000a]. This observation is compatible with

cratonic-like basement lying buried beneath the west Siberian basin [D. Ionov, personal communications, 2002]. *Debayle and Kennett* [2000] found that the thickness of the high velocity lid beneath the fast-moving Australian plate oscillates around 200 km, and *Ritsema and van Heijst* [2000b] find a similar lid thickness beneath the cratons on the slow-moving African plate. Our finding of a comparable lid thickness beneath the Siberian platform on the slow-moving Eurasian plate suggests that very thick cratonic roots may be less common than previously supposed.

[13] **Acknowledgments.** Most of this work was done while K. Priestley was an invited professor at the Ecole and Observatoire des Sciences de la Terre in Strasbourg. We thank J.J. Levêque for discussions on tomography issues, M. Cara, D. McKenzie and B.L.N. Kennett for helpful comments on the manuscript, and Sylvana Pilidou for help with GMT plotting. Constructive reviews by J. Ritsema, A. Zollo, and an anonymous reviewer helped improve this manuscript. We would like to thank Rick Benson and the IRIS DMS for providing the data used in this study. This work is supported by the INSU program 'Intérieur de la Terre'. Supercomputer facilities were provided by the French 'Institute for Development and Resources in Intensive Scientific Computing' (IDRIS). This is Cambridge University Department of Earth Sciences contribution 7249.

References

Alsina, D., and R. Snieder, Constraints on the velocity structure beneath the Tornquist-Teisseyre Zone from beam-forming analysis, *Geophys. J. Int.*, *126*, 205–218, 1996.

Artemieva, I. M., and W. D. Mooney, Thermal thickness and evolution of Precambrian lithosphere: A global study, *106*, 16,387–16,414, 2001.

Bassin, C., G. Laske, and G. Masters, The current limits of resolution for surface wave tomography in North America, *81*, 897, 2000.

Cara, M., and J. J. Lévêque, Waveform inversion using secondary observables, *14*, 1046–1049, 1987.

Cotte, N., H. A. Pedersen, M. Campillo, V. Farra, and Y. Cansi, Off-great-circle propagation of intermediate-period surface waves observed on a dense array in the French Alps, *Geophys. J. Int.*, *142*, 825–840, 2000.

Curtis, A., J. Trampert, R. Snieder, and B. Dost, Eurasian fundamental mode surface wave phase velocities and their relationship with tectonic structures, *103*, 26,919–26,947, 1998.

Debayle, E., SV-wave azimuthal anisotropy in the Australian upper-mantle: Preliminary results from automated Rayleigh waveform inversion, *Geophys. J. Int.*, *137*, 747–754, 1999.

Debayle, E., and B. L. N. Kennett, The Australian continental upper mantle: Structure and deformation inferred from surface waves, *105*, 25,423–25,450, 2000.

Debayle, E., J. J. Lévêque, and M. Cara, Seismic evidence for a deeply rooted low-velocity anomaly in the upper mantle below the northeastern Afro/Arabian continent, *Earth Planet. Sc. Lett.*, *193*, 423–436, 2001.

Ekstrom, G., J. Tromp, and E. W. F. Larson, Measurements and global models of surface wave propagation, *102*, 8137–8157, 1997.

Goodwin, A., *Precambrian Geology: The dynamic evolution of the continental crust*, 666 pp., Academic Press, San Diego, Calif., 1991.

Jahn, B. M., G. Gruau, R. Capdevila, J. Cornichet, A. Nemchin, R. Pidgeon, and V. A. Rudnik, Archean crustal evolution of the Aldan Shield, Siberia: Geochemical and isotopic constraints, *Precambrian Res.*, *91*, 333–363, 1998.

Jaupart, C., and J. C. Mareschal, The thermal structure and thickness of continental roots, *Lithos*, *48*, 93–114, 1999.

Kennett, B. L. N., Approximations for surface-wave propagation in laterally varying media, *Geophys. J. Int.*, *122*, 470–478, 1995.

Lerner-Lam, A., and T. Jordan, Earth structure from fundamental and higher-mode waveform analysis, *Geophys. J. R. Astron. Soc.*, *56*, 759–797, 1983.

Levshin, A., M. Ritzwoller, and L. Ratnikova, The nature and cause of polarization anomalies of surface waves crossing Northern and Central Eurasia, *117*, 577–591, 1994.

Montagner, J. P., Regional three-dimensional structures using long-period surface waves, *Ann. Geophys.*, *4*, 283–294, 1986.

Nataf, H.-C., and Y. Ricard, 3SMAC: An *a priori* tomographic model of the upper mantle based on geophysical modeling, *95*, 101–122, 1996.

Pearson, D. G., S. B. Shirey, R. W. Carlson, F. R. Boyd, N. P. Pokhilenko, and N. Shimizm, Re-Os, Sm-Nd, and Rb-Sr isotope evidence for thick Archean lithospheric mantle beneath the Siberian craton modified by multistage metasomatism, *Geochimica et Cosmochimica Acta*, *59*, 959–977, 1995.

Ritsema, J., and H. van Heijst, Seismic imaging of structural heterogeneity in the Earth's mantle: Evidence for large scale mantle flow, *Science Progress*, *83*, 243–259, 2000a.

Ritsema, J., and H. van Heijst, New seismic model of the upper mantle beneath Africa, *Geology*, *28*, 63–66, 2000b.

Ritzwoller, M., and A. Levshin, Eurasian surface wave tomography: Group velocities, *103*, 4839–4878, 1998.

Tarantola, and Valette, Generalized nonlinear inverse problems, *20*, 219–232, 1982.

Spetzler, J., J. Trampert, and R. Snieder, The effect of scattering in surface wave tomography, *Geophys. J. Int.*, *149*, 755–767, 2002.

Trampert, J., and J. Woodhouse, Global phase velocity maps of Love and Rayleigh waves between 40 and 150 seconds, *122*, 675–690, 1995.

van Heijst, H., and J. Woodhouse, Global high-resolution phase velocity distributions of overtone and fundamental-mode surface waves determined by mode branch stripping, *Geophys. J. Int.*, *137*, 601–620, 1999.

Woodhouse, J. H., Surface waves in a laterally varying layered structure, *37*, 461–490, 1974.

Yoshizawa, K., and B. L. N. Kennett, Determination of the influence zone for surface wave paths, *Geophys. J. Int.*, *149*, 440–453, 2002.

E. Debayle, IPGS - EOST (Ecole et Observatoire des Sciences de la Terre) 5, rue Rene Descartes, F67084 Strasbourg Cedex, France. (eric@tomo.u-strasbg.fr)

K. Priestley, Bullard Laboratories Madingley Rise, Madingley Road, Cambridge, CB3 0EZ, United Kingdom. (keith@esc.cam.ac.uk)

DISTRIBUTION LIST
DTRA-TR-03-33

DEPARTMENT OF DEFENSE

DEFENSE TECHNICAL INFORMATION CENTER
8725 JOHN J. KINGMAN ROAD,
SUITE 0944
FT. BELVOIR, VA 22060-0944
2 CYS ATTN: DTIC/OCA

DEFENSE THREAT REDUCTION AGENCY
8725 JOHN J. KINGMAN ROAD MS 6201
FT. BELVOIR, VA 22060-6218
2 CYS ATTN: TDND/ D. BARBER

DEPARTMENT OF DEFENSE CONTRACTORS

ITT INDUSTRIES
ITT SYSTEMS CORPORATION
1680 TEXAS STREET, SE
KIRTLAND AFB, NM 87117-5669
2 CYS ATTN: DTRIAC
ATTN: DARE

WESTON GEOPHYSICAL CORPORATION
57 BEDFORD STREET
SUITE 102
LEXINGTON, MA 02420
ATTN: JAMES F. LEWKOWICZ